Real and Artificial Forces in the Control of Manipulators: Theory and Experiments

Richard Alan Volpe

21 September 1990

Submitted in partial fulfillment of the requirements
for the degree of Doctor of Philosophy

Department of Physics
The Robotics Institute
Carnegie Mellon University
Pittsburgh, PA 15213

Supported by an Air Force Laboratory Graduate Fellowship and DARPA under contract DAAA-21-89C-0001. The views and conclusions contained in this document are those of the author and should not be interpreted as representing the official policies, either expressed or implied, of the U.S. Air Force, DARPA, or the U.S. Government.

Abstract

This research has explored the problems of moving through an environment while avoiding obstacles, approaching and stably contacting a surface in that environment, and applying force to the surface. To this end, a theoretical and experimental analysis of the following topics has been performed: explicit force and impedance control, impact control, and obstacle avoidance and approach with artificial potentials.

The issue of force control has been addressed in two ways. First, a dynamic model of the manipulator / sensor / environment system has been theoretically developed and experimentally verified. With this model it has been possible to perform the second step of a detailed analysis of previously proposed force control schemes. Moreover, a theoretical framework has been developed which encompasses most control schemes proposed to date, including impedance control and explicit force control. This framework has provided a means by which to compare the stability properties of the various schemes. This theoretical analysis has been supported by experimental implementation and analysis on the CMU DDarm II.

The theoretical framework developed for force control, also yielded new insight into the problem of transition from motion through the environment to contact with it. During this transition there is impact. The developed force control framework revealed a new method of effectively controlling the impact phase and providing stable transition. This scheme has also been successfully implemented on the CMU DDarm II.

To move through an obstructed environment (possibly with moving obstacles) a local obstacle avoidance scheme based on superquadric artificial potentials has been developed. This potential formulation blends the best features of previous ones by eliminating local minima for simple environments, while not unnecessarily removing some parts of workspace. Two forms of the potential energy function provide either object avoidance or approach capability. This scheme has been implemented on the CMU DDarm II and has shown successful avoidance of multiple obstacles in real-time.

Acknowledgements

Six years of graduate school has provided me ample time to acquire a large list of people to whom I am indebted. I hope I don't forget anyone.

First and foremost, I owe my deepest thanks to my family, especially my parents. Their love for me, support of my endeavors, toleration of my quirks, and confidence in my perseverance has made the difference.

Second, I would like to thank my advisor, Pradeep Khosla. Without a good advisor I don't think graduate school would be survivable — luckily, I've had one of the best. I first met Pradeep when he was a graduate student working on the construction of the CMU DD Arm II . Later, after he became a professor in ECE, he gave me the opportunity to work with him and this manipulator. His guidance and expertise has enabled the evolution of the CMU DD Arm II system into an excellent testbed for my research. His prodding has caused me to explore fruitful avenues that I would not have otherwise pursued. The best example of this is his suggestion for me to apply for an AFSOR fellowship, which I was later awarded. His availability and critical eye, has afforded me the opportunity to quickly recognized and discard poor ideas, or foster those which were promising. Overall, he has not just been my advisor and mentor, but also a valued friend.

Next, I would like to thank Takeo Kanade. As co-director of the Robotics Institute and head of the Vision and Autonomous Systems Center, he is a quite busy person. However, he has always been available for me at important moments in my graduate career. In particular, he was the first researcher to give me, a physics student, a chance to do research in robotics. Later, when I was trying to decide between vision and manipulation as a research specialty, he provided the guidance and insight that enable my decision. He is also responsible for the extension of my elliptical potential formulation to superquadrics.

I would also like to thank Steve Shafer, my advisor while I was doing research in computer vision. While I didn't pursue vision for my thesis, I still reserve the right to return to this field in the future. I credit Steve with giving me the enthusiasm for this topic which may eventually cause my return to it. I also thank him for not being angry when I switched to manipulation.

This dissertation would not have been possible without the experimentation and implementation that is at its core. Therefore, I am really lucky to have had the support and help of Don Schmitz, Mark Delouis, Dave Stewart, and all the CS/RI support personnel. Not only did Don design the CMU DD Arm II , but he also wrote much of the code for the system. Along with Dave, he authored the real time operating system for all of the robotic systems in our lab. Mark Delouis is not only an excellent machinist, but he has also maintained all of the electronics for the system. The CS/RI community is a great place to do research, largely due to the incredible facilities and support that are available — thanks to all.

I would also like to thank all those other people who have had input into my research. Nick Papanikolopoulos and Yangsheng Xu have read my work and provided feedback on my methods and analysis. Alan Berger, Philippe Couvignou, Henry Schneiderman, and Jay Cosentino have helped with the system development. Jeff Bennett, Pete Skelly, and Greg Plesur have provided software support.

Next, I would like to thank those people who have been my comrades and cohorts over these past years. Not only have they put up with my dumb jokes and abrasive arguments, but they have been true friends. Even a short list must include: John Krumm, Dave Stewart, Djamel Bouzida, Madeleine Strum, Jeff Rickman, Bernie Renger, and all of my classmates from those pre-qualifier days in physics.

Finally, I would like to thank the Kilte cafeteria. Sad as it may seem, this place kept me fed for the better part of six years. While the food is not the best in the world, it's not bad, and better than what I had the time or inclination to prepare for myself. For too many semesters, dinner with friends at Kilte was the only bright spot in the day.

Contents

1 Introduction **1**

2 The Arm, Sensor, and Environment Model **5**
2.1 Introduction . . . 5
2.2 The Arm Model . . . 5
2.2.1 Arm Composed of a Single Mass . . . 6
2.2.2 Arm With Damping . . . 6
2.2.3 Arm With Damping and Stiffness . . . 7
2.3 Including Higher Order Arm Dynamics . . . 8
2.4 Arm Plus Environment Model . . . 8
2.5 Arm, Environment, and Sensor Model . . . 10
2.6 Arm with Dynamics, Environment, and Sensor Model . . . 11
2.7 Analysis of the Fourth Order Model . . . 13
2.7.1 Vibrational Analysis Without Damping . . . 13
2.7.2 Vibrational Analysis With Damping . . . 15
2.7.3 Hysteresis . . . 17
2.7.4 Experimental Data . . . 20
2.7.5 Simulation . . . 25
2.8 The Resultant Model . . . 28
2.9 Conclusion . . . 28

3 Discussion and Analysis of Explicit Force Control Schemes **32**
3.1 Introduction . . . 32
3.2 Force-Based Explicit Force Control . . . 32
3.2.1 Strategies for Force-Based Explicit Force Control . . . 33
3.2.2 Analysis of Force-Based Explicit Force Control . . . 34
3.2.3 Discussion of Explicit Force Control . . . 42
3.3 Position-Based Explicit Force Control . . . 44
3.3.1 Analysis of Position-Based Explicit Force Control . . . 44
3.4 Conclusions . . . 47

4 Discussion and Analysis of Impedance Control Schemes **49**
4.1 Introduction . . . 49
4.2 Zeroth, First, and Second Order Impedance . . . 50
4.3 Model Based Control . . . 50
4.4 Control with Full Dynamics . . . 51
4.4.1 Computed Torque . . . 52
4.4.2 Resolved Acceleration Control . . . 52
4.4.3 Operational Space Control . . . 52
4.4.4 Second Order Impedance Control . . . 53

4.5 Control with a Steady State Approximation . . . 54
4.5.1 Second Order Impedance Control . . . 54
4.6 Explicit Force Control within Impedance Control . . . 56
4.7 Impedance Control With Other Types of Explicit Force Control . . . 57
4.7.1 Accommodation and Resolved Rate Control . . . 57
4.7.2 Stiffness Control . . . 58
4.8 Conclusion . . . 58

5 Impact Control **60**
5.1 Introduction . . . 60
5.2 Previously Proposed Methods For Impact Control . . . 60
5.2.1 Maximal Active Damping . . . 60
5.2.2 Passive Compliance and Damping . . . 61
5.2.3 Integral Explicit Force Control . . . 61
5.2.4 Impedance Control and Proportional Explicit Force Control . . . 61
5.3 Impact Control . . . 62
5.3.1 Impact Control Without Sensor Dynamics . . . 62
5.3.2 Impact Control With Sensor Dynamics . . . 65
5.4 Conclusion . . . 65

6 Experimental Results **69**
6.1 Introduction . . . 69
6.2 Explicit Force Control . . . 69
6.2.1 Proportional Gain with Feedforward Control . . . 69
6.2.2 Integral Gain Control . . . 70
6.2.3 PD Control . . . 70
6.2.4 Second Order Low Pass Filter Control . . . 76
6.3 Impedance Control . . . 76
6.3.1 Impedance Control Without Dynamics Compensation . . . 80
6.3.2 Impedance Control With Dynamics Compensation . . . 80
6.4 Explicit Force and Impedance Control Conclusions . . . 82
6.5 Impact Control . . . 84
6.5.1 Integral Control . . . 85
6.5.2 Proportional Gain Control with Feedforward . . . 85
6.5.3 Impedance Control . . . 87
6.5.4 Discussion of Impact Control Results . . . 87
6.6 Results with a Stiff Steel Environment . . . 90
6.6.1 Explicit Force Control on the Steel Environment . . . 90
6.6.2 Impact Control on the Steel Environment . . . 92
6.6.3 Discussion of Results with the Steel Environment . . . 94
6.7 Implementation Considerations . . . 94
6.7.1 The Velocity Signal . . . 94
6.7.2 The Force Signal . . . 95
6.7.3 Hybrid Control Switching . . . 96
6.8 Conclusion . . . 96

7 Superquadric Artificial Potential Functions **98**
7.1 Introduction . . . 98
7.2 Review of Obstacle Avoidance . . . 99
7.3 Attributes of Artificial Potentials . . . 100
7.4 Superquadric Potentials . . . 103

7.4.1 Superquadric Isopotential Contours . . . 103
7.4.2 Repulsive Potential Energy Functions . . . 107
7.5 Addition of Superquadric Avoidance Potentials and an Attractive Well . . . 108
7.5.1 Addition of A Superquadric Avoidance Potential to a Distant Attractive Well . . . 111
7.5.2 Addition of a Superquadric Avoidance Potential to a Close Attractive Well: Dynamic Potentials . . . 113
7.6 Simulation . . . 115
7.6.1 End Effector Interaction . . . 115
7.6.2 Link Interaction . . . 116
7.6.3 Simulation Experiments . . . 117
7.7 Experiments . . . 120
7.8 Conclusion . . . 120

8 Summary and Conclusions 125
8.1 Contributions . . . 125
8.2 Conclusions . . . 126
8.3 Future Directions . . . 127

A Previous Work in Explicit Force Control 128
A.1 Force Based Explicit Force Control . . . 128
A.1.1 Proportional Control . . . 128
A.1.2 Integral Control . . . 129
A.1.3 Proportional / Integral Control . . . 129
A.1.4 Proportional / Derivative Control . . . 130
A.1.5 Other . . . 130
A.2 Position Based Explicit Force Control . . . 131

B The CMU DD Arm II System 132
B.1 Physical Description . . . 132
B.2 The CMU DD Arm II System Architecture . . . 132

List of Figures

1.1 Position control block diagram. . . . 2
1.2 Explicit force control block diagram. . . . 2
1.3 Impedance control block diagram. . . . 3
1.4 Impedance control block diagram with the controller divided. . . . 4
1.5 Impedance control block diagram redrawn to show the inner explicit force controller. . . . 4

2.1 Single mass arm model. . . . 6
2.2 Block diagram for a single mass arm model. . . . 6
2.3 Single mass arm model with damping. . . . 7
2.4 Block diagram for single mass arm with damping. . . . 7
2.5 Single mass arm model with damping and stiffness. . . . 7
2.6 Block diagram for single mass arm with damping and stiffness. . . . 7
2.7 Revision of block diagram in Figure 2.6 to show explicit force command. . . . 8
2.8 Physical model of arm with higher order dynamics. . . . 8
2.9 Physical model of a second order arm interacting with second order environment. . . . 9
2.10 Block diagram for model in Figure 2.9. . . . 9
2.11 System of Figure 2.9 modified to include sensor dynamics. . . . 10
2.12 Block diagram of system in Figure 2.11. . . . 11
2.13 Revision of block diagram in Figure 2.12 to show commanded force. . . . 11
2.14 Physical model of sixth order system. . . . 12
2.15 General fourth order model of arm, sensor, and environment system. . . . 12
2.16 Linear relationship of force to displacement. . . . 18
2.17 Force as a function of displacement with hysteresis present. . . . 19
2.18 Force as a function of velocity with hysteresis present. . . . 20
2.19 Experimental setup for force oscillation experiments. . . . 21
2.20 Force versus position data for arm pushing quasi-statically on environment. . . . 22
2.21 Force versus position data for static compression of force sensor with a clamp. . . . 22
2.22 The measured time response of force, position, and velocity after the system has been excited. 23
2.23 The measured damping of the environment. . . . 23
2.24 The measured hysteresis curve of force versus position. . . . 24
2.25 The measured hysteresis curve of force versus velocity. . . . 24
2.26 The addition of the measured position and velocity, multiplied by the determined constants, yields a close match to the measured force. . . . 26
2.27 Simulated time response of position, velocity, and force, using the estimated parameter values. 26
2.28 Simulation result of force versus velocity using estimated parameters. . . . 27
2.29 Simulation result of force versus position using estimated parameters. . . . 27
2.30 Simulated time response of position, velocity, and force using modified parameter values. . . 29
2.31 Simulation result of force versus velocity using the modified parameters. . . . 29
2.32 Simulation result of force versus position using modified parameters. . . . 30
2.33 The poles and zeros of the fourth order system. . . . 30

2.34 An enlargement of Figure 2.33 showing all but the leftmost pole of the original plot. 31

3.1 Block diagram of a generic force-based, explicit force controller. 33
3.2 Root locus for the fourth order model under proportional gain explicit force control. 35
3.3 Enlargement of root locus in Figure 3.2. 35
3.4 Bode plots for the fourth order system under proportional gain explicit force control. 36
3.5 Block diagram a force-based explicit force controller with proportional gain and unity feedforward. 37
3.6 Block diagram a force-based explicit force controller with proportional gain and extra feedback for reaction force compensation. 37
3.7 Root locus for the fourth order model under integral gain explicit force control. 38
3.8 Enlargement of root locus in Figure 3.7. 39
3.9 Bode plots for the fourth order system under integral gain explicit force control. 40
3.10 Comparison of proportional and integral gain root loci. 41
3.11 Root locus for the fourth order model under derivative gain explicit force control. 41
3.12 Enlargement of root locus in Figure 3.11. 42
3.13 Bode plots for the fourth order system under derivative gain explicit force control. 43
3.14 Block diagram of a generic position-based, explicit force controller. 44
3.15 Reformulation of the block diagram of generic position-based, explicit force controller. . . . 45
3.16 Root locus for the fourth order model under explicit force control with a second order lowpass filter. 46
3.17 Enlargement of root locus in Figure 3.16. 47
3.18 Bode plots for the fourth order system under explicit force control with a second order lowpass filter. 48

5.1 Root locus for the second order model under proportional gain explicit force control. 62
5.2 Root locus for the second order model under negative proportional gain explicit force control. 63
5.3 Enlargement of root locus in Figure 5.2. 63
5.4 Root locus for the second order model for $K'_{fp} = K_{fp} - 1$. 64
5.5 Bode plots for the second order system under negative proportional gain explicit force control. 66
5.6 Root locus for the fourth order model under negative proportional gain explicit force control. 67
5.7 Enlargement of root locus in Figure 5.6. 67
5.8 Root locus for the fourth order model for $-1 \leq K_{fp} < \infty$ or $0 \leq K'_{fp} < \infty$. 68

6.1 Experimental data of proportional gain explicit force control with feedforward. 71
6.1 (continued) Experimental data of proportional gain explicit force control with feedforward. . 72
6.2 Experimental data of integral gain explicit force control. 73
6.3 Experimental data from PD control. 74
6.4 Filtered and unfiltered force signals. 74
6.5 Calculated force derivative used in PD control. 75
6.6 The lag of the filtered force causes the force derivative to be in phase with the measured force. 75
6.7 Experimental data of second order low pass force controller. 77
6.7 (continued) Experimental data of second order low pass force controller. 78
6.7 (continued) Experimental data of second order low pass force controller. 79
6.8 Experimental data of impedance control without dynamics compensation. 81
6.8 (continued) Experimental data of impedance control without dynamics compensation. 82
6.9 Experimental data of impedance control with dynamics compensation. 83
6.9 (continued) Experimental data of impedance control with dynamics compensation. 84
6.10 Experimental data from an impact with integral force control. 85
6.11 Experimental data of proportional gain explicit force control with feedforward during impact. 86

6.11 (continued) Experimental data of proportional gain explicit force control with feedforward during impact. . . . 87
6.12 Experimental data of impedance control during impacts. . . . 88
6.13 Experimental data of impact control with transition to integral gain force control. . . . 89
6.14 Experimental data of proportional gain explicit force control with feedforward against steel environment (z direction). . . . 90
6.15 Experimental data of proportional gain explicit force control with feedforward against steel environment (x direction). . . . 91
6.16 Experimental data of integral gain explicit force control on the steel environment (z direction). 91
6.17 Experimental data of integral gain explicit force control on the steel environment (x direction). 92
6.18 Impact control on the steel pedestal in the z direction. . . . 93
6.19 Impact control on the steel pedestal in the x direction. . . . 93
6.20 Velocity phase lag due to averaging. . . . 95

7.1 A repulsive potential added to an attractive well. . . . 102
7.2 The FIRAS potential. . . . 102
7.3 The isopotential contours of the FIRAS potential in Figure 7.2. . . . 104
7.4 Local minimum creation by the FIRAS potential. . . . 104
7.5 Superquadric isopotential contours for a rectangle. . . . 106
7.6 Superquadric isopotential contours for a trapezoid. . . . 106
7.7 Superquadric isopotential contours for a triangle. . . . 109
7.8 The superquadric avoidance potential for a rectangle. . . . 109
7.9 The superquadric avoidance potential for a triangle. . . . 110
7.10 The superquadric approach potential for a rectangle. . . . 110
7.11 The superquadric approach potential for a triangle. . . . 114
7.12 Dynamic superquadric avoidance potential. . . . 114
7.13 Successful avoidance of an obstacle using the FIRAS potential. . . . 118
7.14 Unsuccessful avoidance of an obstacle using the FIRAS potential. . . . 118
7.15 Successful avoidance by a two link manipulator of an obstacle surrounded by a superquadric potential. . . . 118
7.16 Geometrically limited motion of a two link manipulator avoiding an obstacle surrounded by a superquadric potential. . . . 119
7.17 Successful avoidance by a three link, redundant manipulator of an obstacle surrounded by a superquadric potential. . . . 119
7.18 Successfully navigation around four obstacles (a). . . . 121
7.19 Successfully navigation around four obstacles (b). . . . 121
7.20 Smooth approach and contact of a rectangle surrounded by a superquadric approach potential. 122
7.21 Smooth approach and contact of a triangle surrounded by a superquadric approach potential. 122
7.22 Experimental data from one obstacle avoidance. . . . 122
7.23 Experimental data from two obstacle avoidance. . . . 124

B.1 The hardware of the CMU DD Arm II system. . . . 133
B.2 System architecture for the CMU DD Arm II. . . . 134

Chapter 1

Introduction

A very general description of a robot manipulator is a non-rigid mechanical assembly with actuating devices that exert forces along the degrees of freedom. Usually the assembly is composed of rigid links, but increasingly flexible links are being employed. Usually the links are made of metal, but alternative materials are sometimes utilized. Usually the links are connected serially (like the bones of an 'arm'), but sometimes there are parallel connections. Usually the connections are rotary, but sometimes they are prismatic. Usually the forces are exerted by electric motors, but often there are hydraulic or pneumatic actuation systems. Independent of the particular manifestation of the robot manipulator, the problem that remains is to *control* it, or dictate its behavior. More specifically: given a manipulator, how should the actuating devices be commanded, such that the proper forces are exerted along the degrees of freedom, resulting in a desired behavior?

Preliminary to answering the control question is the need for a description of the desired behavior. In general, the desired behavior of a manipulator is to do useful work on the environment, or to *manipulate* it. (The environment being everything that is not part of the robot, and within its reach.) By formal definition and heuristic description, work always entails force and motion. Thus, the manipulator must move to specific locations in its environment and impart specific forces. There are three distinct phases to this process: motion through the environment, impact with the environment, and exertion of forces on the environment. The purpose of this dissertation is to examine ways to provide a manipulator with the ability to perform well in each of these phases, and to smoothly move from one phase to another.

Motion through the environment can be completely described in terms of the position of the manipulator. Impact and forceful interaction with the environment require a description in terms of force as well as position. Thus we can see that a specific description of the desired behavior of a manipulator can be provided in terms of the positions it occupies and possibly the forces it exerts. (The derivatives of these quantities, such as velocity, may be obtained from them directly.) We can therefore rephrase the above statement of the control problem: How should the actuating devices be commanded such that the manipulator occupies the desired position and exerts the desired force on the environment?

Implicit in the statement of this problem is the ability to monitor the actual position of the manipulator and the forces exerted by it. If this is not done, it is impossible to determine the performance of the robot arm. However, if this is done the commands to the actuating devices are a function not only of the desired position and force values, but also of the measured ones. This process is known as *feedback control*. The function that relates the desired and measured values to the actuation command is called the *controller*. Thus, it is the controller that is key to our problem, which can be rephrased once again: What are the best position and force controllers for robot manipulators?

The qualitative description of 'best' is usually supported with many quantitative measurements: stability, rise time, overshoot, settling time, steady-state error, tracking error, algorithmic complexity, control rate, etc. Usually there is a trade-off in performance between each of these. And how each of these should relate to the desired task is often unclear. What usually is clear is whether a particular controller is sufficient for the desired task. An appraisal of this sufficiency can usually be obtained from the above criteria.

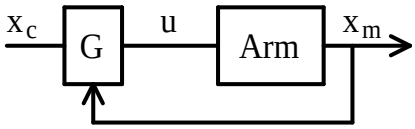

Figure 1.1: Position control block diagram.

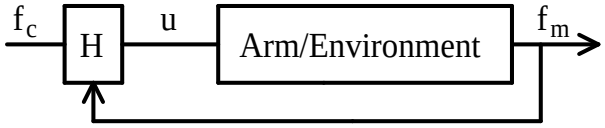

Figure 1.2: Explicit force control block diagram.

In an attempt to achieve sufficiency, simple schemes are usually tried first. It is common that the controller be composed of a simple differencing between the desired and measured values. This difference may then be multiplied by a proportionality constant (P control), differentiated (D control), and/or integrated (I control). PID control is often incorporated into more sophisticated schemes, yielding better results.

Thus, when position control was historically selected first to be investigated, PID position controllers were the choice. However, position controllers have evolved from simple PID joint controllers to very sophisticated algorithms that include dynamic model calculations, Cartesian space projections of errors, velocity and acceleration feedback, adaptive gains, optimization, etc. Figure 1.1 shows the block diagram of a generic position control scheme. Each of the above controllers are represented by the block lettered G.

The state of the art of manipulator position control far exceeds that of manipulator force control. In fact, position controlled manipulators can be used to perform some tasks that require interaction with the environment, such as pick and place operations and spot welding. However, these allowed tasks usually require that the manipulator does not contact a stiff, mechanically grounded environment. Such contact can result in large reaction forces exerted on the arm for very small position errors. Since many manipulators are not backdriveable because of their gearing, these reaction forces will cause damage to the manipulator. Also, the environment may be damaged by this excessive force. One simplistic solution is to insert mechanical compliance between the position controlled manipulator and the environment. However, this compliance is open loop, and adds uncontrolled degrees of freedom to the manipulator structure.

Further, there are a whole class of tasks that seem to implicitly require force control of the manipulator: pushing, scraping, grinding, pounding, polishing, twisting, etc. Thus, force control of the manipulator becomes necessary in at least one of the degrees of freedom of the manipulator; the other degrees of freedom remain position controlled. Mason formalized this idea and called it Hybrid Control [45]. Simply put, the manipulator should be force controlled in directions in which the position is constrained by environmental interaction, and position controlled in all orthogonal directions.

The Hybrid Control formalism does not specify what particular type of position or force control should be used. It only partitions the space spanned by the total degrees of freedom into one subspace in which position control is employed, and another in which force control is employed. In the position control subspace, the previously mentioned strategies remain successful. However, in the force control subspace, two main conceptual choices have emerged: *explicit force control* and *impedance control*. Figures 1.2 and 1.3 are simple block diagrams of these two types of control schemes. The major difference between these schemes is the commanded value: explicit force control requires commanded force, while impedance control requires commanded position. In order for these to be feedback controllers, explicit force control needs force measurement, while impedance control needs position measurement. In addition, impedance control requires force measurement — without it an impedance controller reduces to a position controller.

These force control strategies must perform two specific functions. First, they must provide *impact control*: stability during the transient phase of impact with the environment. Second, they must provide *force*

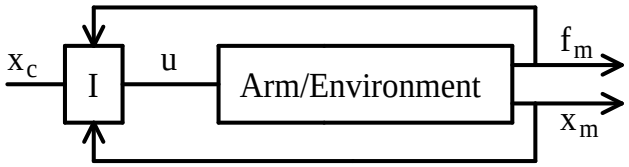

Figure 1.3: Impedance control block diagram.

trajectory tracking capability. It is not necessary or expected that a controller which is best for impact control is also best for force tracking. The study of force controllers in this thesis will conclusively determine which form is best for each function.

Ideally, an explicit force controller attempts to make the manipulator act as pure force source, independent of position. Like position control, the obvious first choice has been some manifestation of PID control (i.e. P, PD, PI, etc.). These have met with varying amounts of success depending on the characteristics of the particular actuators, arm links, sensor, and environment. All of these components have dynamics which may be excited during constrained motion. Therefore, considering the success of complex position controllers, it may be valuable to include some of the following in force control algorithms: extensive models of the above dynamic components (possibly non-linear), adaptive compensation, friction compensation, etc. But these more complex control schemes will probably include PID control within them, and the best form of PID has not been conclusively shown before. Therefore, much of this thesis has concentrated on understanding PID control as an explicit force controller.

Alternatively, impedance control has been presented as a method of stably interacting with the environment. This is achieved by providing a *dynamic* relationship between the robot's position and the force it exerts. A complete introduction to impedance control is beyond the scope of this discussion and the reader is referred to the previous work of other researchers [22, 28]. The basic tenet of impedance control is that the arm should be controlled so that it behaves as a mechanical impedance to positional constraints imposed by the environment. This means that the force commanded to the actuators is dependent on its position: $f = \mathcal{Z}(x)$, where $\mathcal{Z}$ may be a function or an operator. If the impedance is linear, it can be represented in the Laplace domain as $F(s) = Z(s)X(s)$. (For comparison, an equivalent and possibly more familiar electrical impedance equation relates voltage to current: $V(s) = Z(s)i(s)$.) The resultant behavior of the manipulator is obvious: if it is unconstrained it will accelerate; if it is constrained the forces from the actuators will be transmitted through the arm and exerted on the environment.

In the first case of no environmental interaction, the impedance relation may be used to dictate the force exerted on the manipulator by its actuators as a function of the position of the end effector. This force as a function of position may be fully described in terms of a potential field. Sophisticated position control strategies can be devised by suitable construction of *artificial potentials* that model the environment yet do not really exist in it. This thesis presents a new strategy based on superquadric artificial potentials that is useful for object avoidance and approach.

However, the artificial potential formulation as a position control method is essentially *open loop* impedance control — open loop with respect to real, measurable forces. When dealing with the second case of physical environmental interaction, force feedback must be used in the control of the mechanical impedance of the manipulator. For linear impedance relationships, the force feedback loop may be separated as in Figure 1.4. Further, it can be seen that this figure may be modified as in Figure 1.5 to show that the force feedback loop is part of an internal explicit force controller. Thus, an impedance controller that utilizes force feedback contains an explicit force controller.

Figure 1.5, as simple as it may be, summarizes this entire thesis. First, it can be seen that an arm / environment model is necessary for the plant of the system. This model is developed in the next chapter. Second, an explicit force controller is present in the system. A theoretical analysis of a complete spectrum of explicit force control strategies is given in Chapter 3. Third, the outer position loop indicates that this is an

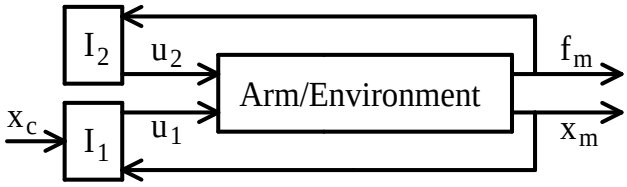

Figure 1.4: Impedance control block diagram with the controller divided into its position part, I_1, and its force part, I_2.

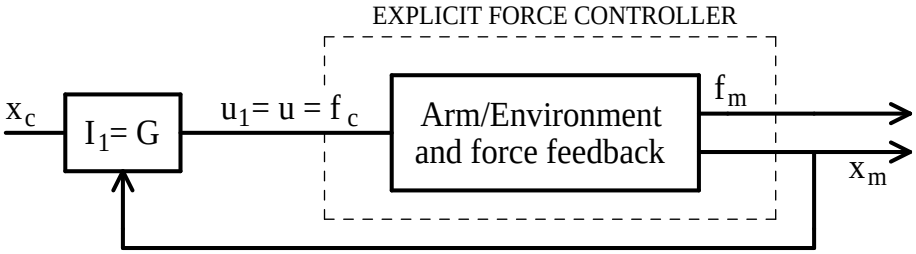

Figure 1.5: Impedance control block diagram redrawn to show the inner explicit force controller.

impedance controller. A theoretical analysis of a complete spectrum of impedance control strategies is given in Chapter 4. Fourth, the presence of both force and position state variables indicates that the system must cope with moving through the environment to contact with it. The control of the intervening period of impact is discussed in Chapter 5. Chapter 6 provides experimental results which strongly support the conclusions of the force, impedance, and impact control chapters. Also, the structure of the controller does not preclude the substitution of a calculated (instead of measured) quantity for the feedback force. Chapter 7 presents a method of object avoidance and approach that relies on such artificial forces.

Finally, it is noteworthy that the order of presentation in this dissertation is the reverse of the physical sequence of motion through the environment, impact, and force exertion. The inversion of the order was apparent in the above breakdown of the components of the controller block diagram of Figure 1.5. This reverse order permits the understanding of each underlying layer of the problem in turn, facilitating the step by step understanding of a complete problem solution.

Chapter 2

The Arm, Sensor, and Environment Model

2.1 Introduction

In the previous chapter a general description of controllers was given without any specific description of the arm or environment that formed the plant to be controlled. To discuss the controllers more specifically, it is first necessary to develop a detailed model of the arm, sensor, and environment system. Also, it is necessary to convincingly demonstrate that this model is an accurate and sufficient representation of the plant for which the controller will be developed. Previous research has not experimentally evaluated the correctness of the plant model or only done so on a one degree of freedom (DOF) system [13, 14, 31, 74]. In this chapter, models of increasing complexity will be discussed. Then, experimentation with a six DOF manipulator will show the validity and sufficiency of the chosen arm / sensor / environment model.

2.2 The Arm Model

A full description of the dynamics of a serial, n DOF, rigid-link robot arm is provided by the following equation:

$$\tau = D(\theta)\ddot{\theta} + h(\theta, \dot{\theta}) + g(\theta) + V(\dot{\theta}) \tag{2.1}$$

where τ is a vector of the joint torques, D is the inertia matrix, h is a vector of the nonlinear Coriolis and centripetal forces, g is a vector of the gravitational forces, V is a vector of the passive damping forces (possible non-linear), and θ is a vector of the angular joint positions. All vectors are $n \times 1$, all matrices $n \times n$. A full development of this equation can be found in [16].

In this discussion it is assumed that g, and V either do not exist or are eliminated by some form of active compensation. For an earth based robot, g may be compensated for by a feedforward signal; a space based arm, however, would need no such compensation. For a direct drive arm V does not exist; for a viscously damped arm it may be eliminated by active feedback [10].

Thus, without any loss of generality, the manipulator may be represented simply by an equation that includes joint torques, inertia, and acceleration:

$$\tau = D(\theta)\ddot{\theta} + h(\theta, \dot{\theta}) \tag{2.2}$$

In Section 4.4.3 it will be shown that if the arm is not in a singular configuration, the inverse of the Jacobian may be used to express this dynamic relationship in Cartesian space as:

$$F = \Lambda(\theta)\ddot{x} + \mu(\theta, \dot{\theta}) \tag{2.3}$$

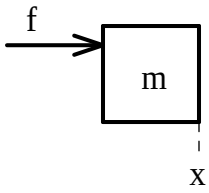

Figure 2.1: Single mass arm model.

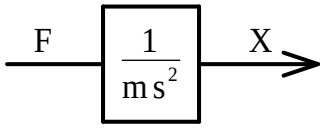

Figure 2.2: Block diagram for a single mass arm model.

where

$$\Lambda(\theta) = (JD^{-1}J^T)^{-1} \tag{2.4}$$

and

$$\mu(\theta, \dot{\theta}) = -\Lambda \dot{J}\dot{\theta} + (J^T)^{-1}h(\theta, \dot{\theta}). \tag{2.5}$$

Since μ is a function of θ and $\dot{\theta}$ it may be actively compensated for in the same manner as g and V above. If the arm is constrained and $\dot{\theta}$ is small, then μ may be ignored [28, 19]. Either way, a linear, n DOF model in Cartesian space is obtained.

This model is still more complex than necessary. Since Λ is not usually diagonal, the forces and accelerations from different directions are coupled. However Λ can be diagonalized. In order to simplify the analysis it will be assumed that the Cartesian end effector frame is aligned with the eigenvectors of Λ. Thus, each DOF may be considered independently. Although a translational DOF is used for the following discussions, the results are directly applicable to rotational DOFs as well.

2.2.1 Arm Composed of a Single Mass

The initial model chosen for analysis is a second order lumped parameter system which has discrete dynamic attributes that include mass, damping, and stiffness. Figure 2.1 shows the arm represented as a mass, m, acted upon by a force, f, and at a position, x. This simple system is represented by the equation:

$$m\ddot{x} = f. \tag{2.6}$$

which has the frequency domain transfer function:

$$\frac{X}{F} = \frac{1}{ms^2}. \tag{2.7}$$

Figure 2.2 shows a block diagram for this system.

2.2.2 Arm With Damping

An initial modification to this model is performed by explicit inclusion of damping. As mentioned earlier, damping may be naturally present in the arm, may be actively included, or both. Figure 2.3 shows a physical model of the system. The equation of motion is:

$$m\ddot{x} \;=\; f - (c + K_v)\dot{x} \tag{2.8}$$

where c is the natural damping and K_v is the active damping. The transfer function for this system is:

$$\frac{X}{F} = \frac{1}{ms^2 + (c + K_v)s}. \tag{2.9}$$

The block diagram for this system is shown in Figure 2.4. Since the experimental studies were with the CMU DD Arm II which has practically no natural damping, only the active damping case ($c = 0$) will be considered unless otherwise noted.

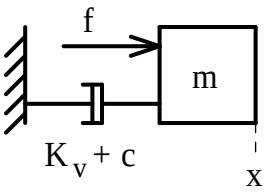

Figure 2.3: Single mass arm model with damping.

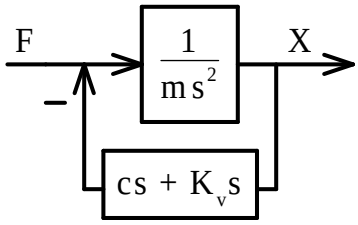

Figure 2.4: Block diagram for single mass arm with damping.

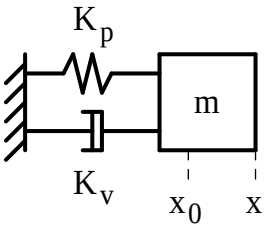

Figure 2.5: Single mass arm model with damping and stiffness.

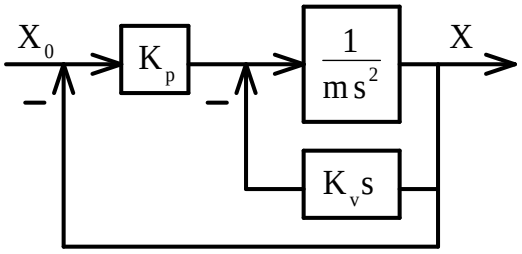

Figure 2.6: Block diagram for single mass arm with damping and stiffness.

2.2.3 Arm With Damping and Stiffness

Another modification to the above model is the inclusion of stiffness. Again, the arm may have stiffness due to its mechanical structure or due to active stiffness control. Since the natural stiffness is due to the flexibility of the materials that make up the arm it is typically much larger than the active stiffness. Also, if the manipulator has at least six Cartesian DOF, there is no direction in which the stiffness is only composed of mechanical stiffness. Thus, this natural stiffness is usually ignored. The next section will discuss a case in which it is not. Note, this is the dynamic situation as viewed by the actuators and does not include nonlinear phenomena such as stiction. For instance, if the gearing of a manipulator is not back-driveable, the arm may be mechanically very stiff from the environment. Many actuators, including direct and harmonic drives, are back-driveable however.

The active stiffness of a manipulator is usually provided by proportional control of the position. In this case, the desired actuator force is given by $f = K_p(x_0 - x)$, where x_0 is the commanded position, and K_p is position gain of the active controller and determines the stiffness of the system. Figure 2.5 shows a physical model of the system. The equation of motion is:

$$m\ddot{x} = K_p(x_0 - x) - K_v\dot{x} \tag{2.10}$$

the corresponding transfer function for this system is:

$$\frac{X}{X_0} = \frac{K_p}{ms^2 + K_v s + K_p}. \tag{2.11}$$

which is depicted in the block diagram shown in Figure 2.6.

It is worth noting that the above does not necessarily have to be represented as a position controlled system. If $f = K_p x_0$ is considered to be the desired actuator force, then the equation of motion is:

$$m\ddot{x} = f - K_p x - K_v\dot{x} \tag{2.12}$$

A clear physical diagram of this is not really possible. However, using the transfer function for this system,

$$\frac{X}{F} = \frac{1}{ms^2 + K_v s + K_p}. \tag{2.13}$$

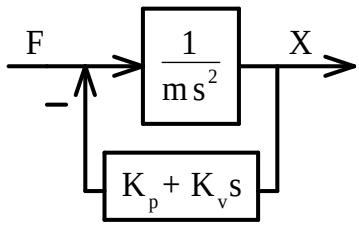

Figure 2.7: Revision of block diagram in Figure 2.6 to show explicit force command.

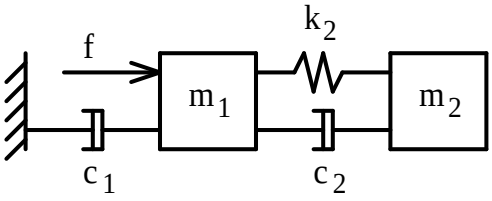

Figure 2.8: Physical model of arm with higher order dynamics.

it can be shown that the controller block diagram becomes Figure 2.7. This representation will be useful later.

2.3 Including Higher Order Arm Dynamics

Representing the arm as a second order system prevents the modeling of any higher order modes of vibration. It has been recognized by some researchers that the arm has higher order dynamics that may need to be modeled [13, 14, 53, 74]. Figure 2.8 shows a two mass, fourth order model of a robot arm. The extra dynamics provided by k_2 and c_2 exist within the actuators or the arm linkage. When included in the following discussions, it is assumed that these dynamics are from the linkage, since the CMU DD Arm II has no actuator dynamics. Therefore, the dynamics represent the manipulator beyond the actuator.

For the position controlled arm with rigid links that is not interacting with the environment, this case is meaningless for two reasons. First the stiff links will not have their dynamics excited by the manipulator motion in free space. Second, the actuation forces are usually based on the position of a degree of freedom read at the actuator location. For example, joint resolvers are mounted on the motor axis. The actual location of the end effector is never known, but assumed to be correctly calculated by the forward kinematics. If the links are flexed, the joint positions may erroneously indicate that the arm's end effector is positioned correctly. Thus, the actuation forces in the block model depend on the position of mass m_1; the varying position of m_2 does not effect the controller (except by the disturbance of the reaction forces transmitted through k_2 and c_2).

The link flexibilities may become important if the arm is force controlled and if the force measurements are made at the endpoint of the arm. This issue will be further discussed below after the environment and force sensor models have been introduced. Until then, the second order arm model will be used.

2.4 Arm Plus Environment Model

Now that a model of the manipulator has been introduced, it is necessary to discuss an environmental model. Some researchers have made no assumptions about the structure of the environment, and have assumed instead that interaction with it will produce measurable forces [54, 24, 22, 28, 18, 43]. Other researchers, usually those working with a compliant system or sensor, have modelled the environment as a mechanical ground [56, 71]. Still others have recognized that the environment has some compliance, and therefore have modelled it as a simple stiffness [69, 70, 50, 31, 51, 12, 26, 36, 73, 25, 11]. Finally, other researchers have modeled the environment as a complete second order system with components of mass and damping, as well as stiffness [13, 14, 28, 74]. This last form of the environmental model recognizes that the environment has oscillatory modes of its own, but simplifies the overall analysis by only considering the first mode. Thus, the second order model is more restrictive than just a general environment that exerts measurable force on the arm. However, the specific representation of its dynamic components will permit a better understanding of the interaction between the arm and the environment.

Using a second order model, it is valuable to explicitly describe the interaction of the environment with the arm model. Figure 2.9 shows the coupled system, where m_e, c_e, and k_e represent the modeled environmental

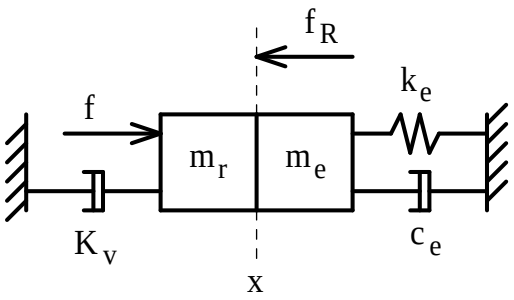

Figure 2.9: Physical model of a second order arm interacting with second order environment.

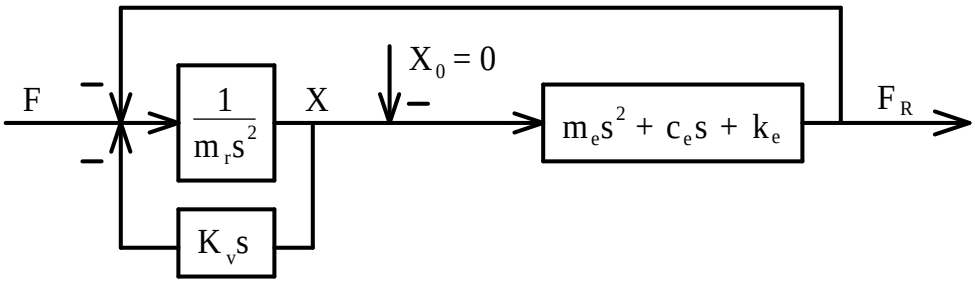

Figure 2.10: Block diagram for model in Figure 2.9.

mass, damping, and stiffness, and f_R is the reaction force exerted by the environment on the arm. The undisturbed position of the environment, x_0, is assumed to be zero without any loss of generality. The disturbed position is the same as the arm position, x.

Notice that the arm mass and environmental mass are directly in contact. However, for this system to provide force controlled interaction there must be a force sensor. Initially, it will be assumed that a 'magic' force sensor exists between the masses. The measured force is then equivalent to the reaction force: $f_m = f_R$. Also, the manipulator position is equal to the environmental position: $x = x_r = x_e$. All this implies is that the sensor dynamics are not being modelled, which is reasonable if the arm and environment stiffnesses are much less than that of the sensor. Since the force sensor used consists of strain gauges mounted on aluminum, it has a very high stiffness, satisfying the assumption. In the next section the model will be expanded to include sensor dynamics; until then it is useful to proceed with the development without them.

The model of the arm and environment can be described by the following set of equations:

$$m_r\ddot{x} = f - f_R - K_v\dot{x} \tag{2.14}$$
$$m_e\ddot{x} = f_R - k_e x - c_e\dot{x} \tag{2.15}$$

or

$$(m_r + m_e)\ddot{x} + (K_v + c_e)\dot{x} + k_e x = f \tag{2.16}$$
$$m_e\ddot{x} + c_e\dot{x} + k_e x = f_R. \tag{2.17}$$

These equations illustrate the concepts of impedance and admittance presented by Hogan [22]. In that framework it can be seen that the first equation shows how the actuation force f exerted on the system yields a position x. And complementary to this, the second equations shows that the position constraint, x, impressed on the environment, yields a reaction force, f_R. Viewed in this way, it can be seen that the block diagram in Figure 2.10 represents the system in Figure 2.9. From the block diagram, the transfer function of the system is:

$$\frac{F_r}{F} = \frac{F_m}{F} = \frac{m_e s^2 + c_e s + k_e}{(m_r + m_e)s^2 + (K_v + c_e)s + k_e}. \tag{2.18}$$

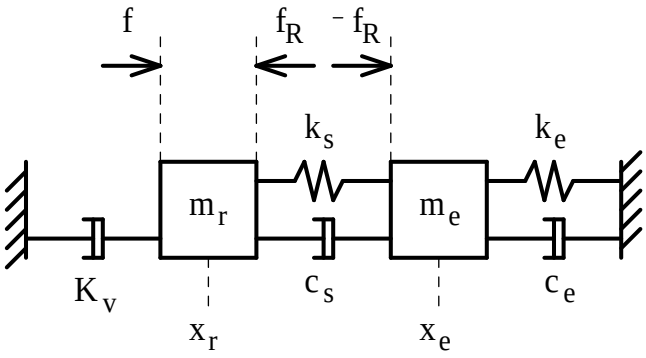

Figure 2.11: System of Figure 2.9 modified to include sensor dynamics.

2.5 Arm, Environment, and Sensor Model

While a very stiff force sensor may not always exhibit its dynamics, under certain circumstances they may become important. The use of a stiff robot position controller, contact with a stiff environment, or impact with the environment may excite the sensor dynamics. Therefore, it is sometimes necessary to include the sensor in the model. A second order model of the sensor dynamics can be included in the previous model by placing a spring and damper between the robot mass and environment mass, as shown in Figure 2.11. Any mass that the sensor may have is included in either the arm or environment mass. The sensor stiffness is k_s, and its damping is c_s. Also x_r and x_e are the robot and environment positions (that is, the positions of their mass components). The reaction force experienced by the arm is labeled f_R. The negative of this force, $-f_R$, is experienced by the environment, since the sensor spring and damper are ideal components and transmit forces applied to them.

This modified system may be described by the following equations:

$$m_r\ddot{x}_r = f - K_v\dot{x}_r - k_s(x_r - x_e) - c_s(\dot{x}_r - \dot{x}_e) \quad (2.19)$$

$$m_e\ddot{x}_e = -k_s(x_e - x_r) - c_s(\dot{x}_e - \dot{x}_r) - k_e x_e - c_e\dot{x}_e. \quad (2.20)$$

These can be rewritten in terms of the reaction force as:

$$m_r\ddot{x}_r + K_v\dot{x}_r = f - f_R \quad (2.21)$$

$$m_e\ddot{x}_e + c_e\dot{x}_e + k_e x_e = f_R \quad (2.22)$$

and

$$f_R = k_s(x_r - x_e) + c_s(\dot{x}_r - \dot{x}_e) \quad (2.23)$$

The Laplace transforms of the above equations yields three useful intermediate transfer functions for the arm (A), environment (E), and sensor (S).

$$A = \frac{X_r}{F - F_R} = \frac{1}{m_r s^2 + K_v s} \quad (2.24)$$

$$E = \frac{X_e}{F_R} = \frac{1}{m_e s^2 + c_e s + k_e} \quad (2.25)$$

$$S = \frac{F_R}{X_r - X_e} = c_s s + k_s \quad (2.26)$$

Thus the block diagram of the system can be constructed as shown in Figure 2.12. The transfer function for the sensor and environment (G), relating X_r to F_R, is given by:

$$G = \frac{F_R}{X_r} = \frac{S}{1 + SE} = \frac{(m_e s^2 + c_e s + k_e)(c_s s + k_s)}{m_e s^2 + (c_s + c_e)s + (k_s + k_e)} \quad (2.27)$$

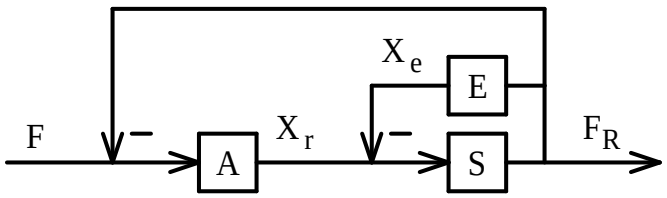

Figure 2.12: Block diagram of system in Figure 2.11.

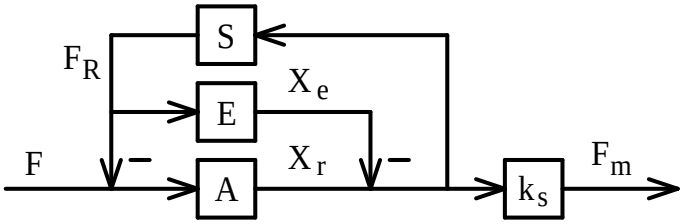

Figure 2.13: Revision of block diagram in Figure 2.12 to show commanded force.

The dynamics of the sensor can be removed if $k_s \to \infty$ and $k_e \to 0$. Then the above equation reduces to:

$$G = m_e s^2 + c_e s + k_e \tag{2.28}$$

which is the same as the environmental transfer function alone, as shown in Figure 2.10.

Further, the entire transfer function, relating F to F_R, may be obtained as:

$$\frac{F_R}{F} = \frac{AG}{1+AG} = \frac{AS}{1+AS+ES} \tag{2.29}$$

$$= \frac{(m_e s^2 + c_e s + k_e)(c_s s + k_s)}{(m_e s^2 + (c_s + c_e)s + (k_s + k_e))(m_r s^2 + c_r s) + (m_e s^2 + c_e s + k_e)(c_s s + k_s)} \tag{2.30}$$

Again, the dynamics of the sensor can be removed if $k_s \to \infty$ and $k_e \to 0$. The transfer function then reduces Equation (2.18), which is just the transfer function of the system without the sensor, as expected.

Equation (2.30) is not, however, the transfer function which can be used for control purposes. This is because the force sensor does not measure the reaction force, f_R, but instead measures the deformation of the sensor spring, $x_r - x_e$. This measurement is multiplied by the spring constant, k_s, to obtain the measured force value, f_m. The revised block diagram is shown in Figure 2.13. The revised transfer function is:

$$\frac{F_m}{F} = \frac{Ak_s}{1+AS+ES} = \frac{(m_e s^2 + c_e s + k_e)k_s}{(m_e s^2 + (c_s + c_e)s + (k_s + k_e))(m_r s^2 + c_r s) + (m_e s^2 + c_e s + k_e)(c_s s + k_s)} \tag{2.31}$$

which has the same characteristic equation as before, while the numerator has only been changed by the omission of the sensor damping. Equation (2.31) agrees with the result derived in reference [13].

Thus, a model of the coupled arm, environment, and sensor system has been established. Although this model ignores arm dynamics, a modified interpretation of the model components can address the discrepancy. This will be discussed in the next section.

2.6 Arm with Dynamics, Environment, and Sensor Model

Following the discussion from the previous three sections, it seems necessary to include the dynamics of the arm and force sensor. Including both would require a sixth order model as shown in Figure 2.14. However,

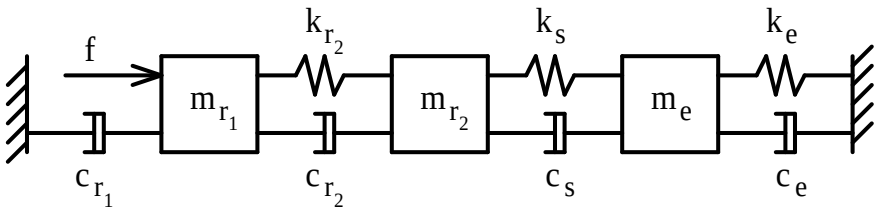

Figure 2.14: Physical model of sixth order system.

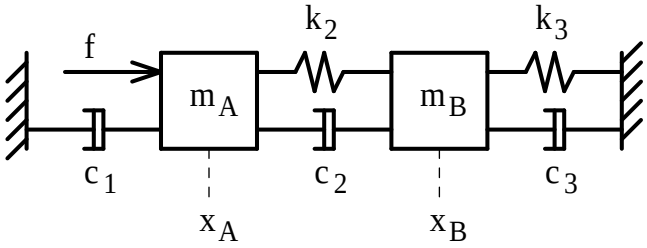

Figure 2.15: General fourth order model of arm, sensor, and environment system.

this is unnecessarily complex, and the order of the model can be reduced. As was described in Section 2.3, the dynamics attributed to the arm are beyond the actuator. These dynamics are due to vibration of the physical structure of the manipulator. For the case of the CMU DD Arm II , this structure is made of aluminum. As was described in Section 2.4 the force sensor is also made of aluminum. Neither of these physical structures has the discrete dynamic components that have been used to represent them. Instead, they are distributed systems whose modes of dynamic excitation have been represented by a discrete system approximation. Since the arm structure and force sensor are of similar construction and connected physically, they should be treated as a single unit. And since only lowest order modes of excitation have been of concern, the arm structure and force sensor can be represented as a single second order system. Thus, the previous model can be reduced, and represented by the general model in Figure 2.15. Similarly, the previous transfer function, Equation (2.31) can be rewritten as:

$$\frac{F_m}{F} = \frac{(m_B s^2 + c_3 s + k_3)k_2}{(m_B s^2 + (c_2 + c_3)s + (k_2 + k_3))(m_A s^2 + c_1 s) + (m_B s^2 + c_3 s + k_3)(c_2 s + k_2)} \tag{2.32}$$

While this model appears to be the same as in Figure 2.11, it represents slightly different components of the physical system.

Similar to the earlier model, the parameters k_3 and c_3 represent the stiffness and damping of the environment. Also, the parameters k_1 and c_1 are the stiffness and damping of the arm. As discussed previously, it is usually assumed that $k_1 = 0$, but it is useful in the following analysis to keep this parameter in the equations for symmetry purposes.

Unlike before, the parameter m_A represents mass of the actuator, arm, *and* sensor, while the parameter m_B represents mass of the environment, sensor, *and* arm. As described above, this overlap is due to the fact that the arm beyond the actuator and the sensor are lumped together in a first order model. Part of their total mass must be on either side of the spring and damper which causes any oscillation. This spring and damper are represented by k_2 and c_2. These parameters are equal to the serial addition of the stiffness and damping from the outer arm and sensor:

$$k_2 = \frac{1}{\frac{1}{k_s} + \frac{1}{k_{\text{outerarm}}}} \qquad c_2 = \frac{1}{\frac{1}{c_s} + \frac{1}{c_{\text{outerarm}}}} \tag{2.33}$$

Considering that the outer arm is made of the same material as the sensor but is longer in length, its stiffness is just a fraction of the sensor stiffness. This is true for the damping as well. Thus,

$$k_s = \frac{k_{\text{outerarm}}}{\lambda} \qquad c_s = \frac{c_{\text{outerarm}}}{\lambda} \tag{2.34}$$

and, therefore,

$$k_s = (1+\lambda)k_2 \qquad c_s = (1+\lambda)c_2 \tag{2.35}$$

where λ is the nonnegative proportionality factor and is linearly related to the relative lengths of the outer arm and the force sensor (assuming constant cross sectional area). Considering the relative lengths of the CMU DD Arm II linkage and the Lord force sensor, it is expected that λ will be on the order of ten for this system.

Thus, a fourth order model has been developed for the arm, sensor, and environment system which considers only first order vibrations in each of these components. Further analysis of these vibrations is presented in the following sections.

2.7 Analysis of the Fourth Order Model

Given the model previously developed, it is necessary and important to explore its validity. To do this, a vibrational analysis will be performed and the effects of hysteresis will be discussed. Subsequently, the analytic results will be compared with experimental results.

2.7.1 Vibrational Analysis Without Damping

In this section a vibrational analysis of the model shown in Figure 2.15 will be performed. Similar analysis can be found in many standard physics textbooks [58]. However, the analysis here deals with the asymmetric case and an approximate result will be derived for the case of underdamped vibration.

First, the kinetic and potential energy of the system are:

$$T = \frac{1}{2}m_A\dot{x}_A^2 + \frac{1}{2}m_B\dot{x}_B^2 \tag{2.36}$$

$$V = \frac{1}{2}k_1x_A^2 + \frac{1}{2}k_2(x_B - x_A)^2 + +\frac{1}{2}k_2x_B^2. \tag{2.37}$$

Lagrange's formulation may be used to obtain the equations of motion:

$$\frac{d}{dt}\left(\frac{\partial L}{\partial \dot{x}_i}\right) - \frac{\partial L}{\partial x_i} = Q_i \tag{2.38}$$

where $L = T - V$ and Q_i are the generalized forces. Direct application yields:

$$m_A\ddot{x}_A + k_1x_A - k_2(x_B - x_A) = -c_1\dot{x}_A - c_2(\dot{x}_A - \dot{x}_B) + f \tag{2.39}$$

$$m_B\ddot{x}_B + k_1x_B + k_2(x_B - x_A) = -c_3\dot{x}_A - c_2(\dot{x}_B - \dot{x}_A) \tag{2.40}$$

The general solutions

$$x_A = A_Ae^{pt} \qquad x_B = A_Be^{pt} \tag{2.41}$$

are used, where p is a complex number and A_A and A_B are constants. Thus, the equations may be written as:

$$\begin{bmatrix} m_Ap^2 + c_Ap + k_A & -(c_2p + k_2) \\ -(c_2p + k_2) & m_Bp^2 + c_Bp + k_B \end{bmatrix} \begin{bmatrix} x_A \\ x_B \end{bmatrix} = 0 \tag{2.42}$$

where

$$k_A = k_1 + k_2 \tag{2.43}$$
$$k_B = k_2 + k_3 \tag{2.44}$$
$$c_A = c_1 + c_2 \tag{2.45}$$
$$c_B = c_2 + c_3. \tag{2.46}$$

The modes of vibration can be obtained by ignoring the damping forces (i.e. let $f = c_1 = c_2 = c_3 = 0$). Thus, the equations reduce to the eigenvalue formulation:

$$\begin{bmatrix} \frac{k_A}{m_A} + p^2 & \frac{-k_2}{m_A} \\ \frac{-k_2}{m_B} & \frac{k_B}{m_B} + p^2 \end{bmatrix} \begin{bmatrix} x_A \\ x_B \end{bmatrix} = 0 \tag{2.47}$$

The determinant of the matrix yields the characteristic equation of the system:

$$p^2 + p\left(\frac{k_A}{m_A} + \frac{k_B}{m_B}\right) + \frac{k_A k_B - k_2^2}{m_A m_B} = 0, \tag{2.48}$$

which has the solution:

$$p^2 = -\frac{m_B k_A + m_A k_B}{2 m_A m_B}\left[1 \pm \sqrt{1 - \frac{4 m_A m_B \left(k_A k_B - k_2^2\right)}{\left(m_B k_A + m_A k_B\right)^2}}\right]. \tag{2.49}$$

If the argument of the square root is less than one and greater than zero, p is purely imaginary. From Equations (2.43) and (2.44) it is apparent that the term $k_A k_B - k_2^2$ is positive. Therefore, its worst case value is $k_A k_B - k_2^2 \rightarrow k_A k_B$. In this case the argument of the radical becomes:

$$1 - \frac{4 m_A m_B \left(k_A k_B\right)}{\left(m_B k_A + m_A k_B\right)^2} = \frac{\left(m_B k_A - m_A k_B\right)^2}{\left(m_B k_A + m_A k_B\right)^2} < 1 \tag{2.50}$$

Thus p is a purely imaginary number, $i\omega$, where ω is the natural frequency of the coupled system and an eigenvalue of the equations. For the case of no robot actuator stiffness ($k_1 = 0$), this reduces to:

$$\omega^2 = \frac{m_B k_2 + m_A (k_2 + k_3)}{2 m_A m_B}\left[1 \pm \sqrt{1 - \frac{4 k_2 k_3 m_A m_B}{\left(m_B k_2 + m_A (k_2 + k_3)\right)^2}}\right]. \tag{2.51}$$

It is useful to consider the situation when $k_2 \gg k_3$ (relatively soft environment) while k_1 remains zero. For these conditions the above equation reduces to:

$$\omega^2 \approx \frac{k_2 (m_A + m_B)}{2 m_A m_B}\left[1 \pm \left(1 - \frac{2 k_3 m_A m_B}{k_2 (m_A + m_B)^2}\right)\right] \tag{2.52}$$

(using the binomial expansion, $(1 + x)^n \approx (1 + nx)$, for small x). The two eigenfrequencies are thus:

$$\omega_1 \approx \sqrt{\frac{k_3}{m_A + m_B}} \quad \text{and} \quad \omega_2 \approx \sqrt{k_2\left(\frac{1}{m_A} + \frac{1}{m_B}\right)}. \tag{2.53}$$

These results make intuitive sense. The lower frequency ω_1 corresponds to the case of m_a and m_b acting as a rigid body oscillating on k_3 at ω_1. Similarly, the higher frequency ω_2 corresponds to the case of m_A and m_B oscillating out of phase on spring k_2, neglecting any effect of k_3.

Using the above eigenvalues, the eigenvectors of the system may be obtained. Equation (2.47) provides a relation between the components of the vectors:

$$x_A = \frac{(k_2 + k_3) - m_B\omega^2}{k_2} x_B. \tag{2.54}$$

Again considering the case of $k_2 \gg k_3$, and $k_1 = 0$, the eigenvectors are obtained:

$$\mathbf{v_1} = \begin{bmatrix} 1+\epsilon \\ 1 \end{bmatrix} \qquad \mathbf{v_2} = \begin{bmatrix} -m_B/m_A \\ 1 \end{bmatrix} \tag{2.55}$$

where ϵ is a small positive value. These vectors correspond directly to the oscillatory modes described above. Note, these vectors are not orthogonal, which is to be expected since the matrix in Equation (2.47) is not symmetric.

2.7.2 Vibrational Analysis With Damping

Having solved for these oscillatory modes, it is useful to look at the case with damping. In this case, the characteristic equation may be obtained from Equation (2.42) as:

$$\begin{aligned} p^4 m_A m_B + p^3(m_B c_A + m_A c_B) \; &+ \; p^2(m_B k_A + m_A k_B + c_A c_B - c_2^2) \\ &+ \; p(c_B k_A + c_A k_B - 2c_2 k_2) + (k_A k_B - k_2^2) \; = \; 0 \end{aligned} \tag{2.56}$$

In general this will yield two complex solutions and their conjugates.

For the underdamped case, these poles will be close to the undamped poles, but moved slightly to the left of the imaginary axis. For example, consider the low frequency poles. As described in the previous section these poles represent an approximately second order system of mass equal to $m_A + m_B$ oscillating on the spring k_3. The addition of damping, $c_1 + c_3$, to this system moves the poles to the points

$$p = \frac{c_1 + c_3}{2(m_A + m_B)} \pm \sqrt{\frac{(c_1 + c_3)^2}{4(m_A + m_B)^2} - \frac{k_3}{(m_A + m_B)}} \tag{2.57}$$

or

$$p \approx \sigma \pm i\omega_1 \tag{2.58}$$

where the decay parameter σ is:

$$\sigma = \frac{c_1 + c_3}{2(m_A + m_B)} \tag{2.59}$$

and ω_1 is given in Equation (2.53). This estimation will prove useful later in this chapter when analyzing data of the oscillations of the real system.

The fourth order characteristic equation above may be solved exactly for its four poles. These values can then be used in one of the following relations, which are obtained from Equation (2.42):

$$x_B = \frac{m_A p^2 + c_A p + k_A}{c_2 p + k_2} x_A \tag{2.60}$$

$$x_B = \frac{c_2 p + k_2}{m_B p^2 + c_B p + k_B} x_A \tag{2.61}$$

Since the characteristic equation is effectively obtained by setting these two relations equal, the value of p obtained from it must yield the ratio of x_B/x_A. However, this ratio has an extremely messy exact solution. The exact solutions for p are very complicated to begin with, and then they must be substituted in one of the equations above. Little insight into the significance of the parameter values would be obtained from such a brute force solution. Instead the following assumptions are made:

1. $p \rightarrow \pm i\omega$	The system is underdamped and the eigenvalues of the undamped system will be used.
2. $k_2 \gg c_2\omega$, $k_3 \gg c_3\omega$	The system is underdamped.
3. $k_2 \gg k_3$	The arm linkage and force sensor are much stiffer than the environment.
4. $k_1 = 0$	There is no position gain in the control law, and there are no actuator dynamics. Open loop force control is used.
5. $\omega^2 = -\frac{k_3}{m_A+m_B}$	Only the low frequency oscillations will be considered.

As was stated earlier, Equations (2.60) and (2.61) must be identical. However, letting $p \approx \pm i\omega$ will remove from the first equation any dependence on the parameter c_3. Similarly, the second equation will not depend on c_1. (Terms that do not have dependence on c_1 or c_3 will remain the same.) Thus, using either equation exclusively removes information. One way around this problem is to use a solution that includes the union of terms from the two solutions based on the approximation of $p \approx \pm i\omega \approx \sqrt{k_3/(m_A + m_B)}$.

Another obstacle to a meaningful approximate solution is the fact that it is not possible to directly measure the value of x_b (at least with our experimental system). Instead, the force sensor may be used to obtain the difference between x_A and x_B:

$$f_m = k_s \Delta x_s = k_2(1+\lambda)\Delta x_s = k_2(x_B - x_A). \tag{2.62}$$

It will prove useful in this development to introduce a relation between the masses, m_A and m_B. The sum of these masses may be written as the multiple of either:

$$m_A + m_B = \alpha m_A \qquad \text{and} \qquad m_A + m_B = \beta m_B \tag{2.63}$$

or

$$m_B = (\alpha - 1)m_A \qquad \text{and} \qquad m_B = \frac{1}{\beta - 1} m_A \tag{2.64}$$

and therefore

$$\alpha = \frac{\beta}{\beta - 1} \qquad \text{and} \qquad \beta = \frac{\alpha}{\alpha - 1}. \tag{2.65}$$

Using these relations and the approximation for p yields:

$$m_A p^2 = -\frac{k_3}{\alpha} \qquad \text{and} \qquad m_B p^2 = -\frac{k_3}{\beta} \tag{2.66}$$

Thus, both Equations (2.60) and (2.61) can be used in Equation (2.62) and the union of the terms from the two results can be taken. Equation (2.60) yields:

$$\begin{aligned} f_m^{(1)} &= k_2(x_B - x_A) \qquad (2.67)\\ &= k_2 \left[\frac{m_A p^2 + c_A p + k_A}{c_2 p + k_2} - 1 \right] x_A \\ &= k_2 \left[\frac{m_A p^2 + c_1 p + k_1}{c_2 p + k_2} \right] x_A \\ &= k_2 \left[\left(\frac{-\frac{k_3}{\alpha} + c_1 p + k_1}{c_2 p + k_2} \right) \left(\frac{c_2 p^* + k_2}{c_2 p^* + k_2} \right) \right] x_A \end{aligned}$$

$$
\begin{aligned}
&= k_2 \left[\frac{c_1 c_2 |p|^2 + k_2 \left(k_1 - \frac{k_3}{\alpha}\right) + c_1 k_2 p + c_2 \left(k_1 - \frac{k_3}{\alpha}\right) p^*}{c_2^2 |p|^2 + c_2 k_2 (p + p^*) + k_2^2} \right] x_A \\
&\approx \frac{1}{k_2} \left[c_1 c_2 |p|^2 + k_2 \left(k_1 - \frac{k_3}{\alpha}\right) + p \left(c_1 k_2 - c_2 \left(k_1 - \frac{k_3}{\alpha}\right)\right)\right] x_A \\
&\approx \left[\frac{k_3 c_1 c_2}{k_2 \alpha m_A} + \left(k_1 - \frac{k_3}{\alpha}\right)\right] x_A + \left[c_1 + \frac{c_2}{k_2}\left(\frac{k_3}{\alpha} - k_1\right)\right] \dot{x}_A
\end{aligned} \tag{2.68}
$$

Similarly, Equation (2.61) yields:

$$
f_m^{(2)} \approx \left[-\frac{k_3 c_2 c_3}{k_2 \alpha m_A} - \frac{k_3 c_3^2}{k_2 \alpha m_A} - \frac{k_3}{\alpha} - \frac{k_3^2}{k_2 \alpha^2}\right] x_A + \left[\frac{k_3 c_2}{k_2 \alpha} - c_3 \right] \dot{x}_A \tag{2.69}
$$

Comparing Equations (2.68) and (2.69) it is seen that those terms which do not contain c_1 or c_3 appear in both expressions. In particular, c_3 terms do not appear in the first result, and c_1 terms do not appear in the second result. This is just as expected. To gain a good first order approximation of the equation for f_m it is necessary to include all terms that appear at least once in both results. This gives:

$$
f_m \approx \left[\frac{k_3}{k_2 \alpha m_A} \left(c_2 \left(c_1 - c_3 \right) - c_3^2 \right) - \frac{k_3}{\alpha} \left(1 + \frac{k_3}{k_2 \alpha} \right) + k_1 \right] x_A + \left[c_1 - c_3 + \frac{c_2}{k_2} \left(\frac{k_3}{\alpha} - k_1 \right) \right] \dot{x}_A \tag{2.70}
$$

Using the assumptions that $k_2 \gg k_3$ and $k_1 = 0$, this reduces to:

$$
f_m \approx -\frac{k_3}{\alpha} x_A + \left[c_1 - c_3 + c_2 \frac{k_3}{k_2 \alpha} \right] \dot{x}_A \tag{2.71}
$$

(For the case of $c_3 > c_1$, this is a lower bound on the magnitude of the x_A term, and a first approximation. As can be seen in Equation (2.70), it will actually be more negative.) The above equation may be written as:

$$
f_m = -K' x_A - C' \dot{x}_A \tag{2.72}
$$

where K' and C' are the effective stiffness and damping measured by the sensor.

The relationship of f_m to x_A seems reasonable — the measured force is equal to the value of $-k_3 x_a$, modified only be the parameter α.

However, the value of C' seems strange at first glance. Obviously, the introduction of damping to the system can make the measured force proportional to the velocity, $\dot{x}_a$. However, it can be seen that this term can take on negative and positive values. For positive values, it appears at first that the system is not conservative. But a very simple and intuitive explanation can be provided to show that the system remains a conservative one.

When the system is oscillating at the low eigenfrequency the masses are moving symmetrically, with m_A having a larger amplitude than m_B. As m_A moves toward the environment, k_2 is compressed and a force is measured. However, the dampers c_1 and c_2 resist the motion of m_A. Thus, they both diminish the magnitude of the measured force.

In summary, the introduction of damping to the oscillatory system has caused a change of phase of the oscillations. This phase change shows up as a velocity term in the approximation for the measured force. In the next section the effects of this phase change on the system will detailed.

2.7.3 Hysteresis

When damping is added to an oscillating system, energy is lost during the cycle of motion. If the oscillation is maintained by a driving force, then the energy lost due to damping is replaced every cycle. However, the addition and subtraction of energy are not in phase. If they were, the damping would be instantaneously negated, and the system would oscillate as if it were undamped.

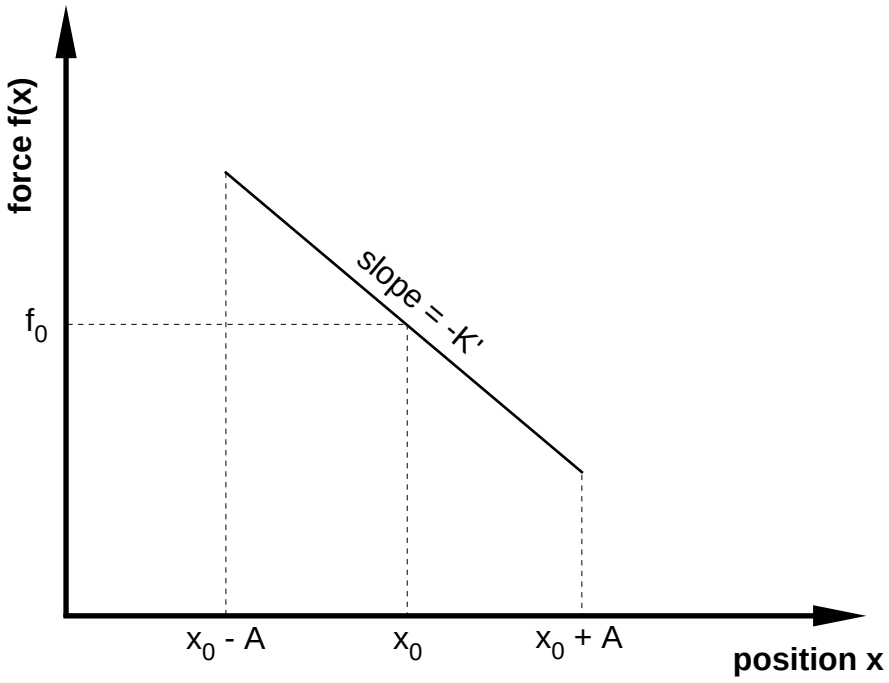

analyzed. Equation (2.72) shows that this may be thought of as a second order system with an arbitrary mass, and spring and dampers C' and K'. In this reduced model, the measured force f_m is equivalent to the sum of the forces experience by the mass:

$$f = m\ddot{x} = -K'x - C'\dot{x} \tag{2.73}$$

(For convenience, the subscripts have been dropped.) For such a system, the quasi-static motion of x would yield a straight line of slope $-K'$ and amplitude A, as shown in Figure 2.16. (Note, this figure contains an offset $f_0 = -K'x_0$ which may be added to both sides of the above equation.) For the dynamic situation in which the damped system is driven so that there is no loss in amplitude, the force is described by Figure 2.17. This makes intuitive sense. The value of f is no longer dependent on just x, but also on the direction of motion. Motion in the positive direction causes the measured force to be reduced by a negative damping force. Motion in the negative direction causes the measured force to be increased by a positive damping force. This phenomenon of the separation of the paths traveled is called *hysteresis*, and the connected curve is called a *hysteresis loop*.

A pertinent questions is: What is the geometric shape of the hysteresis loop? A steady state oscillation can be described by [59]:

$$x = A\sin(\omega t + \phi) \tag{2.74}$$

$$\dot{x} = A\omega\cos(\omega t + \phi) \tag{2.75}$$

Thus, the damping force can be obtained:

$$F_D = -C'\dot{x} = -C'A\omega\cos(\omega t + \phi) = -C'A\omega\sqrt{1 - \sin^2(\omega t + \phi)} = -C'A\omega\sqrt{1 - \left(\frac{x}{A}\right)} \tag{2.76}$$

or

$$\left(\frac{F_D}{C'A\omega}\right)^2 + \left(\frac{x}{A}\right)^2 = 1 \tag{2.77}$$

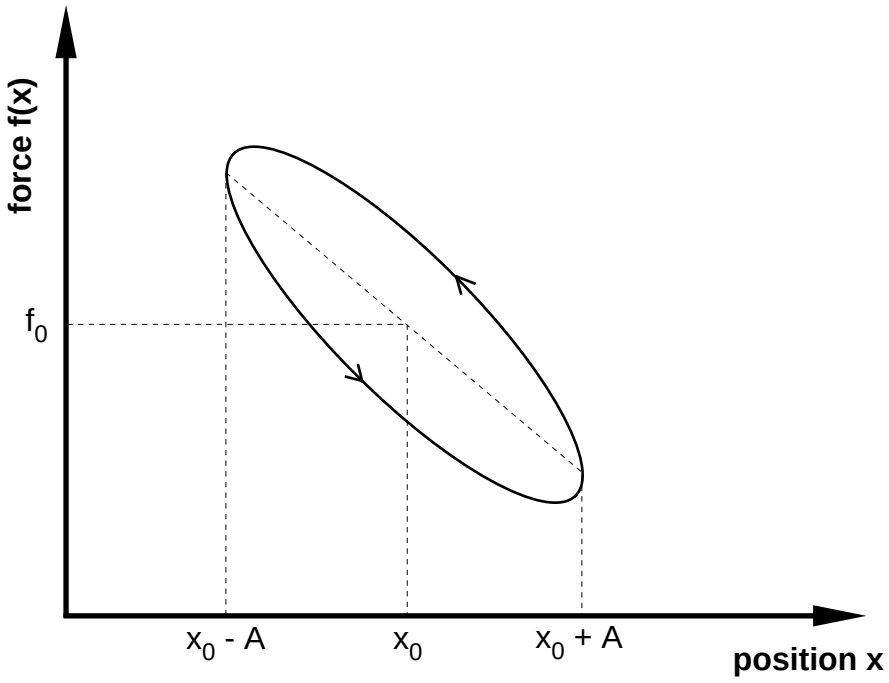

direction of travel about this hysteresis curve it is noted that when moving from the negative x direction, the damping force, $-C'\dot{x}$, must be positive for $C' > 0$. Thus, for $C' > 0$, the hysteresis loop is counterclockwise. For $C' < 0$, the hysteresis loop is clockwise.

However, this is just the description of the damping force. To get the value of the measured force, the spring force must be added as in Equation (2.73). This is the equivalent of adding a line to an ellipse. The addition of a line to an ellipse mathematically yields a rotated ellipse, but the semi-major axis is not parallel to the line. Since the slope of the line added is important, it is useful to think of the new contour as a *skew* ellipse. Thus, the addition of the spring force to the damping force yields the measured force as a skew ellipse with an axis at slope $-K'$, as shown in Figure 2.17.

A similar analysis may be performed for the hysteresis curve of $f(\dot{x})$. In this case it is the positional force which causes a separation of the paths. Therefore, it is necessary to look at the positional force, F_P:

$$F_P = -K'x = -K'A\sin(\omega t + \phi) = -K'A\sqrt{1 - \cos^2(\omega t + \phi)} = -K'A\sqrt{1 - \left(\frac{\dot{x}}{A\omega}\right)} \tag{2.78}$$

or

$$\left(\frac{F_P}{K'A}\right)^2 + \left(\frac{\dot{x}}{A\omega}\right)^2 = 1 \tag{2.79}$$

which, again, is the equation of an ellipse. The direction of travel about this hysteresis loop may be obtained by considering the situation at the extremes of oscillation when the velocity is zero. When switching from a positive to negative velocity, the force must be in the negative direction. Thus the direction of travel is clockwise for $K' > 0$.

Again, it is necessary to add an offset to obtain the measured force. From Equation (2.73) it is seen that the damping force must be added. This again yields a *skew* ellipse with an axis at slope $-C'$, as shown in Figure 2.18.

Finally, if the system is not driven to maintain a constant amplitude the oscillations will decay. This causes the continuous elliptical curves to change to elliptical spirals that converge on zero.

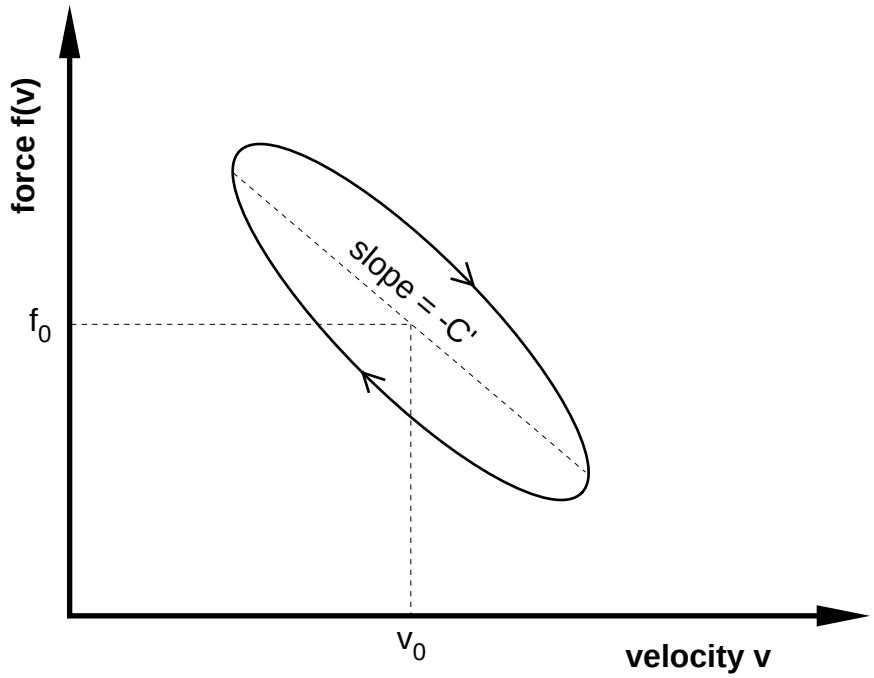

k_2 and k_3:

$$k_{\text{measured}} = \frac{k_2 k_3}{k_2 + k_3} \tag{2.80}$$

According to Approximation 3 of Section 2.7.2, the measured spring constant can be reduced to $k_3 \approx 10^4$ N/m.

(Note: In this and all subsequent data presented, the parameter f_m may be represented by MezForc_wd[2], the z component of the measured force in the world frame. Similarly, the parameter x_A may be represented by MezP[2], the z component of the measured position in world frame.)

Another test was performed to measure the stiffness of the force sensor. To do this, the sensor was removed from the arm and compressed in a C-clamp. Compression of the sensor was measured with a micrometer, and the forces were measured by the sensor itself. The data is shown in Figure 2.21. The measured spring constant, k_s was about 5×10^6 N/m.

Given this initial data, and the model development of the previous sections, it is possible to analyze the response of the entire system to small oscillations. To obtain the data, the arm was placed against the environment as shown in Figure 2.19. The arm was given an open-loop command to exert 20N of force

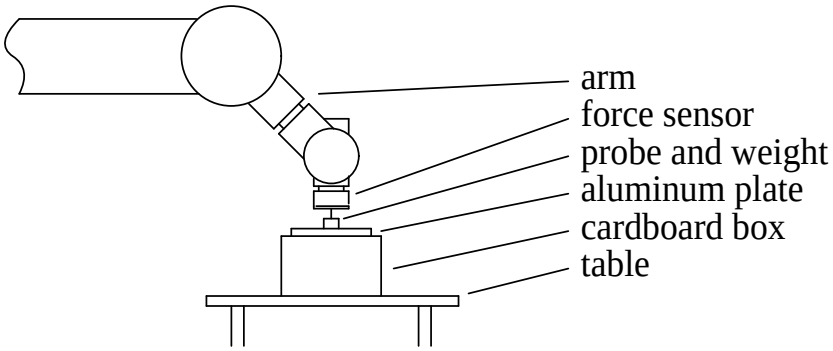

Figure 2.19: Experimental setup for force oscillation experiments.

against the surface. (Incidentally, the measured open-loop force of 18.6N indicates the need for closed-loop force control.) Then the environmental surface was struck softly so as to excite only low frequency oscillations. The measured force, position and velocity of one of these tests is shown as a function of time in Figure 2.22. While damping is present, the system is obviously underdamped, which matches the earlier assumptions.

First, the frequency of oscillation is about 90 radians/second. Equation (2.53) and Assumption 5 in Section 2.7.2 then indicate $m_A + m_B = 1.2$ kg.

Second, the environmental damping parameter c_3 may be obtained using Equation (2.59) and (2.41). Figure 2.23 is a plot of the natural logarithm of the absolute value of the peak oscillations of the measured force. The slope of the line in this graph gives the value of the decay parameter σ. This slope is -11.3. Thus, $c_3 = -2(m_A + m_B)\sigma - c_1 = 17\,\mathrm{N}\cdot\mathrm{s/m}$.

The above time response of force, position, and velocity, may also be graphed so as to show the hysteresis curves of the response. Figure 2.24 shows the measured force as a function of displacement. The slope of the elliptical spiral yields $K' \approx 10^4$ N/m. Figure 2.25 shows the measured force as a function of velocity. The slope of this elliptical spiral indicates that $C' \approx 66\ \mathrm{N}\cdot\mathrm{s/m}$. Figure 2.26 shows that these are valid values of K' and C' by comparing the measured force with the force calculated from Equation (2.72). Using these values of K' and C' in a comparison of Equations (2.72) and (2.71) should provide estimates of all unknown dynamic parameters in the fourth order model.

First, it is known that $K' \approx k_3/\alpha$. Since both K' and k_3 are approximately 10^4 N/m, $\alpha \approx 1$. However, Equation (2.64) shows that α cannot be exactly unity or m_B is zero. Therefore, it is assumed that the data indicates that $m_A \gg m_B$. It will be assumed that $\alpha \approx 1.1$, or equivalently, m_B is less than m_A by an order of magnitude: $m_B = 0.1 m_A$. Therefore, from the previous result using the frequency of oscillation, $m_A \approx 1.1$ kg and $m_B \approx 0.1$ kg.

Second, it is known that from Equations (2.72) and (2.71) that

$$c_2 \approx \frac{k_2\alpha}{k_3}(C' - c1 + c3) \tag{2.81}$$

All that is unknown is the ratio of k_2/k_3. However, from Equation (2.35) it is known that k_2 will be less than k_s. As stated then, the geometric comparison of the lengths of the force sensor and the outer arm indicated that k_2 will be about an order of magnitude less than the force sensor stiffness of 5×10^4 N/m. It is also known from Assumption 3 in Section 2.7.2 that $k_2 \gg k_3$, and therefore is at least an order of magnitude larger than the environmental stiffness of 10^4 N/m. Thus, $10^5\mathrm{N/m} < k_2 \leq 5 \times 10^5\mathrm{N/m}$. Letting $k_2 \approx 5 \times 10^4$, implies that $(1 + \lambda) = 10$, and the above equation yields $c_2 \approx 4400$.

In review, the following parameters values were obtained using the described means and assumptions:

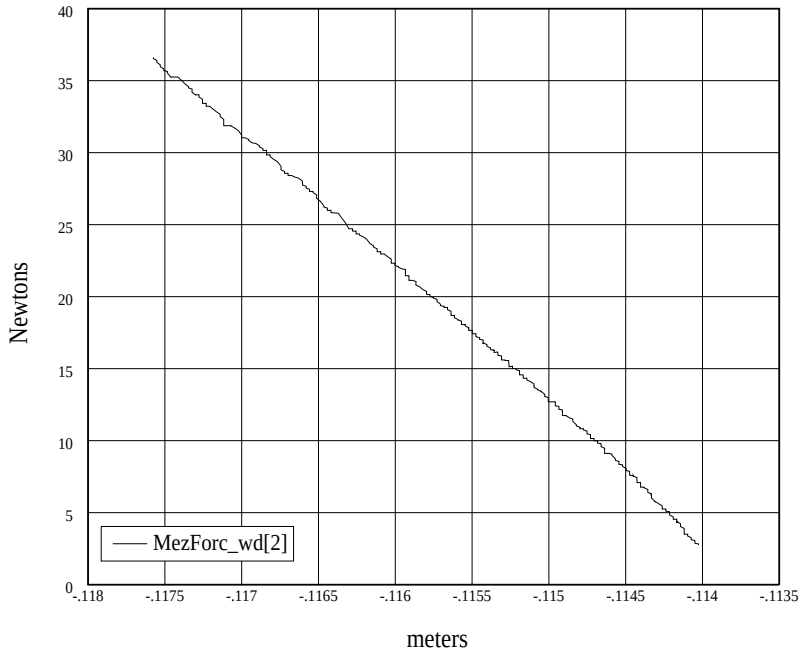

Figure 2.20: Force versus position data for arm pushing quasi-statically on environment. The slope indicates $k_e \approx 9340$ N/m.

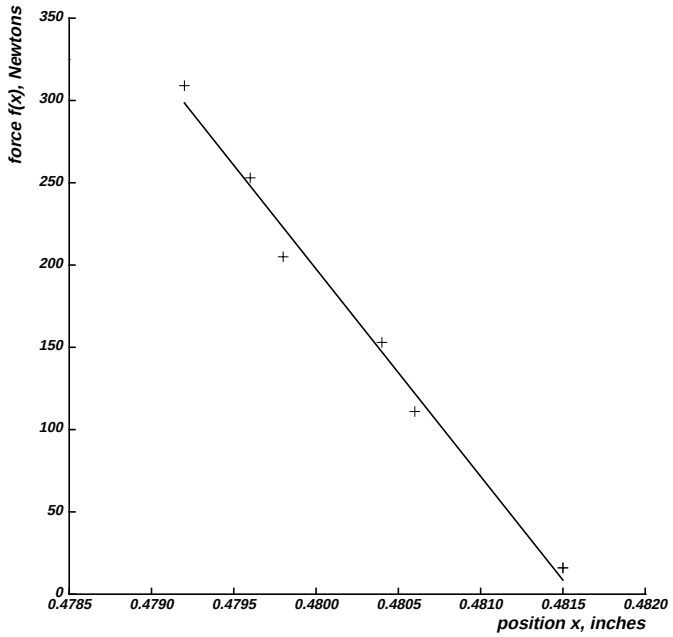

Figure 2.21: Force versus position data for static compression of force sensor with a clamp. The slope indicates $k_s = 5 \times 10^6$ N/m.

.

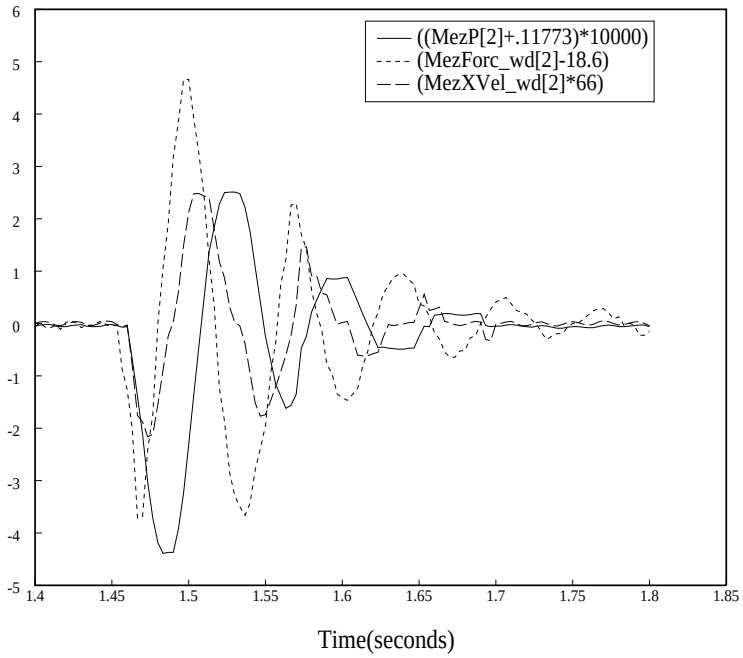

Figure 2.22: The measured time response of force, position, and velocity after the system has been excited.

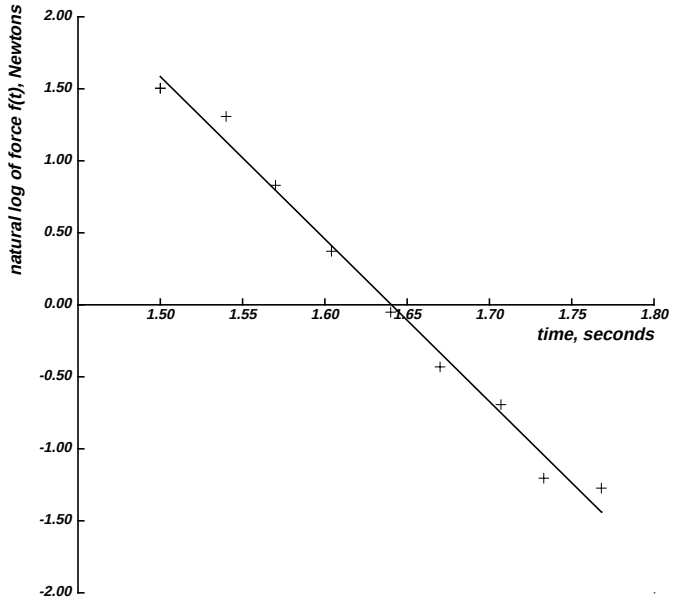

Figure 2.23: The measured damping of the environment. The slope of -11.3 is the decay constant of the environment.

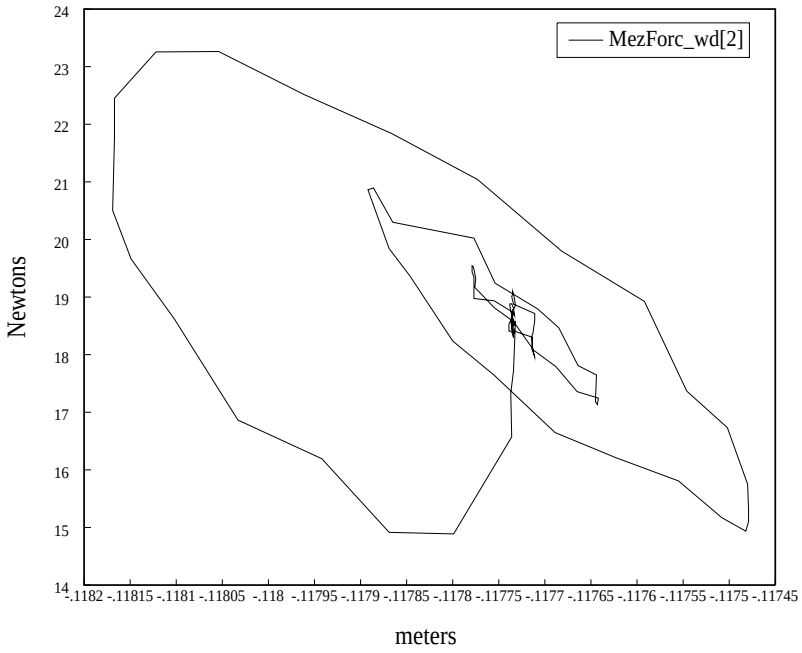

Figure 2.24: The measured hysteresis curve of force versus position.

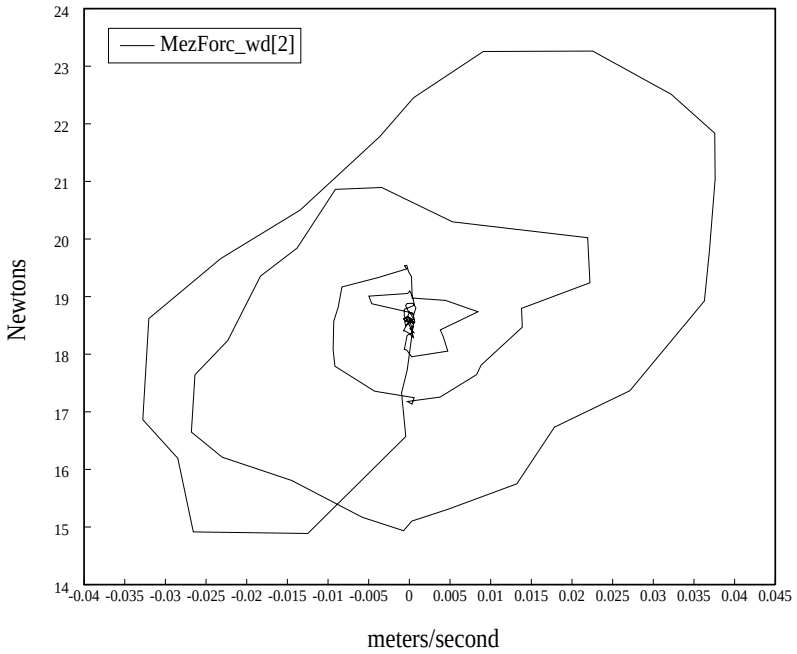

Figure 2.25: The measured hysteresis curve of force versus velocity.

$k_1 = 0$ N/m	Direct Drive motors have no intrinsic stiffness, and none was provided actively.
$k_3 \approx 10^4$ N/m	Quasi-static measurement of force versus displacement assuming $k_2 \gg k_3$.
$m_A + m_B = 1.2$ kg	Measurement of oscillating frequency, assuming low frequency underdamped vibration.
$c_3 = 17\,\mathrm{N \cdot s/m}$	Measured directly or from decay envelope.
$K' \approx 10^4$	Measurement of force versus position hysteresis loop skew.
$C' \approx 66$	Measurement of force versus velocity hysteresis loop skew.
$m_A = 1.1$ kg, $m_B = 0.1$ kg	$K' \approx k_3$ indicates $\alpha \to 1$. It is assumed that $\alpha \approx 1.1$ or $m_A/m_B \approx 10$.
$k_s = 5 \times 10^6$ N/m	Direct measurement.
$\lambda \approx 10$	Geometric estimation.
$k_2 \approx 5 \times 10^5$ N/m	Condition that $k_3 \ll k_2 = k_s/(1+\lambda)$.
$c_1 = 10\,\mathrm{N \cdot s/m}$	Controlled damping.
$c_2 = 4235\,\mathrm{N \cdot s/m}$	From calculation based on small damping approximation.

2.7.5 Simulation

To test the parametric values obtained experimentally in the previous section a simulation of the system was performed. Figure 2.27 shows the time response of the measured force, position, and velocity. This compares favorably with the real data in Figure 2.22. The frequency of the simulation is 84 radians/second, compared with 90 radians/second for the data.

The simulated force versus velocity hysteresis loop is shown in Figure 2.28. This is compared to the real data in Figure 2.25. The slope of $64\,\mathrm{N \cdot s/m}$ is very close to the data value of $66\,\mathrm{N \cdot s/m}$. Notice too, that this graph exhibits a negative skew axis, further justifying the earlier explanation of this phenomenon.

The simulated force versus position hysteresis loop is shown in Figure 2.29. This is compared to the real data in Figure 2.24. Although the slope of the skew axis is smaller in the simulation by about 30%, this can be attributed to the model inaccuracies and experimental error. Since the main concern has been with the order of magnitudes of the spring constants, this is a reasonably good result.

The slope of the force versus position curve is determined mainly by the value of k_3. To improve its slope, k_3 can be increased by 30% to 13000 N/m. Changing k_3 alters other parameters also. The following parameter list results:

$$\begin{aligned} m_a &= 1.46\,\mathrm{kg} \\ m_b &= 0.14\,\mathrm{kg} \\ k_1 &= 0 \\ k_2 &= 5 \times 10^5\,\mathrm{N/m} \\ k_3 &= 13000\,\mathrm{N/m} \end{aligned}$$

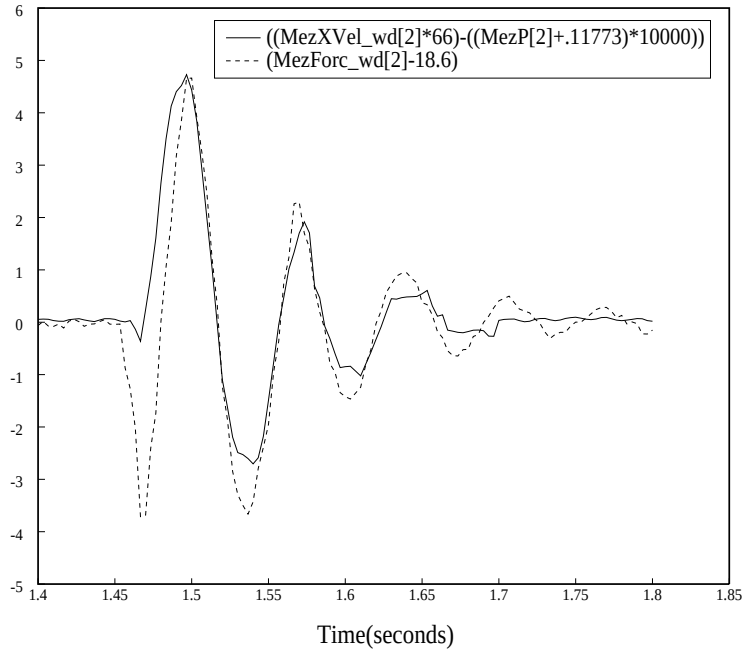

Figure 2.26: The addition of the measured position and velocity, multiplied by the determined constants, yields a close match to the measured force.

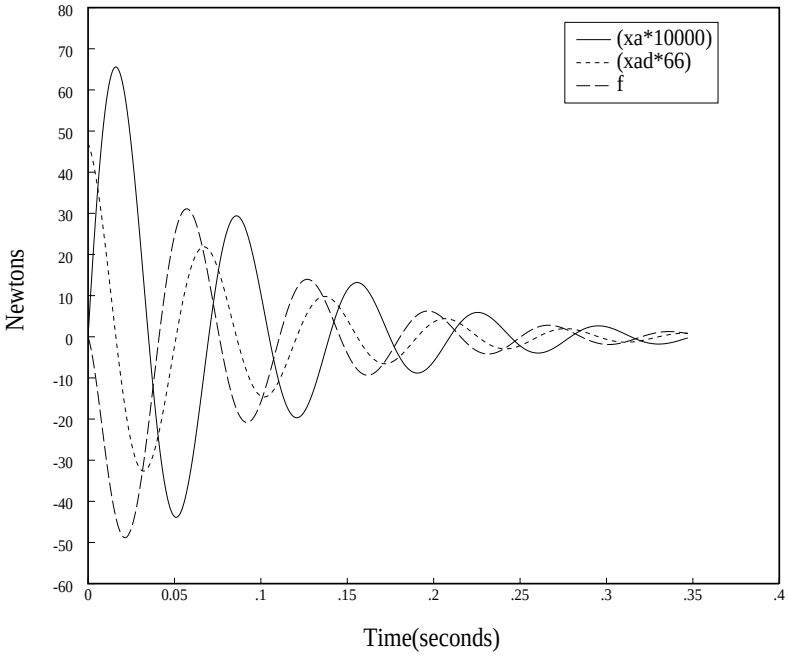

Figure 2.27: Simulated time response of position, velocity, and force, using the estimated parameter values.

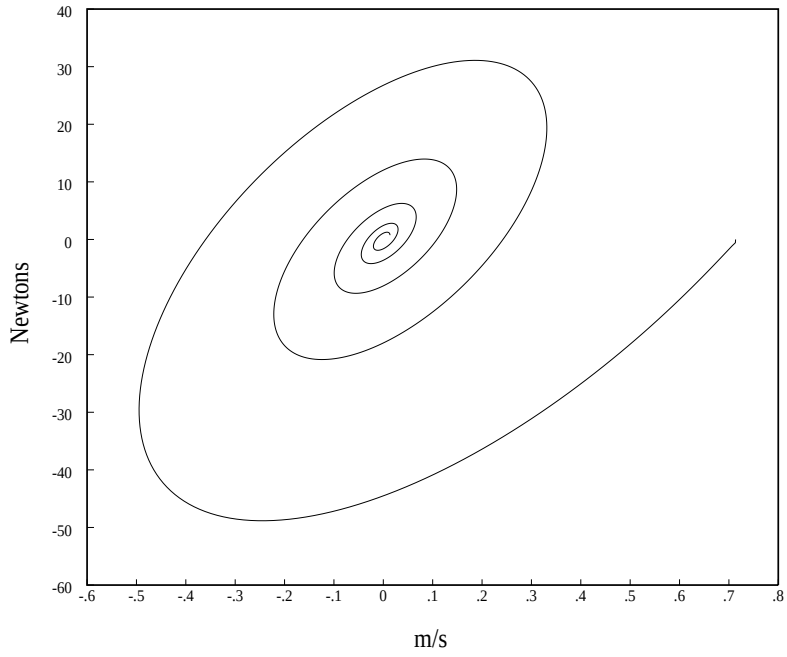

Figure 2.28: Simulation result of force versus velocity using estimated parameters.

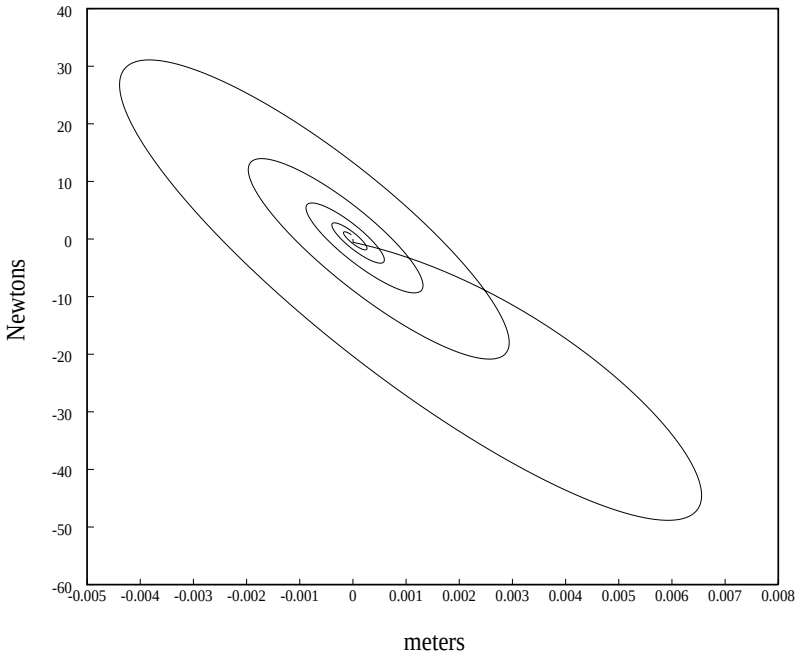

Figure 2.29: Simulation result of force versus position using estimated parameters.

$$
\begin{aligned}
c_1 &= 10\ \mathrm{N \cdot s/m} \\
c_2 &= 3651\ \mathrm{N \cdot s/m} \\
c_3 &= 26.3\ \mathrm{N \cdot s/m}
\end{aligned}
$$

The results of using these parameters within the simulation are shown in Figures 2.30 through 2.32. As can be seen, only the force versus position curve changes significantly, increasing its slope to 9333 N/m, which agrees very closely with the data. This result is consistent with Equation (2.70), the comments following Equation (2.71), and the parameter estimates of the last section. Unless otherwise indicated, these parameter values will be used for all subsequent illustrative examples.

2.8 The Resultant Model

The purpose of this analysis has been to obtain reasonable estimates of the system parameters. These values will be useful to provide a plant model when discussing force control strategies. For these purposes, even order of magnitude approximations will prove to be acceptable. Discrepancies between quantities like the value of k_3 in the data and simulations are therefore viewed as unimportant. In fact, the correspondence between experimentation and simulation indicated that the developed fourth order model is accurate and useful.

This fourth order model will be used as the plant in the analysis of force control strategies in the subsequent chapters. However, for those discussions it will be more useful to use the pole/zero representation of the plant. For completeness, this representation is introduced here. The locations of poles and zeros for this plant are shown in Figure 2.33 and all but the left most pole is shown in more detail in Figure 2.34. The complex pole/zero pairs are due mainly to the environment. The other pole pair is due mainly to the sensor dynamics. These pole pairs will therefore be called the environment and sensor poles, respectively, in future discussions. It can be seen that the sensor poles are fairly far removed from the environmental ones, and are located farther into the left half plane. Usually, the leftmost sensor pole will be ignored.

Finally, it is important to note that the derived model parameters make the fourth order system extremely different than that presented in reference [13]. In that discussion, based on theoretical analysis only, it was assumed that the pole zero pairs were to the left of two complex conjugate poles. As has been shown from experimental data, this is not the case for a very common environment. As will be shown in the following chapters, this difference in the arm / sensor / environment model results in extremely different conclusions about the stability properties of the various force control schemes analyzed and implemented.

2.9 Conclusion

In this chapter, a fourth order model of the arm, sensor, environment system has been developed. The development included the consideration of each of the components of the model as second order systems capable of representing the lowest order oscillations of that component. While the outer arm dynamics were briefly included in the development, it was shown that they could be merged with the sensor dynamics to yield a fourth order model of the entire system. Analysis of this model without damping was used to derive an approximate solution for the damped case. Many assumptions, based on the reality of the experimental system, helped reduce the solution to just a few dominant terms. Comparing these terms with experimental data of the system undergoing small oscillations yielded approximated values for all of the parameters in the model. To justify the obtained values, and thereby the approximations used, a simulation of the fourth order model was performed. The results compare favorably with the experimental data.

Having developed this fourth order model, and demonstrated its viability, it is again necessary to consider the control question. A discussion of explicit force control and impedance control of this plant will begin in the next chapter.

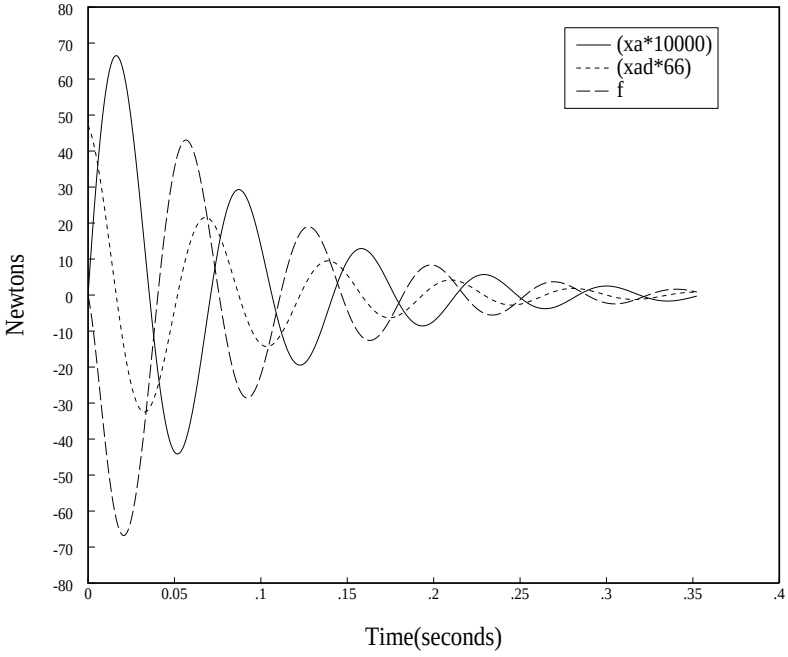

Figure 2.30: Simulated time response of position, velocity, and force using modified parameter values.

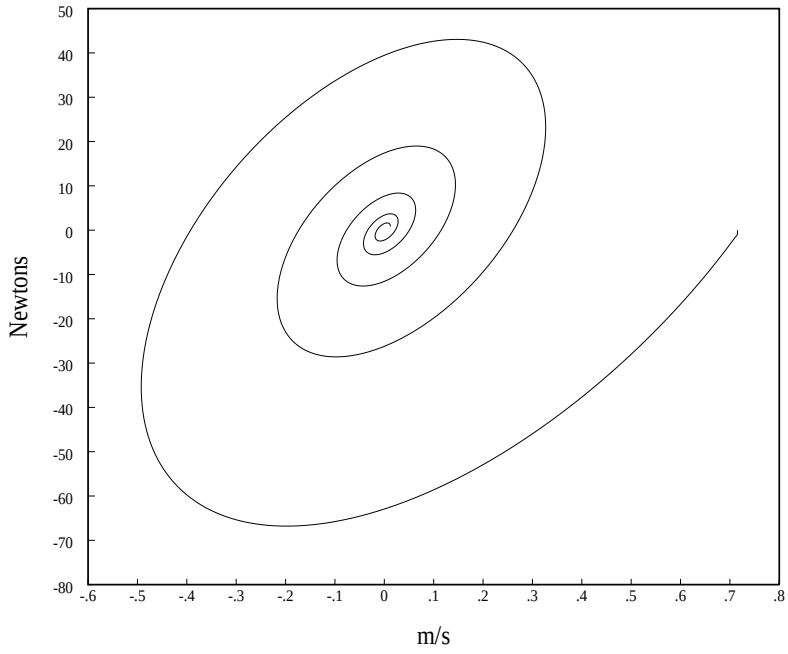

Figure 2.31: Simulation result of force versus velocity using the modified parameters.

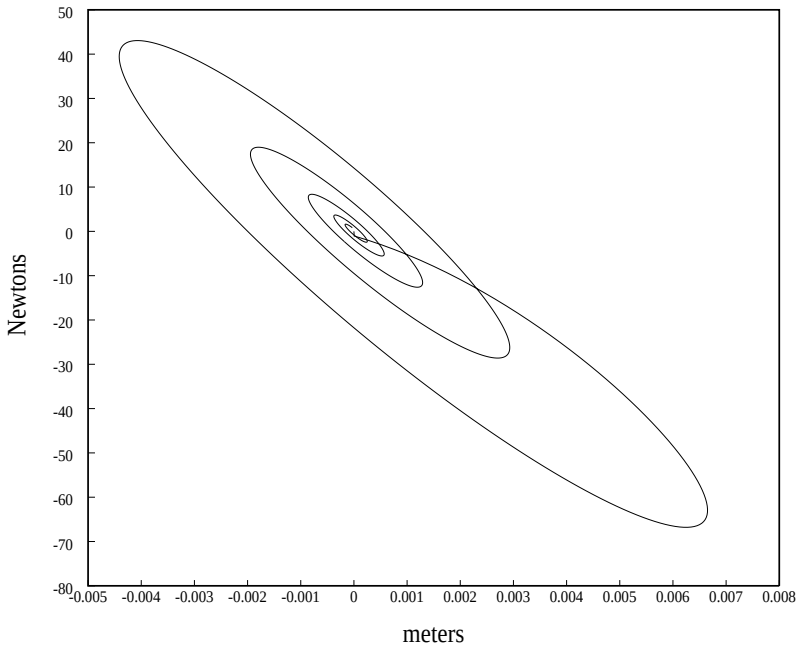

Figure 2.32: Simulation result of force versus position using modified parameters.

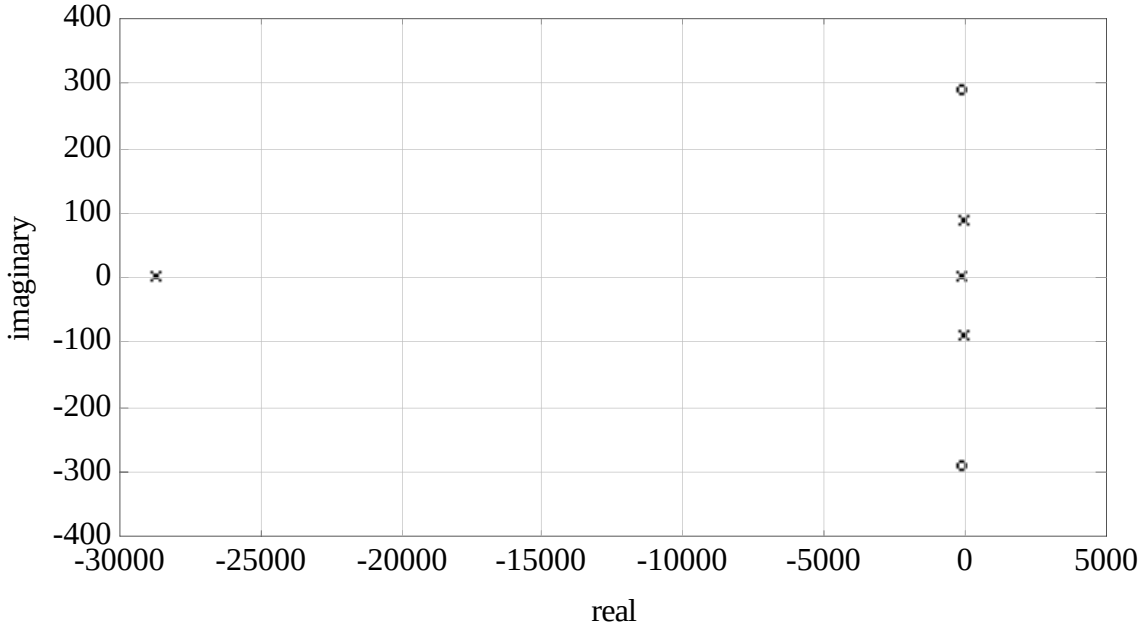

Figure 2.33: The poles and zeros of the fourth order system.

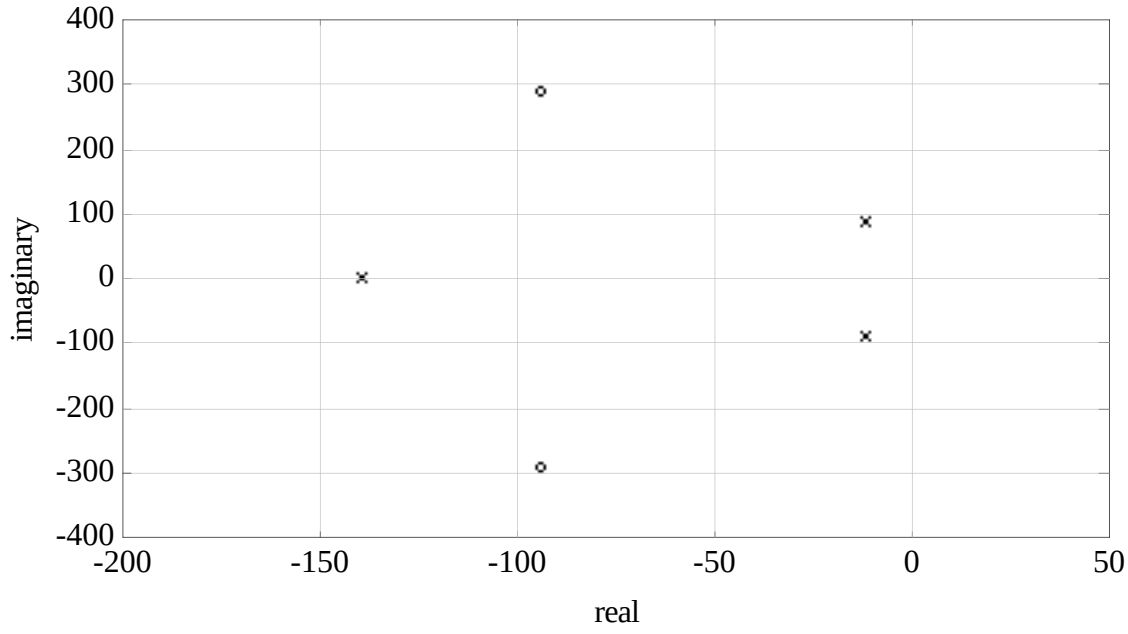

Figure 2.34: An enlargement of Figure 2.33 showing all but the leftmost pole of the original plot.

Chapter 3

Discussion and Analysis of Explicit Force Control Schemes

3.1 Introduction

Having developed the model of the arm / sensor / environment, it becomes the plant for a force controller which must be designed to stably maintain forces inside this system. As discussed earlier, two main approaches have been proposed for this purpose: *explicit force control* and *impedance control*. However, it has also been pointed out conceptually in Chapter 1 that every impedance controller contains an explicit force controller. Therefore, this chapter will discuss explicit force control. Using the plant model developed, each of the specific controllers discussed will be analyzed for stability. Where possible, this analysis will be compared with the reported results of other researchers. Later, Chapter 6 will present an experimental analysis as well.

As discussed in Chapter 1, explicit force control involves the direct command and measurement of force values. The goal of this type of control is to have the output follow the input as closely as possible. Two types of explicit force control have been proposed: force-based, and inner position loop based. By far the most commonly discussed, the force-based techniques usually involve the use of some form of PID control, as well as various simple forms of filtering. Inner position loop controllers, as the name suggests, have an outer force control loop that provides position command to an inner position-based controller.

While many of these controllers have been analyzed before, this has not been done with an experimentally determined plant transfer function. As will be seen, erroneous conclusions about the stability of the system can result without a specific system model. Further, the analysis in this chapter draws the force and position-based strategies together, into one coherent framework, for the first time. This framework provides greater understanding of how gain variations affect stability, and suggests a new lowpass filter control technique.

The chapter is organized as follows. First, force-based explicit force control techniques will be presented and analyzed. Second, position-based explicit force control strategies will similarly be presented and analyzed. Finally, it will be shown how the two are the same, indicating which particular schemes will be most successful.

3.2 Force-Based Explicit Force Control

Force based explicit force control describes a force controller that compares the reference and measured force signals, processes them, and provides an actuation signal directly to the plant. The reference force may also be fedforward and added to the signal going to the plant.

Some previous researchers have also employed an active damping signal which effectively changes the plant, by introducing a nonzero c_1 into the plant transfer function, as seen in Equation (2.32). This damping

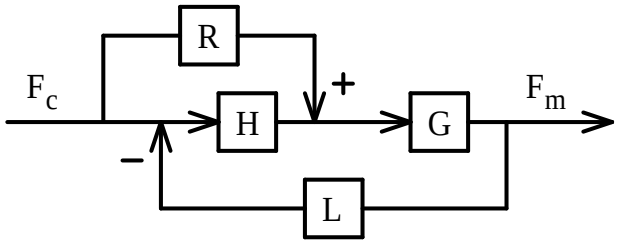

Figure 3.1: Block diagram of a generic force-based, explicit force controller.

term moves the environmental poles closer to the real axis but does not generally change the plant structure. This is because the environment is generally very stiff, and active damping is usually not large enough to move these poles to the real axis and make the system nonoscillatory. To be consistent with the model presented in Chapter 2, active damping with $K_v = 10$ will be used unless otherwise indicated.

Therefore, the general control diagram is shown in Figure 3.1, where G is the plant, H is the controller, and R is the feedforward transfer function, and L is a force feedback filter. The plant G may be represented by the fourth order model of Equation (2.32) or the reduced second order model given by Equation (2.18). Active damping, if present, is included in G. The controller H is usually some subset of PID control (i.e. P, I, PD, etc.). The specific forms of these controllers will be discused next. In the sequel, these schemes will be analyzed and the analytical results will be compared with previous results obtained by other researchers. Experimental results with the DD Arm II will be presented in the Chapter 6.

3.2.1 Strategies for Force-Based Explicit Force Control

This section presents the force-based explicit force control strategies that have been considered for this research. Appendix A presents an overview of strategies that have been considered by other researchers. The strategies presented here are either a generalization of those, or selected to be the most promising for the reasons given. In all cases, the joint torques commanded by these schemes are obtained through the transpose of the Jacobian, and gravity compensation is employed.

Proportional Control The chosen form of proportional gain force control is:

$$f \;=\; f_c \;+\; K_{fp}(f_c - f_m) \;-\; K_v \dot{x}_m \tag{3.1}$$

The feedforward term is necessary to provide a bias force when the force error is zero — without it the system is guaranteed to have a steady state force error.

Integral Control The chosen form of integral control is extremely simple:

$$f \;=\; K_{fi} \int (f_c - f_m) dt \;-\; K_v \dot{x}_m \tag{3.2}$$

Proportional–Integral Control The form of PI control considered for this discussion is:

$$f \;=\; K_{fp}(f_c - f_m) \;+\; K_{fi} \int (f_c - f_m) dt \;-\; K_v \dot{x}_m \tag{3.3}$$

No force is fed forward since the integral term can provide the needed bias force.

Proportional–Derivative Control The most basic form of PD control considered is:

$$f \;=\; f_c \;+\; K_{fp}(f_c - f_m) \;+\; K_{fd}\frac{d}{dt}(f_c - f_m) \;-\; K_v\dot{x}_m \tag{3.4}$$

As with proportional control, the feedforward term is necessary to provide a bias force at steady state.

Proportional–Derivative Control Often, the force signal is very noisy and must be filtered before a derivative may be taken. Therefore, a simple dominant pole filter may be employed in the feedback path ($L = a/(s+a)$). The resultant control law in the Laplace domain is:

$$F(s) \;=\; F_c(s) \;+\; [K_{fp} + K_{fd}s]\left[f_c - \left(\frac{a}{s+a}\right)f_m\right] \;-\; K_v s X_m \tag{3.5}$$

3.2.2 Analysis of Force-Based Explicit Force Control

Given the wide spectrum of approaches and results reported in the literature, it is worthwhile to take a second look at these control strategies. Each will be analyzed below using the plant model previously developed.

Proportional Control

For proportional control, $H = K_{fp}$, and $L = 1$ in Figure 3.1. While the value of the feedforward term R does not affect the characteristic equation, a value different than unity will not cancel the reaction force from the environment, and the controller will not converge to the desired value. The feedforward term will be discussed further below. The closed loop transfer function with the feedforward term is:

$$\frac{F_c}{F_m} = \frac{(1 + K_{fp})G}{1 + K_{fp}G} \tag{3.6}$$

This is a Type 0 System and will have a nonzero steady-state error for a step input. The root locus of this system is shown in Figures 3.2 and 3.3. The corresponding Bode plots are shown in Figure 3.4.

As can be seen from the root locus, both the sensor poles and the environment poles move away from the real axis for increased proportional gain. Thus the system becomes more oscillatory. However, the environmental poles go to a pair of zeros, while the sensor poles go to infinity. Thus, the system remains stable, but oscillations are likely to occur near the natural frequency of the environment. Further, note that the poles can move into the right half plane, making the proportional gain controller unstable. This is contrary to the predictions of other researchers, and results from the use of a plant model that was not experimentally derived [14].

The Bode plots further illustrate this problem. There is a resonance peak from the environment dynamics, which corresponds to the normal mode discussed in the last chapter. After this peak there is a 40 dB/decade drop-off which gives a minimum phase margin of $\sim 15^\circ$ at $K_{fp} \approx 1$.

The addition of a feedback lowpass filter, $L = \frac{1}{s+a}$, can reduce the magnitude of the resonance peaks. The corresponding closed loop transfer function becomes:

$$\frac{F_c}{F_m} = \frac{(R + K_{fp})G}{1 + K_{fp}(\frac{1}{s+a})G} \tag{3.7}$$

The root locus is modified by the presence of a pole on the real axis that moves left from $s = -a$. Depending on the magnitude of a, this pole can reduce the response of the resonance peak. For $a \to \infty$ this becomes a pure proportional controller. For $a \to 0$ this scheme is very similar to integral control, discussed below. (For this reason, filtered proportional control will not be implemented later in Chapter 6.) Improved response with lowpass filtering has been reported [1].

It will prove useful later (in a discussion of Impedance Control) to now discuss the feedforward term in more detail. As stated above, it is desirable that the feedforward term be unity ($R = 1$) in order to cancel the

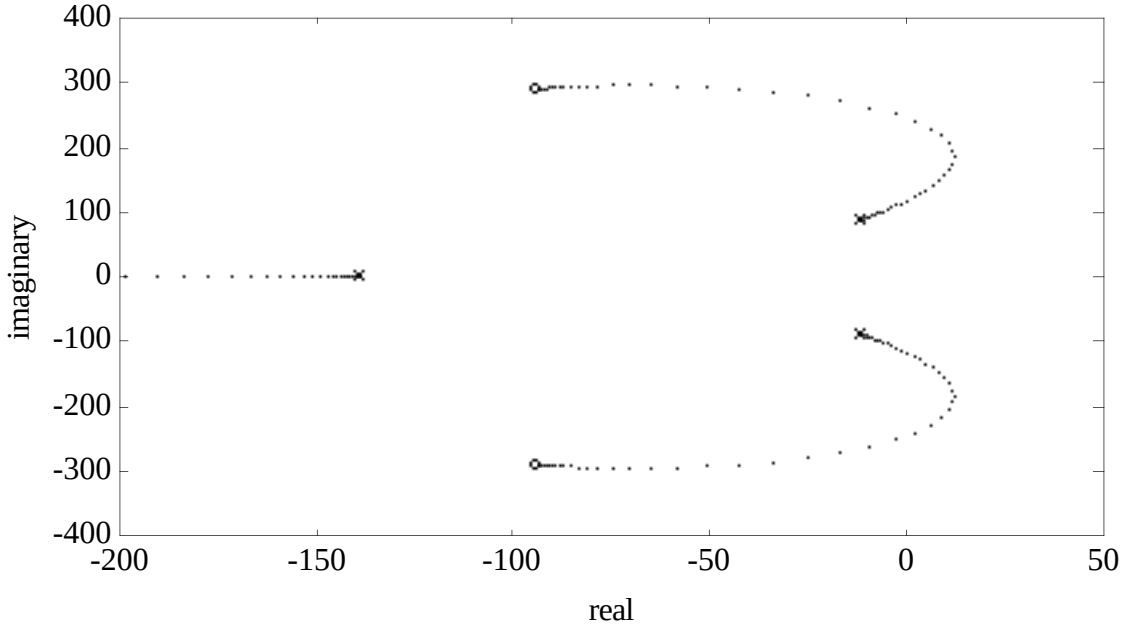

Figure 3.2: Root locus for the fourth order model under proportional gain explicit force control.

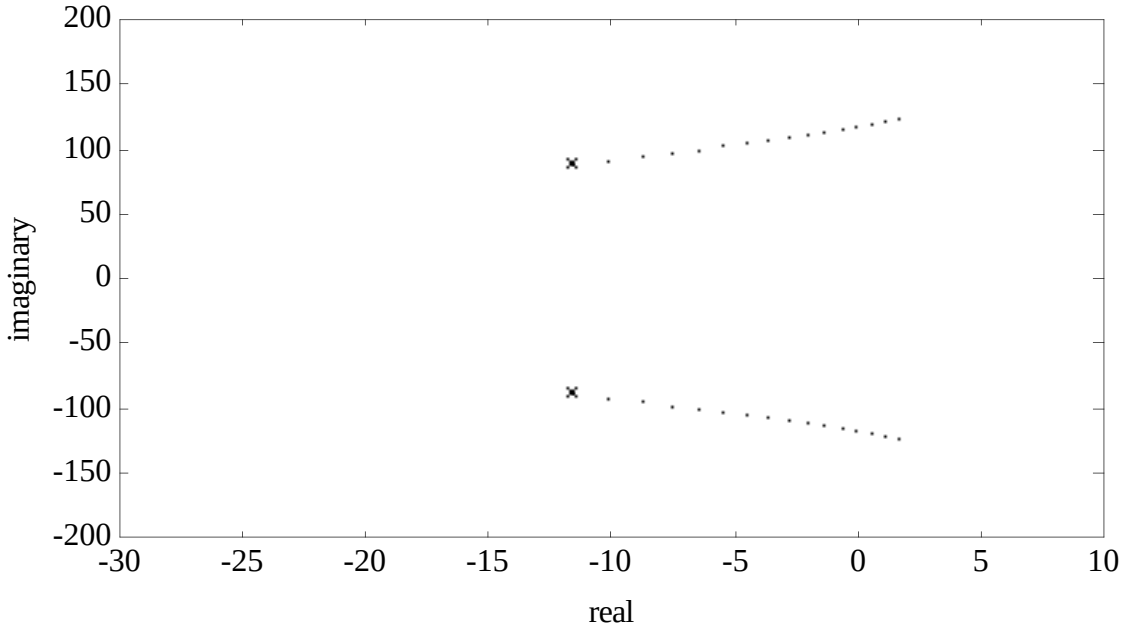

Figure 3.3: Enlargement of root locus in Figure 3.2 with K_{fp} values of 0 to 1.5 in steps of 0.1 .

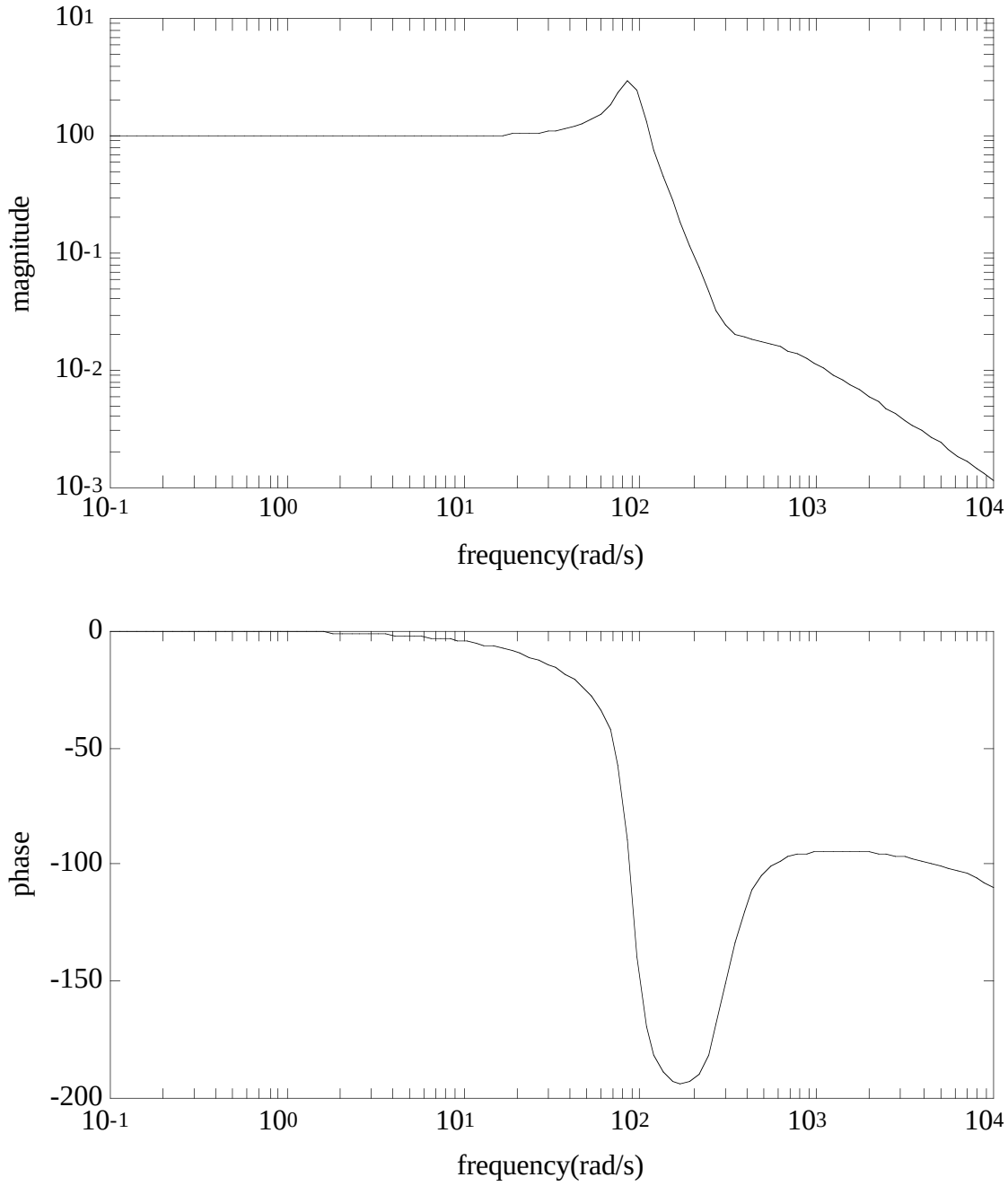

Figure 3.4: The resonance peak occurs near the natural frequency of the environment. The gain margin is 1.2 at $\omega = 118\mathrm{rad/s}$, which corresponds to the root locus crossing to the right half plane in Figure 3.3.

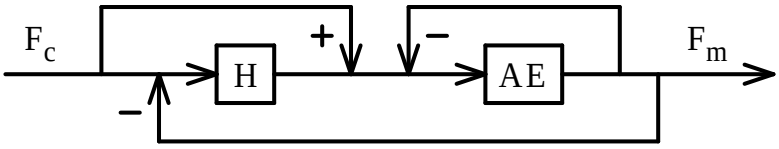

Figure 3.5: Block diagram a force-based explicit force controller with proportional gain and unity feedforward. The plant G has be expanded into its components, and the sensor dynamics have been ignored.

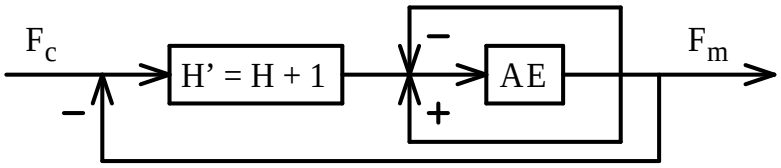

Figure 3.6: Block diagram a force-based explicit force controller with proportional gain and extra feedback for reaction force compensation. The plant G has be expanded into its components, and the sensor dynamics have been ignored.

environmental reaction force during steady state. Also, it will be assumed that no feedback filtering is being employed ($L = 0$). Further, the plant will be expanded into its arm and environmental components, but the sensor dynamics will be ignored. This yields a block diagram for the system as in Figure 3.5. The transfer function of this system is:

$$\frac{F_m}{F_c} = \frac{(H+1)G}{1+(H+1)G} \tag{3.8}$$

$$= \frac{H'G}{1+H'G} \tag{3.9}$$

where $H' = H + 1$. It is seen directly that an equivalent block diagram of the system may be constructed as in Figure 3.6. Viewed in this way, the reaction force is negated explicitly, and the proportional gain may have values $H' = K'_{fp} \geq 0$ or $H = K_{fp} \geq -1$. Thus, the proportional gain of the original controller may be as small as negative one. The use of negative gains like this have appeared in the literature previously [19, 23]. However, this result is usually presented within the framework of impedance control. As will be seen in the next chapter, the impedance controllers for which this result as obtained actually contain proportional gain explicit force control, which mandates the result.

Integral Control

For integral control, $H = \frac{K_{fi}}{s}$, and $L = 1$ in Figure 3.1. A nonzero feedforward term yields the following transfer function:

$$\frac{F_c}{F_m} = \frac{(R + \frac{K_{fi}}{s})G}{1 + \frac{K_{fi}}{s}G} \tag{3.10}$$

Letting R be unity places a closed loop zero at $s = -K_{fi}$ which limits the effectiveness of the integrator pole. Also, a feedforward signal is not necessary since the integrator will eliminate any steady state error for a constant input. Therefore, R is set to zero and the transfer function is:

$$\frac{F_c}{F_m} = \frac{\frac{K_{fi}}{s}G}{1 + \frac{K_{fi}}{s}G} \tag{3.11}$$

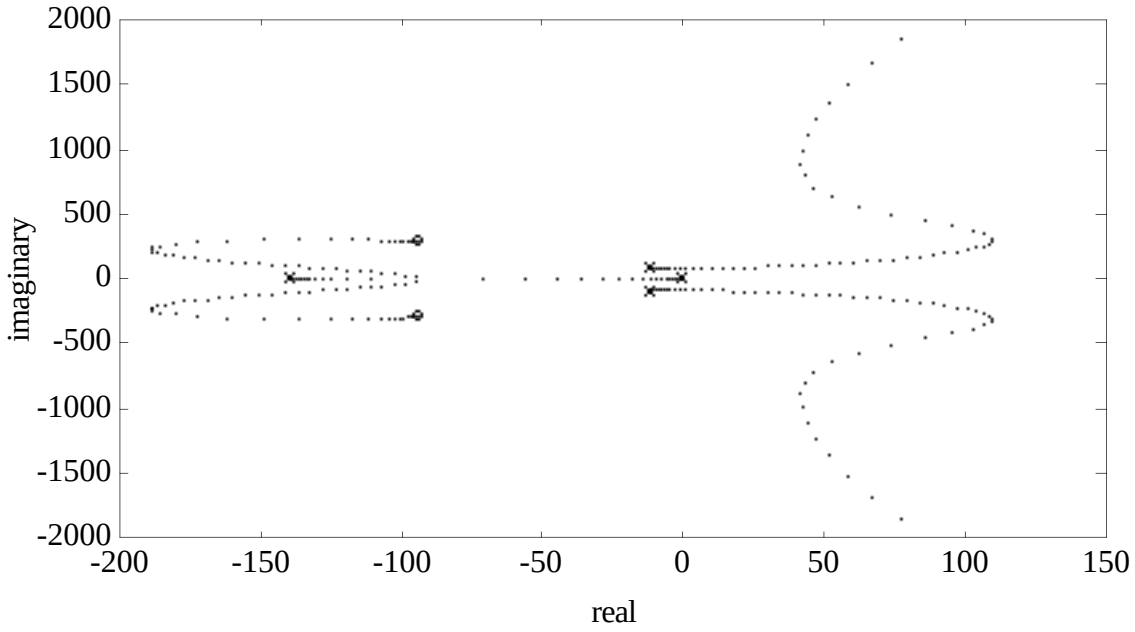

Figure 3.7: Root locus for the fourth order model under integral gain explicit force control.

This is a Type 1 System and has a finite error to a ramp input. The root locus of this system is shown in Figures 3.7 and 3.8. The corresponding Bode plots are shown in Figure 3.9.

As can be seen in the root locus plot, the introduction of the integral pole moving to the left causes the environmental and sensor poles to move right. The environmental poles can actually move into the right half plane before completing their semicircular trajectory to a pair of zeros. This has been previously viewed as destabilizing [14]. In the previous section, the sensor poles caused this same behavior from a proportional controller. The two root loci are compared in Figure 3.10. As can be seen, the loci are similar except that the integral controller has the benefit of a dominant low pass pole on the real axis. The Bode plots indicate that the low pass nature of integral control hides the resonance spikes well below unity magnitude. The point of zero phase margin indicates a maximum integral gain of $K_{fi} \approx 10$.

Proportional–Integral Control

A PI controller is a linear combination of the above two schemes. In this case, $H = K_{fp} + \frac{K_{fi}}{s}$, $L = 1$, and for reasons mentioned above, $R = 0$. Therefore, the transfer function is:

$$\frac{F_c}{F_m} = \frac{\left(K_{fp} + \frac{K_{fi}}{s}\right) G}{1 + \left(K_{fp} + \frac{K_{fi}}{s}\right) G} \tag{3.12}$$

Obviously, the behavior is a combination of the behaviors of pure proportional and pure integral control. The appearance of the root locus and Bode plots will depend on the gain which is varied.

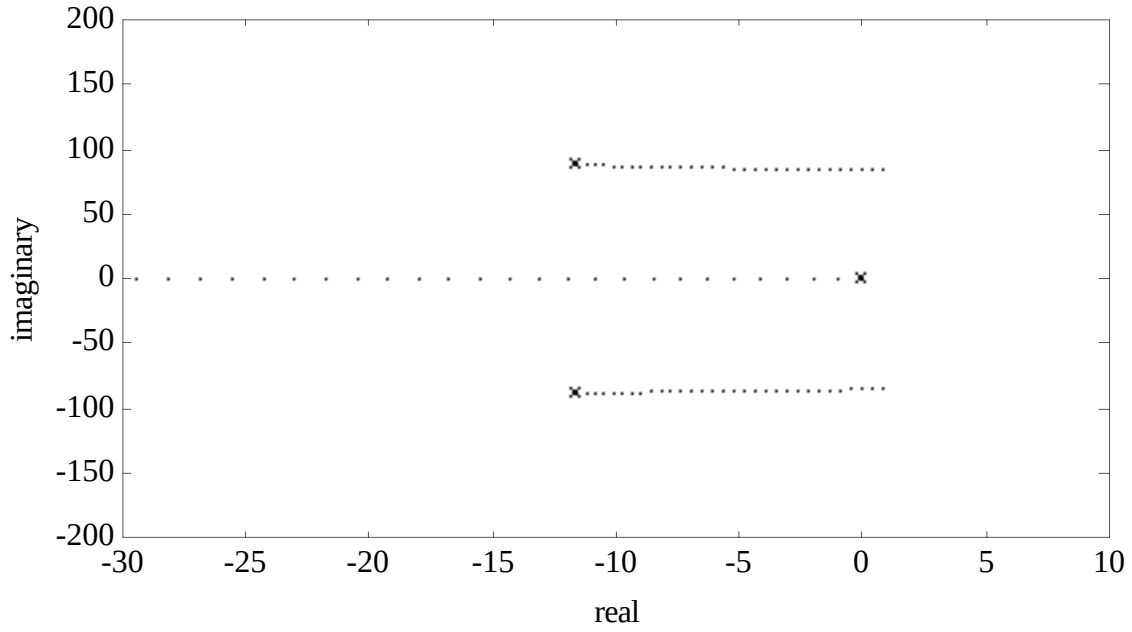

Figure 3.8: Enlargement of root locus in Figure 3.7 with K_{fi} values of 0 to 30 in steps of 1.

Proportional–Derivative Control

A PD controller includes a derivative term with the proportional control discussed above. In this case, $H = K_{fp} + sK_{fd},\ L = 1$, and for reasons mentioned above, $R = 1$. Therefore the transfer function is:

$$\frac{F_c}{F_m} = \frac{(R + K_{fp} + K_{fd}s)G}{1 + (K_{fp} + K_{fd}s)G} \tag{3.13}$$

Choosing a specific value of K_{fp} with $K_{fd} = 0$ will determine the starting place of the root locus of K_{fd}. This starting place will be somewhere on the root locus of K_{fp} in Figure 3.2. Independent of the starting point the root locus will have similar characteristics. For K_{fp} large, the derivative term will have no influence, so the controller and its root locus can be approximated as those for proportional control alone. For $K_{fp} = 0$ this scheme will reduce to pure derivative control which will not follow the reference force. However, the transfer function and associated root locus for $K_{fp} = 0$ represent the extreme of the behavior for a PD controller. Just as the behavior of PI control was intuited from that of P and I control alone, the behavior of PD control can be best understood by studying its extremes of pure proportional and pure derivative control. Thus, K_{fp} is considered zero in the following discussion. The resulting root locus is shown in Figure 3.11 and 3.12 The corresponding Bode plots are shown in Figure 3.13.

As can be seen in the root locus plot, for a certain range of gains, derivative control moves all of the poles further left, thus appearing to make the system more stable. For this reason, PD control has been predicted to be very stable [14].

However, the Bode plots of the system shows a major problem with this approach. Derivative control acts as a band pass filter, passing the resonant frequency. This surely will drive an underdamped system into oscillation.

Another implementational factor must be considered with respect to derivative control. Typically, the feedback signal from a force sensor is very noisy. One example can be seen in Figure 6.4. Taking the derivative of such a signal is not advisable. However, filtering may be effective. Passive filtering may be

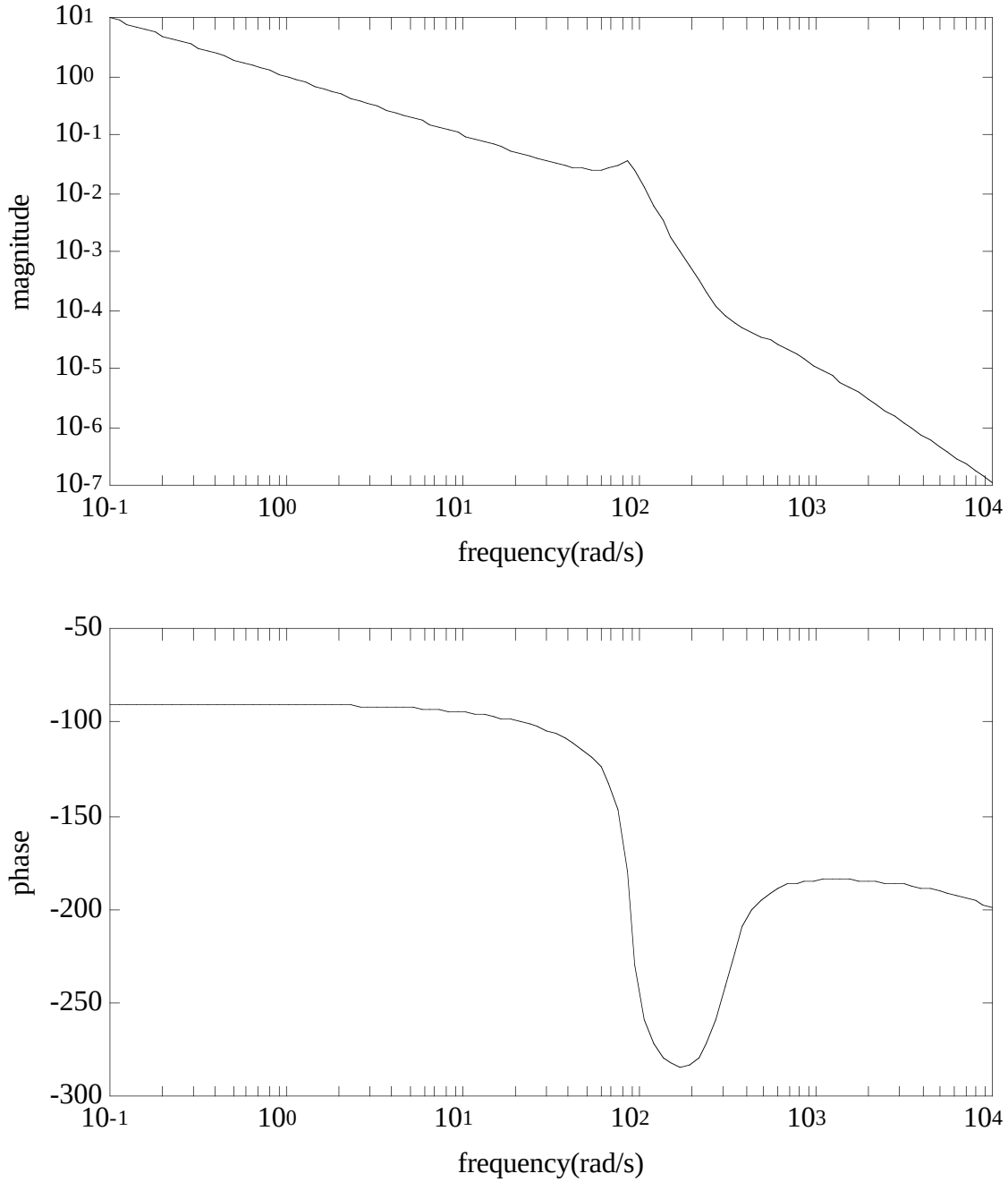

Figure 3.9: The resonance peak corresponds to the natural frequency of the environment, but remains under a magnitude of one for gains of ~ 10. The phase margin remains near $90\,\mathrm{deg}$ as well. The gain margin is 28 at $\omega = 85\mathrm{rad/s}$, which corresponds to the root locus crossing to the right half plane in Figure 3.8.

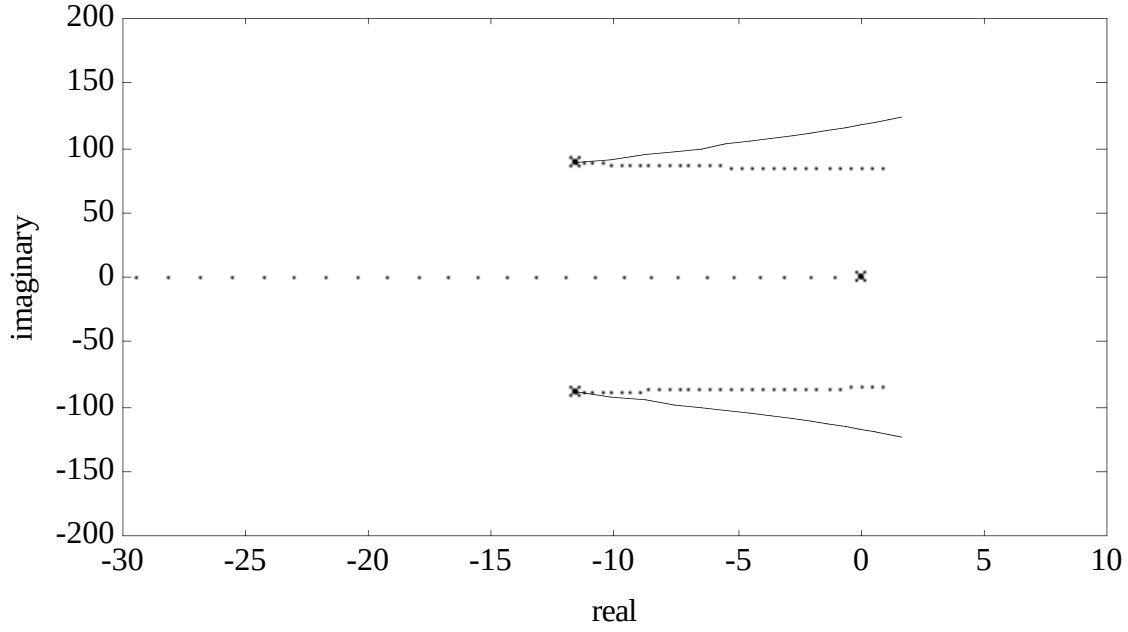

Figure 3.10: Comparison of proportional (solid) and integral (dotted) gain root loci.

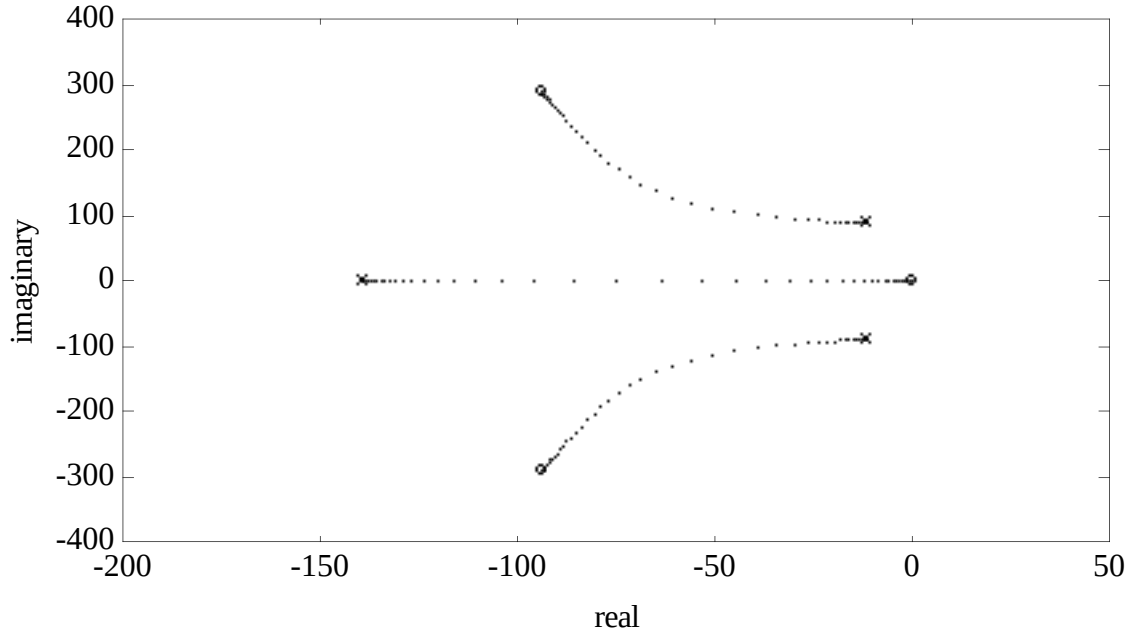

Figure 3.11: Root locus for the fourth order model under derivative gain explicit force control.

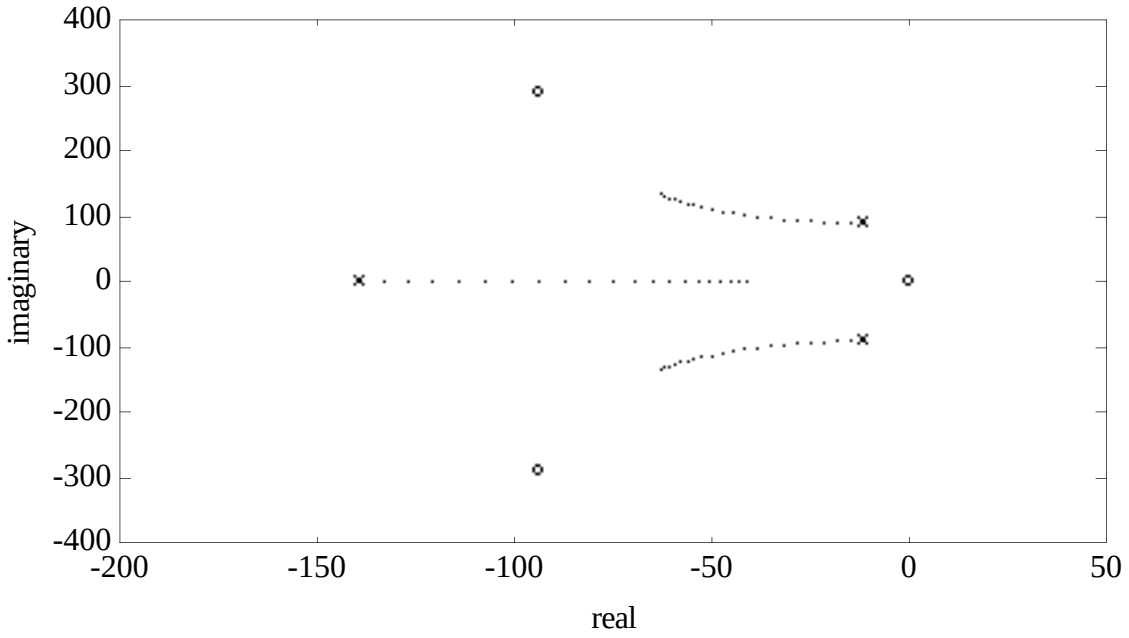

Figure 3.12: Enlargement of root locus in Figure 3.11 with K_{fd} values of 0 to 0.02 in steps of 0.001 .

accomplished by the use of a compliant sensor or sensor cover. As mentioned earlier, this method can introduce uncontrolled degrees of freedom to the system, or reduce the effective force that may be applied. Alternatively, active filtering may be used. This will be discussed next.

Filtered Proportional–Derivative Control

To filter the force signal a dominant pole filter may be used, placing the transfer function $L = \frac{a}{s+a}$ in the feedback path. Therefore the transfer function becomes:

$$\frac{F_c}{F_m} = \frac{(R + K_{fp} + K_{fd}s)G}{1 + (K_{fp} + K_{fd}s)\left(\frac{a}{s+a}\right)G} \tag{3.14}$$

As before, K_{fp} is chosen to be zero for this analysis. Choosing $a \to \infty$ will not make an effective filter of the high frequency noise. Choosing $a \to 0$ will make this a proportional gain controller. Thus, the extreme case of lowpass filtering changes this to a proportional gain controller. Proportional gain control has already been shown to ineffectively mask the resonance oscillation of the system.

For the case of nonzero K_{fp} and $a \to 0$, the characteristic equation becomes that of a PI controller. As discussed before, the responses of this controller will be between that of P and I control alone.

3.2.3 Discussion of Explicit Force Control

It seems apparent from the above analysis that explicit force control with the experimentally determined plant is best accomplished by integral control. First, the integral controller is a Type 1 System and will have zero steady-state error for a constant reference force. Second, an integral control acts as a low pass filter, reducing the chance of resonance oscillations occurring in the system. This is deemed to be very important. Higher order modes of oscillation can cause the assumed model to become invalid and actually make the system nonlinear, especially if separation from the environment occurs.

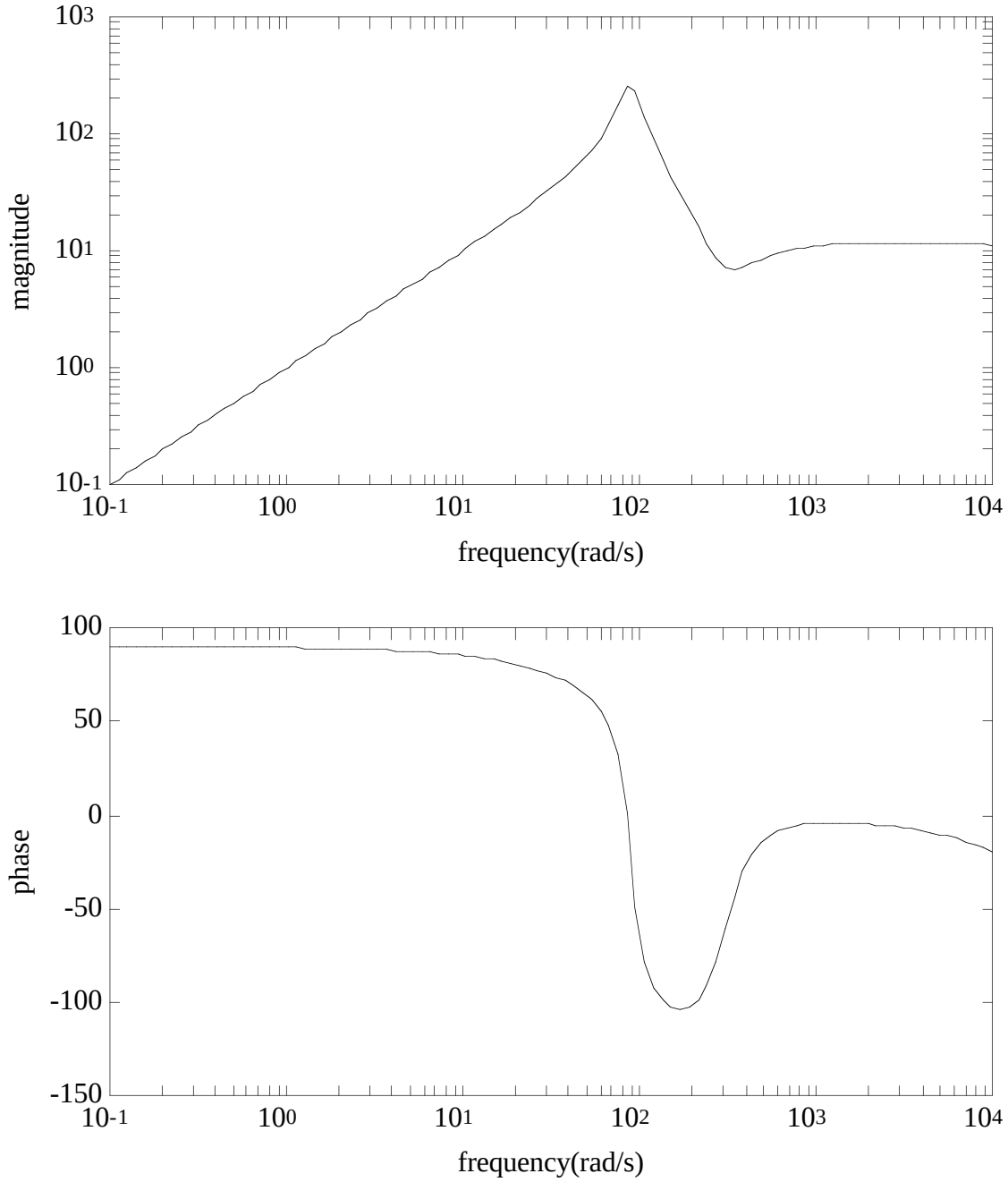

Figure 3.13: The resonance peak corresponds to the natural frequency of the environment. Thus, this controller acts as a band pass filter for the resonant frequency of the system.

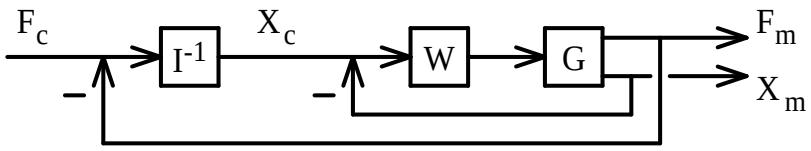

Figure 3.14: Block diagram of a generic position-based, explicit force controller.

One of the main arguments against integral control is that it does not permit fast force trajectory tracking. However, this goal is simply not achievable for a manipulator that is not mechanically attached to the environment. A simple argument should demonstrate this point. Consider a manipulator that is pressing on a surface with a natural frequency of oscillation. Between the manipulator and the surface there is no physical compliance. Consider also that the manipulator is to reduce its applied force. If the rate of the reduction is greater than the natural frequency of the environment then contact will be lost. In other words, the arm will pull away faster than the environment can respond. Lost contact can cause instability to develop and should be avoided. Therefore, it can be simply put that *the force control response time is limited by the environmental dynamics.* This is seen directly in the integral control root locus and Bode plots above, Figures 3.8 and 3.9. The limiting value of K_{fi} obtained from the phase margin in the Bode plots, places the integral pole just to the right of the environmental poles.

3.3 Position-Based Explicit Force Control

A second class of explicit force controllers consists of those based on an inner position loop. These controllers were probably implemented first for practical reasons — most commercial manipulators have built in position controllers and don't allow direct access to actuator torques. As shown in Figure 3.14, the outer force loop provides a reference position to the inner position loop. In this diagram, W is the position controller which is typically a PD controller:

$$W = K_p + K_v s \tag{3.15}$$

The commanded force is transformed into a commanded position through an admittance, which is described as the inverse of a second order impedance:

$$I = m_f s^2 + c_f s + k_f \tag{3.16}$$

Again the joint torques are obtained through the transpose of the Jacobian, and gravity compensation is employed. The plant damping, c_1 in the system plant G, is again provided actively by the velocity gain K_v.

Appendix A presents an review of position-based force control implementations that have been performed by other researchers.

3.3.1 Analysis of Position-Based Explicit Force Control

Ensuring a Type 1 System

As has been stated previously, a Type 1 System is desirable because it has zero steady-state error to a constant input. Previous analysis of the position-based controllers, especially that of DeSchutter, indicates the need to consider three controllers that must become Type 1 Systems [11]. These are: position and velocity feedback, position feedback only, and no inner loop feedback. The previous work, coupled with the plant model developed in this thesis, indicates a new and novel way in which to view inner position loop-based explicit force control. As will be seen, the previously reviewed force-based explicit force controllers are actually a subset of this strategy.

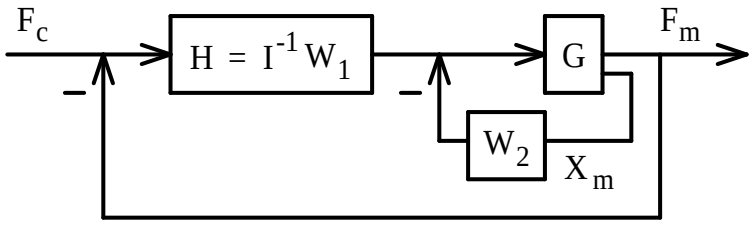

Figure 3.15: Reformulation of the block diagram of generic position-based, explicit force controller.

Consider first the position-based force controller that uses velocity as well as position feedback ($W = K_p + K_v s$). Deschutter's results indicated that the outer force controller providing commanded positions must have at least one free integration. To achieve this the force controller must be $I = s(m_f s + c_f)$. This is essentially a second order low pass filter. Contrary to this is the first order low pass filter which will have a nonzero steady state error [25].

Next, consider the position-based force controller that uses only velocity feedback ($W = K_v s$). For this scheme, the outer force loop must provide a reference velocity, as well as satisfy the criterion of at least one free integration. This implies $I = m_f s$. Notice that this scheme is exactly what has previously been considered as explicit force control with active damping. Viewed in this way, the velocity feedback is not just added to improve damping. Instead, it is part of a inner loop, position-based, feedback controller.

Finally, the third case of no inner loop ($W = 0$) reduces to the second case since the transfer function of the arm, sensor and environment does not change form when the active damping is removed. This is because velocity feedback is still present in the system even though it is not from active feedback.

Position-Based Explicit Force Control Viewed as Force-Based Explicit Force Control

Having shown the correspondence between position-based and force-based explicit force control, it is possible to change the first into the second. Consider separating the position controller in Figure 3.14 into two parts, W_1 and W_2. Figure 3.15 shows the resultant controller block diagram.

It can now be seen that the inner loop is identical to Figure 2.7, the model of an arm with damping and stiffness for the case of no environmental interaction. With the environment included, its mass, damping, and stiffness parameters simply add to those of the arm. The result is still essentially the same. Thus, K_p is equivalent to k_1 in the fourthorder model of the plant. From, Equation (2.18) it can be seen that the addition of more stiffness to the characteristic equation ($k_e \rightarrow k_e + k_1$), will make the poles more oscillatory. Thus, the innerloop position controller makes the plant more stiff and oscillatory. The resultant outer loop force controller, however, can still assume any of the forms of force-based control previously discussed. This is shown below. It is therefore concluded that *position-based force control differs only from force-based force control by the addition of stiffness to the plant. Further, this additional stiffness is destabilizing.*

The outer loop of the position-based force control can be shown to assume the form of any of the force-based explicit force controller previously discussed. Consider the form of the controller shown in Figure 3.15. It is also apparent that the controller now has a form previously associated with force-based explicit force control, where

$$H = \frac{W_1}{I} = \frac{K_p + K_v s}{m_f s^2 + c_f s + k_f} \tag{3.17}$$

Notice that all of the explicit force controllers can be constructed from this transfer function:

Proportional Control 1	$K_{fp} = K_p/k_f \quad K_v = m_f = c_f = 0$
Proportional Control 2	$K_{fp} = K_v/c_f \quad K_p = m_f = k_f = 0$
Integral Control 1	$K_{fi} = K_p/c_f \quad K_v = m_f = k_f = 0$

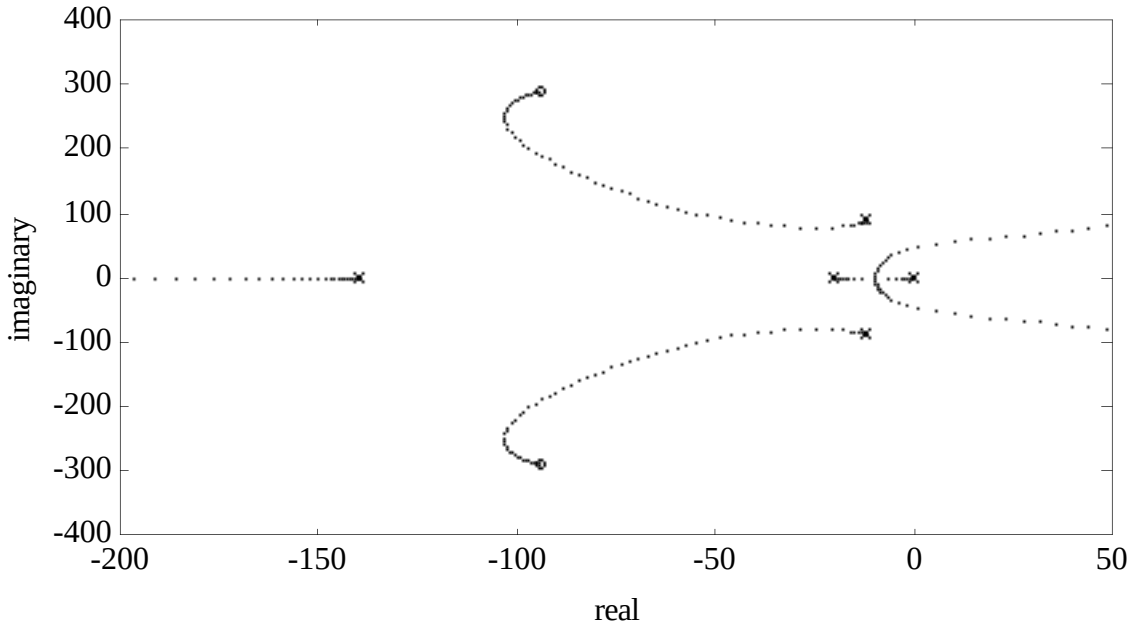

Figure 3.16: Root locus for the fourth order model under explicit force control with a second order lowpass filter.

Integral Control 2	$K_{fi} = K_v/m_f \quad K_p = c_f = k_f = 0$
Derivative Control	$K_{fd} = K_v/k_f \quad K_p = m_f = c_f = 0$
PI Control	$K_{fp} = K_v/c_f, K_{fi} = K_p/c_f \quad m_f = k_f = 0$
PD Control	$K_{fp} = K_p/k_f, K_{fd} = K_v/k_f \quad m_f = c_f = 0$
Filtered P Control	$K_{fp}/(s+a) = K_p/(c_f s + k_f) \quad K_v = m_f = 0$
Filtered PD Control	$(K_{fp}+K_{fd}s)/(s+a) = (K_p+K_v s)/(c_f s+k_f) \quad m_f = 0$
2^{nd} Order Low Pass Filter	$K_{fp}/(s(s+a)) = K_p/(s(m_f s + c_f) \quad K_v = k_f = 0$

The only new controller in this list is the second order lowpass filter. It will be discussed in the next section.

Root Locus and Bode Plots

Finally, it is worthwhile to look at the root locus and Bode plots for a what has been called a position-based explicit force controller. As has been discussed above, the only controller from that is newly introduced by this concept is the second order low pass filter. Like the first order dominant pole introduced by low pass filtering or integral control, the two poles introduced by a second order filter should be placed to the right of the environment poles. Since the controller has been chosen to be Type 1, one of the poles is constrained to begin its locus at the origin. Thus the other should begin to the left of the environmental poles. As the gain is increased, the filter poles on the real axis will come together and give a double pole filter. Ideally, this double pole should be just to the right of the environmental poles. A root locus for $a = 20$ is shown in Figures 3.16 and 3.17. The corresponding Bode plots are shown in Figure 3.18.

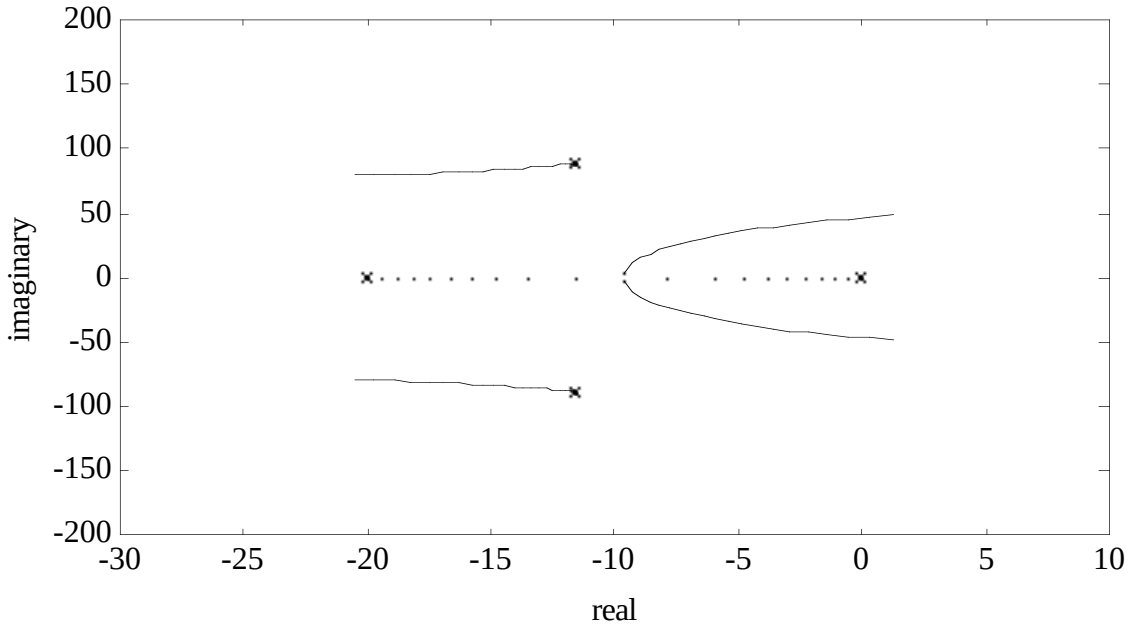

Figure 3.17: Enlargement of root locus in Figure 3.16 with K_f values of 0 to 2000 in steps of 10. The poles move very slowly once off the real axis.

3.4 Conclusions

This chapter has presented a stability analysis of various explicit force control routines using the plant model developed in Chapter 2. This work is unique in its broad coverage of control strategies and use of an experimentally determined plant model. The results also contradict the predictions of other researchers [14], but are confirmed by experimental implementation (as will be shown in Chapter 6).

This analysis has indicated that integral control is the best choice for explicit force control. This is because of its simple form, lowpass nature, and its zero steady state error for a constant reference force. A possible second choice is the second order lowpass filter. Although, slightly more complicated than simple integral control it promises to filter the force oscillations better with two real axis poles. Proportional control is the third choice. However, with this controller the dominant poles are complex, indicating that oscillations will occur for even low gains. Further, the analysis shows that proportional gain control becomes unstable, which has not previously been predicted. Finally, any control using the derivative of the force signal does not seem promising. This type of controller will act as a band pass filter at the natural frequency of the system. Also, obtaining a good derivative of the force signal may prove difficult.

The behavior of the proportional gain force controller should be kept in mind. As will be seen in the next chapter, the most common forms of impedance control contain proportional gain explicit force control within them. This will prove interesting, since it has been shown in this chapter that proportional control of force is not best.

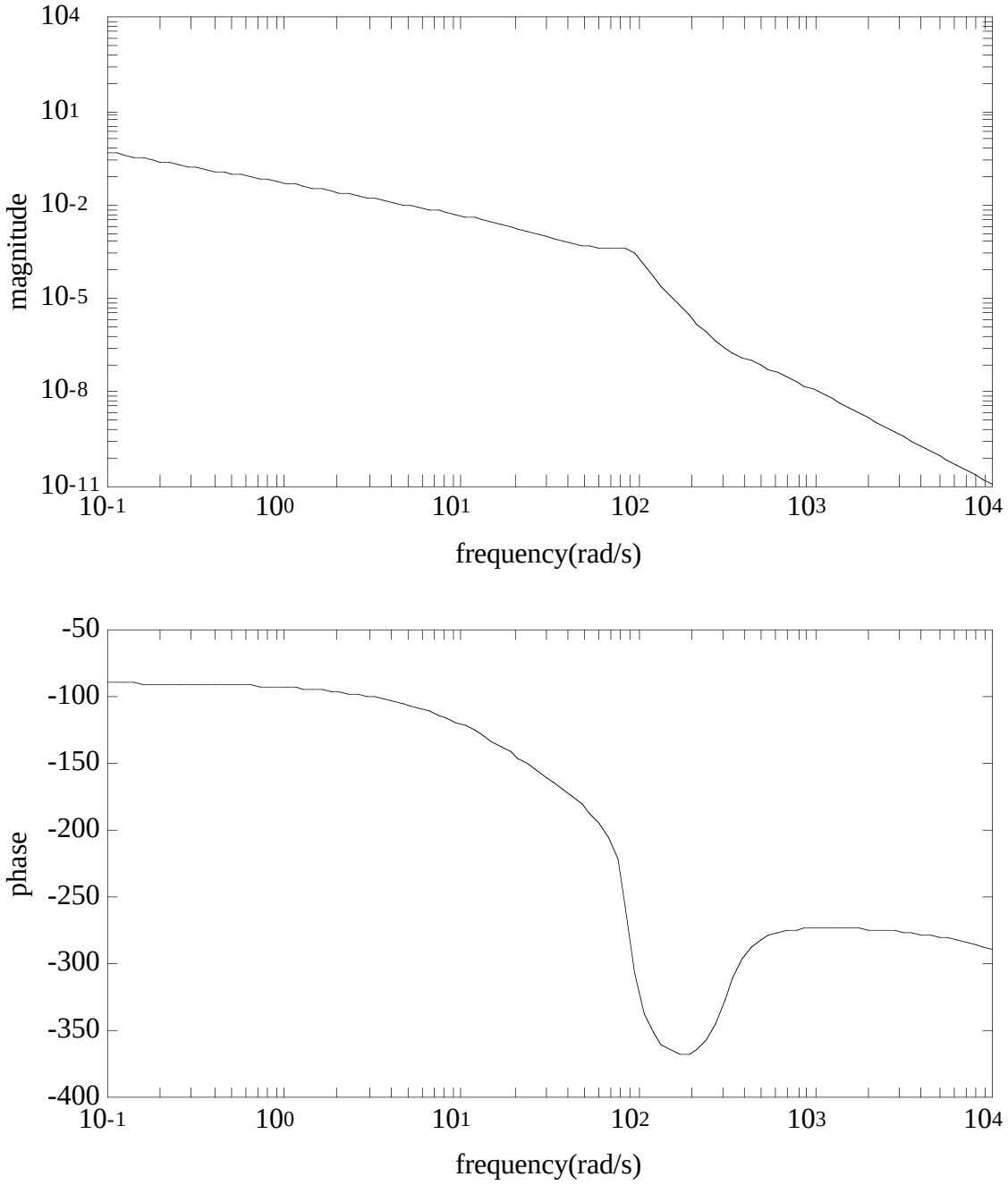

Figure 3.18: Note that the resonance peak is almost completely suppressed. The gain margin is 1854 at $\omega = 48$, which corresponds to the root locus crossing to the right half plane in Figure 3.17.

Chapter 4

Discussion and Analysis of Impedance Control Schemes

4.1 Introduction

As discussed earlier, Impedance Control is a strategy that controls the dynamic relation between the manipulator and the environment. The force exerted on the environment by the manipulator is dependent on its position and its impedance. Usually this relation is expressed in Cartesian space as:

$$f = \mathcal{Z}(x). \tag{4.1}$$

The impedance consist of two components, that which is physically intrinsic to the manipulator, and that which is given to the manipulator by active control. It is the goal of Impedance Control to mask the intrinsic properties of the arm and replace them with the target impedance.

In general, the impedance can have any functional form. As will be seen in Chapter 7 such general impedances are useful for obstacle avoidance. However, it will be made clear in this chapter that sensor based, feedback controlled interaction with the environment requires the impedance to be linear and of second order at most. This is for two reasons. First, the dynamics of a second order system are well understood and familiar. Second, for higher order systems it is difficult to obtain measurements corresponding to the higher order state variables.

To implement Impedance Control, model based control can be used. This type of scheme relies on the inverse of the Jacobian. A second type of controller which uses the transpose of the Jacobian is sometimes employed. However, it will be shown that this type of controller is really a reduced version of the first, and ignores all non-linearities of the system.

More important to this thesis, both forms of Impedance Control will be shown to contain proportional gain explicit force control (with feedforward). Also, for stiff environments the position feedback is essentially constant, and impedance control reduces directly to proportional gain force control. The role of proportional gain force control in impedance control, and their equivalence when in contact with stiff environments, has not been recognized or demonstrated previously.

This chapter is organized as follows. First, the order of the desired impedance will be discussed and the implications for implementation will be shown. Second, the Jacobian transpose and the Jacobian inverse implementation strategies will be presented and discussed. Then, much of the previous research in Impedance Control will be discussed. It will be shown how each strategy fits into the Impedance Control framework. Also, it will be shown how each scheme contains explicit force control. In this way and with knowledge from the previous chapter, it will be possible to make comments on the efficacy of each strategy.

4.2 Zeroth, First, and Second Order Impedance

A linear impedance relation may be represented in the Laplace domain as:

$$F = Z(s)X. \tag{4.2}$$

The order of the polynomial $Z(s)$ is the order of the impedance.

The simplest form of an impedance controller has a zeroth order impedance. In this case Z is a constant and

$$F = KX. \tag{4.3}$$

The impedance parameter K is the desired stiffness of the manipulator. When a manipulator has no intrinsic stiffness, K dictates the apparent stiffness of the arm. This is accomplished with active control that uses position feedback. The value of the active stiffness is the position feedback gain.

A more typical form of an impedance controller is a first order impedance. In this case:

$$F = (Cs + K)X. \tag{4.4}$$

The added parameter C is the desired damping of the manipulator. It is equal to the sum of the active and natural damping. The active damping is accomplished by velocity feedback in a position controlled system. The value of the active damping is the velocity feedback gain. Since the active damping can be modified, C can take on any value which maintains stability. In fact, negative active damping can be used to eliminate the appearance of any damping in the arm. This is rarely desirable, since damping has a stablizing effect.

The last form of Impedance Control that shall be considered here is a second order type. The second order impedance controller has the form:

$$F = \left(Ms^2 + Cs + K\right) X. \tag{4.5}$$

The new parameter M is the desired inertia of the manipulator. While the arm has an intrinsic inertia due to its mass, this can be modified by active feedback. It follows from the previous two cases that acceleration feedback can be used for this purpose. In this case, the value of active inertia is the acceleration feedback gain. Its value can be used to adjust M. Few researchers have proposed such acceleration feedback schemes for Impedance Control [18]. This is because an acceleration measurement typically requires a second derivative, which will be extremely noisy. Instead, force feedback is used, as will be shown.

4.3 Model Based Control

Model based control involves the use of a dynamic model of the manipulator to determine the actuation torques [6]. As will be seen, a Cartesian space position control law which includes the dynamic model of the arm must utilize the inverse of the Jacobian.

Consider the mathematical representation of the physical arm and its modelled counterpart:

$$\text{Physical} : \quad \tau_A = D_P(\theta)\ddot{\theta} + h_P(\theta, \dot{\theta}) + g_P(\theta) - \Gamma_P \tag{4.6}$$

$$\text{Modelled} : \quad \tau_A = D_M(\theta)u + h_M(\theta, \dot{\theta}) + g_M(\theta) - \Gamma_M \tag{4.7}$$

where τ_A are the actuator torques, D is the manipulator inertia, h are the Coriolis and centripetal torques, g is the gravitational torque, Γ are the reaction torques from environmental interactions, and u is the control signal. The idea of model based control is to compute the actuator torques according to the model (the latter equation), and apply them to the arm (the former equation). Thus, this control strategy is often know as *computed torque*. The resultant acceleration of the arm is:

$$\ddot{\theta} = D_P^{-1}\left[D_M u + (h_M - h_P) + (g_M - g_P) - (\Gamma_M - \Gamma_P)\right] \tag{4.8}$$

$$\approx u \tag{4.9}$$

The approximation is valid for any reasonably good model of the manipulator. It has been shown that knowledge of the manipulator inertias to within 10% is sufficient [32].

The very important result of computed torque is that it provides a way to compensate for all of the non-linearities of the manipulator dynamics. Thus, a linear control signal, u, will provide the desired joint accelerations in the manipulator. The problem them becomes one of choosing u, which is essentially the desired joint accelerations.

For a Cartesian space position controller, the desired joint acceleration must be obtained from the desired Cartesian acceleration. First, it is known that:

$$\dot{x} = \mathcal{R}\mathcal{J}\dot{\theta} = J\dot{\theta} \tag{4.10}$$

where $\mathcal{R}$ is a rotation matrix from the end effector frame to the world frame, and $\mathcal{J}$ is the manipulator Jacobian. Taking the derivative of this equation and solving for the angular acceleration gives the control signal:

$$u \;=\; \ddot{\theta} \;=\; J^{-1}\left(\ddot{x} - \dot{J}\dot{\theta}\right) \tag{4.11}$$

where J is the manipulator Jacobian. Thus it is still necessary to define the desired Cartesian acceleration. This is accomplished by specifying the desired behavior of the manipulator to be a second order impedance:

$$M\ddot{x} - C\Delta\dot{x} - K\Delta x = f. \tag{4.12}$$

The impedance parameters, M, C, and K may be chosen. The variable x and its derivatives are obtained from the transformation of the corresponding angular values:

$$\Delta x \;=\; x_c - x_m \quad = \quad x_c - \mathcal{F}(\theta_m) \tag{4.13}$$

$$\Delta\dot{x} \;=\; \dot{x}_c - \dot{x}_m \quad = \quad \dot{x}_c - J\dot{\theta}_m \tag{4.14}$$

where $\mathcal{F}$ represents the forward kinematics, and c and m denote the commanded and measured quantities. For a physical system represented by Equation (4.12), the commanded values act as offsets to the variable (measured) quantities.

Finally, the force, f, corresponds to the physical force exerted on the manipulator $J^T f = \Gamma_P$. Thus,

$$f \;=\; f_{\text{reaction}} \;=\; -f_{\text{applied}} \;\approx\; -f_{\text{measured}} \;\equiv\; -f_m. \tag{4.15}$$

This value of the measured force may then be substituted into Equation (4.12) for the desired behavior and Equation (4.7) for the arm model.

Summarizing,

$$\tau_A \quad = \quad Du + h + g + J^T f_m \tag{4.16}$$

$$u \quad = \quad J^{-1}\left(\ddot{x}_u - \dot{J}\dot{\theta}_m\right) \tag{4.17}$$

$$\ddot{x}_u \quad = \quad M^{-1}\left[(C\Delta\dot{x} + K\Delta x) - f_m\right] \tag{4.18}$$

$$\Delta x \quad = \quad x_c - L(\theta_m) \tag{4.19}$$

$$\Delta\dot{x} \quad = \quad \dot{x}_c - J\dot{\theta}_m \tag{4.20}$$

The next two sections will illustrate the use of these equations. The first section shows the use of the full dynamics implementation, while the second section shows the use of a steady state simplification.

4.4 Control with Full Dynamics

This section illustrates the control schemes that have utilized the model based control described in the previous section.

4.4.1 Computed Torque

Computed Torque was the first scheme to use Equation (4.16) to calculate and compensated for the nonlinear dynamics of a manipulator [44]. However, the trajectory is still expressed in joint space as:

$$u \;=\; \ddot{\theta}_c \;+\; K_\omega(\dot{\theta}_c - \dot{\theta}_m) \;+\; K_\theta(\theta_c - \theta_m) \tag{4.21}$$

It has been shown that the fastest method of calculating the Computed Torque is by using Newton-Euler recursion [32].

4.4.2 Resolved Acceleration Control

Resolved Acceleration Control was the first scheme to use Equation (4.17) to resolve the desired Cartesian acceleration into joint space, for use in the Computed Torque scheme [40]. The Cartesian acceleration was specified as:

$$u \;=\; \ddot{x}_c \;+\; K_v(\dot{x}_c - \dot{x}_m) \;+\; K_p(x_c - x_m) \tag{4.22}$$

It can be seen that this equation corresponds to Equation (4.18) where

$$K_v \;=\; M^{-1}C \tag{4.23}$$

$$K_p \;=\; M^{-1}K \tag{4.24}$$

$$\ddot{x}_c \;=\; -M^{-1}f_m \tag{4.25}$$

This last equation seems strange at first, since Resolved Acceleration Control does not interact with the environment ($f_m = 0$). However, the feedforward acceleration can be thought of as the result of an *artificial force*. This force is exerted by the environment only in computer model of the world, and is calculated from the gradient of a modelled *artificial potential* field. One excellent use of artificial forces is for obstacle avoidance strategies in which objects to be avoided are surrounded by repulsive potentials. This concept will be discussed at length in Chapter 7.

4.4.3 Operational Space Control

Operational Space Control was the first formulation to resolve the dynamic equations into Cartesian space [29]. This scheme is essentially equivalent to Resolved Acceleration Control [34]. It appears very different, however, because the dynamic equations are expressed in Cartesian, or *operational* space. The transformation of Equation (4.16) can be readily accomplished by using the relation:

$$\tau = J^T F \tag{4.26}$$

Thus, from Equations (4.16) and (4.18) with $f_m = 0$:

$$\begin{aligned} F_A \;=\; (J^T)^{-1}\tau_A \;&=\; \left(J^T\right)^{-1} D J^{-1}\left(\ddot{x} - \dot{J}\dot{\theta}\right) \;+\; \left(J^T\right)^{-1} h \;+\; \left(J^T\right)^{-1} g \\ &=\; \left(J^T\right)^{-1} D J^{-1}\ddot{x} \;+\; \left(J^T\right)^{-1}\left(h - D J^{-1}\dot{J}\dot{\theta}\right) \;+\; \left(J^T\right)^{-1} g \\ &=\; \Lambda(x)\ddot{x} \;+\; \mu(x,\dot{x}) \;+\; p(x). \end{aligned} \tag{4.27}$$

where $p(x)$ is the gravity compensation term and μ is the corrected Coriolis and centripetal forces. Also, the relation

$$D(\theta) = J^T \Lambda(x) J \tag{4.28}$$

expresses how the manipulator inertia is related to its Cartesian space counterpart, which is the expression of the inertia at the end effector of the arm. The above equation for the arm dynamics may be further modified by pre-multiplying by the transpose of the Jacobian:

$$\tau \;=\; J^T F \;=\; J^T \Lambda(x)\ddot{x} \;+\; \tilde{b}(\theta,\dot{\theta}) \;+\; g \tag{4.29}$$

where

$$\tilde{b} = h - DJ^{-1}\dot{J}\dot{\theta} \tag{4.30}$$

The above two equations represent the heart of the operational space representation.

The value of $\ddot{x}$ is obtained from the equivalent of Equation (4.18) with $M = 1$. Since it only appears as a ratio with the arbitrary constants C and K, any value other than unity provides equivalent results. Also in Equations (4.16) and (4.18), $f_m = 0$ since this scheme does not consider environmental interaction. Unlike Resolved Acceleration Control, no artificial force is employed to provide a feedforward acceleration term, $\ddot{x}_c$. Thus,

$$\ddot{x}_c = \left(C\Delta\dot{x} + K\Delta x\right). \tag{4.31}$$

The absence of a feedforward term is one of the small ways in which this scheme differs from Resolved Acceleration Control. Another possible difference is that the Operational Space formulation was expanded to include the case of redundant manipulators. However, the same methodology can be used for Resolved Acceleration Control since the modifications are only with respect to the calculation of $\ddot{x}_c$, which becomes more general than Equation (4.18). In fact, it has been pointed out that Resolved Acceleration and Operational Space Control are essentially equivalent, and they also are part of the larger category of Geometric Control Theory [34].

Finally, it should be pointed out that the Operational Space formulation is mostly valuable as a conceptual tool. For implementational purposes, the arm dynamics are best calculated with the Resolved Acceleration formulation, which is expressed in joint space and utilizes the speed of the Computed Torque technique directly.

4.4.4 Second Order Impedance Control

Unlike the above two schemes, this scheme utilizes force feedback in its use of Equation (4.18). This should mean little difference in the expression of the control, but again it looks very different. First, Equations (4.17), (4.18) in (4.16) yield:

$$\tau \;=\; DJ^{-1}M^{-1}\left(C\Delta\dot{x} + K\Delta x - f_m\right) \;-\; J^{-1}\dot{J}\dot{\theta} \;+\; h \;+\; g \;+\; J^T f_m. \tag{4.32}$$

Equation (4.28) then gives:

$$\tau \;=\; J^T\Lambda M^{-1}\left(C\Delta\dot{x} + K\Delta x - f_m\right) \;-\; J^T\Lambda\dot{J}\dot{\theta} \;+\; h \;+\; g \;+\; J^T f_m. \tag{4.33}$$

Next, this controller employs the mobility tensor W which is the inverse of the Cartesian representation of the manipulator mass:

$$W \equiv \Lambda^{-1} \tag{4.34}$$

Using this relation in the above equation gives:

$$\tau \;=\; J^T W^{-1}M^{-1}\left(C\Delta\dot{x} + K\Delta x - f_m\right) \;-\; J^T W^{-1}\dot{J}\dot{\theta} \;+\; h \;+\; g \;+\; J^T f_m \tag{4.35}$$

$$\;=\; J^T W^{-1}M^{-1}\left(C\Delta\dot{x} + K\Delta x\right)h \;-\; J^T W^{-1}\dot{J}\dot{\theta} \;+\; J^T\left(1 - W^{-1}M^{-1}\right)f_m \;+\; g \tag{4.36}$$

Adding confusion to this equation is the inclusion of the following identity:

$$h \;=\; \left[J^T\left(J^T\right)^{-1}DJ^{-1}JD^{-1}\right]h \;=\; J^T W^{-1}JD^{-1}h \tag{4.37}$$

This changes the above equation to:

$$\tau \;=\; J^T W^{-1}M^{-1}\left(C\Delta\dot{x} + K\Delta x\right) \;+\; J^T W^{-1}\left(JD^{-1}h - \dot{J}\dot{\theta}\right) \;+\; J^T\left(1 - W^{-1}M^{-1}\right)f_m \;+\; g \tag{4.38}$$

This is the expression of Impedance Control in the above references.

Second order impedance control differs from the schemes previously presented, because it uses force feedback. First, this feedback is used in the physical model of the arm dynamics, Equation (4.16). This is equivalent to introducing end effector forces into the Newton-Euler dynamics calculations. Second, the feedback is used in the impedance relation, Equation (4.18). While Equation (4.16) effectively linearizes the arm, Equation (4.18) modifies the Impedance Control signal to compensate for the experienced force.

It can now be seen that it is the force feedback in the control signal which modifies the apparent inertia of the arm [23]. Equation (4.33) best shows this effect. In this controller, as with the previous ones, the premultiplication of K and C by ΛM^{-1} changes nothing. However, this is not true for the force feedback signal f_m. The term ΛM^{-1} is a mass ratio that reduces or increases the amount of actuator torque applied. For simplicity sake, it will be assumed that the impedance parameters are diagonal in the Cartesian space defined by the eigenvectors of Λ. In this case, ΛM^{-1} (or its diagonalized counterpart) can be thought of as a matrix of mass ratios along the diagonal. Since Λ is due to the physical inertia of the arm, it is the impedance parameter M which determines each ratio. For $M \rightarrow 0$ the ratio becomes very large; for a small measured force, a large accelerating torque is applied to the arm. Thus, the apparent inertia of the arm is reduced. (It is important to remember that the external force does not cause the acceleration because it has been effectively negated by the $J^T f_m$ term.) Similarly, for $M \rightarrow \infty$ the ratio becomes very small; for a large measured force, a small accelerating torque is applied to the arm. Thus, the apparent inertia of the arm is increased. In this way, second order impedance control not only changes the stiffness and damping properties of the arm, but its inertia as well.

4.5 Control with a Steady State Approximation

This section discusses some control schemes that have used a steady state approximation of the model based control strategy outlined previously. For the steady state, all velocities in the dynamics equations are assumed zero. Therefore, all compensation terms with velocity dependence are zero:

$$\dot{\theta} \;=\; \dot{J} \;=\; h\left(\theta, \dot{\theta}\right) \;=\; 0 \tag{4.39}$$

Thus, Equations (4.16) through (4.18), and Equation (4.28) gives:

$$\tau_A \;=\; J^T \Lambda M^{-1} \left[(C\Delta\dot{x} + K\Delta x) - f_m \right] \;+\; J^T f_m + g \tag{4.40}$$

Because no dynamic compensation is done in this scheme, the matrices ΛM^{-1}, $\Lambda M^{-1} C$, and $\Lambda M^{-1} K$ can be chosen to be diagonal gain matrices.

While not as accurate as the full dynamics representation, this approach has one major advantage. There is no inverse of the Jacobian, which can become singular. Therefore, this type of control scheme is much more robust but much less accurate, especially for situations in which the velocity is not really zero. However, these differences disappear when the arm is constrained by a stationary environment. The following section describes a control scheme which subscribed to this reduced dynamics framework.

4.5.1 Second Order Impedance Control

Second order impedance control without dynamics compensation has been investigated by Kazerooni [28] and Hamilton [19]. The approach introduced by Kazerooni was to linearize the equations describing the manipulator by considering small displacements only. Thus, the target second order impedance is present in the following equation:

$$\left(Ms^2 + Cs + K\right) \delta x = \delta f \tag{4.41}$$

The manipulator dynamics, similar to Equation (4.6), are:

$$\tau = D_P(\theta)\ddot{\theta} + h_P(\theta, \dot{\theta}) + g_P(\theta) \tag{4.42}$$

where τ is the sum of torques given by:

$$\tau = T_s \tau_A + J^T F_e \tag{4.43}$$

where T_s is the gear ratios, and F_e are the external forces. For the DD Arm II $T_s = 1$. From Equation (4.15) it is known that:

$$F_e = -f_m \tag{4.44}$$

Considering the small displacement approximation, these equations become:

$$T_s \delta\tau \;=\; D\delta\ddot{\theta} \;+\; \frac{\partial g}{\partial \theta} \;+\; J^T \delta f_m \tag{4.45}$$

In the following discussion, it will be assumed that the gravity compensation term is provided separate from the impedance controller. Thus, this term will not appear explicitly again.

Also introduced in this development is a first order model of the actuator dynamics:

$$\frac{\delta\dot{\tau}_{Ai}(t)}{\lambda_i} \;+\; \delta\tau_{Ai}(t) \;=\; \delta u_i(t) \qquad i = 1, 2, \ldots N \tag{4.46}$$

where λ_i is the bandwidth of each of the N actuators, and u is the input signal. The introduction of the actuator dynamics makes Kazerooni's development more precise for manipulators that have dynamics. However, the DD Arm II used later in the experiments of Chapter 6 does not have actuator dynamics. Also, this addition obscures the role of the impedance parameters in the final solution. Comparisons with other schemes, therefore, become difficult. For the remainder of this discussion Hamilton's formulation will be followed instead.

Hamilton, while first introducing the actuator dynamics, neglects them if λ is large. In this case, the control signal is assumed equal to the actuator torques:

$$\tau_{Ai} = u_i \qquad \lambda_i \to \infty \tag{4.47}$$

The control law is chosen to be a generic linear controller based on position, velocity, and force feedback.

$$u = G_\theta(\theta_c - \theta_m) - G_\omega \dot{\theta}_m - G_f f_m \tag{4.48}$$

where G_i are the gain matirces to be chosen as in the Computed Torque method, u can be substituted for the acceleration in Equation (4.45).

$$\left(Ds^2 + K_\omega s + K_\theta\right)\delta\theta \;=\; \left(J^T - K_f\right)\delta f_m \tag{4.49}$$

where K_i are obtained from G_i by including the gearing ratios. Comparing this equation for the physical system under small perturbation, with that for the target impedance, Equation (4.41) gives the following relations:

$$\begin{aligned} M &= \left(J^T + K_f\right)^{-1} D J^{-1} \\ C &= \left(J^T + K_f\right)^{-1} K_\omega J^{-1} \\ K &= \left(J^T + K_f\right)^{-1} K_\theta J^{-1} \end{aligned} \tag{4.50}$$

which can be inverted to give:

$$\begin{aligned} K_f &= D J^{-1} M^{-1} - J^T \\ K_\omega &= D J^{-1} M^{-1} C J \\ K_\theta &= D J^{-1} M^{-1} K J \end{aligned} \tag{4.51}$$

or, using Equation (4.28) the inertia matrix can be transformed into Cartesian space:

$$\begin{aligned} K_f &= J^T \Lambda M^{-1} - J^T \\ K_\omega &= J^T \Lambda M^{-1} C J \\ K_\theta &= J^T \Lambda M^{-1} K J \end{aligned} \tag{4.52}$$

Hamilton presents three methods for the selection of the gain matrices to ensure stability and positive definiteness. The first method, however, supercedes the other two. This method requires diagonalizing Λ and choosing the position and velocity gains in the resulting frame. This is equivalent to the method of gain selection mentioned in the previous section. In fact, using Equations (4.52) with Equations (4.48), (4.47), (4.43), (4.44), and (4.10) gives:

$$\tau = J^T \Lambda M^{-1} \left(-K\delta x - C\delta\dot{x} - f_m\right) + J^T f_m + g \tag{4.53}$$

$$= J^T \Lambda M^{-1} \left(-K\delta x - C\delta\dot{x}\right) + J^T \left(1 - \Lambda M^{-1}\right) f_m \tag{4.54}$$

The first equation is identical to Equation (4.40) as expected. The second equation is equal to Equation (4.38), considering the steady state assumptions in Equation (4.39). Thus, this scheme is the same as the former without the velocity dependent dynamics, as predicted.

4.6 Explicit Force Control within Impedance Control

The two second order impedance controllers reviewed above can be shown to contain explicit force control. This aspect of impedance control has not previously been recognized. While Hogan recognized some correspondence between Impedance Control and explicit force control [23], the relation was not specifically or clearly stated. A general argument supporting this new interpretation was presented in the introduction. Now, it will be shown explicitly for the impedance controllers described previously in this chapter. Later, it will be shown how this framework includes both Stiffness Control, and Accommodation Control.

Consider the two second order impedance controllers represented by Equations (4.33) and (4.53), repeated here for convenience:

$$\begin{aligned} \tau &= J^T \Lambda M^{-1} \left(-K\delta x - C\delta\dot{x} - f_m\right) + J^T f_m + g \\ \tau &= J^T \Lambda M^{-1} \left(C\Delta\dot{x} + K\Delta x - f_m\right) - J^T \Lambda \dot{J}\dot{\theta} + h + g + J^T f_m \end{aligned}$$

These equations are the same except for the inclusion of velocity dependent dynamics, as previously discussed. Furthermore, the terms that compensate for velocity dependent forces and gravity can be considered feedforward terms, and ignored for the remainder of this discussion. What is left is an equation for torque of the form:

$$\tau = J^T K_f'(f_c - f_m) + J^T f_m - J^T K_v \dot{x}_m \tag{4.55}$$

$$f_c = K(x_c - x_m) + C\dot{x}_c \tag{4.56}$$

$$K_f' = \Lambda M^{-1} \tag{4.57}$$

This formulation is very similar to the proportional gain explicit force controller discussed in Chapter 3. Since velocity feedback was used in the explicit force controllers, the only major difference here is the use of the feedback position in the calculation of the commanded force. The commanded velocity can be assumed to be zero ($\dot{x}_c = 0$), which is usually the case.

In the above formulation, the impedance parameters K and C determine the commanded force used in an explicit force controller with a proportional gain of ΛM^{-1}. The term $J^T f_m$ can be seen to negate the

reaction force that is experienced by the arm. As expressed in the transfer function of Equation (3.9) the stability of this controller is guaranteed for $K_f' \geq 0$. This is equivalent to the condition:

$$\Lambda M^{-1} \geq 0 \tag{4.58}$$

(Again, it is assumed that the matrices K_f' and ΛM^{-1} are diagonal. Therefore the inequality is considered to refer to each of the elements individually.) This loosely implies that the open loop pole location of the root locus corresponds to the impedance parameter $M \to \infty$ and the zeros indicate a value of $M \to 0$. Of course, this statement is only true if the principal axes of Λ and M are parallel.

It is also important to note that force control is often used when the manipulator is in contact with a stiff environment, and $\dot{x}_m = 0$ and x_m is an arbitrary constant, which can be set to zero. Thus, the commanded force reduces to:

$$f_c \;=\; Kx_c + C\dot{x}_c \tag{4.59}$$

which has no dependence on position feedback. Again, it is the usual case that the commanded velocity is zero. It can, therefore, be seen that *second order impedance control against a stiff environment is equivalent to explicit force control with proportional gain and feedforward.*

Finally, the presence of a proportional force controller inside the impedance controller presented leads to the following question: Do other impedance controllers actually contain other types of explicit force control? The answer is obviously yes. Two of the more famous ones will be reviewed next.

4.7 Impedance Control With Other Types of Explicit Force Control

4.7.1 Accommodation and Resolved Rate Control

Accommodation control has the following form [69, 68]:

$$\tau \;=\; K_\theta(\theta_r - \theta_m) \;+\; K_\omega(\dot{\theta}_r - \dot{\theta}_m) \tag{4.60}$$

$$\dot{\theta}_r \;=\; \dot{\theta}_c - J^{-1}K_{fa}f_m \tag{4.61}$$

This formulation may be modified (using the Laplace domain representation):

$$T \;=\; \frac{K_\theta}{s}\left(\left(s\Theta_d - J^{-1}K_{fa}F_m\right) - s\Theta_m\right) \;+\; K_\omega\left(\left(s\Theta_d - J^{-1}K_{fa}F_m\right) - s\Theta_m\right) \tag{4.62}$$

$$\;=\; \left(\frac{K_\theta}{s} + K_\omega\right)\left(sJ^{-1}\left(X_d - X_m\right) - J^{-1}K_{fa}F_m\right) \tag{4.63}$$

$$\;=\; \left(\frac{K_\theta}{s} + K_\omega\right)J^{-1}\left(s\Delta X - K_{fa}F_m\right) \tag{4.64}$$

$$\;=\; \left(\frac{J^TK_xJ}{s} + J^TK_vJ\right)J^{-1}K_{fa}\left(K_{fa}^{-1}s\Delta X - F_m\right) \tag{4.65}$$

$$\;=\; J^T\left(\frac{K_xK_{fa}}{s} + K_vK_{fa}\right)\left(K_{fa}^{-1}s\Delta X - F_m\right) \tag{4.66}$$

Thus, Accommodation Control has the form of an impedance controller with no dynamics compensation, and a PI internal force controller. Comparing with the form of the previous impedance controllers examined:

$$M \;=\; \left(K_vK_{fa}\right)^{-1}\Lambda \tag{4.67}$$

$$C \;=\; K_{fa}^{-1} \tag{4.68}$$

$$K \;=\; 0 \tag{4.69}$$

Thus, this controller provides no stiffness to the arm, and a damping that is inversely proportional to the accommodation gain. The apparent inertia of the arm can be modified by the proportional gain as previously discussed. However, the integral gain, $K_x K_{fa}$, does not cleanly map into physical impedance analog.

It is also important to note that the PI gain matrices, $K_x K_{fa}$ and $K_v K_f a$ are not diagonal. This is because the original gains, K_θ and K_ω where diagonal in joint space. Obviously, if decoupled Cartesian behavior is desired the matrices should be chosen diagonal in Cartesian space, not joint space.

Finally, it can be seen that the removal of a force feedback signal, $F_m = 0$, gives a PI controller which follows a commanded damping force only. This controller is usually expressed in the form of Equation (4.64). Because the inverse Jacobian is used to resolve the Cartesian velocities into joint space, this is known as Resolved Rate Control.

4.7.2 Stiffness Control

Stiffness control has the following form [54]:

$$T = K_\omega s\left(\Theta_c - \Theta_m\right) + T_c + K_{fs}\left[\frac{s+a}{s+b}\right]\left(T_c - T_m\right) + \frac{K_{fs}}{s}\left(T_c - T_m\right) \tag{4.70}$$

$$T_c = T_b + K_\theta\left(\Theta_c - \Theta_m\right) \tag{4.71}$$

$$K_\theta = J^T K_x J \tag{4.72}$$

where K_x is a diagonal Cartesian gain matrix, T_b is a bias torque vector, $(s+a)/(s+b)$ is lead-lag filter. The bias torque can be eliminated by considering the following identity:

$$T_b = J^T F_b = J^T K_x \Delta X_b = J^T \left(J^T\right)^{-1} K_\theta J^{-1} \Delta X_b = K_\theta \Delta \Theta_b \tag{4.73}$$

Thus the bias commanded position can be offset by a bias value in either Cartestian or joint space:

$$\Delta\Theta = \left(\Theta_c + K_\theta^{-1} T_b\right) - \Theta_m \tag{4.74}$$

The above expression of Stiffness control can be modified so that it can be more easily compared with the developed framework.

$$T = K_\omega s\Delta\Theta + J^T K_x J\Delta\Theta + K_{fs}\left[\frac{s+a}{s+b} + \frac{K_{fs}}{s}\right]\left(J^T K_x J\Delta\Theta - T_m\right) \tag{4.75}$$

$$= K_\omega s\Delta\Theta + J^T K_x \Delta X + K_{fs}\left[\frac{s+a}{s+b} + \frac{K_{fs}}{s}\right] J^T\left(K_x \Delta X - F_m\right) \tag{4.76}$$

In this form, Stiffness control can be seen to be a variation of Impedance Control with an internal force controller that uses integral and lead-lag compensation, and a feedforward signal. While, the impedance stiffness parameter is obvious ($K = K_x$), other correspondence is not so strict. The active damping is performed in joint space and is not passed though the explicit force controller. Inertial modification does not appear since there is not proportional force gain. However, this controller was designed for stiffness control only, and modification of other impedance characteristics is not a design goal. Therefore, this is a zeroth order, or at best a first order impedance controller.

4.8 Conclusion

This chapter has provided a review of some of the major Impedance Control strategies that have been proposed. It is well known that the stiffness and damping of the manipulator can be modified by position and velocity feedback. This is usually the type of control that is provided in position controlled arms. However,

if the manipulator is to interact with the environment, then force sensing is usually employed in a method of actively modifying the apparent inertia of the manipulator. This force feedback loop constitutes an inner loop explicit force controller.

This chapter has made clear for the first time the fact that impedance control schemes that modify the arm's inertia are effectively using explicit force control with proportional gain and feedforward (plus a damping term). In this case, inertial modification is equivalent to changing the force control gain. Further, for a stiff environment the second order impedance control is equivalent to proportional gain force control. This will be demonstrated experimentally in Chapter 6.

Finally, recognition of equivalence of second order impedance control to explicit force control with proportional gain has provided some new understanding. The first insight is that other impedance control schemes contain other explicit force control strategies (PI for example). However, pursuing these different impedance control strategies does not seem worthwhile when the explicit force controllers can be used directly. A second insight is that proportional force control gains down to negative one can be stably used, and are equivalent to impedance mass ratios increasing to infinity. This knowledge is extremely useful for the stable control of impacts with the environment, as will be discussed in the next chapter.

Chapter 5

Impact Control

5.1 Introduction

There are two extreme modes of operation for a manipulator: position controlled motion through free space, and force controlled interaction while constrained by the environment. Obviously the manipulator must change from one mode to the other readily. Usually switching from constrained force control to unconstrained position control presents no problems. However, switching from free space motion to constrained force control has the significant problem of impact forces. These forces can be very large, and can drive an otherwise stable controller into instability. Typically, it is the force control strategy that must deal with this transient phenomenon, since the large force does not occur until after contact has occurred. However, the natural elasticity of an impact, or the response of the force controller to the transient, can cause the manipulator to rebound from the environment. Thus, the manipulator is once again unconstrained. This phenomenon can establish oscillatory behavior. Obviously it is the goal of any controller to pass through this transitory period successfully, and have the manipulator stably exerting forces on the environment in the end. The controller must, therefore, pass through the impact phase by attempting to maintain contact with the environment until all of the energy of impact has been absorbed. To maintain stability and contact during this phase, a novel method of *impact control* is presented in this chapter.

Previous research in force control has treated the impact phase as a transient that is dealt with by the same controller used to follow commanded force. The form of the force controller is typically one of those strategies that has been presented in Chapters 3 and 4. In this chapter it will be shown that the best implementation of these strategies for force following is insufficient for impact control. But, the impact controller presented here still fits into the complete framework of force control that has been developed. To understand this, the previous schemes will be briefly discussed and their weaknesses revealed. Then a newly proposed impact control strategy will be presented in the context of explicit force control and impedance control.

5.2 Previously Proposed Methods For Impact Control

Previous work in force control has not employed any changes in the force controller structure (variable gains or controller type). Instead the impact phase is treated as a transient that must be dealt with by the controller and gains chosen for force control (once contact has been established). At most, modification of the control strategy has been attempted through active damping and/or passive compliance and damping.

5.2.1 Maximal Active Damping

One proposed method of dealing with the impact problem is to employ maximal damping during the impact phase [31]. Any force controller may be used; proportional control was used in this reference. The goal of

this strategy is to damp out the oscillations caused by the transition. While this may be successful for soft environments, stiff environments have oscillations with small amplitudes and high frequencies. This makes damping difficult for two reasons. First, changes in position of the environmental surface may be smaller than the resolution of the manipulator's position measurement devices. In this case, no velocity will be sensed. Second, for fast oscillations the calculated velocity signal will lag its ideal value and the damping force may cause instability by being applied out of phase with the true velocity of the surface. This phase lag problem will be discussed in Section 6.7.1. These problems are compounded by the fact that a stiff environment which causes them will also cause a larger impact force and need active compensation the most. Thus, this scheme fails when most needed.

5.2.2 Passive Compliance and Damping

Another method for absorbing the shock of impact is to use passive compliance, either on the end effector or in the environment. Some researchers have proposed the use of soft force sensors [53, 71]. Another suggests the use of compliant 'skin' for the force sensor [1]. These methods appear to provide stable impact in two ways. First, the material used naturally provides passive damping that helps absorb some of the energy of impact, without the resolution or time lag problems of active damping. Second, the compliance of the material lessens the effective stiffness of the system. Following from the argument of the last paragraph, this lessening of the stiffness helps active damping work. Because the end effector remains in contact with the environment over larger ranges of displacements for the same experienced force, the displacement will not be below the resolution of the arm's position measurement devices. Thus a velocity may be determined and active damping employed.

There are problems with passive compliance. First, it may not be modified without physical replacement of the material. Second, it limits the effective stiffness of the manipulator during position control. Third, it eliminates precise knowledge of the position of the environment. And fourth, it limits the forces that may be applied — beyond a certain range of operation the compliant material is not linear and is prone to physical failure.

5.2.3 Integral Explicit Force Control

As was discussed in Chapter 3, integral force control acts as a low pass filter. Thus, for impact transients, the high frequency components might be filtered effectively. For impacts with low energy or with an inelastic environment this may be sufficient. Otherwise, bouncing may occur for high energy impacts or stiff environments. Results consistent with this analysis have been reported [74]. However, the conclusion presented in this reference is that integral control (with damping) is best for impact. This contradicts the experimental results obtained with the DD Arm II and reported in Chapter 6. There, integral control is shown to be very oscillatory (at best) during impacts. This is because of the nonlinearity introduced by loss of contact with the surface. This nonlinearity makes the system model invalid and the stability predictions false for impacts. The result is integrator windup and severe hopping on the surface.

5.2.4 Impedance Control and Proportional Explicit Force Control

As was described in the previous chapter impedance control against a stiff environment is equivalent to explicit force control with proportional gain. This type of scheme has been tried by many researchers [23, 27, 31, 73, 1]. However, the proportional gain in these implementations is not tuned for the best impact response. For explicit force controllers the gain is tuned for optimal command following once contact has been established. For impedance schemes, the proportional gain is chosen to obtain the desired inertia for free space motion or force exertion, but not impact. These implementations place the poles well off the real axis in Figure 3.2. Thus the resultant system is oscillatory and bouncing will occur after impact. This is consistent with simulation and experimental results [14, 1]. A solution to this problem is to use a different proportional gain for the impact phase. This will be discussed in the next section.

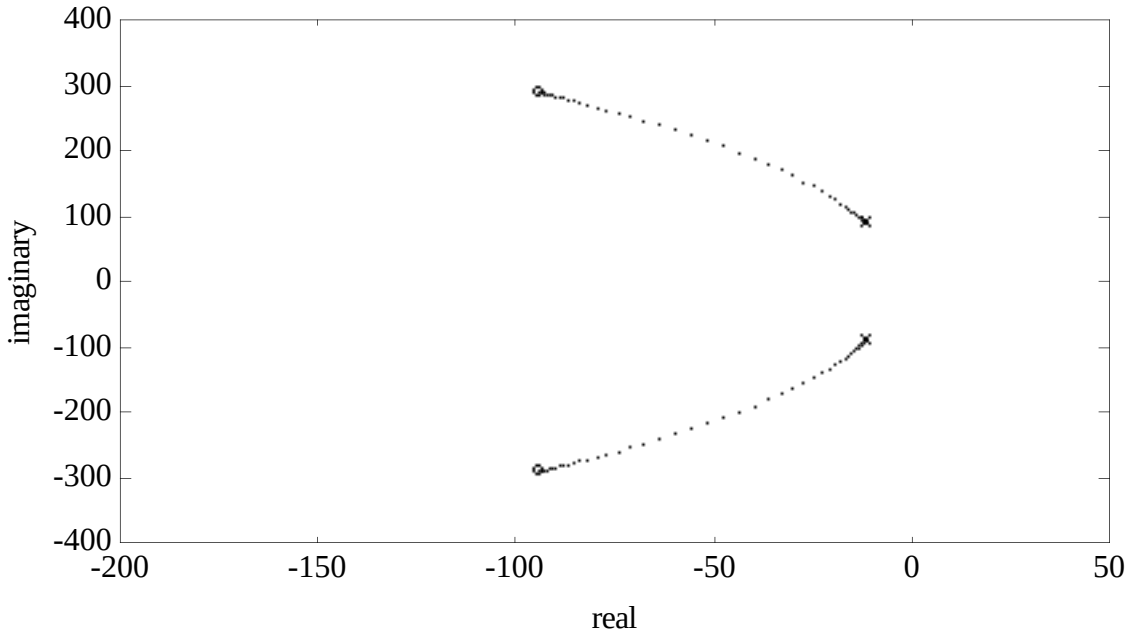

Figure 5.1: Root locus for the second order model under proportional gain explicit force control.

5.3 Impact Control

Impact control is best introduced in a discussion that involves a simplified system without sensor dynamics. This is equivalent to removing the sensor poles from the model developed in Chapter 2. After the initial discussion without sensor dynamics, the full fourth order model will be used as the plant of the impact controller. All model parameter values for the analyses are from Chapter 2.

5.3.1 Impact Control Without Sensor Dynamics

The model of the arm / environment plant that neglects sensor dynamics was developed in Section 2.4. The block diagram of the plant is shown in Figure 2.9 and the corresponding transfer function is given by Equation (2.18). For a proportional gain explicit force controller with this plant, the root locus is shown in Figure 5.1. (Comparing this locus with that of Figure 3.2 shows the effect of ignoring the sensor poles.) If the proportional gain is made negative, the resultant root locus is the complement of the previous one, as shown in Figure 5.2. It can be seen that for very small and very large negative gains, the poles are in the left half plane and the system is stable. The case of very large gains will be ignored, since the model will surely be invalid under this extreme due to nonlinearities and modelling errors. However, for small negative gains the model is valid and the system is stable. Further, the roots move to the real axis, eliminating any oscillatory behavior. Figure 5.3 shows an enlargement of this part of the locus. The root locus crosses into the right half plane for $K_{fp} < -1$. This is consistent with the analysis of proportional force control in Section 3.2.2. In that section it was shown that for a proportional gain explicit force controller, elimination of feedforward signal and inclusion of a reaction force feedback compensation signal provides an equivalent controller with gain $K'_{fp} = K_{fp} - 1$. Thus, the root locus may be expressed in terms of K'_{fp} as in Figure 5.4. Observing this root locus it is immediately apparent that the most stable gain is the one that places the two poles at the point where the roots leave the real axis. Ignoring the sensor dynamics, an approximate value of this gain may easily be determined. Using the notation of Section 2.5 and the proportional force controller of Figure 3.5

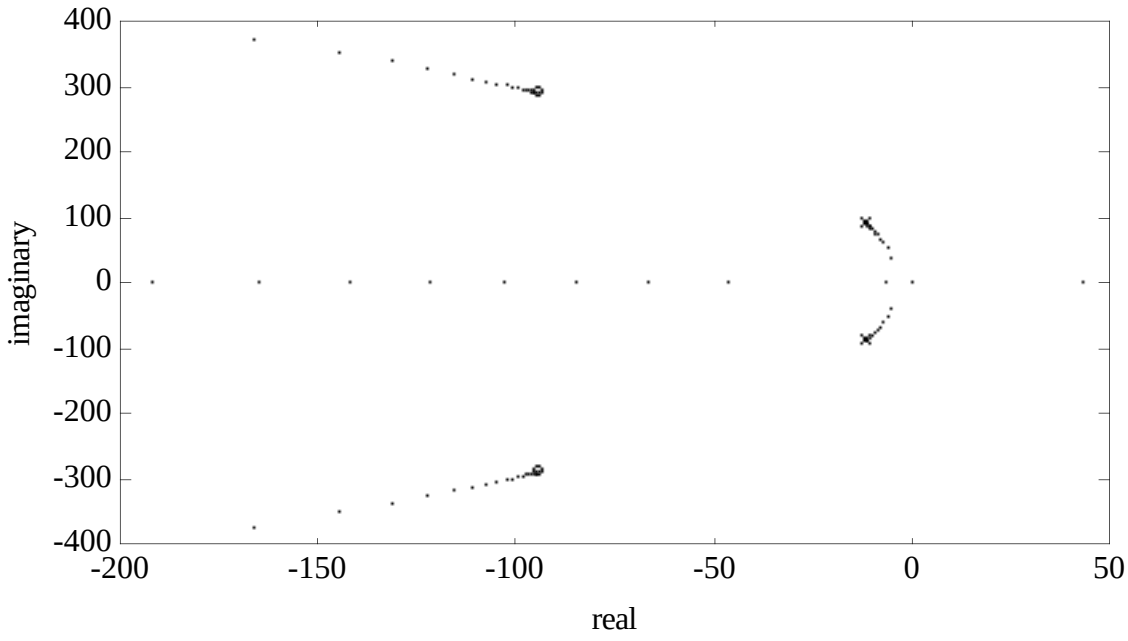

Figure 5.2: Root locus for the second order model under negative proportional gain explicit force control.

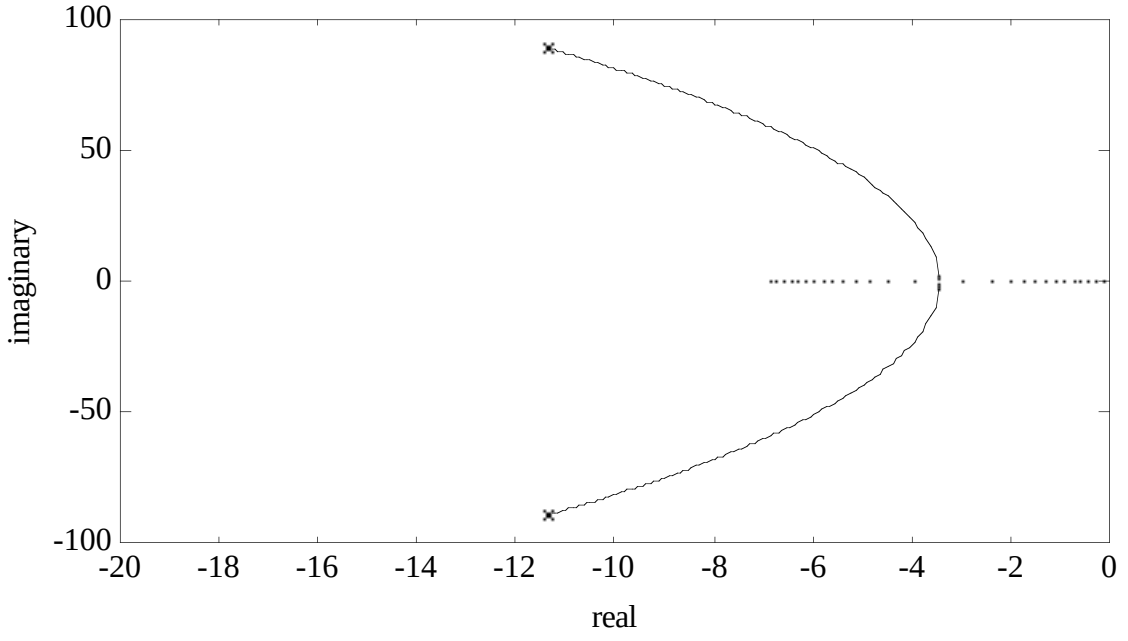

Figure 5.3: Root locus for the second order model under negative proportional gain explicit force control for K_{fp} from 0 to -1 in steps of 0.0001 . The double root occurs for $K_{fp} \approx -0.9985$.

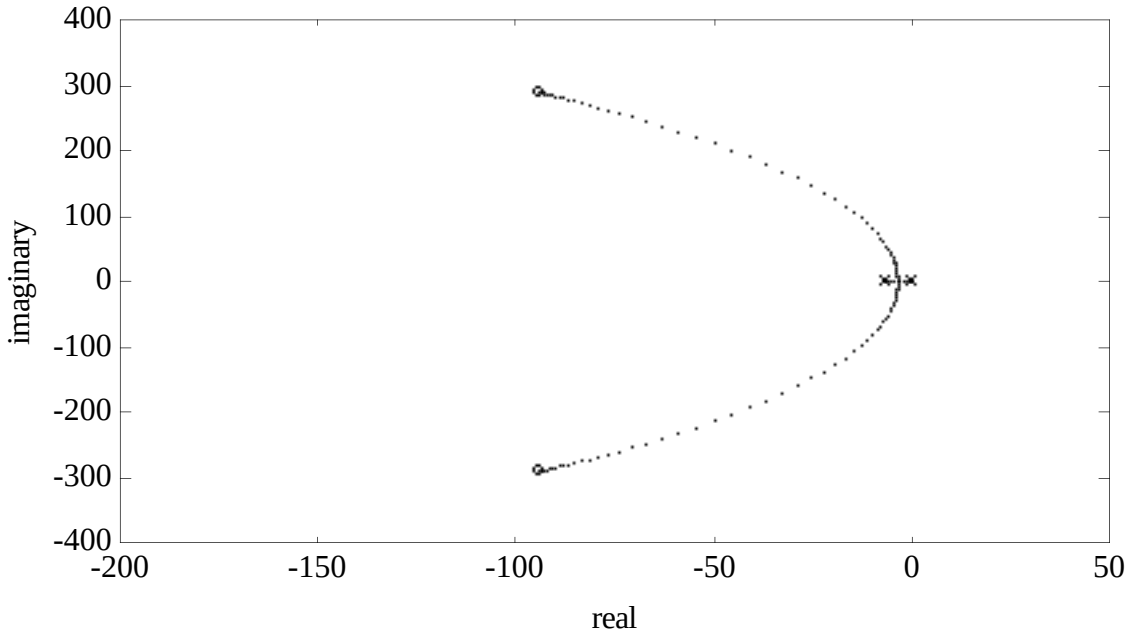

Figure 5.4: Root locus for the second order model for $K'_{fp} = K_{fp} - 1$. The double root occurs for $K'_{fp} \approx 1.5 \times 10^{-3}$.

the transfer function of this system is:

$$\frac{F_m}{F} = \frac{K'_f AE}{1 + K'_f AE} \tag{5.1}$$

which has the characteristic equation:

$$(m_r + K'_f m_e)s^2 + (K_v + K'_f c_e)s + K'_f k_e = 0 \tag{5.2}$$

The roots of this system are at:

$$s = \frac{-(K_v + K'_f c_e) \pm \sqrt{(K_v + K'_f c_e)^2 - 4(m_r + K'_f m_e)K'_f k_e}}{2(m_r + K'_f m_e)} \tag{5.3}$$

The system is critically damped when the argument of the radical is zero. This criterion yields a second order equation in K'_f:

$$(c_e^2 - 4m_e k_e)K'^2_f + (2c_e K_v - 4m_r k_e)K'_f + K_v^2 \tag{5.4}$$

which has the roots:

$$K'_f = \frac{(4m_r k_e - 2c_e K_v) \pm \sqrt{(4m_r k_e - 2c_e K_v)^2 - 4(c_e^2 - 4m_e k_e)K_v^2}}{2(c_e^2 - 4m_e k_e)} \tag{5.5}$$

$$= \frac{(4m_r k_e - 2c_e K_v) \pm 4\sqrt{m_r^2 k_e^2 - m_r k_e c_e K_v + m_e k_e K_v^2}}{2(c_e^2 - 4m_e k_e)} \tag{5.6}$$

$$\approx \frac{(4m_r k_e - 2c_e K_v) \pm 4m_r k_e}{-8m_e k_e} \tag{5.7}$$

$$\approx \frac{c_e K_v}{4m_e k_e} \tag{5.8}$$

using the previously verified assumption of large k_e, and considering only the positive root. Thus, the double root of the characteristic equation occurs for quite a small value of the proportional gain. There are three equivalent ways to view this result:

Proportional force control with reaction force compensation. This is the controller in Figure 3.6. In this case, the controller does not utilize the force error signal since $K_f' \approx 0$. However, the reaction force of the impact is directly negated by a feedback signal. Viewed this way, the impact controller does not bounce because the oscillations in the commanded force and those in the experienced force are equal and opposite. Thus the surface is at a node of two interfering pressure waves. No net force means no net acceleration. Any initial oscillation is damped out by natural and active damping.

Proportional force control with negative gain and a feedforward signal. This is the controller in Figure 3.5. While this controller looks different than above, it has been shown in Section 3.2.2 that it is equivalent to proportional force control with reaction force compensation. In this case the controller multiplies the force error by $K_f = K_f' - 1 \approx -1$. There is also a feedforward signal of the commanded force.

Second order impedance controller with large target mass. As discussed in Chapter 4, a second order impedance controller is equivalent to a explicit force controller when in contact with a stiff environment. Second order impedance controllers employ a proportional gain, ΛM^{-1}, where Λ is the arm mass, and M is the desired mass. Viewed in this way, the impact controller matches the apparent mass of the arm to the stiffness and damping of the environment such that the resultant system is critically damped. More imprecisely, it can be said that the arm is made to appear so massive that it can't bounce.

Finally, it is worthwhile to look at the Bode plots for this system in Figure 5.5. The negative proportional gain, or the reaction force feedback compensation (depending on the representation) causes the system response to be greatly out of phase with the disturbance. At the resonance frequency of ~ 90 rad/sec, this phase difference is $\sim 140°$. Thus, the disturbance force and the response to it destructively interfere, and cancel the force oscillations due to impact.

5.3.2 Impact Control With Sensor Dynamics

Including the sensor dynamics may change the above analysis somewhat by introducing an additional set of poles. Obviously, if the sensor poles are far from the environmental poles they will have little effect, and the above results will remain the same. However, the fourth order model that was previously developed has one pole relatively close to the environmental poles and zeros. The effect on the root locus of $-K_{fp}$ is shown in Figure 5.6. The major difference introduced by the sensor pole is that the environmental poles never become purely real. However, they do move closer to the real axis, and achieve their minimum imaginary parts for values of K_{fp} near negative one ($K_{fp} \approx -0.8$). Figure 5.7 shows the locus for $-1 \leq K_{fp} \leq 0$. Also, the sensor pole moves to the right on the real axis and passes the environmental pole pair. Thus, for gains close to negative one, this pole act as a lowpass filter, eliminating oscillations. For completeness the entire root locus for $-1 \leq K_{fp} < \infty$ or $0 \leq K_{fp}' < \infty$ is shown in Figure 5.8.

5.4 Conclusion

This chapter has presented a new impact control strategy based on a proportional gain explicit force controller with a feedforward signal and negative gains. It has been shown previously and in this chapter that this controller is equivalent to second order impedance control with a large target mass. It is readily apparent that this impact control method can not be used for tracking input force commands since the input force command is largely ignored. However, it still provides an excellent method of maintaining stability and contact with the environment during the transition from motion through free space to contact with the environment. Once

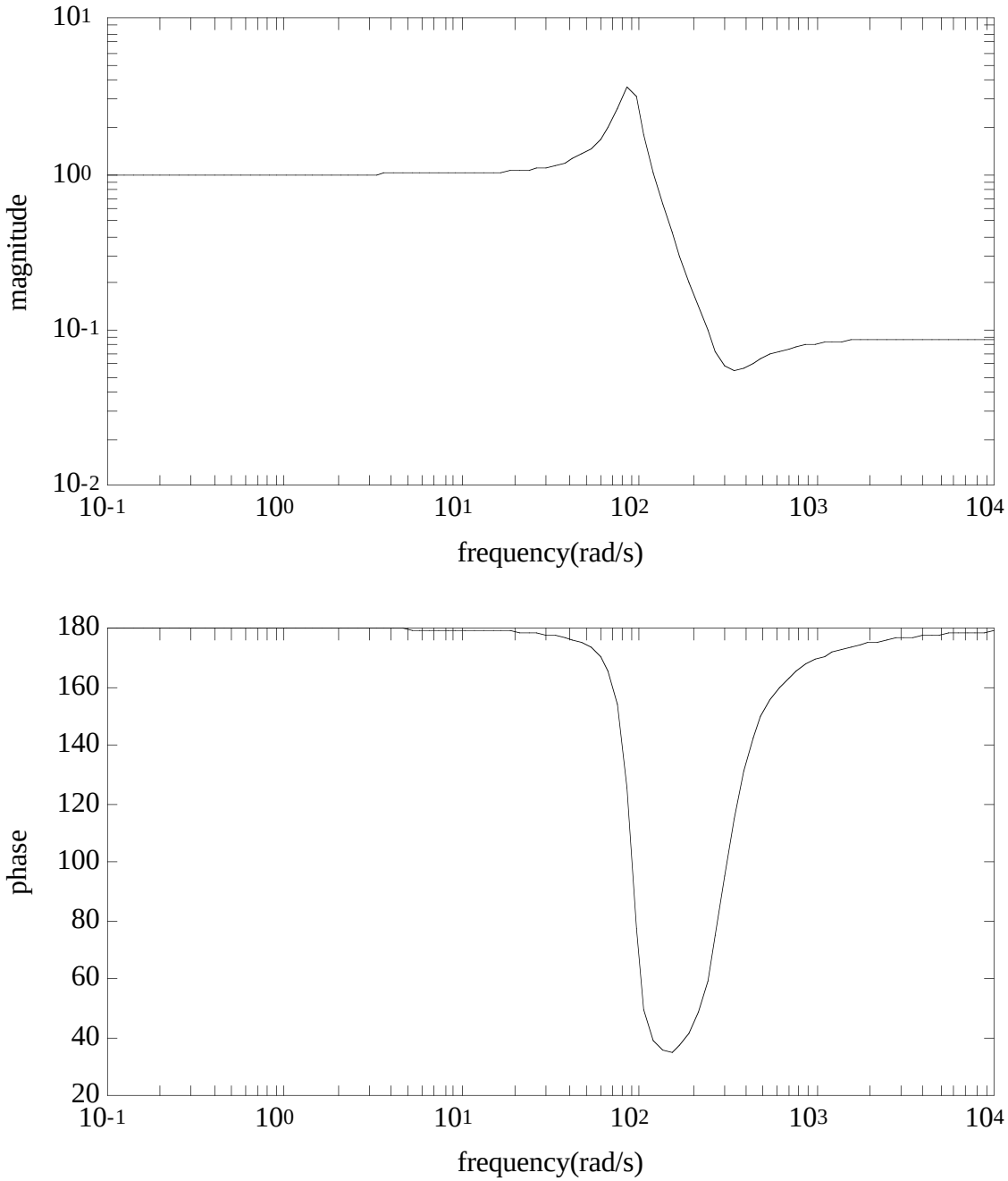

Figure 5.5: Bode plots for the second order system under negative proportional gain explicit force control. The phase at the resonance peak is approximately $140°$. Thus, the force response of the system is out of phase with the disturbance from the environment, causing cancellation.

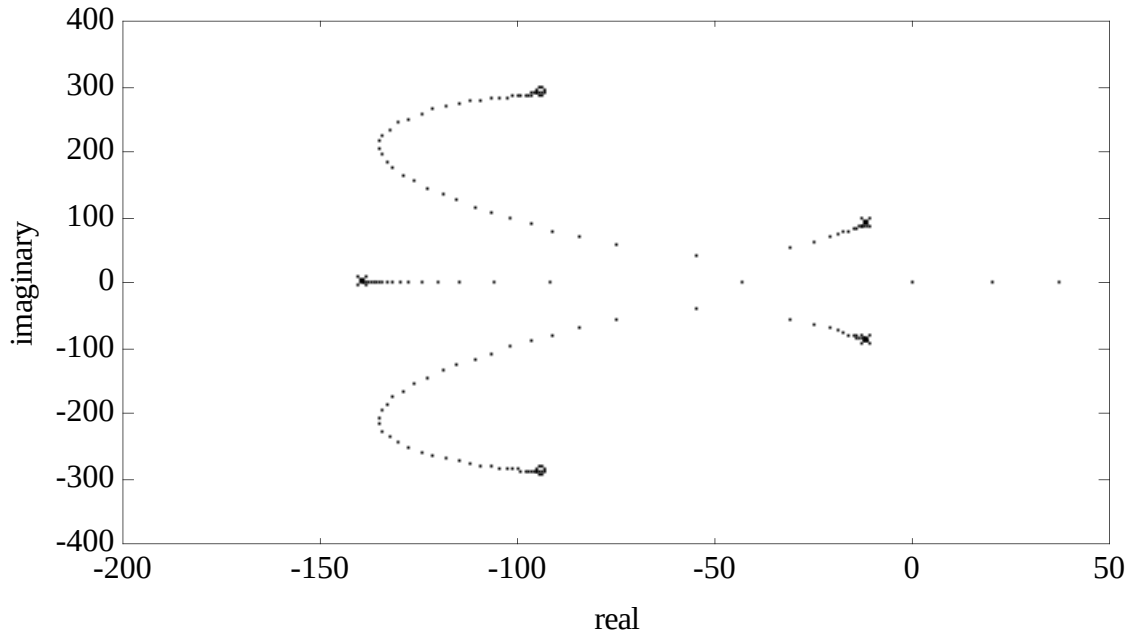

Figure 5.6: Root locus for the fourth order model under negative proportional gain explicit force control.

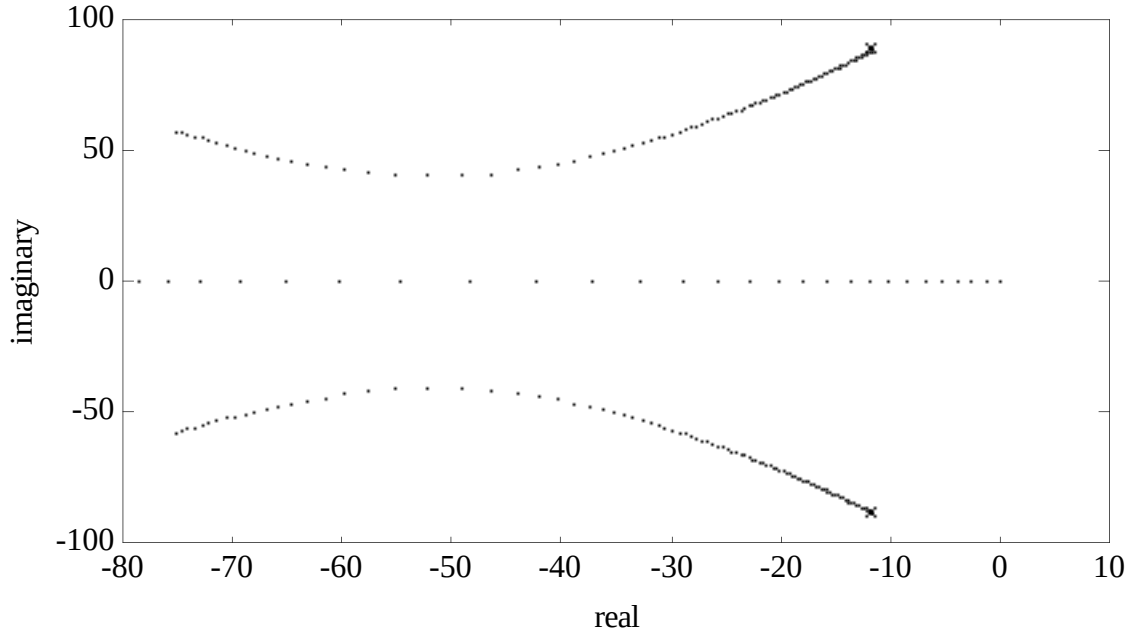

Figure 5.7: Enlargement of root locus in Figure 5.6 with K_{fp} values from -1 to 0 in steps of 0.01 . The gain for closest approach of the locus to the real axis is $K_{fp} \approx -0.8$.

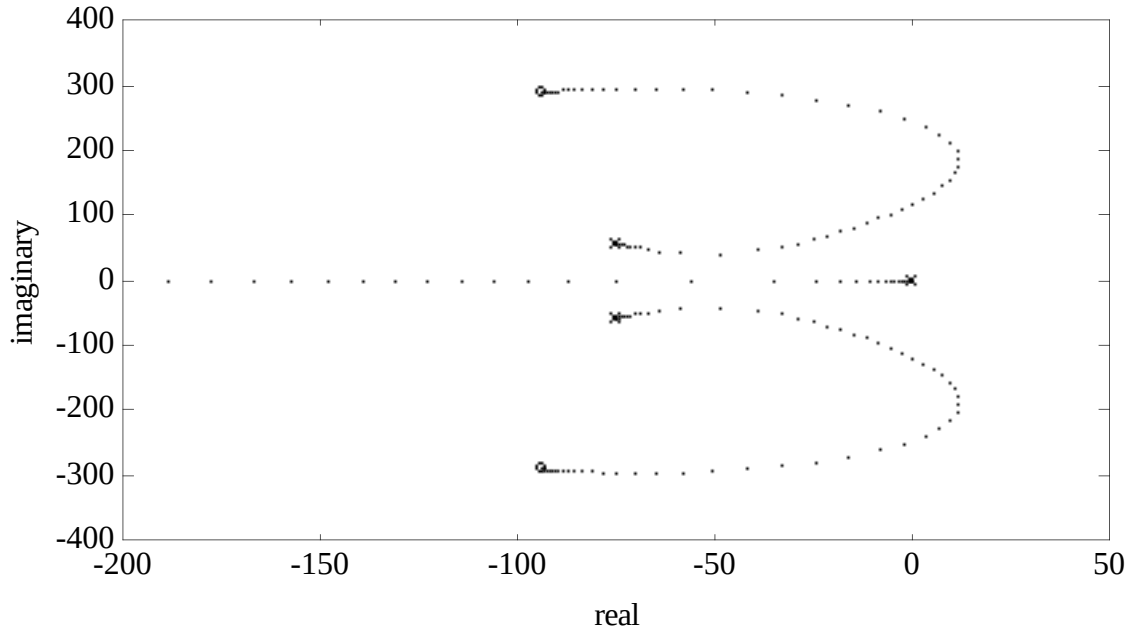

Figure 5.8: Root locus for the fourth order model for $-1 \leq K_{fp} < \infty$ or $0 \leq K'_{fp} < \infty$.

contact has been established and the energy of impact has been dissipated, one of the previously discussed force control strategies may be employed.

Chapter 6

Experimental Results

6.1 Introduction

This chapter presents the data obtained from the implementation of the explicit force, impedance, and impact control strategies discussed previously. All experiments were performed with the CMU DD Arm II and implemented under the Chimera II real time operating sytem [57] with the computer architecture described in Appendix B. This experimental review of force control methodologies is unique in its breadth — never has such a complete spectrum of strategies been implemented on the same system. The commonality amongst the experiments has permitted the ability to objectively compare and contrast these strategies, and draw conclusions about the efficacy of each. The results support the previous analysis and show: the superiority of integral force control for force trajectory tracking, the near equivalence of second order impedance control and proportional gain explicit force control, and the effectiveness and stability of the proposed impact control strategy.

First in this chapter, data collected from explicit force control strategies is presented. These include proportional control with feedforward, integral control, and proportional–derivative control. Then, the results of second order impedance control with and without dynamics compensation is shown. Impact control, in its two manifestations of proportional explicit force control and impedance control, was also implemented and compared. All of these tests were conducted using the environment modelled in Chapter 2. The results compare excellently with the analysis of Chapters 3, 4, and 5. Finally, results are presented from tests conducted with the best of these controllers on a very stiff environment.

6.2 Explicit Force Control

This section presents the results of implementing the explicit force control schemes presented in Chapter 3. All of these schemes were implemented in a hybrid control framework in which the force was controlled in one direction (world frame z axis), and all other directions were position controlled. To be consistent with the arm / sensor / environmental model developed, active damping was provided ($K_v = 10$) in the force controlled direction. The control rate was 300 Hz. The chosen reference force trajectory has steady state, step, and ramp components and is shown as a dashed curve in all of the graphs. The measured force response of the system is shown as a solid curve.

6.2.1 Proportional Gain with Feedforward Control

The first controller to be discussed is proportional gain force control with the reference force fedforward. The exact form of the control law used is:

$$\tau \;=\; J^T \left[\, f_c + K_{fp}(f_c - f_m) \;-\; K_v \dot{x}_m \right] \;+\; g. \tag{6.1}$$

Figures 6.1 (a) through (h) show the response of this controller to the commanded force trajectory. There are several things to note about the response profiles to variations in the proportional gain. First, as predicted by the model, the system exhibits the characteristics of a Type 0 system: finite steady state error for a step input and unbounded error for a ramp input. Second, for an increase in position gain, the steady state error reduces, but at the cost of increasingly larger overshoot. As correctly predicted by the root locus of developed system model in Figure 3.3, this control scheme causes instability at $K_{fp} \approx 1$. Also, the fact that the environmental poles are always off the real axis can be seen in the steady state oscillations that occur at the system's natural frequency (~ 15 Hz), particularly after the step input. Finally, it can be seen that negative proportional gains are increasingly more stable, but the response of the system approaches zero as $K_{fp} \rightarrow -1$.

One possible improvement to the performance to steady state error of this controller is to increase the feedforward signal by a factor that would make that error small for the open loop case ($K_{fp} = 0$). Figure 6.1 (d) shows that a feedforward term of approximately $1.4\, f_c$ would be necessary. This, however, would not eliminate the oscillations that are present, especially after the step input.

6.2.2 Integral Gain Control

Integral explicit force control was implemented with the following form of control law:

$$\tau \;=\; J^T \left[K_{fi} \int (f_c - f_m) dt \;-\; K_v \dot{x}_m \right] \;+\; g. \tag{6.2}$$

Figures 6.2 (a) through (e) show the response of this controller to the commanded force trajectory. The most notable aspect of this controller is the dominance of the integrator pole on the real axis for low gains. This causes the system to be Type 1, as is apparent from the zero steady state error to the step input and constant error to the ramp input. As predicted, this pole acts as a low pass filter until it moves past the environment poles. This happens gradually as the gain increases past $K_{fi} \approx 10$ as shown in the root locus diagram of Figure 3.8. Also predicted by that model is that the system becomes unstable for gains near $K_{fi} = 30$. The real system is not unstable until K_{fi} reaches the upper thirties, which implies a small modelling error. Also, the model previously presented does not explain the nonlinear response seen for $K_{fi} = 37.5$. For a linear system, the envelopes of the two dominant oscillations would be the same, which is obviously not the case. This limitation of the model is not significant, since it does not manifest itself within the desirable operating range of this controller.

6.2.3 PD Control

Proportional / Derivative control was also implemented. Simple differencing of the measured force signal to obtain the derivative was unsuccessful because of the extremely noisy nature of the force signal. Therefore, the force feedback signal was lowpass filtered by using the transfer function $L = a/(s+a)$ in the feedback path in Figure 3.1. The reference signal is not filtered. Therefore, the implemented control law in the Laplace domain is:

$$\tau(s) \;=\; J^T \left\{ F_c(s) \;+\; [K_{fp} + K_{fd} s] \left[F_c(s) - \left(\frac{a}{s+a} \right) F_m(s) \right] \;+\; K_v s \; X(s) \right\} \;+\; g. \tag{6.3}$$

Figure 6.3 shows the response of the system, as well as the reference force and filtered force (long dash curve), for $K_{fp} = 0.5$, $K_{fd} = 0.01$, and $a = 10$. The results are not much better than for proportional gain alone. As will be described below, improvements in the performance of this controller can not be made by varying the gains given here.

First, increasing the derivative gain does not improve the response of the system because the amplified low frequency noise can still drive the system unstable. While Figure 6.3 seems to show a fairly smooth filtered force signal, Figure 6.4 shows a closer view of a section of the curve. Obviously, much of the noise has been removed, but some still remains. With a large enough gain the noise will dominate. Moving the filter pole to the right ($a < 10$) will eliminate this noise, but it introduces a more serious problem of lag.

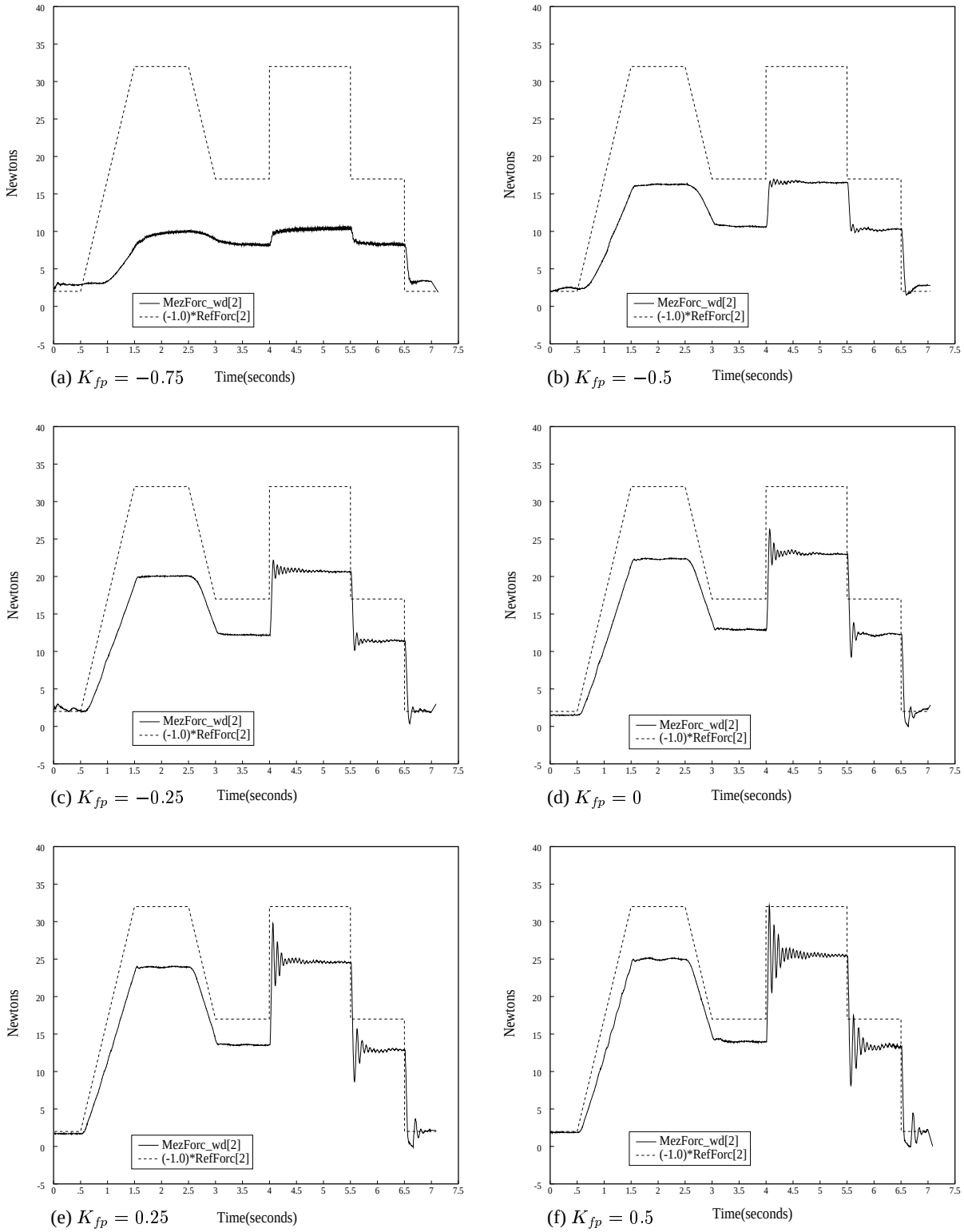

(a) $K_{fp} = -0.75$ (b) $K_{fp} = -0.5$

(c) $K_{fp} = -0.25$ (d) $K_{fp} = 0$

(e) $K_{fp} = 0.25$ (f) $K_{fp} = 0.5$

Figure 6.1: Experimental data of proportional gain explicit force control with feedforward. The proportional gain varies from -0.75 to 1.

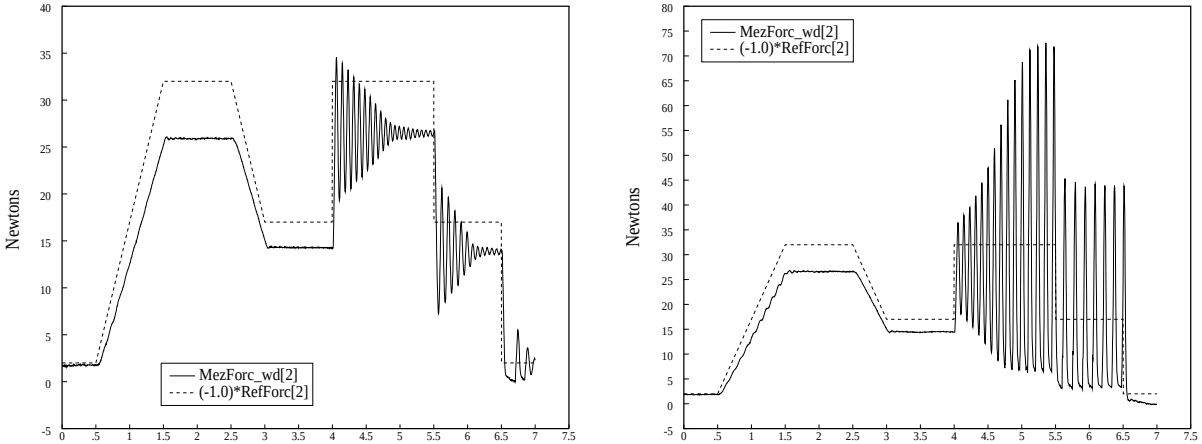

(g) $K_{fp} = 0.75$ (h) $K_{fp} = 1$

Figure 6.1: (continued) Experimental data of proportional gain explicit force control with feedforward. The proportional gain varies from -0.75 to 1.

Figure 6.5 shows that the calculated derivative (solid curve) appears accurate. (The dotted curve is the measured force.) However, it is apparent from this figure and Figure 6.3 that there is lag introduced by the filtering process. This lag becomes extremely important when it is a significant portion of the period of oscillation of the system. Figure 6.6 shows the original force signal (solid), the filtered force signal (short dash), and the derivative of the filtered signal (long dash). For this oscillation frequency, the filtering process causes the filtered force to lag the measured force by one quarter cycle. This makes the force signal $180°$ out of phase with the ideal derivative signal. Thus, the proportional gain act as a destabilizing negative derivative gain. Further, the derivative of the filtered signal leads it by one quarter cycle. Thus, the derivative is in phase with the originally measured force and the derivative gain acts as a proportional gain. Increasing the derivative gain causes greater oscillations exactly when the effective damping is being reduced by the proportional gain. This obviously will cause the system to go unstable.

It can be concluded from this discussion than the filter pole should be significantly larger than the natural frequency of the system, However, it also must be small enough to effectively filter the noise of the force sensor. These two criteria could not be met with our system. To be fair, most systems will never meet this criteria. Force controlled systems are most challenged by stiff environments that have high natural frequencies. It is unlikely that a sensor can be built that has noise only at frequencies much greater than the natural frequencies of these environments.

One solution, however, is to use a soft force sensor or compliant covering on the sensor. The compliance acts as a lowpass filter with no time delay. In this way, the derivative of the force signal may be used under the condition that the time necessary to calculate it is not significant. In this case, without a noisy force signal, simple differencing of the current and most recent force samples will usually suffice. Thus, all that is required is that the force sampling frequency is not of the same order of magnitude as the natural frequency of the system. Successful PD force control with a soft force sensor has been reported elsewhere [71].

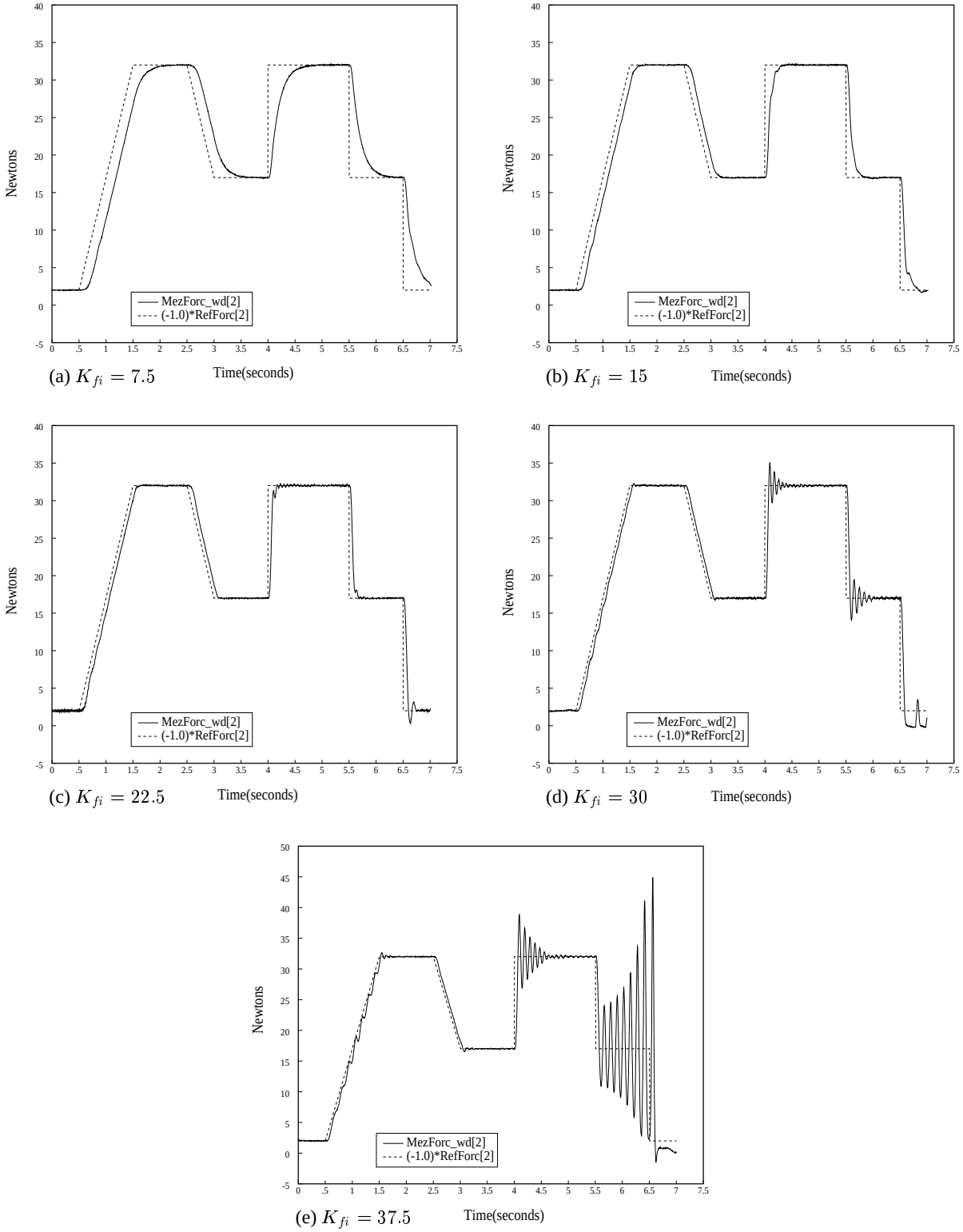

(a) $K_{fi} = 7.5$ (b) $K_{fi} = 15$

(c) $K_{fi} = 22.5$ (d) $K_{fi} = 30$

(e) $K_{fi} = 37.5$

Figure 6.2: Experimental data of integral gain explicit force control feedforward. The integral gain varies from 7.5 to 37.5.

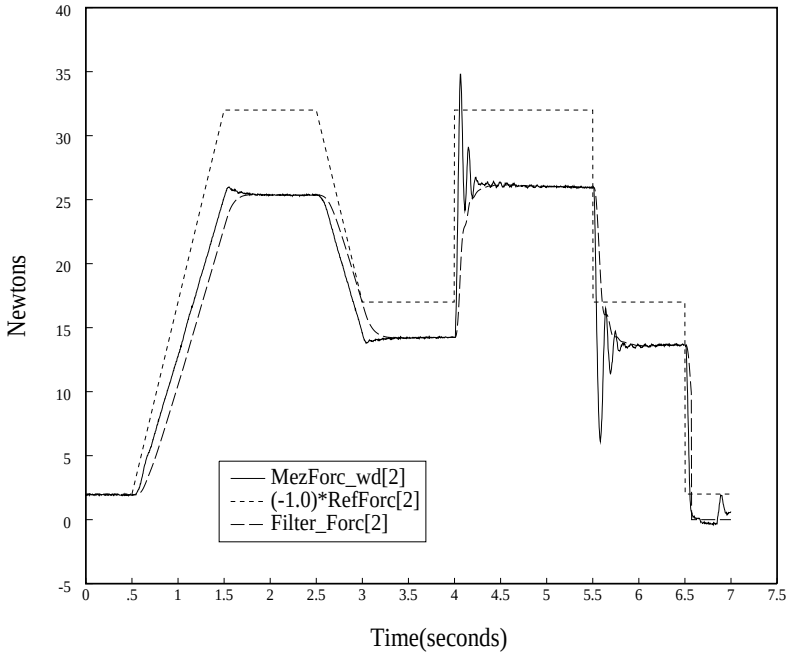

Figure 6.3: Experimental data from PD control with $K_{fp} = 0.5$ and $K_{fd} = 0.01$

.

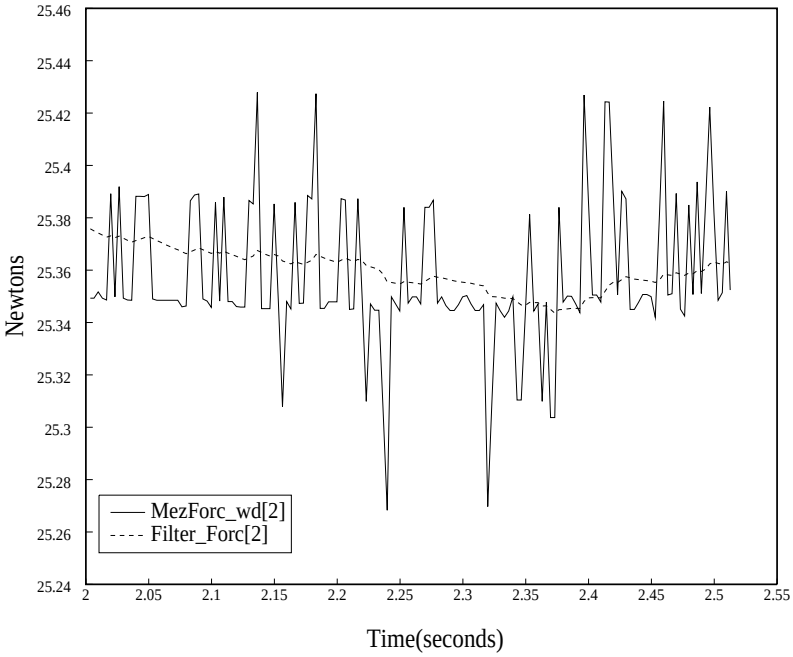

Figure 6.4: Filtered and unfiltered force signals for PD control.

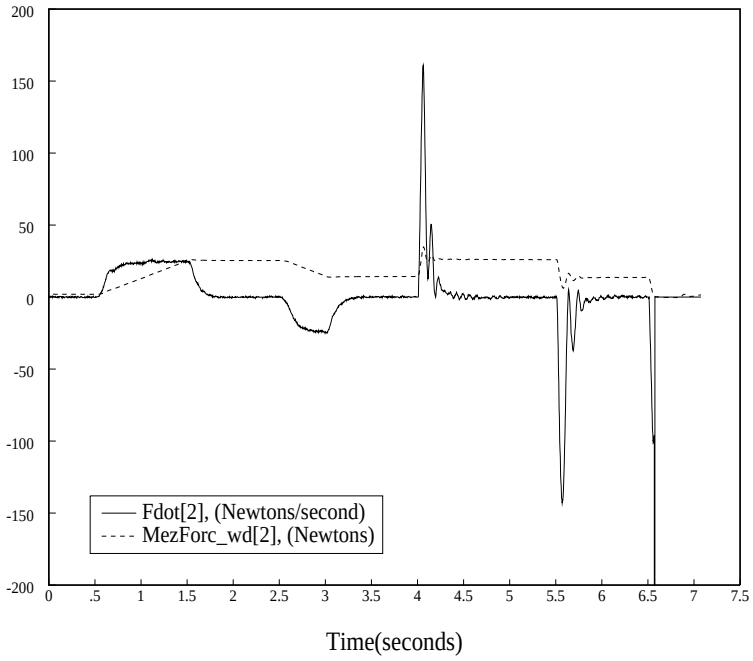

Figure 6.5: Calculated force derivative and measured force signal used in PD control.

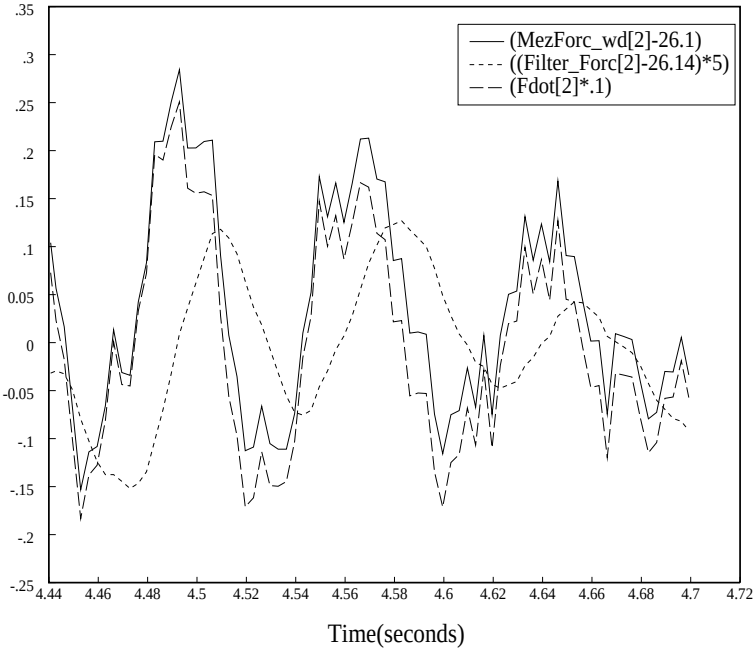

Figure 6.6: The lag of the filtered force causes the force derivative to be in phase with the measured force.

6.2.4 Second Order Low Pass Filter Control

As discussed in Section 3.3.1, a second order low pass filter controller has been implemented. The following control law was used:

$$\tau(s) \;=\; J^T \left[\frac{K_{fp}}{s(s+a)} \left(F_c(s) - F_m(s)\right) \;+\; K_v s\, X(s) \right] \;+\; g. \tag{6.4}$$

Figures 6.7 show the response of this system for three distinct regions of operation: filter poles meeting on the real axis to the right of, near, and to the left of the environment poles. This behavior was previously shown if Figure 3.17.

Figures 6.7 (a) through (c) show the response for $a = 15$ and increasing gain K_{fp}. Referring to the root locus in Figure 3.17, it can be see that the rightmost pole dominates in (a), until the two poles on the real axis meet in (b), and then leave the real axis in (c). For the small gain case, the dominant pole acts much like the single pole of the integral controller presented previously. Because a is small, the filter poles meet to the right of the environmental poles and dominate the response for low frequencies. Notice that the oscillations present in (c) are not close to the natural frequency of the environment, as was true with the previous controller results presented.

Figures 6.7 (d) through (f) show the response for $a = 45$ and increasing gain K_{fp}. Again, the three graphs refer to the poles spread on the real axis (d), together on the real axis (e), and off the real axis (f). Again, the one filter pole dominates for low gains, making the response look like integral control. The response continues to look like integral control as the poles meet in the vicinity of the environmental poles (e). The response in Figure 6.7 (e) was the best obtained with this controller. In (f) the poles have again moved off the real axis, as indicated by the oscillations.

Finally, Figures 6.7 (g) through (i) show the response for $a = 180$ and increasing gain K_{fp}. Again, the three graphs refer to the poles spread on the real axis (g), together on the real axis (h), and off the real axis (i). Again, the first two graphs look much like integral control. However, this time the third graph also looks like integral force control with gain that is too high. This is intuitively correct since the meeting point of the filter poles for such a high value of a is to the left of the environment poles. Thus, the right filter pole acts like the integral control pole until it is moves far to the left of the environment poles, at which point its influence is negligible. The influence of the second filter pole remains negligible throughout.

Thus, it can be concluded that this control scheme is only marginally better than integral control. While the double pole on the real axis promises to be a better low pass filter, its location must still be close to the real axis projection of the environmental poles to minimize lag. This placement reduces its ability to better suppress the oscillation of the system. Further, this controller is much more difficult to tune since it requires the adjustment of two parameters instead of one. For these reasons it is not preferable to pure integral control. However, this implementation does successfully demonstrate that position-base explicit force control, as discussed in Section 3.3.1, is stable and useful.

6.3 Impedance Control

This section presents the results of implementing the second order impedance control schemes presented in Chapter 4. The major schemes discussed there were impedance control with and without dynamics compensation. To be consistent with the arm / sensor / environmental model developed, active damping was provided ($K_v = 10$). The control rate was 300 Hz when not providing dynamics compensation, and 250 Hz when dynamics compensation was included. The position reference trajectories are chosen such that given the stiffness of the controller, the trajectory should provide the same force profile as commanded for the explicit force controllers. This allows direct comparison with those controllers. As will become apparent, both forms of impedance control (with and without dynamics compensation) respond the same as proportional gain explicit force control with feedforward.

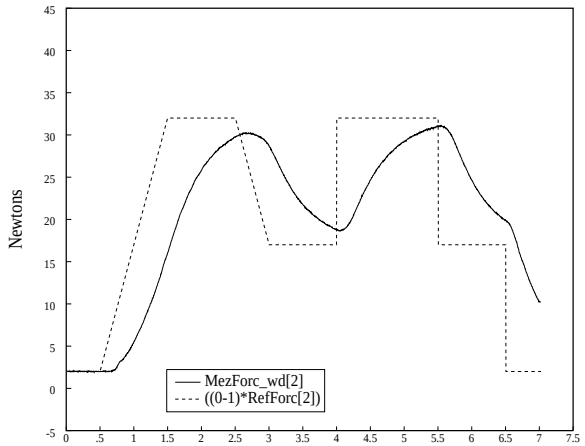

(a) $a = 15$, $K_{fp} = 33$

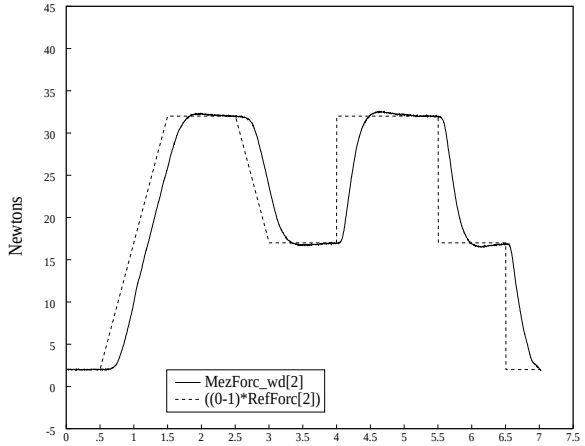

(b) $a = 15$, $K_{fp} = 100$

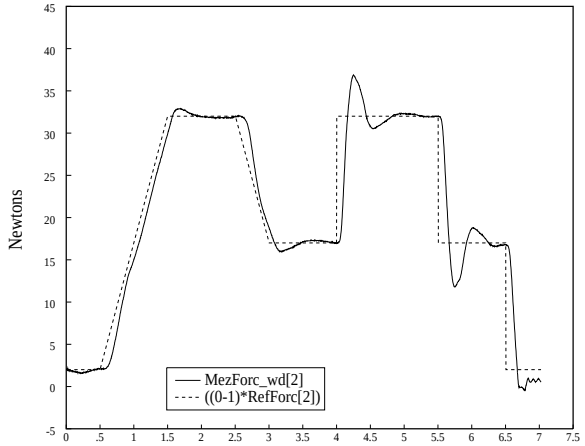

(c) $a = 15$, $K_{fp} = 300$

Figure 6.7: Experimental data of second order low pass force controller for $a = 15$, K_{fp} varied.

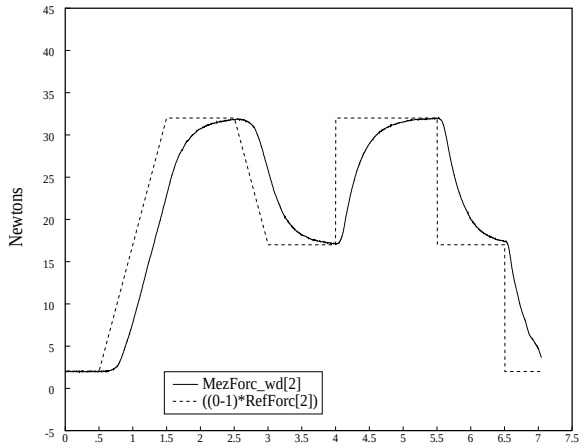

(d) $a = 45, K_{fp} = 200$

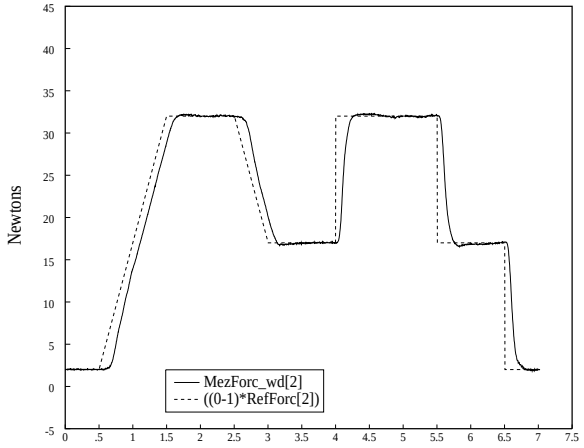

(e) $a = 45, K_{fp} = 600$

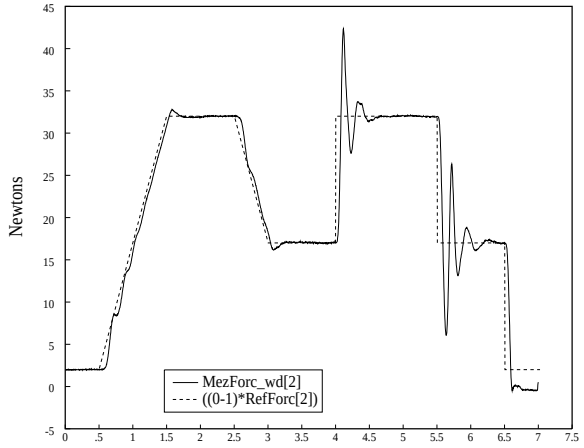

(f) $a = 45, K_{fp} = 1800$

Figure 6.7: (continued) Experimental data of second order low pass force controller for $a = 45$, K_{fp} varied.

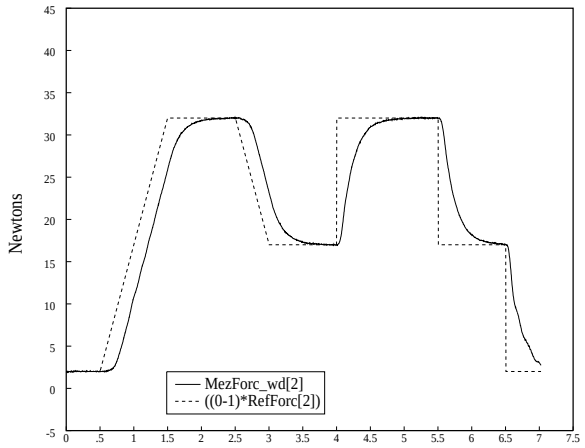

(g) $a = 180, K_{fp} = 1200$

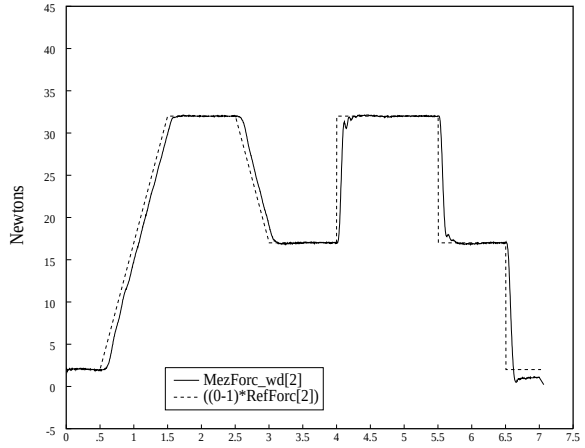

(h) $a = 180, K_{fp} = 3600$

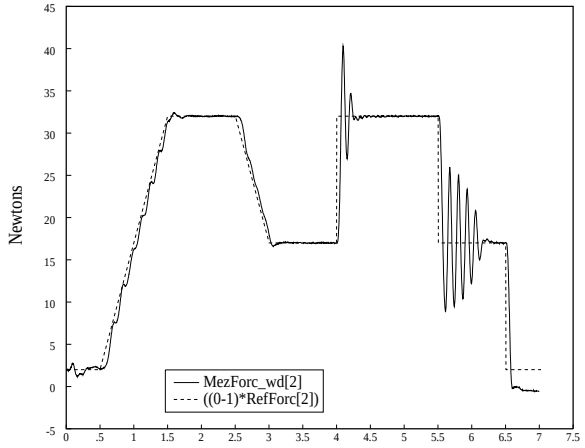

(i) $a = 180, K_{fp} = 7200$

Figure 6.7: (continued) Experimental data of second order low pass force controller for $a = 180$, K_{fp} varied.

6.3.1 Impedance Control Without Dynamics Compensation

When in contact with a stiff environment, the manipulator will not move very much or very quickly in the direction normal to the environment. As was shown in Section 4.5, this enables a steady state approximation that eliminates the need to calculate the inverse dynamics and the inverse Jacobian. The control law has the following form of Equation (4.40), which is repeated here:

$$\tau_A \;=\; J^T \Lambda M^{-1} \left[(C(\dot{x}_c - \dot{x}_m) + K(x_c - x_m)) - f_m \right] \;+\; J^T f_m + g. \tag{6.5}$$

For these experiments $K = 150$ and $C = 10$. As discussed in Sections 4.6 and 3.2.2, the mass ratio, ΛM^{-1}, is equivalent to the proportional force gain plus one:

$$\Lambda M^{-1} = K_{fp} + 1 \tag{6.6}$$

Thus, for this controller the mass ratio is chosen to be diagonal in the desired frame and its components (λ/m) set to correspond to the proportional force gains chosen previously. This allows a direct comparison of impedance and force control schemes.

Figures 6.8 (a) through (g) show the response of this impedance controller, and the commanded position trajectory multiplied by the active stiffness in that direction. As is readily apparent, the response of this controller is essentially equivalent that of the proportional gain controller shown in Figures 6.1. This confirms the previous theoretical assertion that *second order impedance control against a stiff environment is equivalent to explicit force control with proportional gain and feedforward compensation.*

6.3.2 Impedance Control With Dynamics Compensation

Second order impedance control can also be implemented with dynamics compensation as shown in Equation (4.32), which is repeated here.

$$\tau \;=\; D J^{-1} M^{-1} \left(C(\dot{x}_c - \dot{x}_m) \;+\; K(x_c - x_m) - f_m \right) \;-\; J^{-1} \dot{J} \dot{\theta} \;+\; h \;+\; g \;+\; J^T f_m. \tag{6.7}$$

As can be seen in Equation (4.33),

$$D J^{-1} M^{-1} = J^T \Lambda M^{-1} \tag{6.8}$$

Thus, the mass ratio, ΛM^{-1} can be thought of a proportional force gain. However, it can be seen from Equations (4.17) and (4.18) that only M can be specified in this scheme.

Usually M is chosen to be diagonal in the task frame along with K and C. As described in Section 4.4.3, when operating in free space ($f_m = 0$) a diagonal M acts as a simple scaling factor to K and C, thereby preventing coupled motion. If M were nondiagonal, its product with diagonal K and C would be nondiagonal, and coupled motion would result. Further, K and C are usually chosen to be diagonal in some task frame which is aligned with environment to be contacted. In this way, the manipulator may be made stiff tangentially to a surface, but soft normal to it. (The velocity gains are usually chosen for critical damping.)

However, when in contact with the environment ($f_m \neq 0$), the ratio of the inertias, ΛM^{-1}, acts as a proportional force gain which is not diagonal in general, because Λ is not diagonal in general. Therefore, it is necessary to determine the effective value of the mass ratio (force gain). This requires finding the dominant element of Λ for the direction in which the environment is contacted.

Finding the dominant component of the inertia matrix is equivalent to finding the effective mass in the direction of concern. Since it is the force which is being controlled, this can only be done by determining the resultant acceleration from an applied force:

$$\ddot{x} \;=\; \Lambda^{-1} f \tag{6.9}$$

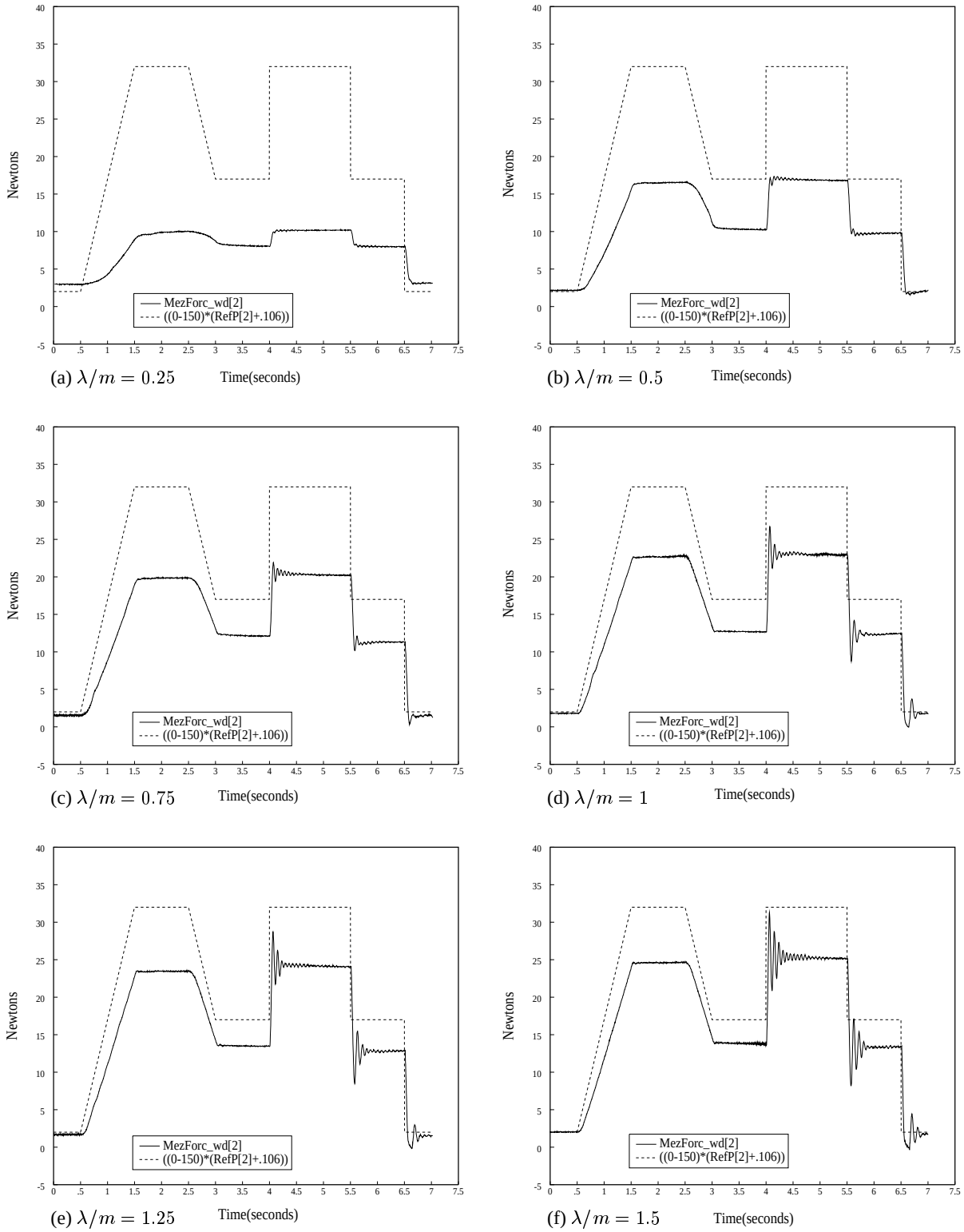

(a) $\lambda/m = 0.25$ (b) $\lambda/m = 0.5$ (c) $\lambda/m = 0.75$ (d) $\lambda/m = 1$ (e) $\lambda/m = 1.25$ (f) $\lambda/m = 1.5$

Figure 6.8: Experimental data of impedance control without dynamics compensation. The mass ratio 'gain' varies from 0.25 to 2.0.

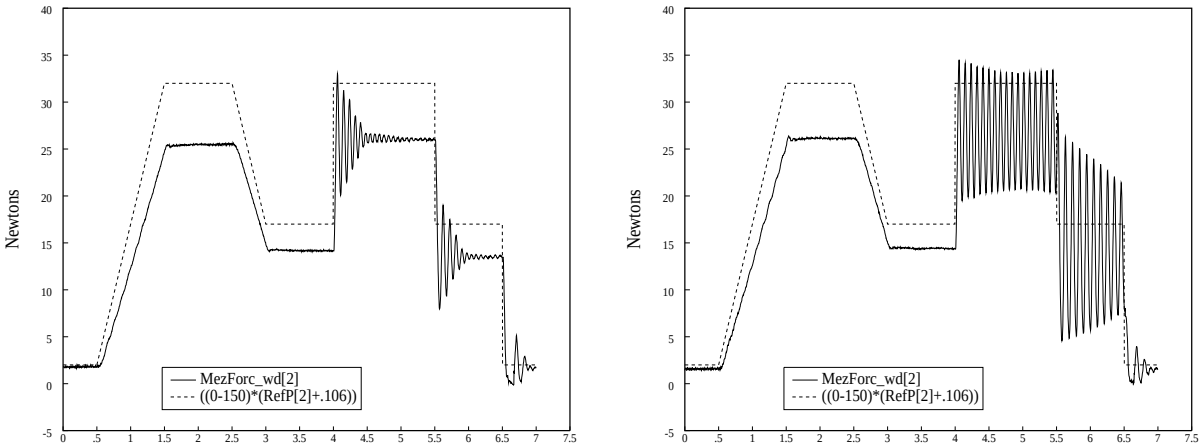

(g) $\lambda/m = 1.75$ (h) $\lambda/m = 2$

Figure 6.8: (continued) Experimental data of impedance control without dynamics compensation. The mass ratio 'gain' varies from 0.25 to 2.0.

The force may be set to be the unit vector in the direction of the surface. For the experiments performed, the z direction was chosen. The actual values of Equation (6.9) were:

$$\ddot{x} = \begin{bmatrix} 0.070 & 0 & -0.053 & 0 & 0 & 0 \\ 0 & 1.671 & 0 & -9.723 & -0.049 & 0 \\ -0.053 & 0 & 0.199 & 0 & 0 & 0 \\ 0 & -9.723 & 0 & 59.9 & -1.272 & 0 \\ 0 & -0.049 & 0 & -1.272 & 2.758 & 0 \\ 0 & 0 & 0 & 0 & 0 & 3226 \end{bmatrix} \begin{bmatrix} 0 \\ 0 \\ 1 \\ 0 \\ 0 \\ 0 \end{bmatrix} \tag{6.10}$$

It is apparent that for forces applied in the z direction to the arm in this configuration, the dominant acceleration is $\ddot{x}_z \approx 0.2\mathrm{m/s}^2$. Thus, the apparent inverse scalar mass is $\lambda_z^{-1} \approx 0.2\ \mathrm{kg}^{-1}$. This implies that the best scalar approximation of the mass in the z direction is $\lambda_z \approx 5$ kg. This value may then be thought of as a scaling factor applied to the variable gain value M_{33} in Equation (6.7).

Figures 6.9 show the response of impedance control with dynamics compensation for $0.1 \leq M_{33}^{-1} \leq 0.45$. The other gains were $K = 150$ and $C = 10$. Using the approximation of $\lambda_z \approx 5$ kg, these gains can be thought of as $0.5 \leq \lambda_z M_{33}^{-1} \leq 2.25$. Thus, a direct comparison can be made between the system response shown in Figures 6.9 and that shown in Figures 6.8 and Figures 6.1. The responses are essentially the same. This comparison supports the analysis above. It also, further supports the conclusion that *second order impedance control, with or without dynamics compensation, is essentially equivalent to explicit force control with proportional gain and feedforward compensation*.

6.4 Explicit Force and Impedance Control Conclusions

It is apparent from the results presented thus far that integral explicit force control works best at force trajectory tracking. Also, PD force control works least well and is unstable due to noise and lag. This is in

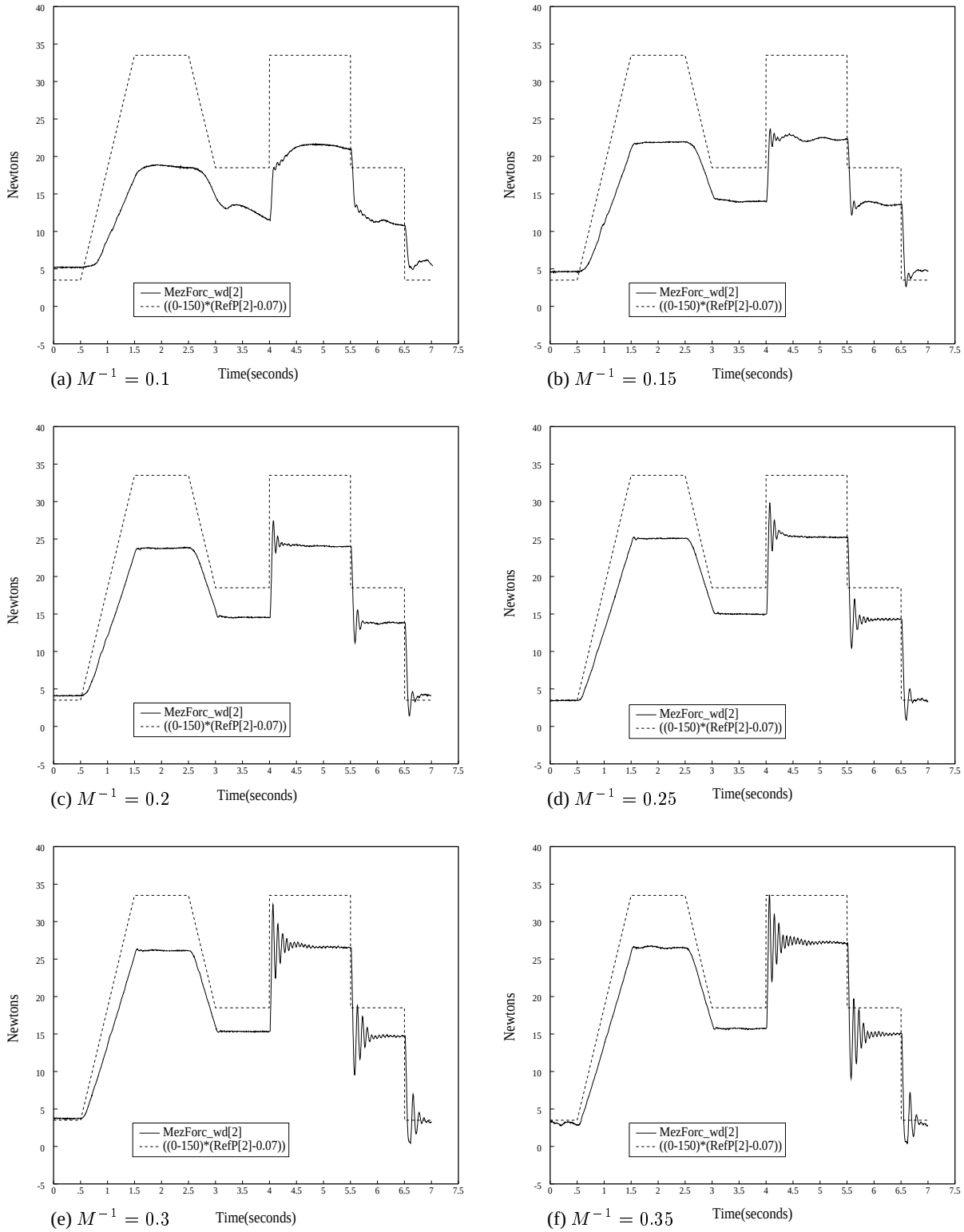

(a) $M^{-1} = 0.1$ (b) $M^{-1} = 0.15$

(c) $M^{-1} = 0.2$ (d) $M^{-1} = 0.25$

(e) $M^{-1} = 0.3$ (f) $M^{-1} = 0.35$

Figure 6.9: Experimental data of impedance control with dynamics compensation. The commanded inverse mass varies from 0.1 to 0.45. This is approximately the same as having a force gain vary from 0.5 to 2.25.

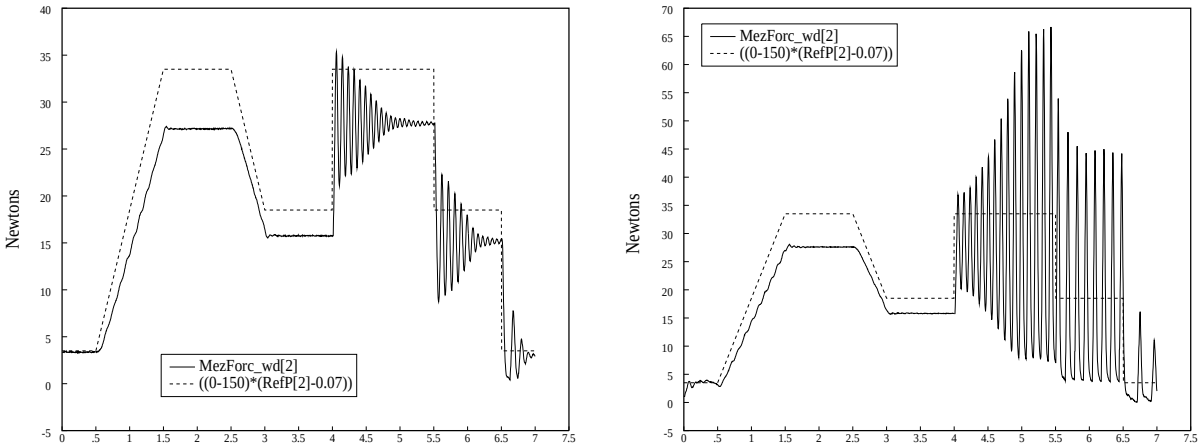

(g) $M^{-1} = 0.4$ (h) $M^{-1} = 0.45$

Figure 6.9: (continued) Experimental data of impedance control with dynamics compensation. The commanded inverse mass varies from 0.1 to 0.45. This is approximately the same as having a force gain vary from 0.5 to 2.25.

direct contradiction to the predictions of other researchers [14]. It is also clear that second order impedance control and proportional gain explicit force control with feedforward are essentially the same thing. Further, Impedance Control is more cumbersome to use since it requires position reference instead of force reference. Note that the reference force is essentially determined by the product of $K(x_c - x_m)$, and either quantity may be varied as long as the product is constant. For the data presented above, K was kept constant at 150. However, other values were tried and the commanded values of x_c adjusted appropriately with no change in the results. This strategy is permissible only if the compression of the environment is small, keeping x_m constant. Alternatively, the stiffness of the manipulator must be small in comparison to the environment. This can easily be seen to be necessary by considering the case where the environment is very soft. The compression of the environment will be large, x_m will approach x_c, $K(x_c - x_m)$ will be reduced, and the force exerted will diminish.

The use of reference positions by Impedance Control is seen as valuable by some researchers, since there is no need to switch from position control mode to force control mode. However, as was discussed in Chapter 5 and as will be seen below, it is useful to have a mode of impact control between motion through free space and constrained force control. Further, no one set of impedance parameters can give good free space motion, impact response, and force tracking. Switching the parameter values could be one solution. But even switching the values will not make second order impedance control the best force controller. Therefore, it seems that if the controller is to be modified at all, the best possible controller for the situation should be chosen: position control with dynamics compensation for free space motion, impact control for impacts, and integral gain explicit force control for force trajectory tracking.

6.5 Impact Control

As discussed in Chapter 5, impact control provides a mode of operation that enables stable transition from motion through free space to contact with the environment. The proposed method for achieving this is negative proportional gain force control with feedforward. Again it will be shown how second order impedance control provides identical results. But first, the results of integral control for impact will be presented.

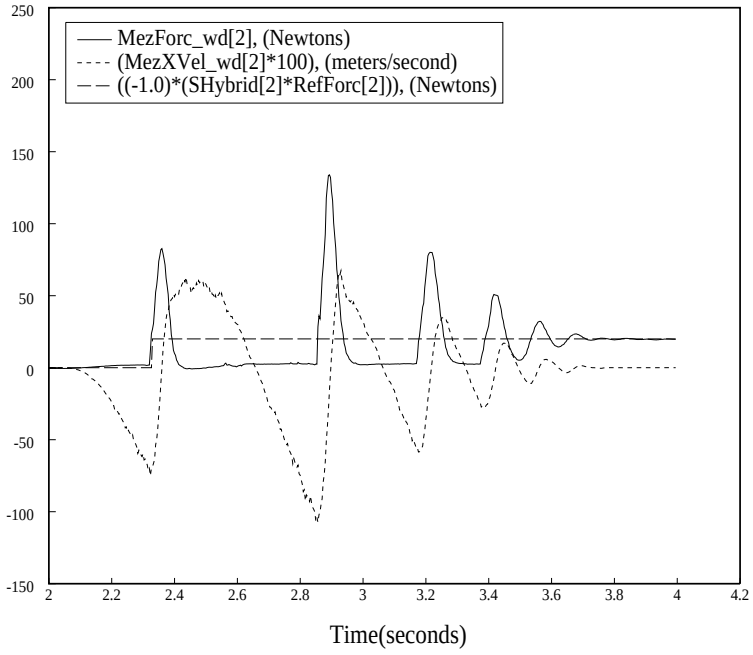

Figure 6.10: Experimental data from an impact with integral force control. The integral gain was $K_{fi} = 7.5$.

For all of the experiments conducted, the manipulator was accelerated toward the environment and struck the surface at the same velocity of ~ 75 cm/s. Although dependent on the controller used, the impact force spike is ~ 90 N. The force spike from impact triggers the impact controller by changing the hybrid control selection switch (SHybrid). A reference force of 20 N is then supplied. A damping gain of $K_v = 10$ is used throughout to maintain consistency with the system model developed in Chapter 2.

6.5.1 Integral Control

In Section 6.2.2 it was shown that integral gain explicit force control provided excellent force tracking capability. Also, it has been reported by other researchers that integral control is useful for control of impacts [74]. However, Figure 6.10 shows that integral control is extremely ill suited for stable impacts. After an initial impact with the environment, the manipulator jumps away and strikes on the environment with a larger force the second time. For the gain value used, $K_{fi} = 7.5$, the system eventually settles to the commanded force. For larger gains it was not possible to attain stability.

6.5.2 Proportional Gain Control with Feedforward

It was predicted in Chapter 5, that negative proportional gain explicit force control would be stable during impacts. Figures 6.11 show impacts for $-1 \leq K_{fp} \leq 0.75$. In Section 6.2.1 it was seen how negative gains suppressed much of the oscillatory behavior of the response when just tracking a force trajectory. This is even more true for the impact response. Figures 6.11 (a) and (b) show this suppression of force oscillation even though velocity oscillations continue. For Figures 6.11 (c) though (h), contact is lost with environment and growing oscillations and repeated impacts occur.

While the stability of the system is best for negative gains, their are two small drawbacks to their use. First, the magnitude of the impact is increased slightly as the $K_{fp} \rightarrow -1$. This is only important if the environment can not withstand any impacts greater than a particular magnitude. Second, the measured force value after the impact transition will be less and less correct as the gain is reduced. This is also apparent for

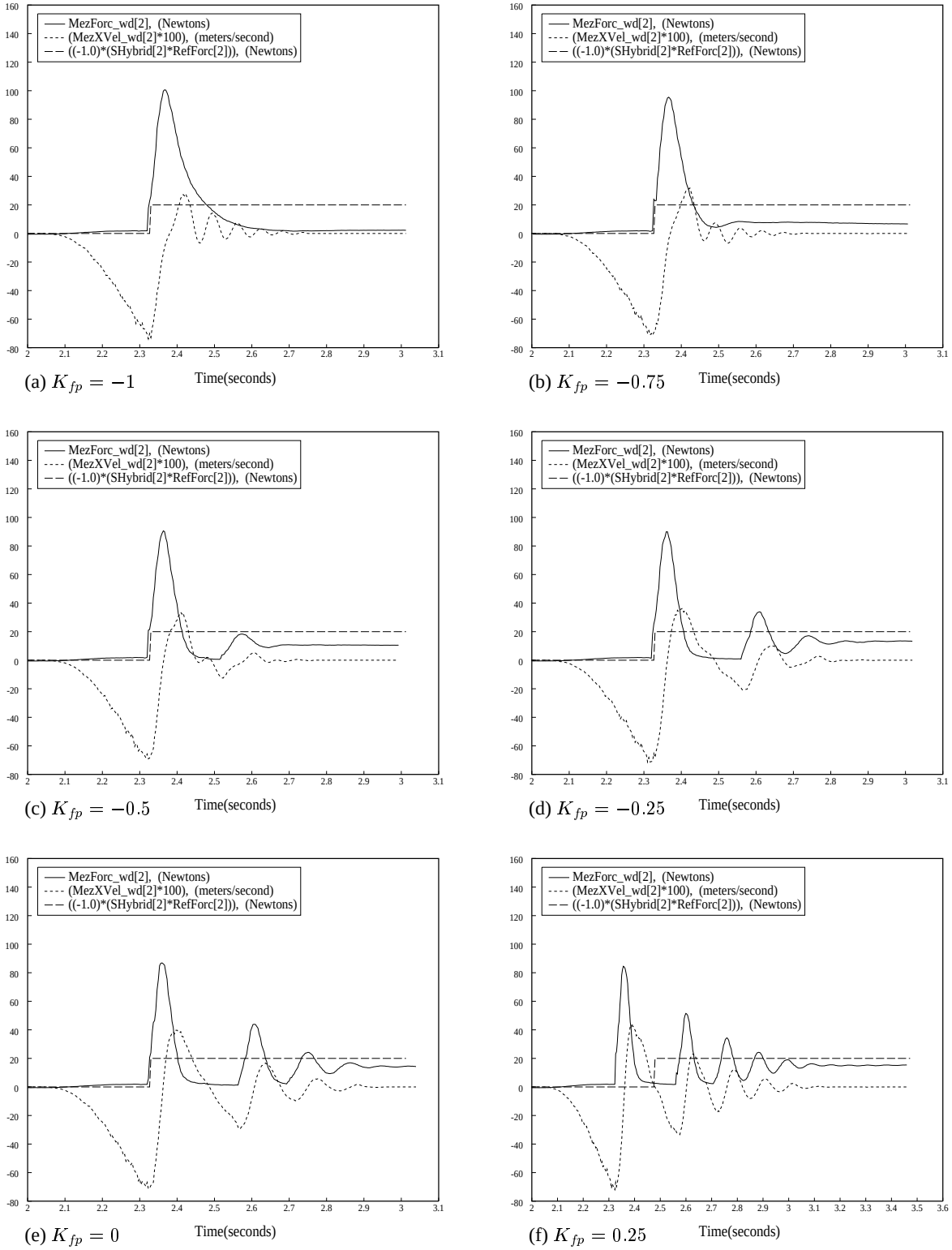

(a) $K_{fp} = -1$ (b) $K_{fp} = -0.75$ (c) $K_{fp} = -0.5$ (d) $K_{fp} = -0.25$ (e) $K_{fp} = 0$ (f) $K_{fp} = 0.25$

Figure 6.11: Experimental data of proportional gain explicit force control with feedforward during impact. The proportional gain varies from -1 to 0.75.

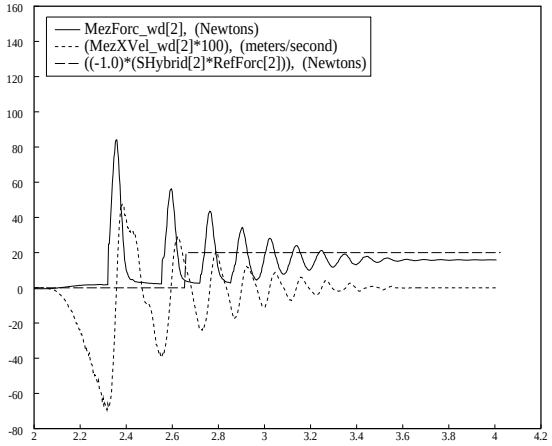

(g) $K_{fp} = 0.5$

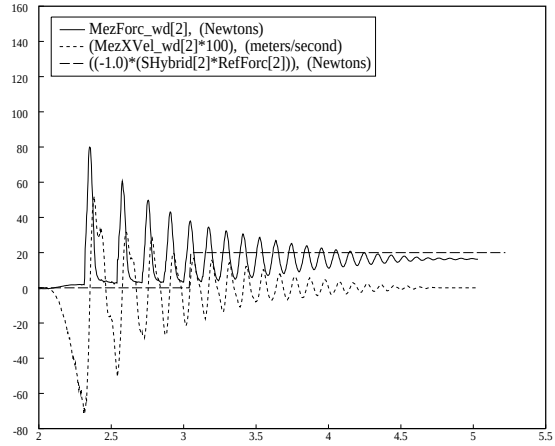

(h) $K_{fp} = 0.75$

Figure 6.11: (continued) Experimental data of proportional gain explicit force control with feedforward during impact. The proportional gain varies from -1 to 0.75.

the response curves of Figure 6.1. It implies that another controller must be used after the impact phase is over. From the previous discussions it is known that integral control is best.

6.5.3 Impedance Control

Second order impedance control without dynamics compensation was tested during impacts. Figures 6.12 show the results for the mass ratio $\Lambda M^{-1} = 0.25, 1, 1.75$. The results compare favorably to the responses for proportional force control with $K_{fp} = -0.75, 0, 0.75$. This is in direct agreement with theory as previously discussed and once again demonstrates the equivalence of impedance control and proportional gain explicit force control.

Note that to obtain a consistent velocity during the free motion phase, the position gain K in Equation (6.5), was varied to keep the product $\Lambda M^{-1} K$ constant. The free space position trajectory was not changed and the resultant velocity of impact was the same for all tests. Also, during and after the impact, the reference position was set such that $K\Delta x = 20$ N. There is, therefore, a discontinuity in the reference position trajectory. The time for the discontinuity was estimated from previous impact results.

6.5.4 Discussion of Impact Control Results

The previous sections have shown that an equivalent, stable impact response can be achieved from proper parameter selection for proportional gain explicit force control and impedance control. The appropriate gain values for this particular system are $K_{fp} \approx -0.75$ for the proportional gain or $\Lambda M^{-1} \approx 0.25$ for the impedance control mass ratio. As discussed in Section 3.2.2, these gains are essentially equivalent.

However, gains that are appropriate for impact suppression are not good for force trajectory tracking. It has been shown that the best force trajectory tracking with these controllers is for drastically different gains: $K_{fp} \approx 0.5$ or $\Lambda M^{-1} \approx 1.5$. Even with these values, the tracking is not close to the performance of integral gain explicit force control.

Further, the impedance control mass ratio that is best for impact control requires very high values of stiffness for free space operation. This can be seen directly from Equation (6.5) in which the mass ratio acts only as a scaling factor to the stiffness and damping when $f_m = 0$. Thus for $\Lambda M^{-1} \approx 0.25$, the stiffness K

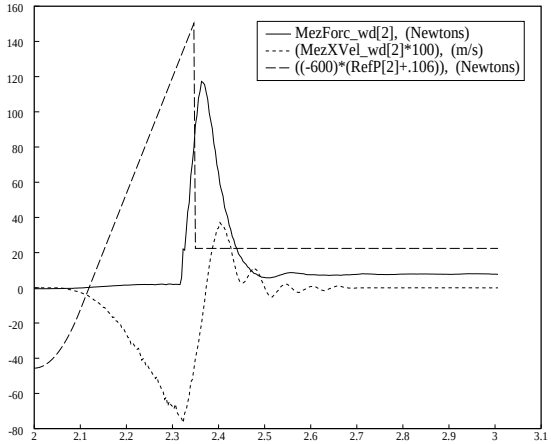

(a) $\Lambda M^{-1} = 0.25$

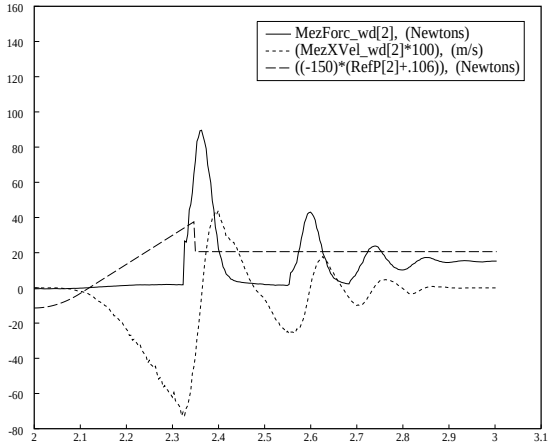

(b) $\Lambda M^{-1} = 1$

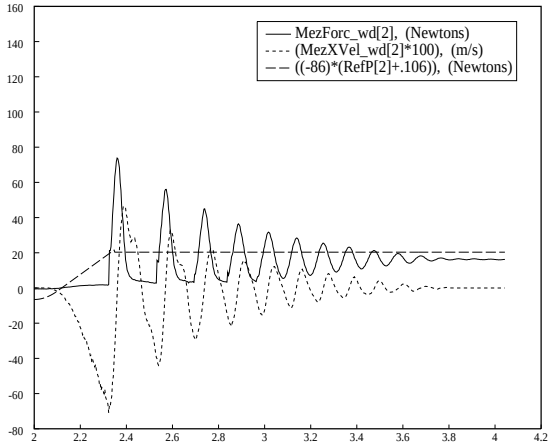

(c) $\Lambda M^{-1} = 1.75$

Figure 6.12: Experimental data of impedance control during impacts for the stated mass ratios.

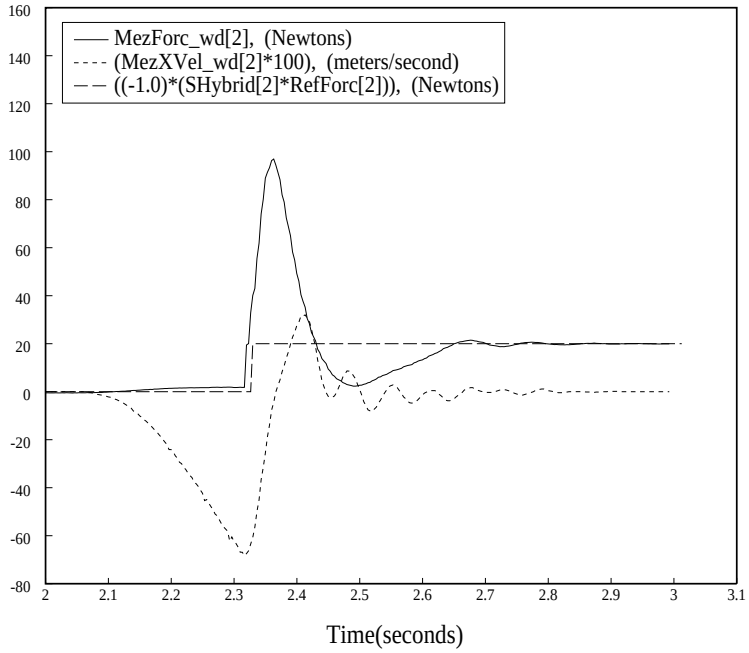

Figure 6.13: Experimental data of impact control with transition to integral gain force control. The impact control phase lasts for 0.15s after the beginning of the impact. This is followed by a period of transition from impact control to integral gain force control which lasts 0.15s. Beyond 0.3s after impact, integral gain force control is used.

must be increased by a factor of four to obtain the same free space response. However, this increase in the stiffness may present a problem when the manipulator is in contact with the environment. As discussed in Section 6.4, higher stiffness can cause a reduction in the force exerted, resulting in even worse force tracking performance for this controller.

Thus, it is concluded that the best solution is to use three distinct controllers. Position control with properly tuned gains should be used for free space motion. Impact control, or proportional gain explicit force control with negative gain, should be used to suppress oscillations and bouncing during the transient phase of impact on the environment. And integral gain explicit force control should be used to track forces once stable contact with the environment has been established.

The transition from position control to impact control is abrupt, and triggered by the impact force spike. The transition method from impact control to integral force control is less obvious. One method of doing this is to have a transition period in which the proportional gain and force feedforward of the impact control are brought to zero, while the integral gain is increased to its best value. Figure 6.13 shows the results of this strategy. The impact control phase lasts for 0.15s (about the width of the impact spike) after the beginning of the impact. This is followed by a period of transition from impact control to integral gain force control which lasts 0.15s. During the transition phase K_{fp} is varied linearly from -0.75 to 0; K_{ff}, the feedforward gain, is varied linearly from 1 to 0; and K_{fi} is varied linearly from 0 to 15. After, this transition period, integral force control is continued with the gain at 15. As can be seen, this simple strategy provides stability through the impact period and excellent position and force control before and after the impact.

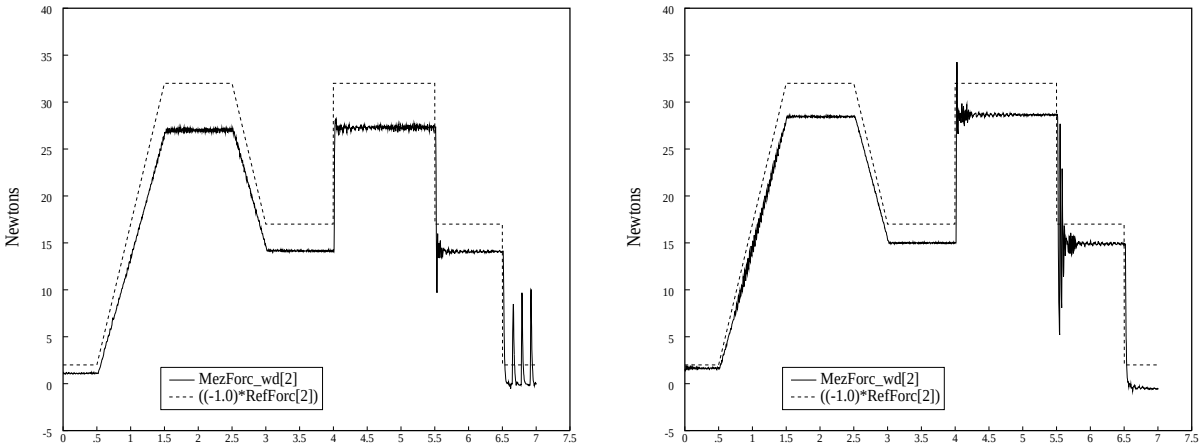

(g) $K_{fp} = 1$ (h) $K_{fp} = 2$

Figure 6.14: Experimental data of proportional gain explicit force control with feedforward against steel environment (z direction).

6.6 Results with a Stiff Steel Environment

All of the results presented previously were obtained with the environment modelled in Chapter 2. To further test the controllers discussed, a very rigid steel pedestal was used as the environment. This pedestal is made from one inch thick steel: two 1 foot square plates at both ends of a cylinder 34 inches long and 8 inches in diameter. The bottom plate is bolted to a concrete floor. Another piece of steel is bolted to the top plate. It consists of two 6 by 1/4 inch steel plates joined at right angles. (This is commonly called 'angle iron'.) The angle iron is 1 foot long and provides a vertical surface which may be pressed or impacted upon.

Two points on this pedestal were used for force trajectory and impact experiments. The first is on the top surface (z direction), directly above the wall of the supporting column. It is the most rigid point on the structure. (This was independently verified by the sound emitted from locations struck with a hammer; the high frequency spots are the stiffest.) The pedestal was mounted such that this spot was very close to the Cartesian position at which all previous experiments were performed. The second spot on the pedestal used for experiments was on the face of the angle iron (x direction). This was much less stiff but still considerably more stiff than the previously modelled environment. Its reduction in stiffness from the top surface is due to flexion of the column and weaknesses in the bolted connections.

The controllers tested were proportional gain force control with feedforward and integral force control. The proportional gain controller was also used with negative gains to test impact control. Impedance control was not tested because of its strong similarity to proportional gain control.

6.6.1 Explicit Force Control on the Steel Environment

First proportional gain control was tried at the two test points on the pedestal. Figures 6.14 show the response for the highest proportional gains used in the z direction. For this stiff direction, the gain is stable even for $K_{fp} = 2$. Figures 6.15 show the response for the highest proportional gains used in the x direction. It is apparent that general behavior of the controller is the same as before for the modelled environment. However, it can also be seen that a stiffer environment permits higher proportional force gains.

Next integral gain control was tried at the two test points on the pedestal. Figures 6.16 show the response for the highest integral gains used in the z direction. Figures 6.17 show the response for the highest integral

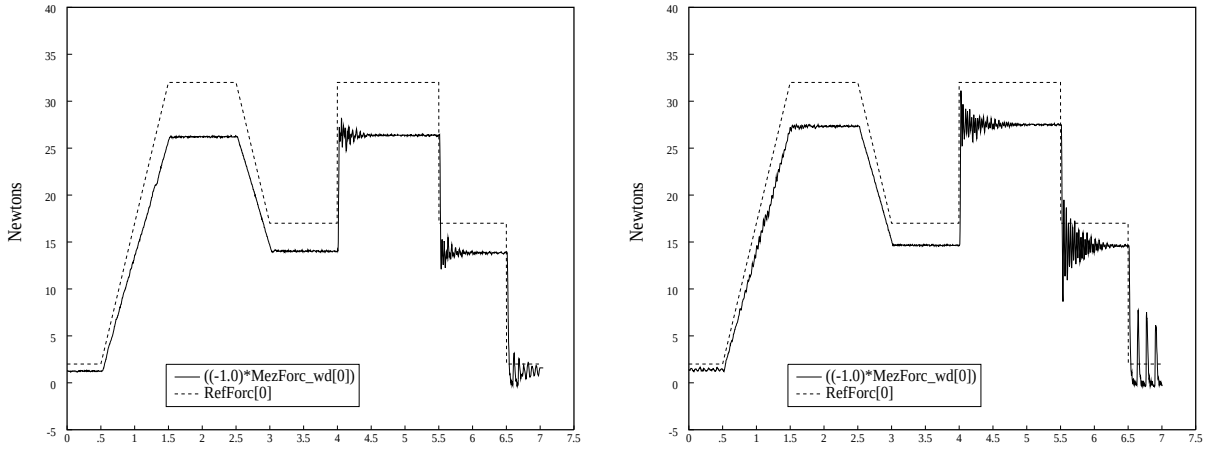

(g) $K_{fp} = 0.5$ (h) $K_{fp} = 1.0$

Figure 6.15: Experimental data of proportional gain explicit force control with feedforward against steel environment (x direction).

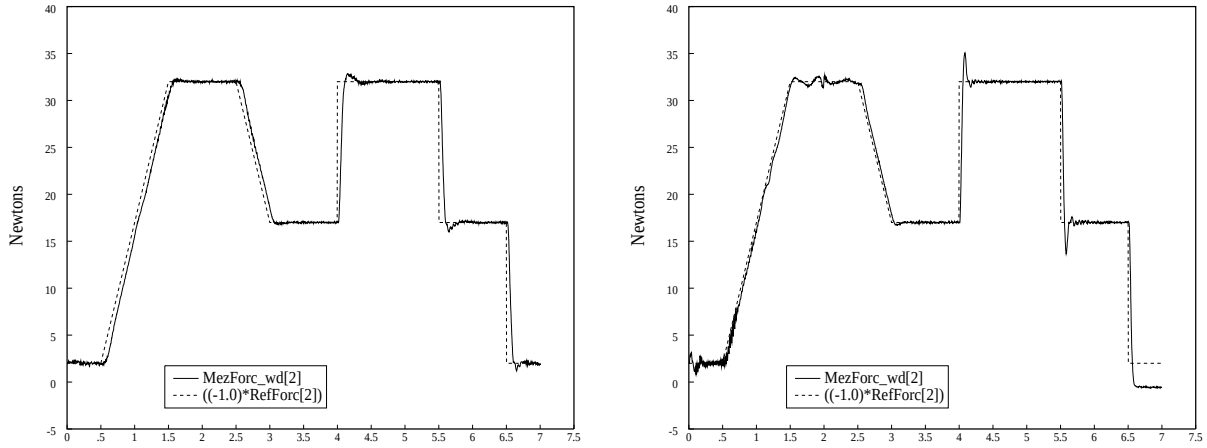

(g) $K_{fi} = 30$ (h) $K_{fi} = 50$

Figure 6.16: Experimental data of integral gain explicit force control on the steel environment (z direction).

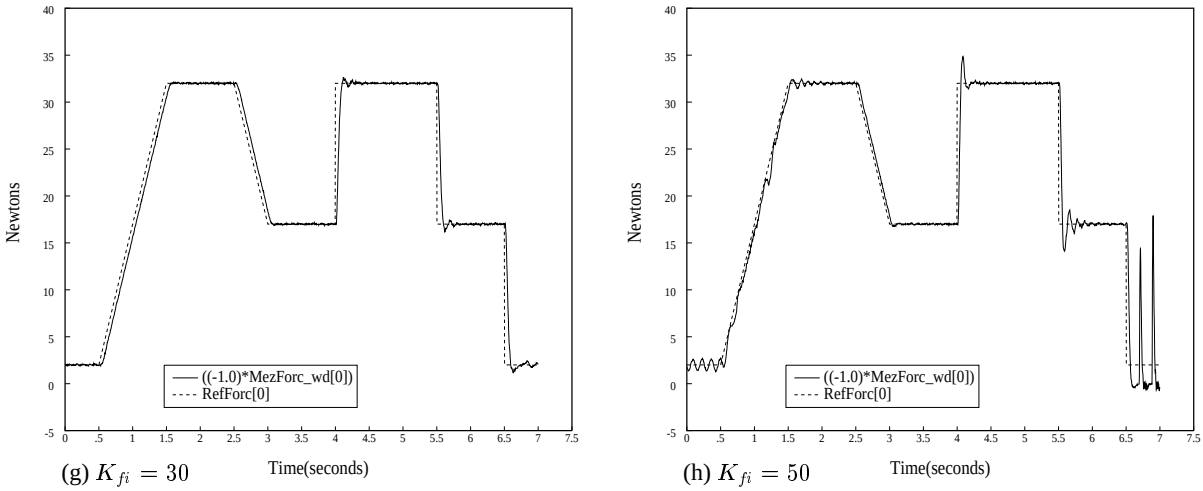

(g) $K_{fi} = 30$ (h) $K_{fi} = 50$

Figure 6.17: Experimental data of integral gain explicit force control on the steel environment (x direction).

gains used in the x direction. For both directions, the gain is still stable for $K_{fi} = 50$. It is apparent that general behavior of this controller is also the same as before with the modelled environment. However, it can also be seen that a stiffer environment again permits higher gains.

The major conclusion to draw from this data is that all of the discussions and results from the analysis of the modelled system carry over to a very stiff environment. In this case it can be assumed that most of the dynamics of the system are within the manipulator and the sensor. Therefore, an infinitely stiff environment (if one could be found) would not provide much different results.

6.6.2 Impact Control on the Steel Environment

To further test the impact controller developed, impacts were made at the two test locations on the steel pedestal. The impact velocity was ~ 40 cm/s. It proved impossible to prevent bouncing during these tests — at least one bounce would always occur.

Figures 6.18 show the response of a z direction impact on the pedestal. The gains compared are for the open loop case of $K_{fp} = 0$, and the best impact response at $K_{fp} = -0.85$. In the case (a), the manipulator bounces several times before coming to rest on the surface. In the case (b), the arm bounces, but returns slowly and softly to the surface, reestablishing contact in less than one second.

Figures 6.18 show the response of an x direction impact on the angle iron face. The cases compared are for a poor impact response with a positive gain of $K_{fp} = 0.75$, and the best impact response at $K_{fp} = -0.75$. Even though both results are oscillatory, it is obvious that the negative gain impact produces peaks that are less numerous and smaller in magnitude.

Two changes to the system were tried to improve the response. First, the impacts were tried with and without the brass weight on the end effector. Without the brass weight, it is guaranteed that contact will occur at only one point. Otherwise it is possible that one edge of the brass weight will strike the steel surface first, causing a torque that will cause an impact of the opposite edge to immediately follow. This type of multiple contact can obscure the resultant data. However, removing the weight produced only minor changes in the response.

The second change was to eliminate damping from the force control law by having $K_v = 0$ after impact. This measure eliminates any side effects of the velocity signal lag as discussed in Section 6.7.1. No difference in the response was observed. The presented results have no damping after impact.

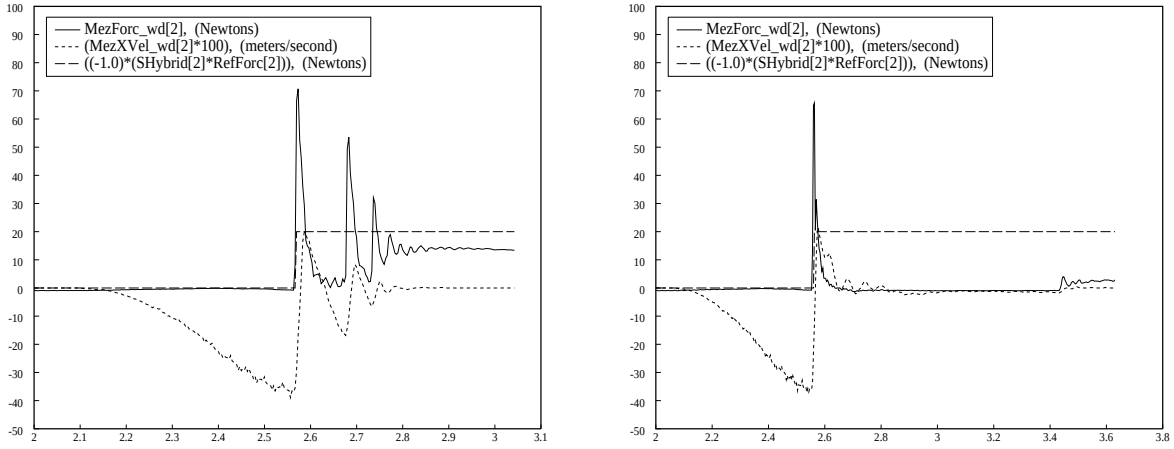

(a) $K_{fp} = 0$ (b) $K_{fp} = -0.85$

Figure 6.18: Impact control on the steel pedestal in the z direction: comparison of $K_{fp} = 0$ (open loop) and $K_{fp} = -0.85$.

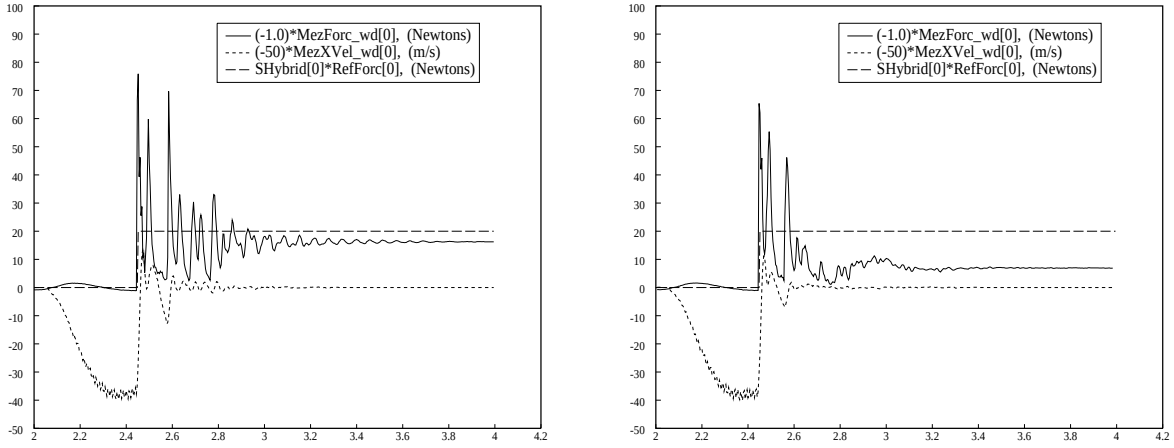

(a) $K_{fp} = 0.75$ (b) $K_{fp} = -0.75$

Figure 6.19: Impact control on the steel pedestal in the x direction with $K_{fp} = 0.75$ and -0.75.

6.6.3 Discussion of Results with the Steel Environment

It is apparent from both the force control and impact results that contact with a very stiff environment does not implicitly cause instability for these control schemes. In fact, the explicit force controllers tend to stay stable for higher gain values. However, the very stiff environment does make the transition from free space motion to contact more difficult. It has been shown that the proposed impact control method improves the transient response. However, this type of impact tends to excite higher frequency components of the system which are not modelled and most likely cannot be controlled. It appears that a better impact response for such stiff environments cannot be obtained without the use of passive energy absorbing components such as a compliant 'skin' between the end effector and the environment. This would effectively reduce the environmental stiffness to that used in the earlier model, making impact without bouncing possible again.

6.7 Implementation Considerations

When implementing the above schemes, there were several practical considerations to be addressed. Some of these can effect the stability or range of operation of a particular controller. Force filtering, because of its close relation to PD force control, has already been discussed in Section 6.2.3. Discussed in this section are other issues such as velocity signal calculation, sampling rates, hybrid control switching, etc.

6.7.1 The Velocity Signal

The angular velocity signal for the CMU DD Arm II is obtained by differencing and averaging the angular position signal. The position signal is a 16 bit absolute position value obtained from pancake resolvers located at each joint. Every control cycle, the position is obtained and placed in a stack. A velocity signal averaged over the past n control cycles can be obtained by simple differencing of the current position with the one n cycles before it:

$$\begin{aligned} v_{avg} &= \frac{1}{n}\left[v(t) + v(t-T) + \cdots + v(t-nT)\right] \\ &= \frac{1}{n}\left[\frac{p(t)-p(t-nT)}{T} + \frac{p(t-T)-p(t-2T)}{T} + \cdots + \frac{p(t-(n-1)T)-p(t-nT)}{T}\right] \\ &= \frac{1}{nT}\left[p(t)-p(nT)\right] \end{aligned} \tag{6.11}$$

Good results are obtained for the CMU DD Arm II with $3 \leq n \leq 10$. The lower number provides a velocity signal with less lag and more noise, and the higher number just the opposite. For free space motion with the CMU DD Arm II , the natural frequency of the system is determined by the stiffness provided by the position gain. This frequency is usually low enough that the velocity signal lag is not significant. However, when the arm is in contact with the environment, the natural frequency of the system is largely determined by the environmental stiffness. This frequency is much higher than in the free space motion case. Higher frequency also means a shorter period. Therefore, the velocity signal lag can become a major portion of the oscillation cycle. Just as with the force derivative delay discussed previously in Section 6.2.3, the velocity signal delay can cause it to act as a position signal. In this case, the velocity gain will add to the already large stiffness of the system, driving it toward instability.

For the tests conducted previously in this chapter, a velocity averaging factor of $n = 3$ was used for joints 4, 5, and 6. A factor of $n = 5$ was used for joints 1, 2, and 3. As can be seen from some of the impact test graphs, the velocity signal has some noise, especially for free space motion before impact. For this reason, a factor of $n = 10$ for joints 1, 2, and 3 is usually used when free space motion is to be performed exclusively. The value $n = 3$ for the last three joints tends to be sufficient at all times.

Since the Cartesian velocity signal contains components from all of the joint signals, the delay will be between three and five cycles. For the control rate of 300 Hz, the delay is between 0.01 and 0.016 seconds.

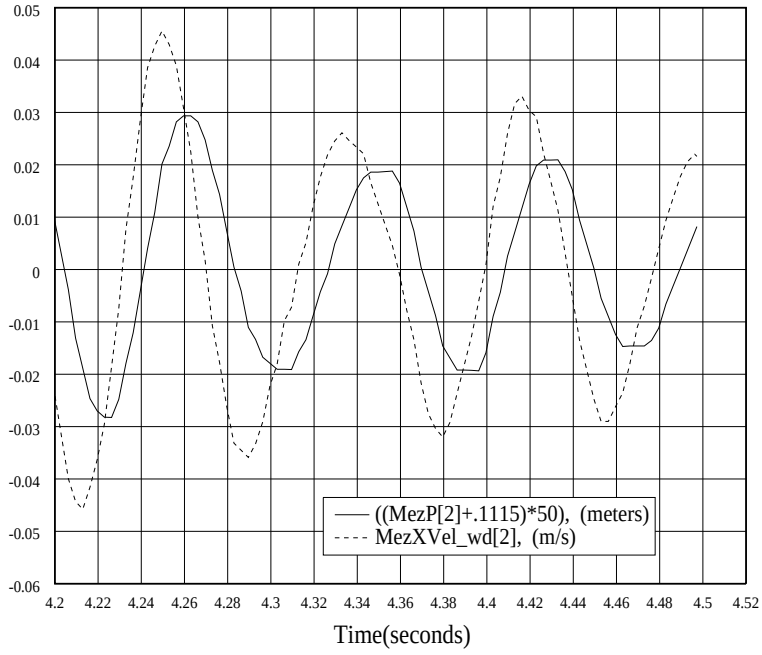

Figure 6.20: Velocity phase lag due to averaging. It can be seen that the velocity signal lags its ideal value by about 0.16s, or 45 degrees.

Figure 6.20 shows the velocity and position signals during proportional gain explicit force control ($K_{fp} = 0.75$), after a step input. The delay of the velocity signal is about 0.01 seconds, or 45° for the 12 Hz oscillation. This also explains why an averaging factor of $n = 10$ is unacceptable. This delay would put the velocity signal in phase with the position signal, and the velocity gain would increase the stiffness of the system instead of the damping.

Note that the use of active damping when the manipulator is in contact with the environment must be used with caution. The time delay from the velocity calculation/filtering is always present. If this delay is a significant part of the natural frequency of the system, then the velocity signal will act as a position signal and add to instability. Further, stiffer environments have higher oscillation frequencies, making the velocity signal least reliable when it would be most useful. Therefore, the damping intrinsic to impedance control, and sometimes used in explicit force control, is always suspect.

Finally, it is worth mentioning that these problems with delay only apply to active damping. Passive damping, as supplied by some soft sensors or end effector covers, will provide damping without time delay. These devices also lower the natural frequency of the system, making active damping possible.

6.7.2 The Force Signal

A LORD 15-50 force sensor was used in all of the experiments. In its factory configuration, it supplies eight strain gauge values at 400 Hz. However, the controllers used usually ran at only 300 Hz. Therefore, one of every four sets of data was ignored. Also, the data set could be as old as one 400 Hz cycle, or 2.5 ms. Since the force oscillations were an order of magnitude slower than the control rate, this asynchronous sampling has no appreciable effect on the stability of the controllers.

The noise in the force signal has several contributors: intrinsic noise, kinematic fluctuations, kinematic inaccuracies, and inertial effects. Intrinsic noise is present in the analog and digital electronics of the sensor system. Kinematic fluctuations are caused by noise in the position signal which causes the world frame transformation to change, and therefore the calculated value of the force in that frame. Compensation for

the weight of the end effector is also position dependent and subject to this noise. Further, the end effector weight compensation is subject to kinematic inaccuracies which can cause the calculated direction of 'down' to be different from the direction of the measured gravitational force. Finally, the inertial effects cause the measured force not to equal the applied force unless the sensor is motionless. All of these factors contribute to a noise amplitude of ~ 0.1 Newtons. This is an order of magnitude above the sensor resolution.

6.7.3 Hybrid Control Switching

With or without impact control, it is necessary to switch from position to force control when using a hybrid control framework. One way to achieve this is to switch to force control when a measured force threshold is exceeded. To prevent force signal noise from causing the switch, a value of 2 N was used for the threshold value for switching *to* force control. Also, since the noise still exists while in force control mode, the measured force may drop below 2 N inadvertently. Thus, a lower threshold value of 1 N was chosen for switching *from* force control.

The switching strategy was implemented in a process that ran parallel to the control process at 150 Hz. This process was part of the joystick controller, and could therefore dictate whether the joystick values were interpreted as commanded velocity (free space motion), or commanded force (constrained motion). This separation of the switching procedure from the control process had one minor effect. It can be seen in some of the impact control graphs presented earlier that the switch does not occur at the exact moment the force goes above the threshold. This has no discernible effect on the results obtained.

Another aspect of the switching strategy is that it could be made unidirectional — only switching to force control was permitted. This is often evident in the force control response graphs presented. When unidirectional, force control will remain in effect even if the measured force is reduced below the threshold, as when the manipulator leaves the surface. The behavior of the controller for this case of contact loss can be quite interesting and illustrative. However, experience showed that some of the controllers tested were sure to become unstable when surface contact was lost. To prevent damage to the system, bidirectional switching was used. Thus, if the end effector lost contact with the environment, the controller reverted to position mode. This can be seen on some of the force response graphs as straight line tail at zero Newtons near the 7 second point.

Finally, it is important to note that when coupled with the impact controller, this switching strategy worked extremely smoothly. Without the impact controller and with nonoptimal explicit force control gains, it was sometimes difficult to get the controller to switch into force control while using the joystick. Also, impacts without the impact controller and with bidirectional switching could send the controller into a bouncing limit cycle. This was true for proportional gain control ($K_{fp} = 0.75$) and integral control ($K_{fi} = 7.5$).

6.8 Conclusion

This chapter has presented the experimental results of implementations of explicit force and impedance control strategies for force trajectory tracking and impact transition. The explicit force control strategies implemented were: proportional with feedforward, integral, filtered feedback proportional–derivative, and second order low pass filtering. Second order impedance control, with and without dynamics compensation, was also implemented. The data permits several important conclusions. First, force trajectory tracking is best accomplished with integral gain explicit force control. Second, impedance control is essentially the same as proportional force control with feedforward. Third, impact control is best accomplished with proportional gain control with negative gain, or equivalently with impedance control with a mass ratio less than one. And fourth, PD force control and damping strategies should not be relied on to provide stability to the system when in contact with the environment, since it is impossible to obtain a true derivative.

The results of this chapter also verify that the model developed in Chapter 2 is correct. The predictions of system behavior made in Chapters 3, 4, and 5 were based on the model and shown to be accurate by the experimentation discussed in this chapter.

These results are unique in many ways. While integral control has been utilized by many researchers, its efficacy has never been experimentally demonstrated against the full spectrum of control strategies. Also, following the guidance of the theoretical analysis of previous chapters it has been possible to show for the first time the commonality of explicit force control and impedance control. This has also provided the insight to develop and demonstrate a new control strategy for hard surface impacts. Finally, some of the pitfalls of implementation of these strategies have been made much more lucid.

Chapter 7

Superquadric Artificial Potential Functions

7.1 Introduction

Previous discussion of impedance and force control has centered around the situation of contact with the environment. It has been shown how explicit force control with proportional gain and feedforward has essentially equivalent responses as second order impedance control. In fact, these strategies are equivalent for the case of a stiff environment. As was discussed in Section 4.6, this connection between the two strategies implies that the impedance parameters K and C can be thought to provide a commanded force as a function of position:

$$f_c = K(x_c - x_m) + C(\dot{x}_c - \dot{x}_m) \tag{7.1}$$

Conversely, this chapter introduces the concept of interpreting the measured force as a position dependent impedance relation:

$$f_m = \mathcal{Z}(x_m) \tag{7.2}$$

When in contact with the environment, this interpretation is not advantageous since the force value can be used directly from measurements, and the impedance function for the environment is not generally known. But when not in contact with the environment, the function $\mathcal{Z}(x)$ can be created. In this case, f_m is not a real force, physically experienced by the manipulator. (Therefore the reaction force compensation term $J^T f_m$ is not used in the control strategies.) Instead, f_m is an *artificial force*, calculated as a function of the manipulator position, and dictating arm motion through the actuator torques. For instance, the artificial force could be a repulsive force that is modelled to exist emanating from an obstacle. Similarly, it could be an attractive force toward a goalpoint. In fact, it can be seen that the commanded force f_c is exactly this type of attractive force. Therefore, in general it is the sum of f_c and f_m which dictate the motion of the manipulator. This one sum of the artificial forces can be obtained from the gradient of an appropriately constructed *artificial potential field*:

$$f_c + f_m = f_{artificial} = -\nabla \phi_{artificial} \tag{7.3}$$

The use of artificial potentials for manipulator control has mainly been proposed to address the obstacle avoidance problem. Other methods have been proposed to address obstacle avoidance, but they are usually very computationally intensive. Artificial potential methods provide a acceptable alternative for obstacle avoidance in real time. However, the artificial potential method does have the problem of local minima which may exist in the potential function. This chapter presents a new artificial potential formulation, based on superquadrics, which eliminates some of these problems. In particular, it is guaranteed that no minima will be created for a single obstacle in an attractive well. Further, this chapter introduces a new concept of object approach using potentials to slow the manipulator and lessen impact forces.

This chapter is organized as follows: First a review of obstacle avoidance strategies will be given, and the domain of artificial potential methods will made clear. Then, in Section 7.3 the attributes of artificial potentials will be outlined by reviewing the work of other researchers. In the course of this review, it will be indicated which aspects of previous schemes are valuable, and which should not be retained. In Section 7.4 the proposed superquadric potential scheme will be described in detail, and its advantages highlighted. In Section 7.5 the addition of the superquadric avoidance potential with global attractive potentials will be mathematically described, and the criterion for the elimination of local minima will be discussed. Also, dynamically changing potentials will be introduced. In Section 7.6 the efficacy of the superquadric potential formulation will be evaluated by simulating both obstacle avoidance and approach. Finally, in Section 7.7 some experimental results of the implementation of the obstacle avoidance potential on the CMU DDARM II are presented.

7.2 Review of Obstacle Avoidance

The problem of moving in space while avoiding collisions with the environment is known as obstacle avoidance or path planning. The obstacle avoidance problem is important for both mobile robots and manipulators [39, 30, 55, 42]. For a mobile robot, the goal is to devise a strategy that will move the robot to its desired destination without colliding with obstacles. In addition, a robust obstacle avoidance scheme should be capable of dealing with moving obstacles. For a manipulator, the problem is more complicated. Not only must the end effector move to the desired destination without collisions with obstacles, but the links of the arm must also avoid collisions. Because this additional requirement is more restrictive, a strategy that works for manipulators can be applied to mobile robots. Therefore, the concern here is with obstacle avoidance for manipulators, and the review of previous work in the field is similarly limited in scope.

Research in the area of obstacle avoidance can be broadly divided into two classes of methodologies: global and local. Global methodologies rely on the description of the obstacles in the configuration space of a manipulator [61, 37, 52]. Local methodologies rely on the description of the obstacles and the manipulator in the Cartesian workspace [30, 3, 35].

Global methodologies require that two main problems be addressed. First, the obstacles must be mapped into the configuration space of the manipulator [37]. Second, a path through the configuration space must be found for the point representing the manipulator. Two techniques are used to generate these paths: geometric searches and artificial potentials. The geometric search technique relies on an exhaustive search of the unoccupied configuration space for a continuous path from the start point to the goal point [61, 39, 38, 55, 15]. If a path exists, it will be found. If multiple paths are found, the best may be chosen. The artificial potential technique surrounds the configuration space obstacles with repulsive potential energy functions, and places the goal point at a global energy minimum [49, 52, 47, 66]. The point in configuration space representing the manipulator is acted upon by a force equal to the negative gradient of this potential field, and driven away from obstacles and to the minimum.

Global methodologies have several disadvantages. The algorithms necessary for global methods are computationally intensive. Also, the computational costs increase quickly as a function of the manipulator's degrees-of-freedom: at least exponentially for geometric search techniques, and at least quadratically for potential energy techniques [52]. Thus, they are suited only for off-line path planning and cannot be used for real-time obstacle avoidance. An immediate consequence is that global algorithms are difficult to use for obstacle avoidance in dynamic environments, where the obstacles are moving in time. Also, when using global algorithms it is very difficult to describe complicated motion planning tasks such as those arising when two manipulators cooperate.

A viable alternative to global methodologies is provide by local ones [30, 3, 35, 64]. Local methodologies also employ the use of artificial potential functions like those discussed previously. However, unlike configuration space potentials, local potentials are expressed in the Cartesian workspace of the manipulator. Obstacles to be avoided are surrounded by repulsive potential functions and the goal point is surrounded by an attractive well. These potentials are added to form a composite potential which imparts forces on a

model of the manipulator in Cartesian space. Torques equivalent to these forces cause the motion of the real manipulator.

The main advantage of local techniques is that they are less computationally demanding than global ones. Thus they can be used in real-time control. Further, they provide the necessary framework to deal with dynamic (changing) environments and can be used for real-time obstacle avoidance. Also, when used with a teleoperated manipulator, local artificial potentials provide low level obstacle avoidance. In this case, the path planning of the manipulator is being performed by the operator and the global methodologies lose their value as robust path planners.

However, local methodologies have one distinct problem: the addition of attractive and repulsive potentials can create local minima in the potential function. Any local minimum will cause the manipulator to experience no net artificial force, and thereby stop at an unintended location. A robust artificial potential function model of the environment should have no local minima [33, 63].

This chapter proposes the use of an artificial potential scheme based on the superquadric, a mathematical function which is employed in computer vision and object modelling techniques [4, 5]. This scheme provides obstacle avoidance capability for manipulators in an environment of stationary or moving objects, preventing end effector and link collisions with these objects. This local avoidance scheme provides obstacle avoidance capability without creating local minima.

The superquadric is a deformable parametric surface and is used as the isopotential surface for the potential function. Since it is deformable, isopotential surfaces near the object may closely model the object, while surfaces further away can be spherical. These spherical surfaces prevent the formation of local minima when this function is added to a larger spherical attractive potential well.

The assignment of potential energy values to the isopotential surfaces determines the repulsive nature of the function. Two possibilities exist: the avoidance potential function, or the approach potential function. The avoidance potential function has a potential energy value at the surface of the object which is larger than the initial kinetic energy of the manipulator. Thus, an energy barrier is established which cannot be surmounted. The easiest way to ensure that the potential energy barrier is large enough is to force the potential function to go to infinity at the object surface.

Also proposed is a second type of artificial potential energy function — the approach potential [63]. Instead of having a potential function go to infinity at the object surface (as with the avoidance potential), the potential energy can go smoothly to a finite value less than the kinetic energy of the manipulator. As the manipulator moves toward the object, it gains potential energy, loses kinetic energy, and slows down. But it always has enough kinetic energy to reach the surface. Thus the approach potential provides deceleration forces that ensure a safe contact velocity at the surface. Once stable contact has been established, force control of the manipulator may begin.

7.3 Attributes of Artificial Potentials

The major interest in artificial potential models has been in realizing obstacle avoidance schemes [35, 33, 48, 21, 65]. These schemes require the addition of attractive and repulsive potentials. An attractive potential well is generally a bowl shaped energy well which drives the manipulator to its center if the environment is unobstructed. However, in an obstructed environment, repulsive potential energy hills are added to the attractive potential well at the locations of the obstacles, as in Figure 7.1. The addition of attractive and repulsive potentials provides obstacle avoidance capability.

In this section, the attributes of the attractive and repulsive potential functions that have been proposed will be reviewed. First, the two types of attractive wells, quadratic and conical, are described. Then, the proposed repulsive potentials are presented and the desirable and undesirable properties that each exhibits are discussed.

The first type of attractive potential function, the quadratic well, is the most widely used [30, 20, 33]. The reason for this is twofold. First, a quadratic potential well provides a linear control law with constant gain.

Consider the quadratic well, U, described by:

$$U(x) = \frac{k}{2}\mathbf{x} \cdot \mathbf{x}, \tag{7.4}$$

where k is constant and $\mathbf{x}$ is a position vector. The force, $\mathbf{F}$, from this potential may be obtained by the gradient:

$$\mathbf{F} = -\nabla U = -k\mathbf{x} \tag{7.5}$$

which is a linear control law (Hooke's Law). Second, all potentials are quadratic for small displacements. This may be seen from the Taylor series expansion in one dimension:

$$U(x_0 + \Delta x) = U(x_0) + \Delta x \frac{dU(x)}{dx}\bigg|_{x=x_0} + \frac{\Delta x^2}{2}\frac{d^2U(x)}{dx^2}\bigg|_{x=x_0} + \dots \tag{7.6}$$

For small displacements, Δx, the higher order terms may be neglected. The force experienced is:

$$F(x_0 + \Delta x) = -\frac{dU(x)}{dx}\bigg|_{x=x_0} - \Delta x \frac{d^2U(x)}{dx^2}\bigg|_{x=x_0} - \dots \tag{7.7}$$

which reduces to Hooke's Law since the first derivative is zero and the second derivative is k. Potentials with positive second derivatives are stablizing, preventing large displacements from being achieved and keeping the approximation valid. Thus the quadratic well is a good attractive potential because of its simple form and because other potentials reduce to it for small displacements.

A second type of attractive potential function, the conical well, has also been proposed [3]. This function is quadratic within a given range and then increases linearly:

$$U(\mathbf{x}) = \begin{cases} k\mathbf{x} \cdot \mathbf{x}, & |\mathbf{x}| < s \\ 2ks|\mathbf{x}| - ks^2, & |\mathbf{x}| \geq s. \end{cases} \tag{7.8}$$

The conical well provides a constant magnitude, centrally attractive, force field for distances larger than s. For smaller distances, the previously described advantages of the quadratic well are utilized.

The second category of potentials, repulsive potentials, are necessary to repel the manipulator away from obstacles that obstruct its path of motion in the global attractive well. It has generally been recognized that a repulsive potential should have a limited range of influence [3, 30]. This prevents an object from affecting the motion of the manipulator when it is far away from the object. Also, the potential function and its derivative must change smoothly and never become discontinuous [3].

Many proposed repulsive potentials have spherical symmetry. One increases cubically with radial distance inside of a circular threshold range [3]. Another has a Gaussian shape [33]. These potentials are useful for surrounding objects with spherical symmetry and singularities in the workspace. Also, when added to a spherically symmetric attractive well they will not create a local minimum (as will be demonstrated subsequently). But a spherically symmetric repulsive potential does not follow the contour of polyhedral objects. For instance, an oblong object surrounded by a sphere effectively eliminates much more volume from the workspace than is necessary or desirable.

Potentials that follow the object shape were proposed to address the insufficiency of radially symmetric potentials. Examples are the GPF and FIRAS functions [35, 30]. The potential energy, $U(r)$, of the FIRAS function is described by:

$$U(r) = \frac{A}{2}\left(\frac{1}{r} - \frac{1}{r_0}\right)^2 \qquad 0 < r < r_0 \tag{7.9}$$

where r is the closest distance to the object surface, r_0 is the effective range, and A is a scaling factor. Figure 7.2 shows this potential for $A = 2$ and $r_0 = 6$. The isopotential contours of this potential function are depicted in Figure 7.3. The GPF function has a similar shape. These functions will be referred to as 'flat-sided' potentials because of the shape of their isopotential contours.

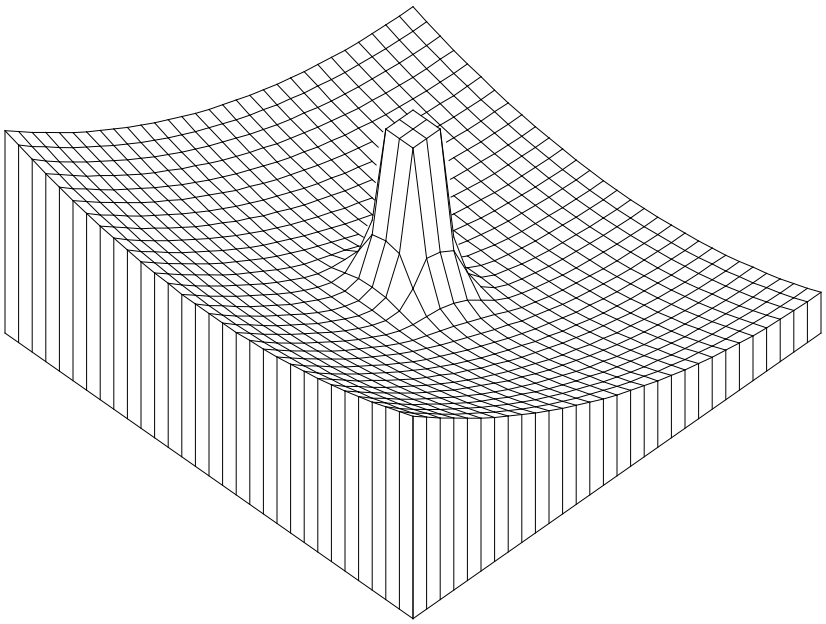

Figure 7.1: A repulsive potential added to an attractive well.

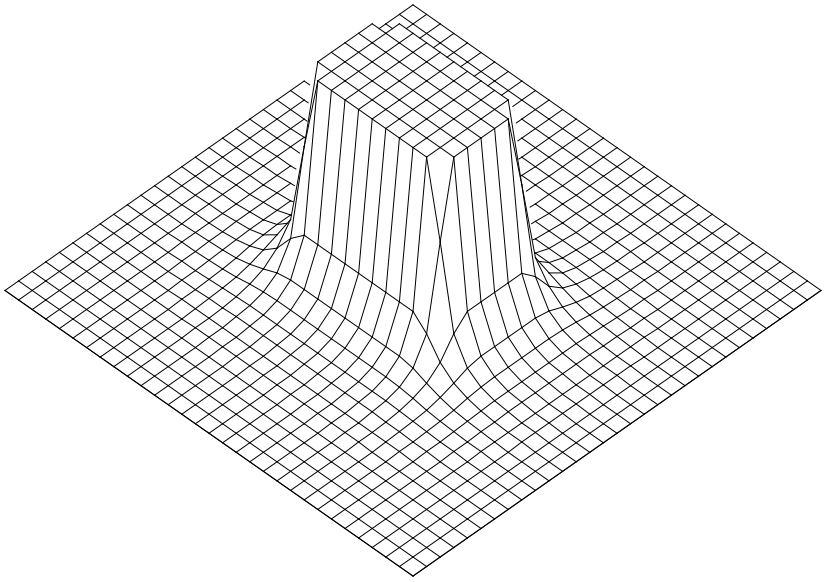

Figure 7.2: The FIRAS potential for $A = 2$ and $r_0 = 6$. Large values have been truncated.

By itself, a flat-sided potential works well. But when this potential is added to an attractive well, local minima appear on the side of the object away from the center of the well. Consider the case depicted in Figure 7.4, where the side of the object away from the attractive well center is tangent to the isopotential contours of the well. Motion along the linear section of the object contour, from point A to point B, passes through changing potential values of the attractive well. At points A and B the attractive well potential is higher than at point C. Since the object potential is the same at A, B, and C, the sum of the object potential and the attractive well potential has a local minimum at point C. It can be seen that any section of an object contour that has a radius of curvature greater than the contour of the attractive well will generate a local minimum 'uphill' from the object. The contour of a circular repulsive potential always has a smaller radius of curvature than the contour of the attractive well in which it is inscribed. Therefore, a circular repulsive potential will not generate local minima in this way.

In summary, a repulsive potential function that is useful for modelling objects in the environment should have the following attributes:

1. The potential should have spherical symmetry for large distances to avoid the creation of local minima when this potential is added to an attractive well.
2. The potential contours near the surface should follow the surface contour so that large portions of the workspace are not effectively eliminated.
3. The potential of an obstacle should have a limited range of influence.
4. The potential and the gradient of the potential must be continuous.

A novel formulation of a repulsive potential function, based on superquadrics, is proposed to satisfy all of the above criteria. Not only is this scheme useful for obstacle avoidance, but it can also be used for obstacle approach. This formulation is presented in the next section.

7.4 Superquadric Potentials

The superquadric potential is a function that has isopotential surfaces shaped like superquadrics. The value of the potential energy at each surface is determined by the potential energy function. Proposed here are two repulsive potential energy functions: the avoidance potential function, and the approach potential function. In this section, the superquadric formulation for isopotential contours is presented, and then the two types of repulsive potential energy functions are described.

7.4.1 Superquadric Isopotential Contours

As is dictated by attributes one and two above, the isopotential contours of a artificial potential function must change from spherical at large distances, to the object shape near the surface.

To obtain isopotential contours that follow the object shape near the surface an object may be surrounded with a superquadric [4, 5]:

$$\left[\left(\frac{x}{f_1(x,y,z)}\right)^{2n} + \left(\frac{y}{f_2(x,y,z)}\right)^{2n}\right]^{\frac{2m}{2n}} + \left(\frac{z}{f_3(x,y,z)}\right)^{2m} = 1 \tag{7.10}$$

where f_1, f_2, and f_3 are scaling functions, and m and n are exponential parameters. Previously we have employed this function in two dimensions ($z = 0$) with constant scaling functions [63]:

$$\left(\frac{x}{a}\right)^{2n} + \left(\frac{y}{b}\right)^{2n} = 1. \tag{7.11}$$

Figure 7.3: The isopotential contours of the FIRAS potential in Figure 7.2.

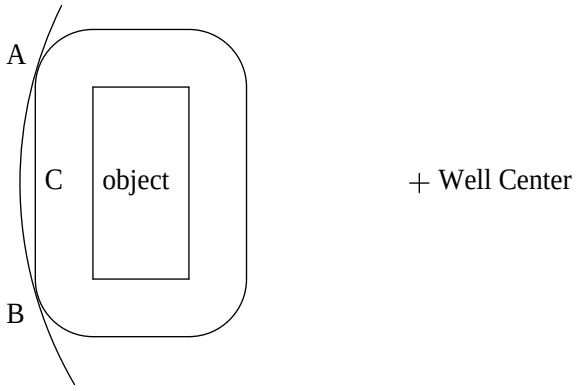

Figure 7.4: The coincidence of isopotential contours at points A and B indicates the presence of a local minimum in the vicinity of point C.

This form is called an n-ellipse where a is the semi-major axis and b is the semi-minor axis [17, 30]. The use of this simpler form in potential functions is first reviewed, and then a generalization to the superquadric potential form is presented.

In order for the above n-ellipse to be useful as a potential function, two constraints should be imposed at the surface of the object: first, the ellipse must touch the corners of the surrounded object (which is rectangular for this case); and second, the area between the object and the ellipse must be minimal. These constraints yield:

$$a = \frac{w}{2}\left(2^{\frac{1}{2n}}\right) \qquad b = \frac{h}{2}\left(2^{\frac{1}{2n}}\right) \tag{7.12}$$

where w is the x dimension of the rectangle, and h is the y dimension.

At the surface of the object, the isopotential contours should match the shape of the surface. This requires that n go to infinity at the surface. However, away from the surface the contours must become spherical in accordance with the first attribute. Letting n go to one will make the contours elliptical. This ellipse may be further modified by a coefficient that multiplies the y term. The contour function thus becomes:

$$\left(\frac{x}{a}\right)^{2n} + \left(\frac{b}{a}\right)^{2}\left(\frac{y}{b}\right)^{2n} = 1 \qquad n \geq 1. \tag{7.13}$$

It is also necessary to have a variable that specifies each contour. The variable acts as a pseudo-distance from the object, being zero at the surface and increasing with successive contours away from the surface. Along the x axis this variable can be made to change linearly. Thus,

$$K = \left[\left(\frac{x}{a}\right)^{2n} + \left(\frac{b}{a}\right)^{2}\left(\frac{y}{b}\right)^{2n}\right]^{\frac{1}{2n}} - 1. \tag{7.14}$$

Figure 7.5 shows a plot of K at regular intervals with n varying from a very large value to a value near unity.

Since the parameter n must vary from infinity to one while K varies from zero to infinity, n is defined as:

$$n = \frac{1}{1 - e^{-\alpha\beta_n K}} \tag{7.15}$$

where α and β_n are adjustable parameters. Unless otherwise noted, β_n will be unity. Other definitions of n are possible, but this form is useful because it is related to the magnitude of the potential, as will be shown in Section 7.4.2.

The above description, expanded to three dimensions, yields an ellipsoid instead of an ellipse. For the three dimensional case, f_3 in Equation (7.10) is a third constant semi-axis, c, and the parameter m can be given the form:

$$m = \frac{1}{1 - e^{-\alpha\beta_m K}}. \tag{7.16}$$

If the parameter β_m is set equal to β_n, then m equals n and Equation (7.10) describes an n-ellipsoid.

The elliptical (ellipsoidal) description may be generalized to the superquadric formulation by using non-constant scaling functions, f_i, in Equation (7.10). This provides a method of deforming the n-ellipse (ellipsoid) to other shapes. This effect can be interpreted as changing the semi-axes of the ellipse (ellipsoid). This is demonstrated by an example in two dimensions for a superquadric contour that snugly surrounds a trapezoid as shown in Figure 7.6. In this case, the semi-minor axis b varies from b_0 to b_1 as the height of the object varies from h_0 to h_1 over its total width, $2w$. Therefore, at the object surface $(K = 0)$,

$$b(x) = mx + d \tag{7.17}$$

$$m = \frac{h_1 - h_0}{2w} = \frac{b_1 - b_0}{2a} \tag{7.18}$$

$$d = \frac{b_1 + b_0}{2}. \tag{7.19}$$

Figure 7.5: The isopotential contours for $K = 0.1$ to $K = 2.6$, and $\alpha = 1.5$.

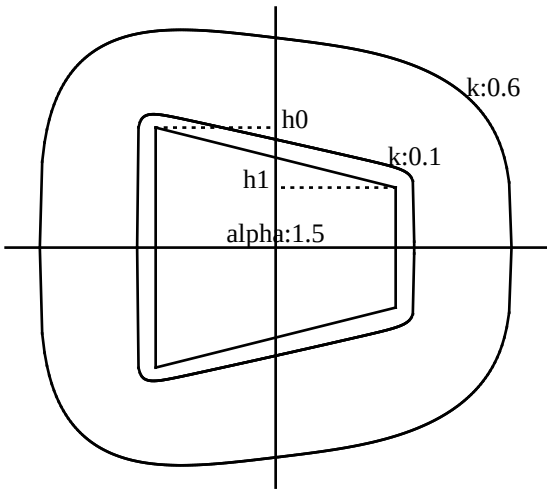

Figure 7.6: Superquadric isopotential contours for a trapezoid.

This value of b provides a superquadric which touches the corners of the trapezoid, with $K = 0$. Superquadric isopotential contours away from the object are obtained by scaling x:

$$f_2 = m\frac{x}{K+1} + d. \tag{7.20}$$

Reducing h_1 to a very small value gives a superquadric model of a triangle, as shown in Figure 7.7.

Finally, this example can be extended into three dimensions for superquadric models of wedges, pyramids, and cones. For a wedge,

$$f_1 = a \tag{7.21}$$

$$f_2 = m\frac{x}{K+1} + d \tag{7.22}$$

$$f_3 = c. \tag{7.23}$$

For a pyramid,

$$f_1 = a \tag{7.24}$$

$$f_2 = m_2\frac{x}{K+1} + d_2 \tag{7.25}$$

$$f_3 = m_3\frac{x}{K+1} + d_3. \tag{7.26}$$

And for a cone oriented along the z-axis,

$$n = 1 \tag{7.27}$$

$$f_1 = m\frac{z}{K+1} + d \tag{7.28}$$

$$f_2 = m\frac{z}{K+1} + d \tag{7.29}$$

$$f_3 = c. \tag{7.30}$$

Thus, a formulation has been developed to describe isopotential contours with superquadrics. With the form of the isopotential contours established, it is necessary to assign potential energy values to them. This is done in the next section.

7.4.2 Repulsive Potential Energy Functions

The potential energy function must assign potential energy values to the isopotential contours defined previously. Two types of repulsive energy functions have been utilized: the avoidance potential, and the approach potential.

The Avoidance Potential

The avoidance potential is a function which surrounds an object and prevents a manipulator from touching the object. This must be true, independent of the manipulator's kinetic energy. The easiest way to ensure this is to set the magnitude of the potential at the surface to infinity. Away from the surface, the energy values must be in accordance with the third and fourth attributes outlined in Section 7.3, and in accordance with natural potentials (e.g. electrostatic, gravitational, etc.) exhibit an inverse dependence on distance. Therefore, the potential function must have a K^{-1} dependence for short distance repulsion, but drop to zero faster than

K^{-1} for large distances. Also, the function and its derivative must be continuous. A function that has these attributes is the Yukawa potential [8]:

$$U(K) = A\frac{e^{-\alpha K}}{K} \tag{7.31}$$

Figures 7.8 and 7.9 show this function with $\alpha = 1$ and $A = 1$ for a rectangle and a triangle.

The parameter α determines how rapidly the potential rises near the object and falls off away from the object. This rate must be related to the rate at which the 'n-ness' of the ellipse changes as expressed in Equation (7.15). These rates have been chosen to be proportional, with the constant of proportionality being β_n in Equation (7.15). Usually, $\beta_n = 1$ and both rates are equal to the value of α.

The parameter A acts as an overall scale factor for the potential. Large values of A will make the object have a spherical field of repulsive force at large distances. Small values of A will allow the object to be approached much more closely. At this closer range, the isopotential contours will have large values of n and will approximate the shape of the object. For the rest of this discussion A will assumed to be unity unless otherwise noted.

The Approach Potential

The approach potential is a function which surrounds an object and decreases the approach speed of the manipulator as it move towards the object. This is achieved by setting the value of the potential energy at the surface of the object to be slightly less than the initial kinetic energy of the manipulator. As the manipulator moves toward the object its kinetic energy is transformed to potential energy, and its velocity decreases. Setting the magnitude of the potential function at the surface less than the initial kinetic energy ensures that the manipulator will always reach the surface.

An appropriate approach potential should have all of the attributes of the avoidance potential, but should go to a finite maximum value at the surface of the object. Therefore, far from the object, the form of the avoidance potential may be used. However, closer to the surface the potential should be Gaussian in nature, the slope smoothly changing to zero at the surface so that no artificial force is experienced when real contact with the environment is established. (At this time, impact control may be employed, as described in Chapter 5.) Because this general form must remain valid for all values of α, a simple polynomial fit is not possible. Proposed is the function, $U(K)$, which satisfies these criteria:

$$U(K) = \begin{cases} \frac{A}{K}e^{-\alpha K}, & K \geq 1 \\ A\exp\left(-\alpha K^{1+\frac{1}{\alpha}}\right), & 1 > K \geq 0 \end{cases} \tag{7.32}$$

Figures 7.10 and 7.11 show this function with $\alpha = 1$ for a rectangle and a triangle.

This section has presented a superquadric isopotential contour formulation and the two types of repulsive potential energy functions. The developed superquadric potentials have the attributes outlined in Section 7.3, but only asymptotically. The major concern raised by this fact is the avoidance potential is never exactly circular (because K is never infinite in practice). Thus, attribute number one may be violated when the avoidance potential is added to a spherical attractive well. This issue is explored analytically in the next section.

7.5 Addition of Superquadric Avoidance Potentials and an Attractive Well

When adding superquadric avoidance potentials to a global attractive well, several situations must be considered. These may be divided into single object and multi-object scenarios.

For a single obstacle (only one avoidance potential), the relation between the positions of the avoidance potential and the global well center is important. Three distinct situations arise. First, the global well center

Figure 7.7: The isopotential contours surrounding a triangle for $K = 0.1$ to $K = 2.6$, and $\alpha = 1.5$.

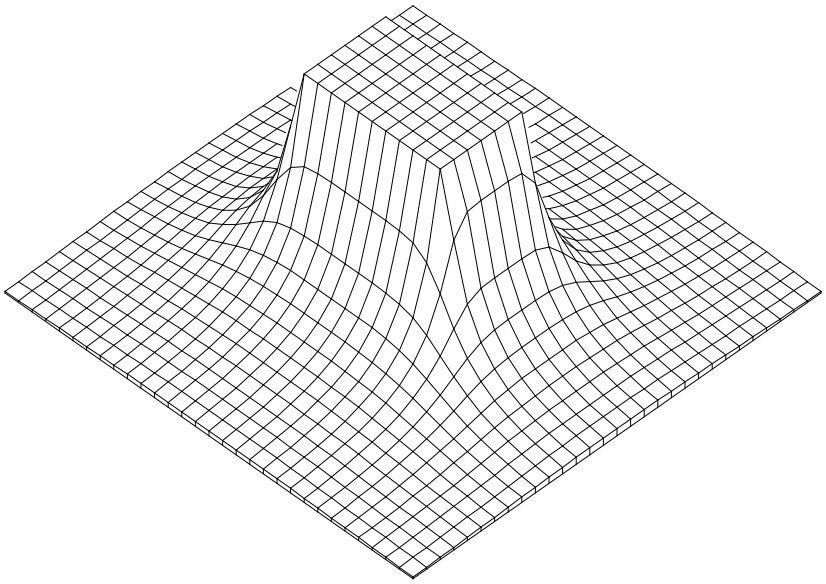

Figure 7.8: The avoidance potential for a rectangle with $\alpha = 1$ and $A = 1$. Large values have been truncated.

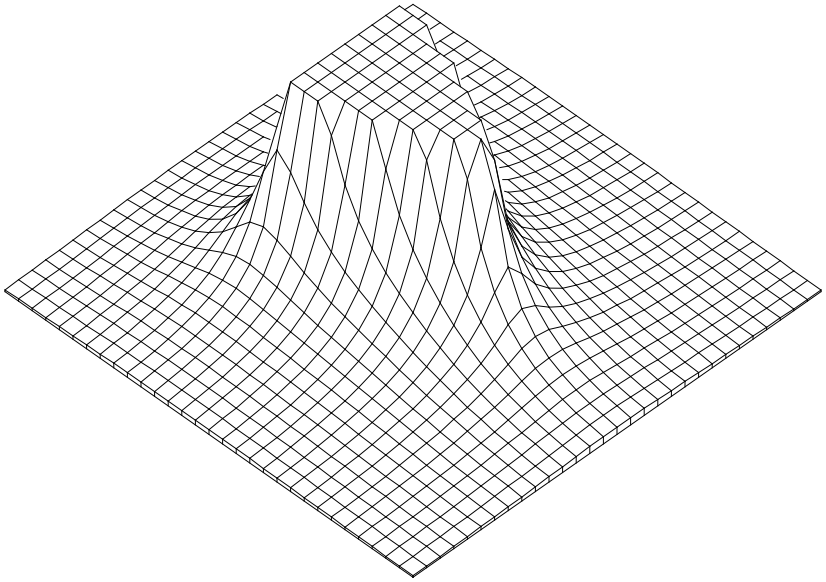

Figure 7.9: The avoidance potential for a triangle with $\alpha = 1$ and $A = 1$. Large values have been truncated.

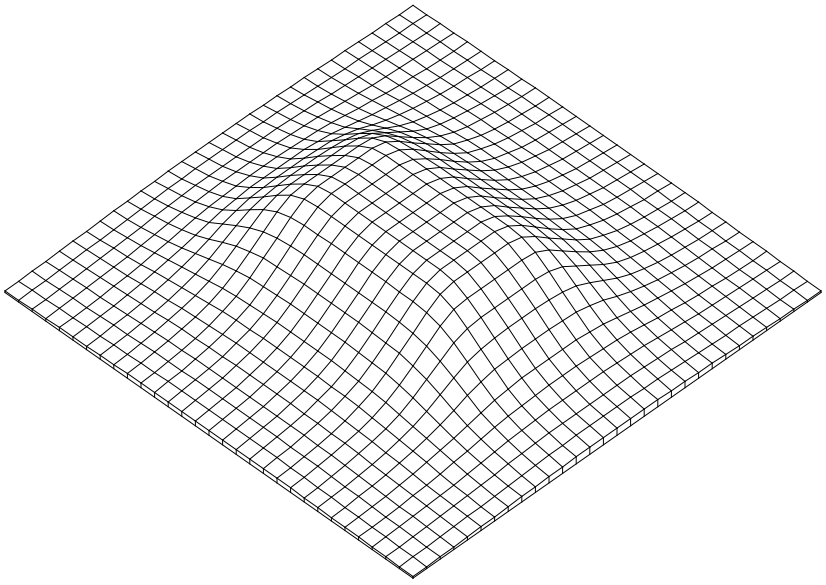

Figure 7.10: The approach potential function for a rectangle with $\alpha = 1$.

is far from the object and is not effected by the object potential. Second, the global well center is inside the object to be avoided. Or third, the situation which is between the above two extremes, the global well center is within the range of influence of the avoidance potential. The second case will not be considered any further since it precludes the possibility of having the manipulator obtain the goal position. The remaining two situations, will be discussed in Sections 7.5.1 and 7.5.2.

If multiple objects are to be added to a global attractive well, the relation of these objects to each other is of primary importance. (The effect of the position of each to the global well center is covered by the single object analysis.) If multiple objects are placed at distances from each other such that the addition of their potential energy is nonzero, then the single object analysis breaks down. For example, multiple objects may be placed in a cluster a such a way that they effectively form a larger object with a concavity that faces away from the global well center. This concavity may cause a local minimum that can trap the manipulator. To avoid this problem, the object cluster and its concave regions may be treated as one large object and surrounded with one potential. However, this solution will obviously not work as the workspace become heavily populated with obstacles. It appears that in this case a higher level trajectory planner will become necessary, and this scenario is not addressed any further. Therefore, the following analysis is restricted to a single obstacle in a global well.

7.5.1 Addition of A Superquadric Avoidance Potential to a Distant Attractive Well

The concern when adding an avoidance potential to a distant attractive well, is that an undesirable minimum may be created 'uphill' from the object. Because the superquadric avoidance potential only becomes a circle asymptotically, a spurious minimum may be present. However, this minimum can effectively be removed by making the depression associated with it smaller than the resolution of the system.

For a rectangular object, the minimum value of α is determined for its worst case orientation. This is when the longest dimension of the object is normal to the shortest distance between the starting position and the attractive well center. In other words, the object is placed 'across' the desired path. In this configuration, the isopotential contours of the object to be avoided are tangent to the isopotential contours of the attractive well. Using a coordinate system centered on the object, and the x-axis along its longest dimension, the isopotential contours have a slope of zero and an infinite radius of curvature along the y-axis. This can be seen by rearranging Equation (7.14) as $y = f(x)$, taking the first and second derivatives, and setting $x = 0$. Mathematically, the superquadric is linear at the axes when $n \neq 1$. Thus, *mathematically* the problem that was described earlier still exists — an isopotential object contour with a radius of curvature larger than the spherical well in which it is placed will definitely cause minima if it is placed tangent to the well. However, this problem can be effectively eliminated for the superquadric potential function by adjusting the parameter alpha. The adjustment makes the depression from the local minimum smaller than the resolution of the system. This solution is presented in detail below.

Consider again a coordinate system centered on the object, oriented as described above. The potential energy, U, has the following form:

$$U = U_o(K) + U_w(\mathbf{x}) \tag{7.33}$$

where the object and well potentials are obtained from Equations (7.31) and (7.4) as:

$$U_o = \frac{e^{-\alpha K}}{K} \qquad \text{and} \qquad U_w = \ell \mathbf{x} \cdot \mathbf{x} \tag{7.34}$$

with ℓ constant and $\mathbf{x} = (x, y - y_0)$, where y_0 is the location of the attractive well center.

First it is necessary to find the local minimum along the y-axis that is on the opposite side of the object from the attractive well center. At this point the total force is zero.

$$0 = \nabla U = \frac{\partial}{\partial x}\left[U_o + U_w\right]\hat{x} + \frac{\partial}{\partial y}\left[U_o + U_w\right]\hat{y} \tag{7.35}$$

or

$$0 = \frac{\partial U}{\partial K}\left[\left(\frac{x}{a}\right)^{2n} + \left(\frac{b}{a}\right)^{2}\left(\frac{y}{b}\right)^{2n}\right]^{\frac{1}{2n}-1}\left(\frac{1}{a}\right)^{2n} x^{2n-1} + 2\ell x \tag{7.36}$$

$$0 = \frac{\partial U}{\partial K}\left[\left(\frac{x}{a}\right)^{2n} + \left(\frac{b}{a}\right)^{2}\left(\frac{y}{b}\right)^{2n}\right]^{\frac{1}{2n}-1}\left(\frac{b}{a}\right)^{2}\left(\frac{1}{b}\right)^{2n} y^{2n-1} + 2\ell(y - y_0) \tag{7.37}$$

where

$$\frac{\partial U}{\partial K} = -e^{-\alpha K}\left[\frac{\alpha}{K} + \frac{1}{K^2}\right]. \tag{7.38}$$

Considering only the y direction at the y-axis ($x = 0$),

$$\left.\frac{\partial U}{\partial y}\right|_{x=0} = \frac{\partial U}{\partial K}\left[\left(\frac{b}{a}\right)^{2}\left(\frac{y}{b}\right)^{2n}\right]^{\frac{1}{2n}-1}\left(\frac{b}{a}\right)^{2}\left(\frac{1}{b}\right)^{2n} y^{2n-1} + 2\ell(y - y_0) \tag{7.39}$$

is a cubic equation of the form:

$$0 = -e^{-\sigma}(\sigma + 1)c + 2\ell(y - y_0)(cy - 1)^2 \tag{7.40}$$

with

$$K(x{=}0) = cy - 1, \qquad c \equiv \left(\frac{b}{a}\right)^{\frac{1}{n}}\left(\frac{1}{b}\right), \qquad \sigma \equiv \alpha K. \tag{7.41}$$

Solving for the one real root of this equation yields:

$$y = \frac{1}{c}\left(M + N + \frac{1}{3}(2 + cy_0)\right) \tag{7.42}$$

where

$$M = \left[-\frac{h}{2} + \sqrt{\frac{h^2}{4} + \frac{g^3}{27}}\right]^{\frac{1}{3}} \qquad N = -\left[\frac{h}{2} + \sqrt{\frac{h^2}{4} + \frac{g^3}{27}}\right]^{\frac{1}{3}} \tag{7.43}$$

$$g = -\frac{1}{3}(y_0 - 1)^2 \tag{7.44}$$

$$h = \frac{1}{27}\left[2 - 6y_0 - 6y_0^2 - 2y_0^3 - 27c\left(\frac{\sigma + 1}{2\ell}\right)e^{-\sigma}\right]. \tag{7.45}$$

Having solved for the y coordinate of the minimum, it is necessary to determine the size of the local depression. This is done by finding the first maximum in the x direction for the y value obtained. The value of x is obtained from Equations (7.36) and (7.37) as:

$$x = \frac{a}{b}\left[\frac{y^{2n-1}}{y - y_0}\right]^{\frac{1}{2n-2}}. \tag{7.46}$$

Given that the resolution of the system being modelled must be less than $2x$, it is only necessary to satisfy the above equation. Because y and n are both functions of σ, this equation can be used for an iterative solution of σ. With a value of σ determined, y and n may be obtained from Equations (7.15), (7.40), and (7.41). Then K and α may be obtained from Equations (7.41). In this way, a minimum value of α may be calculated which permits the addition of attractive and repulsive potentials without the creation of a local minimum.

For a rectangular object in the conical well, a similar analysis may be performed. In this case U_w in Equation (7.33) is obtained from Equation (7.3) as:

$$U_w = 2\ell s|\mathbf{x}| - \ell s^2. \tag{7.47}$$

Therefore, Equation (7.35) yields:

$$0 = \frac{\partial U}{\partial K}\left[\left(\frac{x}{a}\right)^{2n} + \left(\frac{b}{a}\right)^{2}\left(\frac{y}{b}\right)^{2n}\right]^{\frac{1}{2n}-1}\left(\frac{1}{a}\right)^{2n} x^{2n-1} + \frac{2\ell s x}{|\mathbf{x}|} \tag{7.48}$$

$$0 = \frac{\partial U}{\partial K}\left[\left(\frac{x}{a}\right)^{2n} + \left(\frac{b}{a}\right)^{2}\left(\frac{y}{b}\right)^{2n}\right]^{\frac{1}{2n}-1}\frac{b^{2-2n}}{a^2} y^{2n-1} + \frac{2\ell s(y-y_0)}{|\mathbf{x}|}. \tag{7.49}$$

Again, considering only the y direction at the y-axis,

$$\left.\frac{\partial U}{\partial y}\right|_{x=0} = \frac{\partial U}{\partial K}\left[\left(\frac{b}{a}\right)^{2}\left(\frac{y}{b}\right)^{2n}\right]^{\frac{1}{2n}-1}\left(\frac{b}{a}\right)^{2}\left(\frac{1}{b}\right)^{2n} y^{2n-1} + 2\ell s \tag{7.50}$$

is a quadratic equation of the form:

$$0 = -e^{-\sigma}(\sigma+1)c + 2\ell s(cy-1)^2. \tag{7.51}$$

Solving for the meaningful root of this equation yields:

$$y = \frac{1}{c} + \sqrt{\frac{e^{-\sigma}(\sigma+1)}{2\ell s c}}. \tag{7.52}$$

As before, the y coordinate of the minimum is used to determine the size of the local depression. This is done by finding the first maximum in the x direction for the y value obtained. The value of x is obtained from Equations (7.48) and (7.49), and is equivalent to Equation (7.46). As was outlined before, a solution for α may then be obtained.

For non-rectangular objects in quadratic and conical wells, the same analyses may be used as worst case scenarios. The rectangle considered will have the dimensions of the maximum height and width of the non-rectangular object. A valid bound for α is determined since the rectangle is more likely to form a local minima. As was described previously, this is because the superquadric isopotential contours that intersect the object axes at right angles have an infinite radius of curvature at the points of intersection. The parameter α eliminates the local minimum by forcing the depression associated with it to become smaller than the resolution of the system. This is equivalent to saying that the parameter α forces the isopotential contours to circles (within the resolution of the system) at the range of the former minimum. For a non-rectangular object the same value of α will also provide circular isopotential contours at the necessary range, ensuring that these objects will not cause local minima.

7.5.2 Addition of a Superquadric Avoidance Potential to a Close Attractive Well: Dynamic Potentials

The previous analysis determines a value of the parameter α that prevents the formation of a local minimum 'uphill' from the obstacle. However, it is assumed that independent of the value of α, the object potential will be zero at the center of the global attractive well. If this is not the case, the addition of the global well and the object potential will displace the global minimum from the center of the global well. In Figure 7.12(a) the global minimum will move from point C to point D. This implies that the manipulator will not achieve the goal point even though no local minima are present in the environment. Increasing α may eliminate

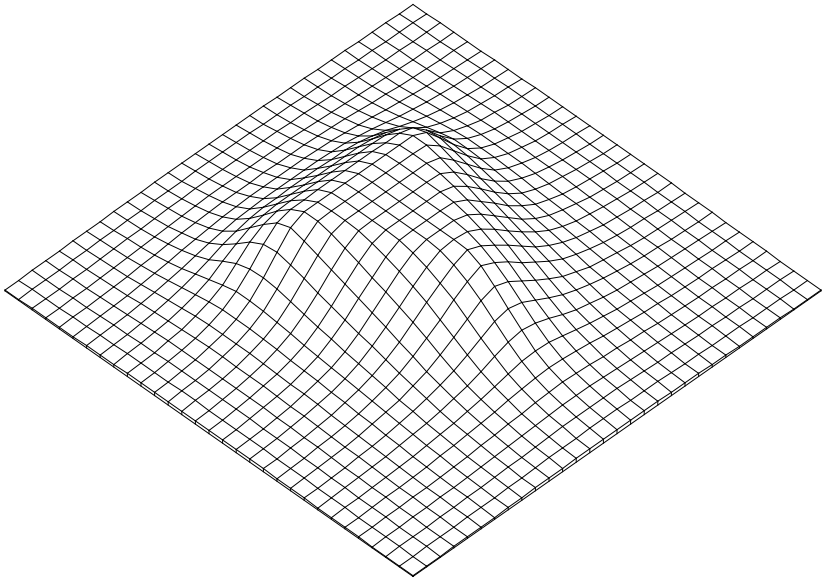

Figure 7.11: The approach potential function for a triangle with $\alpha = 1$.

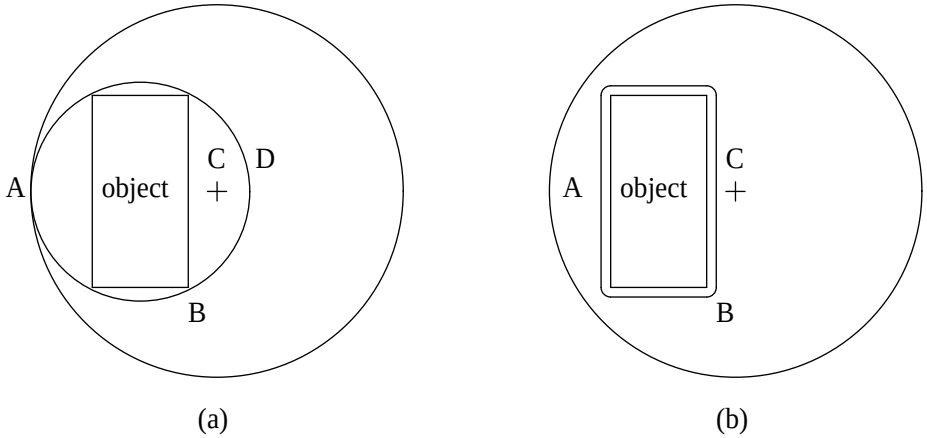

(a) (b)

Figure 7.12: These figures show the effect of having the global well center, point C, very close to an obstacle. In (a) the elimination of a local minimum at point A moves the global minimum from C to D. In (b), reshaping the object potential moves the global minimum to the global well center, point C. This causes the formation of a local minimum at point A. However, if the manipulator has already moved to point B before the potential changes shape, the new local minimum will provide no problem.

this problem by reducing the range of the object potential. However, if the global well center is within the smallest sphere (circle) that can enclose the object, then increasing α will not help. Since there is no way for the isopotential contours to become circular inside this range, the value of the object's avoidance potential can not go to zero, by design. If the parameters A or β_n are modified to force the obstacle potential to zero at the global well center, they will also cause the obstacle potential to become nonspherical, as in Figure 7.12(b). This nonspherical shape will cause the formation of a local minimum on the other side of the obstacle at point A, as discussed in Section 7.3.

Thus a dilemma exists: to avoid the creation of a local minimum, the position of the global minimum must been shifted; and to remove this shift, a local minimum must be created. The only solution to this problem is to dynamically change the potential shape. Thus, if the manipulator is 'uphill' from the object, the parameters must be set to eliminate the formation of the local minimum. As the manipulator moves to the 'downhill' side of the obstacle, near point B in Figures 7.12(a) and 7.12(b), the potential parameters may be changed to shrink the object potential. This will move the global minimum back to the center of the global attractive well at point C in Figure 7.12(b). There will then be the formation of a local minimum 'uphill' from the object at point A in Figure 7.12(b), but this is of no concern since that region of the workspace has already been traversed.

This process of dynamically altering the shape of the avoidance potential is not possible with the potentials that have been previously reviewed, and is presented here as another advantage intrinsic to the superquadric potential formulation.

7.6 Simulation

To test these concepts the performance of two link and three link (redundant) planar manipulators interacting with an artificial potential have been simulated. The motion of these arms is caused by the artificial forces acting on the end effector and the individual links. The end effector is attracted by a goal point and repelled by the obstacle, while the links are repelled by the obstacle if the link interaction is 'on'. The results indicate that the superquadric potentials provide a valid method of obstacle avoidance for a manipulator, and an improvement over existing potential functions.

7.6.1 End Effector Interaction

There are two ways for the arm to react to the artificial forces applied to the end effector. The first method transforms the forces into the corresponding joint torques through the transpose of the Jacobian: $\tau = J^T F$. The joint accelerations can then be derived from the Lagrangian [7]. The second method obtains joint accelerations by directly transforming the Cartesian accelerations that would be experienced by a unit mass in the potential well: $\ddot{\theta} = J^{-1}\left(\ddot{x} - \dot{J}\dot{\theta}\right)$. The first method is desirable because it does not involve the inverse of the Jacobian, which may become singular. For avoidance potentials, the first method is used. But the second method must be used when employing an approach potential.

The approach potential concept requires that the final potential energy of the manipulator be less than or equal to the initial sum of the kinetic and potential energy. Thus, as the arm approaches the object, all of its kinetic energy is converted to potential energy and the arm stops at the surface. While the kinetic energy of the arm may be obtained from the Lagrangian, the artificial potential energy of the arm cannot [7]. (In fact, the potential energy in the Lagrangian is zero because the manipulator used in these simulations is assumed to be operating in a plane perpendicular to the force of gravity.) Instead, the potential energy must be obtained from the position of the manipulator links in the potential well. Even for a two link arm with one dimensional

links and uniform density, λ, this potential energy has the form:

$$PE = \int_{K(\text{base})}^{K(\text{elbow})} A\lambda \frac{e^{-\alpha K}}{K} dK + \int_{K(\text{elbow})}^{K=1} A\lambda \frac{e^{-\alpha K}}{K} dK + \int_{K=1}^{K(\text{end effector})} A\lambda \exp\left(-\alpha K^{1+\frac{1}{\alpha}}\right) dK + PE(\text{potentialwell}) \quad (7.53)$$

assuming that the end effector is at a distance of $K \leq 1$ away from the object. Obviously, this form of the potential energy is intractable. Hence it is not used in the Lagrangian and can not be used in this approach potential scheme.

Instead, the kinetic and potential energy is obtained from the motion of a unit point mass located at the end of the arm. Therefore, the second method of end effector interaction must be used to determine this motion.

7.6.2 Link Interaction

While there are two methods for determining the end effector interaction that will guide it around obstacles, neither method alone will prevent collisions of the links with the obstacles. To prevent these collisions, there must be an interaction of the links with the artificial force field. But a link occupies a region near the obstacles, not just a point. How then should the interaction be calculated? It would be too costly to integrate the total interaction of the link with the field. Also, it is the avoidance of collision that is of primary importance. Therefore, the point on the link which is closest to the obstacle should determine the amount of repulsion experienced. The following is an algorithm which determines the point on a link which is closest to an obstacle.

1. Consider the obstacle corner points with respect to the link sides.
   (a) Consider the line determined by two successive corners of the link. This line defines two half planes, one of which doesn't contain the link.
   (b) If all four of the obstacle corner points are in the halfplane without the link, proceed. Consider only the point which is closest to the halfplane edge.
   (c) Project this obstacle corner point onto the halfplane edge.
      i. If the perpendicular projection is within the side of the link then the obstacle–corner–point / link–side distance is returned as well as the point of projection on the link side.
      ii. Otherwise, the distance from the obstacle corner point to the closer corner of the link side is saved, as well as this link corner's coordinates.
   (d) After considering all four link sides, save the closest distance obtained and the corresponding link corner point.
2. Consider the link corner points with respect to the obstacle sides. Repeat steps 1.a through 1.d, interchanging the roles of the link and obstacle.
3. If steps 1.c.i or 2.c.i have not caused a return, determine the closer of the distances saved in steps 1.d and 2.d, and return this value with the corresponding link corner point.

Once the closest point of the link to the object has been determined, the artificial force is calculated. This force vector and the closest point determine the line of force. The line segment which runs through the axis of rotation of the link, along its length, acts as the lever arm. The point of intersection of the line of force with the line that contains the lever arm determines the length of the lever arm. If the lever arm is longer than the

link length then it is set to the link length. If the lever arm is less than zero (that is, it extends from the axis in the direction opposite of the link) then it is set to zero. The length of this lever arm for link N is denoted a_N.

The torque exerted on the joints is determined by a Jacobian for each link. Thus, for force on the Nth link the torque is $\tau_N = J_N^T F_N$, where the transposes of the Jacobians for a three link manipulator are:

$$J_1^T = \begin{bmatrix} 0 & a_1 C_1 \\ -a_1 S_1 & 0 \\ 0 & 0 \end{bmatrix} \tag{7.54}$$

$$J_2^T = \begin{bmatrix} -l_1 S_1 - a_2 S_{12} & l_1 C_1 - a_2 C_{12} \\ -a_2 S_{12} & a_2 C_{12} \\ 0 & 0 \end{bmatrix} \tag{7.55}$$

$$J_3^T = \begin{bmatrix} -l_1 S_1 - l_2 S_{12} - a_3 S_{123} & l_1 C_1 - l_2 C_{12} + a_3 C_{123} \\ -l_2 S_{12} - a_3 S_{123} & a_2 C_{12} + a_3 C_{123} \\ -a_3 S_{123} & a_3 C_{123} \end{bmatrix} \tag{7.56}$$

where S and C denote sine and cosine, and the subscripts indicate their arguments which are the sum of the corresponding angles. For a two link manipulator, J_1^T and J_2^T may be used, ignoring the third row.

The total torque caused by the interaction of the links with the repulsive field of the obstacle is simply: $\tau = \sum \tau_N$.

7.6.3 Simulation Experiments

Three main situations were examined: 1.) Motion to a goal point while avoiding an object surrounded by a flat-sided potential, 2.) Movement to a goal point while avoiding an object surrounded by the proposed superquadric avoidance potential, 3.) and approach of an object surrounded by the proposed superquadric approach potential. In the first two situations the end effector experiences an attractive force from a goal point and a repulsive force from the obstacle, and the links of the arm experience a repulsive force from the obstacle. For the third situation, the use of a goal point is optional and there is no link interaction.

Flat-Sided Potential

Figure 7.13 shows the simulated manipulator moving from the initial position to the goal position, successfully avoiding the obstacle. In this simulation the FIRAS potential was used as the avoidance potential around the obstacle. For this initial configuration of the manipulator the FIRAS potential works well. However, the repulsive force experienced by the links substantially aids the end effector's motion around the obstacle. To minimize this help, the end effector can be made to approach the obstacle while normal to its surface. This configuration, shown in Figure 7.14 accentuates the effect of the local minimum on the "uphill" side of the obstacle. With the link interaction reduced, the end effector settles into this local depression in the potential and stops.

Superquadric Avoidance Potential

The same arm trajectories have been initiated with the superquadric potential in the circular attractive well. Figures 7.15 and 7.16 show the end effector of a two link manipulator successfully navigating around the obstacle. This confirms the absence of a local minimum 'uphill' from the object. However, with only two degrees of freedom, the arm can not move completely around the obstacle when configured as in the second example — it becomes stuck when the repulsive torque of the obstacle on the second link equals the attractive torque of the goal point on the end effector. This is not a deficiency in the form of the potential, but a deficiency in the two link manipulator. Figure 7.17 shows that a three link design does not have this same problem. The arm is able to 'snake' around the obstacle, and the end effector is able to achieve the goal point.

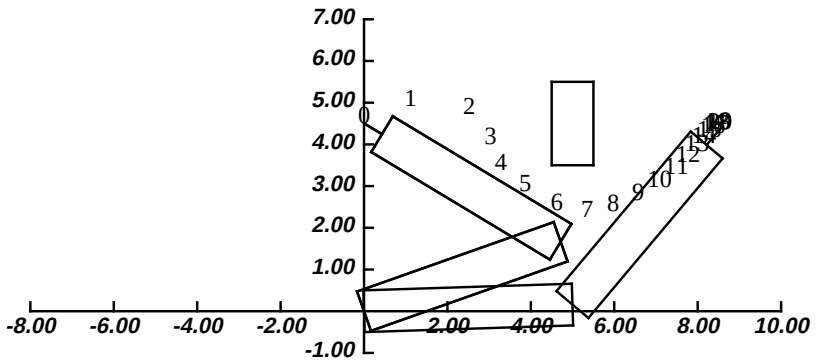

Figure 7.13: Successful avoidance of an obstacle using the FIRAS potential $(r_0 = 1.5)$.

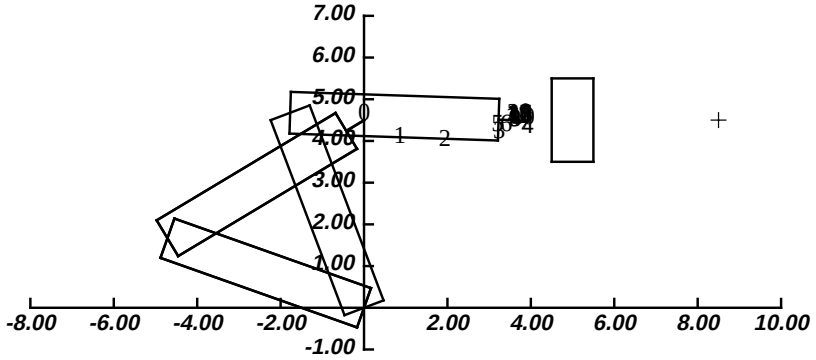

Figure 7.14: Unsuccessful avoidance of an obstacle using the FIRAS potential $(r_0 = 1.5)$. The end effector has settled in a local minimum just 'uphill' from the obstacle.

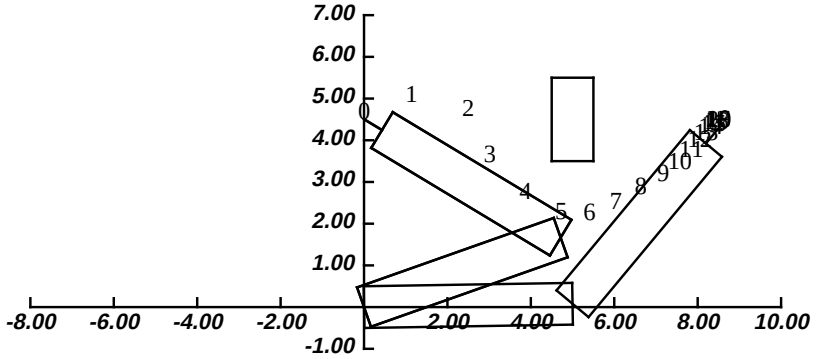

Figure 7.15: Successful avoidance of an obstacle using a superquadric potential $(\alpha = 7.0)$.

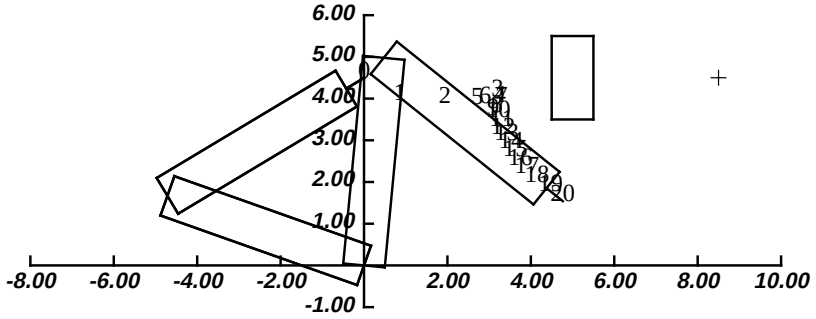

Figure 7.16: Successful avoidance of an obstacle using a superquadric potential. The minimum value of α that will allow avoidance has been used $(\alpha = 4.4)$. The arm is prevented from reaching the goal by its geometric limitations.

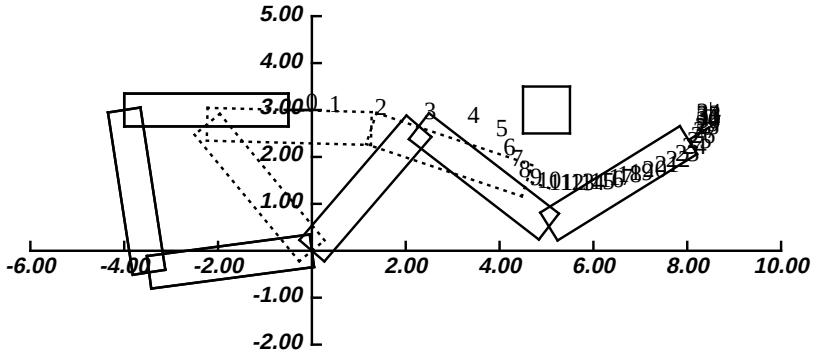

Figure 7.17: Successful avoidance of an obstacle using the newly proposed function. The minimum value of α that will allow avoidance has been used $(\alpha = 3.76)$. The redundancy of the manipulator enables it to 'snake' its way around the obstacle. The dotted manipulator is an intermediate configuration.

A third situation was also examined. Four obstacles surrounded by superquadric avoidance potentials were placed in a conical attractive well. Figures 7.18 and 7.19 show the manipulator successfully navigating between them to achieve the specified goal point. The start and finish points were interchanged for the two simulations. Different trajectories were created, but the traversal time was about the same.

Approach Potential

Finally, the motion of the end effector approaching the surface of a rectangle and a triangle has been simulated in Figures 7.20 and 7.21. For these simulations, no attractive point was used. Instead, the arm was given an initial end effector velocity with its corresponding kinetic energy. The height of the potential at the surface was set to ninety percent of the initial kinetic and potential energy. To eliminate any computational errors due to the discrete time nature of the calculations, the height of the potential was continually modified to ninety percent of the kinetic and potential energy. Also, the end effector was position controlled in the direction parallel to the surface.

7.7 Experiments

The proposed avoidance strategy has been implemented as a controller on the CMU DDARM II system. The current implementation prevents collisions of the end effector with obstacles in a two dimensional horizontal plane. Since the CMU DDARM II is a SCARA configuration arm the end effector hangs down into the plane, eliminating the need for the calculation of link interaction forces.

Figure 7.22 shows multiple paths taken by the end effector in successive experiments from different starting positions in a conical well. The end effector always reaches the goal point even though different directions may be taken around the obstacle. Notice that no local minimum is encountered.

Figure 7.23 shows a path taken to successfully navigate between two obstacles in a conical well. The potential around the rectangle, as evidenced by the path taken, is essentially spherical. This is necessary to prevent the creation of a local minimum in front of it. The path around the triangle, however, follows its shape more closely. This was accomplished by reducing the parameter A. No minimum is created due to the triangle's orientation.

The superquadric avoidance potentials have also been used while the manipulator is under control of a joystick. In this scenario the operator is prevented from inadvertently driving the manipulator into the obstacles by the repulsive force of the avoidance potentials. The obstacle potentials are given a small range (by reducing A) so that very little of the workspace is eliminated. No global well is used. Effectively, this scenario replaces the artificial potential path generation with the much higher level path planning of the operator. However, the superquadric avoidance potentials still remain valuable as a preventative measure against operator error.

The current implementation calculates the artificial forces due to the global well potential and the superquadric object potential. Commanded joint torques may be calculated by use of the transpose of the Jacobian or by using resolved acceleration control [41]. The algorithm runs at a peak speed of 375 Hz for one object, 200 Hz for two objects. Due to the sequential computation of the object potentials, addition of other obstacles to the environment increases the computational requirements linearly. Parallelization of the code could be easily implemented with the addition of more processors, yielding a control rate equal to that for one object. Object positions are currently constant valued variables in the control code, but visual feedback will in the future provide object position data in real time, enabling dynamic obstacle avoidance.

7.8 Conclusion

A novel superquadric potential has been developed that provides obstacle avoidance and object approach capabilities. Robust obstacle avoidance and goal acquisition is achieved by governing the end effector motion with an avoidance potential placed in an global attractive well. Local minima are not generated in the

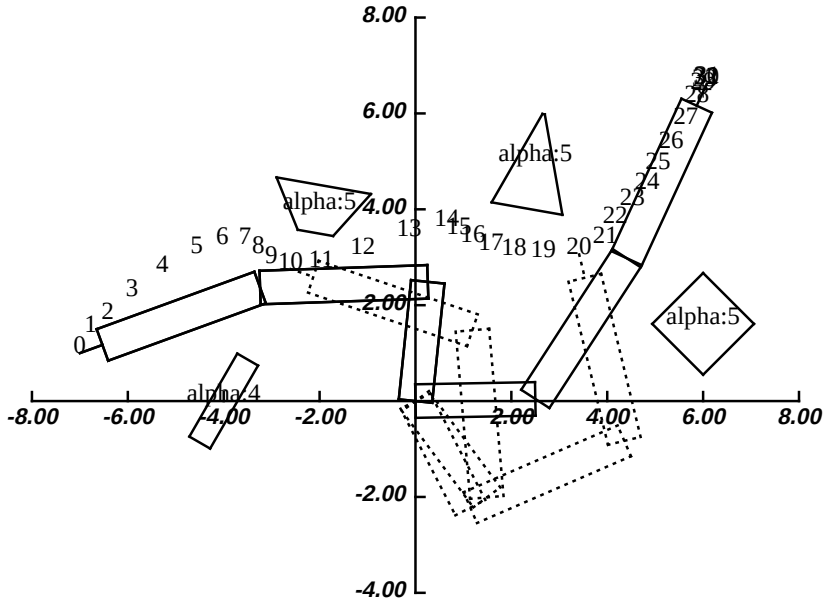

Figure 7.18: Successful navigation around four obstacles using superquadric avoidance potentials and a modified conical attractive well. The dotted manipulators are intermediate configurations.

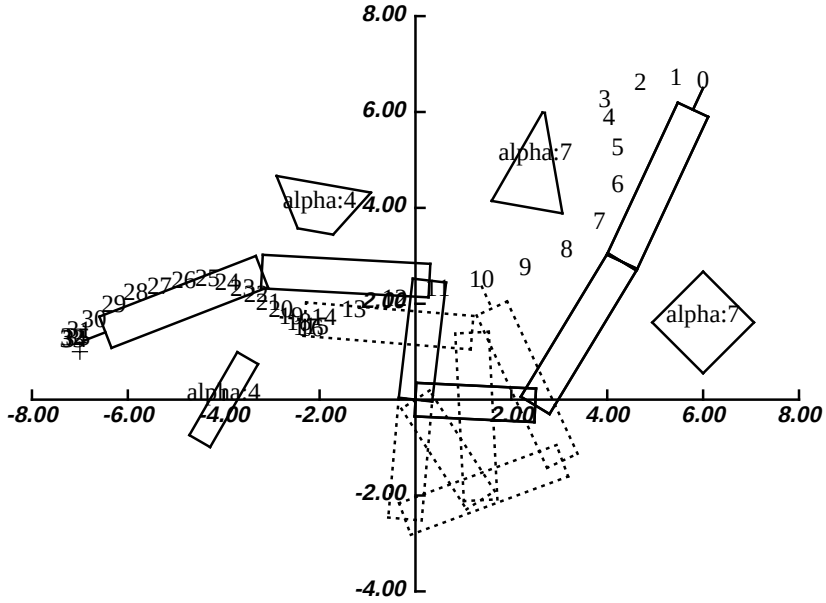

Figure 7.19: The same situation as Figure 7.18 except that the starting and ending points have been interchanged. Notice that a different trajectory has been created but the time of traversal is about the same.

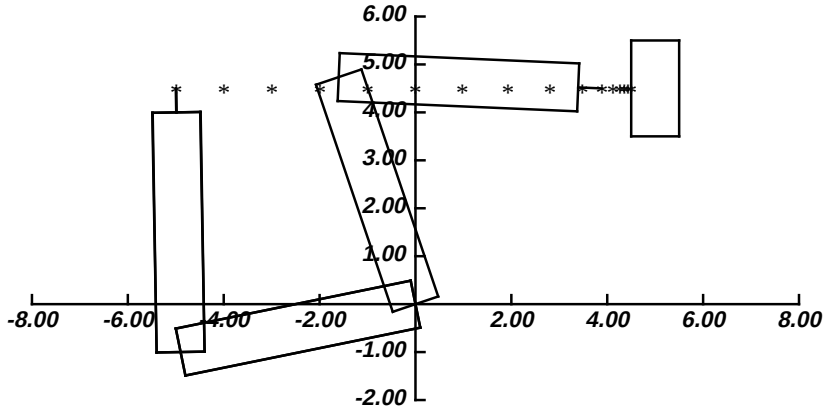

Figure 7.20: This figure shows successful approach and contact with a rectangle surrounded by the proposed approach potential. For this simulation there was no attractive point, but the end effector was position controlled in the y direction. The initial velocity was 1 unit/sec in the x direction. The contact velocity was 0.06 unit/sec.

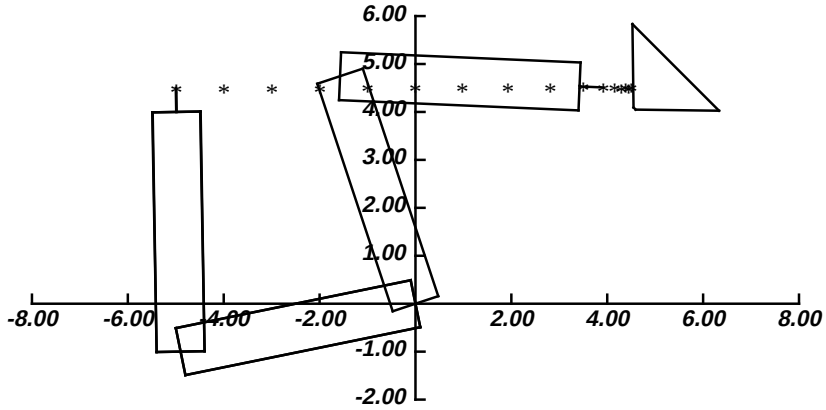

Figure 7.21: This Figure shows successful approach and contact with a triangle surrounded by the proposed approach potential. For this simulation there was no attractive point, but the end effector was position controlled in the y direction. The initial velocity was 1 unit/sec in the x direction. The contact velocity was 0.05 unit/sec.

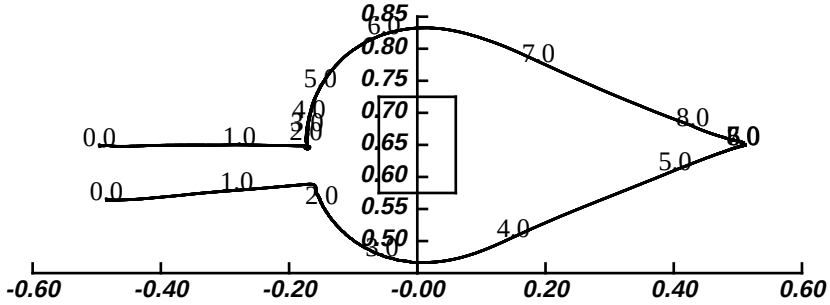

Figure 7.22: Experimental data showing two paths taken to successfully avoid an obstacle by using the superquadric avoidance potential in a conical well. The well parameters are: k = 150 N/m, s = 0.1 m, damping = 150 $\mathrm{N} \cdot \mathrm{s/m}$. The object potential parameters are: α = 20, A = 0.1. The numbers along the paths indicate the time in seconds.

workspace because of the asymptotically spherical nature of the superquadric potential. Link collisions with the environment are also eliminated by this scheme. For object approach, a second form of the superquadric potential may be employed to generate deceleration forces. This scheme reduces contact velocities and forces to tolerable levels. Both the avoidance and approach potentials have been implemented in simulations of two and three link manipulators. The avoidance potentials have been successfully implemented in real time on the CMU DDARM II. The results indicate an improvement over other local potential schemes.

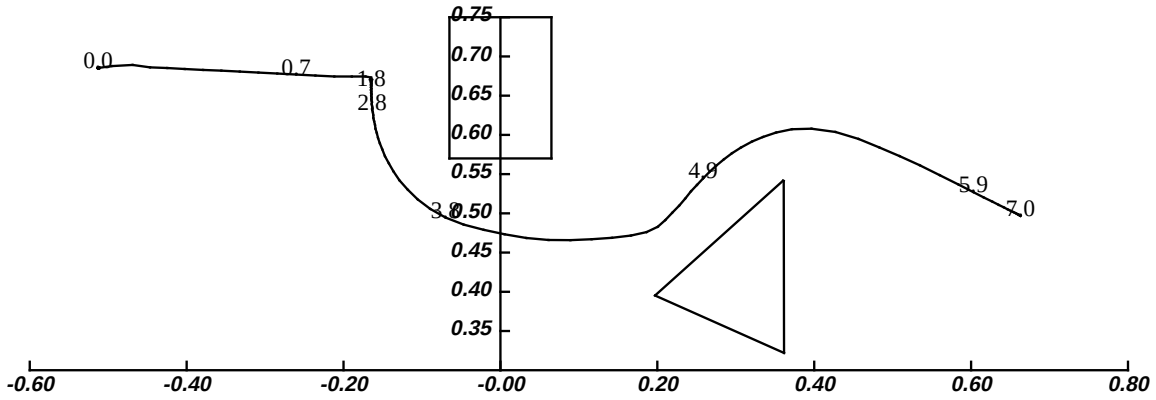

Figure 7.23: Experimental data showing a path taken to successfully navigate between two objects in a conical well. The well parameters are: k = 50 N/m, s = 0.1 m, damping = 25 $\mathrm{N} \cdot \mathrm{s/m}$. For the rectangle, the potential parameters are: α = 6, A = 0.1. For the triangle, the potential parameters are: α = 3, A = 0.01. The numbers along the paths indicate the time in seconds.

Chapter 8

Summary and Conclusions

This dissertation has dealt with the broad problem of having a manipulator move through an environment with obstacles in it, stably impact with a surface in that environment, and subsequently apply force to the surface. To address this problem it was divided into its three natural parts of object avoidance/approach, impact control, and force control. The first part was dealt with by the creation of a new artificial potential formulation based on superquadrics. This potential scheme proved useful for obstacle avoidance without the creation of local minima, and for creating safe approach trajectories to surfaces in the environment. Upon contact with the approached surface, impact control becomes important. This second part of the problem was solved in this thesis by setting the major goal of the controller to be continued contact with the environment, and not force trajectory following. The result was a control scheme that is consistent with previously proposed force control strategies, but only correct for the impact phase (and extremely valuable then). After the energy of impact has dissipated, the third stage, controlling the forces of interaction, becomes dominant. A full spectrum of force control strategies was analyzed on the same arm / sensor / environment system so that they could be experimentally compared and contrasted for the first time. Crucial to this analysis was the development and verification of the fourth order system model. The use of this model in the analysis not only confirmed its correctness, but also explained the behavior of the tested force controllers.

Interestingly enough, it proved useful within the body of this thesis to discuss the above problem parts in exactly the opposite order. This is simply because complete understanding of each requires understanding of the components upon which it is dependent. As has been apparent, a system model is necessary to analyze force control; an understanding of force control is needed to see its relation to impedance control; a review of force and impedance control is necessary to see their essential equivalence (particularly, proportional gain force control), and to see how impact control as well as artificial potential formulations can be derived from both.

8.1 Contributions

This dissertation has made the following unique and important contributions to the solution of the above problem:

- The fourth order model of the of the arm / sensor / environment has been experimentally verified. Correct parameter values have been extracted and physically explained.
- Explicit force control strategies have been theoretically analyzed in the context of the above model, and the stability properties of each explained.
- Explicit force control strategies have been unified under a common framework.
- Second order impedance control has been shown to be essentially equivalent to proportional gain explicit force control with feedforward.

- An stable impact controller has been extracted from the connection of impedance and explicit force control.
- Experimental verification and evaluation has been performed in six DOF, showing the following results:
  - Integral force control is best for force tracking.
  - Proportional force control with feedforward is essentially equivalent to second order impedance control.
  - PD force control is impractical (for stiff force sensors).
  - Force control schemes that employ the derivative of position or force require very high sampling rates.
- Superquadric artificial potentials have been developed as an improvement over previously proposed local obstacle avoidance schemes.
- Artificial potentials have been proposed as a way to generate safe approach trajectories to the environment.

8.2 Conclusions

The following can be concluded from the results presented in this thesis:

- A correct model of the arm / sensor / environment is necessary to understand and predict the behavior of force controllers. However, such a model is not necessary to determine controller gains. Good gain values may be easily determined empirically for new environments.
- Integral force control is the proper choice for superior force trajectory tracking capability. The lag present with this controller cannot be eliminated (by other proposed schemes) without having the manipulator lose contact with the environment. The steady state error to a constant input is zero, and the noise of the system is filtered by the dominant pole. Thus, the response of the system is excellent to the common command of a constant force. Also, the controller follows the slope of a ramp input correctly, only delayed in time.
- Impedance Control and Explicit Force Control are usually considered to be two distinctly different methods of interacting with the environment [70]. However, it has been shown in this dissertation that proportional gain explicit force control with feedforward, and second order impedance control are essentially the same control strategy. They become equivalent for very stiff environments. Ironically, this is exactly the situation for which impedance control has been claimed to be a better choice [22].
- Impact control is the best way to stably contact the environment. It may consist of negative proportional gain explicit force control with feedforward, or second order impedance control with a very large target mass.
- Three separate controllers should be used for the three modes of manipulator operation:
  - Motion through free space: Position or first order impedance control.
  - Impact with environment: Impact control
  - Exertion of forces: Integral gain explicit force control.

  It has been shown that these may be blended together, through proper switching, to provide excellent system behavior.

- Second order impedance control with constant gains is not well suited for free space operation, impact control, *and* force following. Switching the gains improves the performance. However, second order impedance control still remains an inferior force trajectory follower. It seems apparent that if switching is to occur, a switch to a better controller, instead of just better gains, is preferable.
- Superquadric artificial potentials are a superior scheme for local obstacle avoidance. They contain all the advantages of local schemes (speed of computation, ability to deal with moving environments, etc.) but are guaranteed to eliminate local minima for a sparsely populated environment. They are, however, subject to the major shortcoming of local schemes — they are not guaranteed to always find a path to the goal. Therefore, this scheme, as with all local schemes, would be most useful if integrated with a higher level trajectory planner.

8.3 Future Directions

The developments and contributions from this dissertation could be built upon in the following ways:

- Environmental parameter identification done in real time through the use adaptive control theory. This could provide on-line estimation of proper gain values.
- Experimental analysis of explicit force, impedance, (and impact) control with a soft force sensor on the CMU DD Arm II to answer the following questions:
  - Can a better derivative signal really be obtained for force and position when in contact with the environment?
  - Does PD control work better with this sensor?
  - Is the performance of other schemes affected?
- Experimental analysis of the same full spectrum of explicit force, impedance, (and impact) control strategies with different manipulators having different drive systems.
- Experimental implementation of second order impedance control with acceleration feedback instead of force feedback.
- Integration of tactile sensing with force control to perform the following functions:
  - Correct interpretation of inertial force readings when no contact has been made with the environment.
  - Compensation for friction during motion along a surface.
- An implementation of three dimensional superquadric potentials.
- Realtime visual feedback of object position for artificial potential update.

Appendix A

Previous Work in Explicit Force Control

A.1 Force Based Explicit Force Control

Force-based explicit force controllers provide actuation torques which act directly on the manipulator. The block diagram in Figure 3.1 provides a general description of these types of controllers. The following schemes have been previously proposed.

A.1.1 Proportional Control

Wu and Paul, '80 [50] Implemented proportional control of joint torques — essentially explicit force control in joint space ($H = K_{\tau p}$) — on a one DOF manipulator. Active damping was added in joint space as well.

$$\tau = K_{\tau p}(\tau_c - \tau_m) - K_\omega \dot{\theta}_m. \tag{A.1}$$

Khatib and Burdick, '86 [31] Implemented proportional control of force with a feedforward term and active damping:

$$f \;=\; f_c \;+\; K_{fp}(f_c - f_m) \;-\; K_v \dot{x}_m \tag{A.2}$$

and the joint torques are obtained from $\tau = J^T F$

An, '86 [1] Implemented proportional control of force on 3 DOF direct drive arm with and without dominant pole filtering of error signal and feedforward of commanded force. A direct drive arm has no appreciable damping and none was added actively. However, passive compliance was used between the stiff end effector and the stiff environment. It was found that the passive compliance and the dominant pole gave better performance.

In the Laplace domain this control scheme is represented as:

$$F \;=\; F_c \;+\; K_{fp}\left(\frac{a}{s+a}\right)(F_c - F_m). \tag{A.3}$$

Eppinger and Seering, '86, '87 [13, 14] Analyzed second, fourth, and sixth order arm / sensor / environment models. Their analysis produces a model that is not consistent with that which was experimentally determined in Chapter 2. This leads to an erroneous prediction about the stability of the force controller. As discussed in Chapter 2, their analysis may be applicable to a force sensor that is softer and less damped than the environment.

The control strategy employed is simple proportional control with no feedforward term:

$$f = K_{fp}(f_c - f_m) \tag{A.4}$$

This is not practical for real implementation, because $f = 0$ when the error is zero. Usually a bias term of f_c is fedforward to eliminate this problem. However, the lack of the feedforward term does not change the characteristic equations, which are central to their stability analysis.

Youcef-Toumi, '87 [73] Implemented proportion force control with active damping on a one DOF direct drive arm. The force command was not fedforward. Active damping was added. Steady-state errors were reported. Therefore, the control strategy is:

$$f = K_{fp}(f_c - f_m) \; - \; K_v \dot{x}_m \tag{A.5}$$

Wedel and Saridis '88 [67] Implemented proportional force control on a six DOF revolute manipulator. A force feedforward term was used. No active damping was used. Poor results were reported. For completeness, the controller used is:

$$f \; = \; f_c \; + \; K_{fp}(f_c - f_m) \tag{A.6}$$

A.1.2 Integral Control

Townsend and Salisbury, '87 [60] Analyzed the effect of Coulomb friction and stiction on force control with integral feedback. The controller used is:

$$f \; = \; K_{fi} \int (f_c - f_m) dt \tag{A.7}$$

Youcef-Toumi and Gutz, '89 [74] Implemented integral force control with active damping on a one DOF arm.

$$f \; = \; K_{fi} \int (f_c - f_m) dt \; - \; K_v \dot{x}_m \tag{A.8}$$

Experimental results indicated that indicate that the damping term reduces settling time. Gains selected by optimizing a linear model of the system (similar to the one presented in Chapter 2) are reported to provide the best results.

Colgate and Hogan, '89 [9] Uses a unique 'passive physical equivalents' method of analysis to conclude that integral control is unstable when the manipulator is coupled to stiff environments. This is contrary to the analytical and experimental results of Chapters 3 and 6.

Khatib and Vischer '90 [62] Implemented joint space integral torque control. The commanded torque was also fedforward. The controller used is:

$$\tau \; = \tau_c \; + \; K_{\tau i} \int (\tau_c - \tau_m) dt \tag{A.9}$$

It was noted that this controller was selected because open loop dynamics seemed too fast to be controlled, so they were low-pass filtered by this controller. This control was implemented to actively eliminate friction in the joints. (Thus, no active damping was added to the control.) No experiments involving environmental contact were performed.

A.1.3 Proportional / Integral Control

Raibert and Craig, '81 [51] Implemented PI control of joint torques on a six DOF manipulator. Commanded force values were also fedforward. However, this scheme transforms the Cartesian force errors into

joint space before multiplying by proportional gains. The mixing of Cartesian force errors with a diagonal joint space gain matrix was shown by An to sometimes be unstable [2]. The control can be represented as:

$$\tau = J^T f_c + K_{\tau p} J^T (f_c - f_m) + K_{\tau i} \int J^T (f_c - f_m) dt \tag{A.10}$$

where J is the manipulator Jacobian.

Miyazaki and Arimoto, '84 [46] Implemented PI control on a three DOF manipulator. Active damping was also used. The results are stable but noisy. The control law is as follows:

$$f = K_{fp}(f_c - f_m) + K_{fi} \int (f_c - f_m) dt - K_v \dot{x}_m \tag{A.11}$$

Eppinger and Seering, '87 [14] Analyzed PI force control for a linear plant model. No active damping is added. The controller is:

$$f = K_{fp}(f_c - f_m) + K_{fi} \int (f_c - f_m) dt \tag{A.12}$$

Their analysis uses a model that is not consistent with that which was experimentally determined in Chapter 2. This leads to an erroneous prediction of less stability for PI force control. Chapter 6 has shown experimentally that this is not true.

A.1.4 Proportional / Derivative Control

Eppinger and Seering, '87 [14] Analyzed PD force control for a linear plant model. No active damping is added. The controller is:

$$f = K_{fp}(f_c - f_m) + K_{fd} \frac{d}{dt}(f_c - f_m) \tag{A.13}$$

Again, the plant used represents a soft sensor on a manipulator with outer arm dynamics, and in contact with an environment with no dynamics. (The comparison of this plant with the one considered herein has been made previously.) The analysis indicates that PD control is stablizing and adds closed loop bandwidth.

Xu, '88 [71] Implemented PD control on a six DOF arm with a soft force sensor. The controller is again:

$$f = K_{fp}(f_c - f_m) + K_{fd} \frac{d}{dt}(f_c - f_m) \tag{A.14}$$

It is reported that PD control provided an improvement over proportional control on the same system.

Khatib and Vischer '90 [62] Implemented PD torque control. The commanded torque was also fedforward. The controller used is:

$$\tau = \tau_c + K_{\tau p}(\tau_c - \tau_m) + K_{\tau d} \frac{d\tau_m}{dt} \tag{A.15}$$

It was noted that when the closed loop dynamics were too fast to be effectively control, then the value of this control is lost. This control was implemented to actively eliminate friction in the joints. (Thus, no active damping was added to the control.) No experiments involving environmental contact were performed.

A.1.5 Other

Yoshikawa, '87 [72] Used unusual 'Two DOF controller' scheme. The implemented result has one dominant pole at zero and a lag/lead pair at a relatively high frequency. This is effectively an integral controller.

A.2 Position Based Explicit Force Control

Position based explicit force controllers provide a reference position commanded for an inner loop position controller. The block diagram in Figure 3.14 provides a general description of these types of controllers. The following schemes have been previously proposed.

Maples and Becker, '86 [43] Implemented a scheme which can also be classified as an impedance controller because it has an outer impedance loop (as will be disussed later). However, the novelty of their approach lies in the use of another position-based loop inside of the force control loop. This innermost loop is implemented in joint space. Therefore, W is implemented in joint space as $W = K_\theta + K_\omega s$. Position commands to the innermost loop are a combination of commanded position fedforward from the outer impedance loop and a position signal from the force compensator. When in contact with the environment, the first of these signals will be constant, and can therefore be considered zero. The signal from the force compensator is the result of integration of force error. This implies that $I = 1/c_f s$. Therefore, the controller formulation is:

$$X_c = \frac{1}{c_f s}(F_c - F_m) \tag{A.16}$$

$$\tau = (K_\theta + K_\omega s)\mathcal{F}^{-1}(X_c) \tag{A.17}$$

where $\mathcal{F}^{-1}$ is the inverse kinematics of the manipulator.

Limited experimental results are reported. The measured force signal is noisy and oscillatory, but converges to the desired value.

DeSchutter, '87 [11] Analyzed and formalized inner position loop force controllers. The three specific types examined are: position and velocity feedback, position feedback only, and no inner loop feedback. It is shown that for a system in which the inner position loop contains no integration, the outer force loop must be of at least Type 1 in order to avoid steady state error.

Ishikawa, Sawada, Kawase, and Takata, '89 [25] Implemented in six DOF a scheme which can be classified as an inner loop, position-based, explicit force controller.

$$F_c = (c_f s + k_f)X_r \tag{A.18}$$

$$X_c = \frac{1}{c_f s + k_f}(F_c - F_m) \tag{A.19}$$

$$F = K_p(X_c - X_m) \tag{A.20}$$

Although there is a reference position, X_r, as input to the controller, this is equivalent to specifying a commanded force F_c. This controller fits into the position-based force control framework because the force error is multiplied by the inverse of a first order impedance, $I = c_f s + k_f$. This is essentially a low pass filter similar to that discussed previously. It provides a commanded position, X_c, to the internal position controller. Active damping is not used, but passive damping is assumed. They report stability of this controller, but do not discuss accuracy.

Appendix B

The CMU DD Arm II System

B.1 Physical Description

The physical CMU DD Arm II System appears (minus the arm itself) as depicted in Figure B.1. It consists of over ten microprocessors, a force sensor controller, a tactile sensor, a joystick, a camera, joint resolver hardware, and six joint motor amplifiers.

The microprocessor boards are of main concern here. They are located in four backplanes: three VME bus backplanes, and one Multibus backplane. The Sun's VME backplane contains Sun 3/260 Host computer and one end of a VME/VME bus repeater. The second VME backplane contains a Mercury MC3200 floating point processor, at least one Ironics M68020 processor (with 2 serial ports), a parallel IO board, two ends of VME/VME bus repeaters, and one end of a VME/Multibus repeater. The third VME backplane contains an Imaging Technology vision system, a Heurikon M68030 processor, and one end of a VME/VME repeater. The Multibus contains six Texas Instruments TMS32010 joint controllers (320s), one TMS32010 master controller, and one end of the VME/Multibus repeater.

Since it is mainly a computer system, and it is the computational hardware that we are primarily interested in here, it is best to describe the system in terms of its architecture.

B.2 The CMU DD Arm II System Architecture

The CMU DD Arm II System has a multi-tier computer architecture as shown in as in Figure B.2. The user interacts with the system through a Sun 3/260 workstation (d5.ius.cs.cmu.edu) operating under SunOS 4.0. It is connected to file servers and the CS/RI community over Ethernet. A local disk will soon be added.

The real-time control of the CMU DD Arm II is performed by the M680X0 processor(s) residing on a VME backplane that is connected to the Sun through a repeater. These processors operate under *Chimera II*, a real-time, multi-processor, multi-processing operating system [57]. Programs are downloaded to the M680X0 processor(s) through *Chim*, an interface program running on the Sun. For example, the real-time controller and user interface program, *Connie*, runs on the Ironics M68020 in this way. *Connie* communicates with the Sun, the Mercury floating point processor, the force sensor, the tactile sensor, the joystick, and the vision system. It also downloads control code to the Mercury and the 320s, as well as controlling execution rates on these boards.

The Mercury floating point processor also resides on the second VME bus. It is capable of 20 Mflops peak, or about 7 Mflops for optimized C code. This board can be accessed by the user through the Sun for code development, of by *Connie* for real-time control code execution.

Connected to the second VME bus are a third VME bus with a vision system, and a Multibus with the 320 boards. The vision system is not used for the work in this thesis. The six 320 joint controllers calculate the three phase torque values needed by the six amplifiers, as well as obtaining the joint position values from

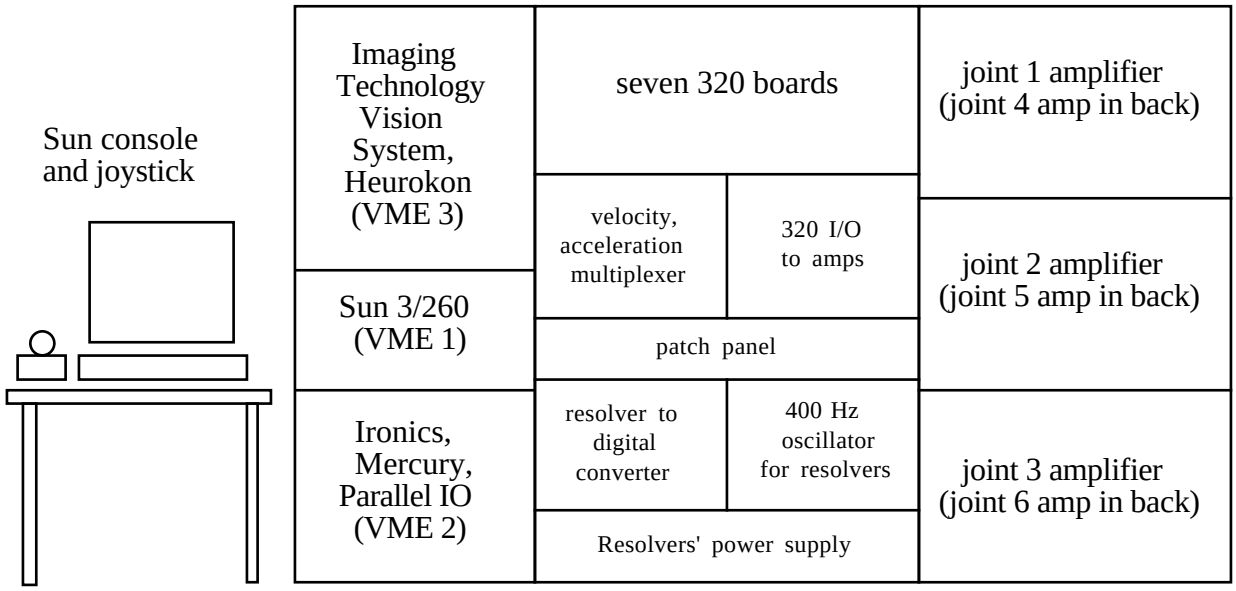

Figure B.1: The hardware of the CMU DD Arm II system.

the joint resolvers. The 320 master controller starts and stops the other six 320 boards. Its other functions have been superceded.

For more detailed information on *Connie, Chim*, the 320 processors, and the system memory configuration, see *The Users' Guide to the DD Arm II.*

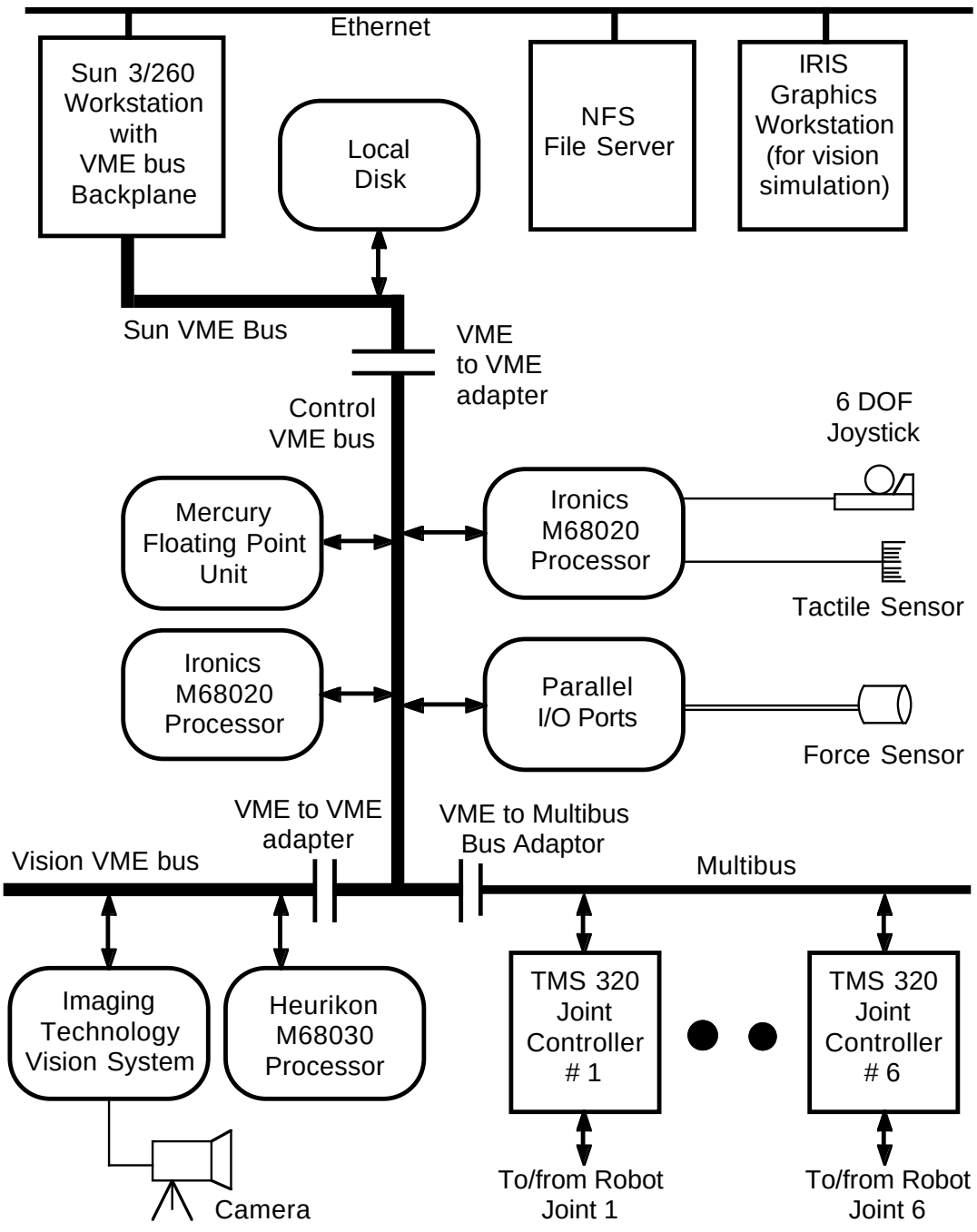

Figure B.2: System architecture for the CMU DD Arm II.

Bibliography

[1] C. An and J. Hollerbach. Dynamic Stability Issues in Force Control of Manipulators. In *Proceedings of the IEEE Conference on Robotics and Automation*, pages 890–896, 1987.

[2] C. An and J. Hollerbach. Kinematic Stability Issues in Force Control of Manipulators. In *Proceedings of the IEEE Conference on Robotics and Automation*, pages 897–903, 1987.

[3] J. R. Andrews and N. Hogan. Impedance control as a framework for implementing obstacle avoidance in a manipulator. In David E. Hardt and Wayne J. Book, editors, *Control Of Manufacturing Processes And Robotic Systems*, pages 243–251. ASME, 1983.

[4] R. Bajcsy and F. Solina. Three dimensional object representation revisited. In *First International Conference on Computer Vision*, pages 231–240, London, England, June 8-11 1987.

[5] A.H. Barr. Superquadrics and angle-preserving transformations. *IEEE Computer Graphics and Applications*, 1:11–23, 1981.

[6] A. Bejczy. Robot Arm Dynamics and Control. Technical Memorandum 33-669, Jet Propulsion Laboratory, Pasadena, CA, February 1974.

[7] M. Brady and others (editors). *Robot Motion: Planning and Control*. MIT Press, Cambridge, MA, 1982.

[8] B. Cohen-Tannoudji, C. Diu, and F. Laloe. *Quantum Mechanics*, volume 2. John Wiley and Sons, New York, 1977.

[9] E. Colgate and N. Hogan. An Analysis of Contact Instability In Terms of Passive Physical Equivalents. In *Proceedings of the IEEE Conference on Robotics and Automation*, pages 404–409, 1989.

[10] J. E. Colgate and N. Hogan. Robust control of dynamically interacting systems. *International Journal of Control*, 48(1):65–88, 1988.

[11] J. De Schutter. A Study of Active Compliant Motion Control Methods For Rigid Manipulators Based on a Generic Scheme. In *Proceedings of the IEEE Conference on Robotics and Automation*, pages 1060–1065, 1987.

[12] J. De Schutter. Improved Force Control Laws For Advanced Tracking Applications. In *Proceedings of the IEEE Conference on Robotics and Automation*, pages 1497–1502, 1988.

[13] S. Eppinger and W. Seering. On Dynamic Models of Robot Force Control. In *Proceedings of the IEEE Conference on Robotics and Automation*, pages 29–34, 1986.

[14] S. Eppinger and W. Seering. Understanding Bandwidth Limitations on Robot Force Control. In *Proceedings of the IEEE Conference on Robotics and Automation*, pages 904–909, Raleigh, N.C., 1987.

[15] B. Faverjon. Obstacle avoidance using an octree in the configuration space of a manipulator. In *Proceedings of the IEEE Conference on Robotics and Automation*, pages 504–512, Atlanta, GA, 1984.

[16] K. Fu, R. Gonzalez, and C. Lee. *Robotics: Control, Sensing, Vision, and Intelligence*. McGraw-Hill, New York, 1987.

[17] M. Gardiner. The superellipse: A curve that lies between the ellipse and the rectangle. *Scientific American*, September 1965.

[18] A. Goldenberg. Implementation of Force and Impedance Control in Robot Manipulators. In *Proceedings of the IEEE Conference on Robotics and Automation*, pages 1626–1632, 1988.

[19] W. Hamilton. Globally Stable Compliant Motion Control For Robotic Assembly. In *Proceedings of the IEEE Conference on Robotics and Automation*, pages 1179–1184, 1988.

[20] H. Hanafusa and H. Asada. Stable prehension by a robot hand with elastic fingers. In M. Brady et al., editors, *Robot Motion: Planning and Control*, pages 323–335. MIT Press, 1982.

[21] N. Hogan. Impedance control: An approach to manipulation. *Journal of Dynamic Systems, Measurement, and Control*, 107:1–24, March 1985.

[22] N. Hogan. Impedance Control: An Approach to Manipulation: Parts I, II, and III. *Journal of Dynamic Systems, Measurement, and Control*, 107:1–24, March 1985.

[23] N. Hogan. Stable Execution of Contact Tasks Using Impedance Control. In *Proceedings of the IEEE Conference on Robotics and Automation*, pages 1047–1054, 1987.

[24] N. Hogan and S.L. Cotter. Cartesian Impedance Control of a Nonlinear Manipulator. In W.J. Book, editor, *Robotics Research and Advanced Applications*, pages 121–128, New York, 1982. ASME.

[25] H. Ishikawa, C. Sawada, K. Kawase, and M. Takata. Stable Compliance Control and Its Implementation for a 6 D.O.F. Manipulator. In *Proceedings of the IEEE Conference on Robotics and Automation*, pages 98–103, 1989.

[26] J. Kahng and F. Amirouche. Impact Force Analysis in Mechanical Hand Design — Part I. *International Journal of Robotics and Automation*, 3(3):158–164, 1988.

[27] H. Kazerooni. Robust, Non-Linear Impedance Control for Robot Manipulators. In *Proceedings of the IEEE Conference on Robotics and Automation*, pages 741–750, 1987.

[28] H. Kazerooni, T. Sheridan, and P. Houpt. Robust Compliant Motion for Manipulators, Parts I and II. *IEEE Journal of Robotics and Automation*, RA-2(2):83–105, June 1986.

[29] O. Khatib. *Commande Dynamique dans l'Espace Operationnel des Robots Manipulateurs en Presence d'Obstacles*. PhD thesis, Ecole Nationale Superieure de l'Aeronautique et del'Espace (ENSAE), December 1980.

[30] O. Khatib. Real-Time Obstacle Avoidance for Manipulators and Mobile Robots. *The International Journal of Robotics Research*, 5(1), 1986.

[31] O. Khatib and J. Burdick. Motion and Force Control of Robot Manipulators. In *Proceedings of the IEEE Conference on Robotics and Automation*, pages 1381–1386, 1986.

[32] P. Khosla. *Real-Time Control and Identification of Direct Drive Manipulators*. PhD thesis, Carnegie Mellon University, Department of Computer and Electrical Engineering, August 1986.

[33] Daniel E. Koditschek. Exact robot navigation by means of potential functions: Some topological considerations. In *IEEE International Conference on Robotics and Automation*, Raleigh, North Carolina, March 31 – April 3 1987.

[34] K. Kreutz. On Manipulator Control by Exact Linearization. *IEEE Transactions on Automatic Control*, 34(7):763–767, July 1989.

[35] B. Krogh. A generalized potential field approach to obstacle avoidance control. In *SME Conf. Proc. Robotics Research: The Next Five Years and Beyond*, Bethlehem, Pennsylvania, August 1984.

[36] D. Lawrence. Impedance Control Stability Properties in Common Implementations. In *Proceedings of the IEEE Conference on Robotics and Automation*, pages 1185–1190, 1988.

[37] T. Lozano-Perez. Spatial planning: A configuration space approach. *IEEE Transactions on Computers*, C-32(2):102–120, 1983.

[38] T. Lozano-Perez. A simple motion planning algorithm for general manipulators. Ai lab memo, MIT, AI Labs, Cambridge, MA, 1986.

[39] T. Lozano-Perez and M. Wesley. An algorithm for planning collision free paths among polyhedral objects. *Comm. of ACM*, 22(10):560–570, 1979.

[40] J. Luh, M. Walker, and R. Paul. Resolved-Acceleration Control of Mechanical Manipulators. *IEEE Transactions on Automatic Control*, 25(3):468–474, June 1980.

[41] J. Luh, M. Walker, and R. Paul. Resolved-acceleration control of mechanical manipulators. *IEEE Transactions on Automatic Control*, 25(3):468–474, June 1980.

[42] V. Lumelsky and K. Sun. Gross motion planning for a simple 3d articulated robot arm moving amidst unknown arbitrarily shaped objects. In *Proceedings of the IEEE International Conference on Robotics and Automation*, pages 1929–1934, Raleigh, North Carolina, March 31 – April 3 1987.

[43] J. Maples and J. Becker. Experiments in Force Control of Robotic Manipulators. In *Proceedings of the IEEE Conference on Robotics and Automation*, pages 695–702, 1986.

[44] B. Markiewicz. Analysis of the Computed-Torque Drive Method and Comparison with the Conventional Position Servo for a Computer-Controlled Manipulator. Technical Memorandum 33-601, Jet Propulsion Laboratory, Pasadena, CA, March 1973.

[45] M. Mason. Compliance and Force Control for Computer Controlled Manipulators. *IEEE Transactions on Systems, Man, and Cybernetics*, 11(6):418–432, June 1981.

[46] F. Miyazaki and S. Arimoto. Sensory Feedback for Robot Manipulators. *Journal of Robotic Systems*, 2(1):53–71, 1985.

[47] W. Newman. Automatic obstacle avoidance at high speeds via reflex control. In *Proceedings of the IEEE Conference on Robotics and Automation*, pages 1104–1109, 1989.

[48] W. S. Newman and N. Hogan. High speed control and obstacle avoidance using dynamic potential functions. In *IEEE International Conference on Robotics and Automation*, Raleigh, North Carolina, March 31 – April 3 1987.

[49] M. Okutomi and M. Mori. Decision of robot movement by means of a potential field. *Advanced Robotics*, 1(2):131–141, 1986.

[50] R. Paul and C. Wu. Manipulator Compliance Based on Joint Torque. In *IEEE Conference on Decision and Control*, pages 88–94, New Mexico, 1980.

[51] M. Raibert and J. Craig. Hybrd Position/Force Control of Manipulators. *Journal of Dynamic Systems, Measurement, and Control*, 103(2):126–133, June 1981.

[52] E. Rimon and E. Koditschek. The construction of analytic diffeomorphisms for exact robot navigation on star worlds. In *Proceedings of the IEEE Conference on Robotics and Automation*, pages 21–26, 1989.

[53] R. K. Roberts. *The Compliance of End Effector Force Sensors for Robot Manipulator Control*. PhD thesis, Purdue University, Department of Mechanical Engineering, December 1984.

[54] J. K. Salisbury. Active Stiffness Control of a Manipulator in Cartesian Coordinates. In *IEEE Conference on Decision and Control*, pages 95–100, New Mexico, 1980.

[55] J. Schwartz and M. Sharir. On the piano movers problem, part ii. Technical Report 41, Courant Institute of Mathematical Sciences, NY, NY, 1982.

[56] A. Sharon, N. Hogan, and D. Hardt. Controller Design in the Physical Domain (Application to Robot Impedance Control). In *Proceedings of the IEEE Conference on Robotics and Automation*, pages 552–559, 1989.

[57] D. Stewart, D. Schmitz, and P. Khosla. Implementing Real-Time Robotic Systems Using Chimera II. In *Proceedings of the IEEE International Conference on Robotics and Automation*, pages 598–603, May 1990.

[58] K. Symon. *Mechanics*. Addison-Wesley, Reading, Massachusetts, 1960. textbook.

[59] W. Thomson. *Theory of Vibration with Applications*. Prentice Hall, NJ, 1981.

[60] W. Townsend and J. Salisbury. The Effect of Coulomb Friction and Stiction on Force Control. In *Proceedings of the IEEE Conference on Robotics and Automation*, pages 883–889, 1987.

[61] S. Udupa. Collision detection and avoidance in computer controlled manipulators. In *Proceedings of the 5-th Joint International Conference on AI*. AI, 1977.

[62] D. Vischer and O. Khatib. Design and Development of Torque-Controlled Joints. In V. Hayward and O. Khatib, editors, *Experimental Robotics I*, pages 271–286. Springer-Verlag Berlin Heidelberg, 1990.

[63] R. Volpe and P. Khosla. Artificial Potentials with Elliptical Isopotential Contours for Obstacle Avoidance. In *Proceedings of the 26th IEEE Conference on Decision and Control*, pages 180–185, Los Angeles, CA, December 9-11, 1987.

[64] R. Volpe and P. Khosla. A Strategy For Obstacle Avoidance and Approach Using Superquadric Potential Functions. In *Proceedings of the 5^{th} International Symposium of Robotics Research*, pages 93–100, Tokyo, Japan, August 28-31 1989. MIT Press.

[65] R. Volpe and P. Khosla. Manipulator Control with Superquadric Artificial Potential Functions: Theory and Experiments. *IEEE Transactions on Systems, Man, and Cybernetics; Special Issue on Unmanned Vehicles and Intelligent Systems*, November/December 1990.

[66] C. Warren. Global path planning using artificial potential fields. In *Proceedings of the IEEE Conference on Robotics and Automation*, pages 316–321, 1989.

[67] D. Wedel and Saridis G. An Experiment in Hybrid Position/Force Control of a Six DOF Revolute Manipulator. In *Proceedings of the IEEE Conference on Robotics and Automation*, pages 1638–1642, 1988.

[68] D. Whitney. Resolved Motion Rate Control of Manipulators and Human Protheses. *IEEE Transactions on Man-Machine Systems*, 10(2):49–53, June 1969.

[69] D. Whitney. Force Feedback Control of Manipulator Fine Motions. *Journal of Dynamic Systems, Measurement, and Control*, pages 91–97, June 1977.

[70] D. Whitney. Historical Perspective and State of the Art in Robot Force Control. In *Proceedings of the IEEE Conference on Robotics and Automation*, pages 262–268, 1985.

[71] Y. Xu and R. Paul. On Position Compensation and Force Control Stability of a Robot with a Compliant Wrist. In *Proceedings of the IEEE Conference on Robotics and Automation*, pages 1173–1178, 1988.

[72] T. Yoshikawa. Dynamic Hybrid Position/Force Control of Robot Manipulators — Description of Hand Contraints and Calculation of Joint Driving Force. *IEEE Journal of Robotics and Automation*, RA-3(5):386–392, October 1987.

[73] K. Youcef-Toumi. Force Control of Direct-Drive Manipulators For Surface Following. In *Proceedings of the IEEE Conference on Robotics and Automation*, pages 2055–2060, 1987.

[74] K. Youcef-Toumi and D. Gutz. Impact and Force Control. In *Proceedings of the IEEE Conference on Robotics and Automation*, pages 410–416, 1989.